Improving gas fixation in acetogenic bacteria

by

David Frederic Emerson

Submitted to the Department of Chemical Engineering
in partial fulfillment of the requirements for the degree of

Doctor of Philosophy in Chemical Engineering

at the

MASSACHUSETTS INSTITUTE OF TECHNOLOGY

September ~~2019~~ 2018

Signature redacted

Author .....
Department of Chemical Engineering
August 9, 2018

Signature redacted

Certified by .....
Gregory Stephanopoulos
Willard Henry Dow Professor of Chemical Engineering and Biotechnology
Thesis Supervisor

Signature redacted

Accepted by .....
Patrick S. Doyle
Chairman, Committee for Graduate Students

Improving gas fixation in acetogenic bacteria

by

David Frederic Emerson

Submitted to the Department of Chemical Engineering
on August 9, 2018, in partial fulfillment of the
requirements for the degree of
Doctor of Philosophy in Chemical Engineering

Abstract

Waste gases are an increasing concern for their impact on the environment. This includes carbon dioxide (CO_2) produced from industry and transportation, and methane from distributed oil wells and shale gas formations. Generally, these gases are released to the environment, or CH_4 is burned to CO_2, as CH_4 is a more harmful greenhouse gas than CO_2. Researchers are increasingly interested in methods to fix these two gases into valuable fuels and chemicals so as to achieve a sustainable economy. However, any such technology must be economically viable to ensure widespread adoption in the regions that these gases are released.

Yet biological gas fixation has many limitations that currently prevent practical implementation. This includes biological limitations such as slow growth rates, and low biomass and product titers. Process limitations are also a concern, as full conversion is desirable and gas mass transfer can be a substantial rate limiting step. Reactors must also be simple and cheap due to the expected cost differential between the reducing equivalents (electricity, H_2, etc.) and the products (fuels and commodity chemicals). This thesis approaches the limitations of gas fixation from three different perspectives to overcome biological limitations and design low cost bioreactors.

Syngas fermentation via the Wood-Ljungdahl pathway is receiving growing attention as a possible platform for the fixation of CO_2 and renewable production of fuels and chemicals. However, the pathway operates near the thermodynamic limit of life, resulting in minimal ATP production and long doubling times. This calls into question the feasibility of producing high-energy compounds at industrially relevant levels. In **Chapter** 2, we investigated the possibility of co-utilizing nitrate as an inexpensive additional electron acceptor to enhance ATP production during autotrophic growth of *Clostridium ljungdahlii*. In contrast to other acetogens tested, growth rate and final biomass titer were improved for *C. ljungdahlii* growing on a mixture of H_2 and CO_2 when supplemented with nitrate. Transcriptomic analysis, $^{13}CO_2$ labeling, and an electron balance were employed to understand how electron flux is partitioned between CO_2 and nitrate. Finally, we propose a pathway for enhanced ATP production from nitrate, and use this as a basis to calculate theoretical yields for a variety of products. This was experimentally confirmed, whereby nitrate

improved heterologous production of 3-hydroxybutyrate, though yields remain much lower than could be theoretically achieved. This work demonstrates a viable strategy for the decoupling of ATP production from carbon dioxide fixation, which will serve to significantly improve the CO_2 fixation rate and the production metrics of other chemicals from CO_2 and H_2 in this host. Future metabolic engineering could greatly increase the yield to those predicted in the theoretical analysis.

In **Chapter** 3, we utilize another electron donor, methanol, for the fixation of CO_2 with the Wood-Ljungdahl pathway. However, the literature is somewhat in disagreement for the mechanism of methanol assimilation by acetogens and the genes involved. Deuterated methanol labeling was used to confirm that methanol was assimilated at the methyl level, indicating that a 3-component methyltransferase system (*mtaABC*) was involved. RNAseq analysis revealed that, while *mtaB* and *mtaC* were likely properly annotated in *Moorella thermoacetica*, *mtaA* was not properly annotated based just on homology. We propose other methyltransferases that were highly upregulated in the presence of methanol as putative *mtaA* genes that must be confirmed with future in vitro assays.

In the final **Chapter**, 4, we propose a potentially inexpensive reactor for the in situ conversion of methane at natural gas well heads. The mass transfer limits of simple reactor were analyzed, and minimum catalytic rates were calculated such that this methane would be full converted.

Thesis Supervisor: Gregory Stephanopoulos
Title: Willard Henry Dow Professor of Chemical Engineering and Biotechnology

Acknowledgments

Graduate school has been a wonderful experience; in part this was due to an enjoyable project. The major reason was the people, from lab mates, to friends, and family, their support led to a successful PhD.

First I'd like to thank Professor Stephanopoulos, as his support was integral for pursuing research that was both interesting and influential. He provided ample opportunity to learn and grow as a scientist and engineer, and has always kept my ideas and projects grounded. I'd like to also thank my committee members, Professor Peter Girguis, Professor Catherine Drennan, and Professor Kristala Prather, as they provided insightful comments and critiques during our meetings. With their support, my research was well rounded and took on new scientific depth.

While in Cambridge, I spent the most time with my lab mates and they had the largest impact on my stay at MIT and Cambridge. Dr. Hamid Rismani was the first to show me the techniques for anaerobic microbiology that took me through my PhD. Ben Woolston was in the cohort before mine, and also my TA in Biochemical engineering at Penn State. Through out my PhD, Ben has always provided substantial contributions to my experiments and research directions. I also greatly enjoyed our collaborations, though I'm definitely not doing any more RNA extractions and qRT-PCR experiments for him. Dr. Devin Currie joined a bit after me, and like Ben, made the lab and our sub-group in the lab lively. Where Hamid left off, Devin picked up in teaching and directing the techniques I used in my projects. And science aside, I will always remember the zany conversations we had at the Muddy and in Meadhall. Dr. Jason King joined and rounded out our sub-group that lasted the majority of my PhD; he brought a much different perspective coming from a Chemistry PhD.

I'd also like mention Kristen Davis and Dr. Jack Hammond; they were in lab for shorter stints, yet I greatly enjoyed the interactions I had with them. I was sad to see them leave; luckily we have all remained in the area. Finally I like to thank my pseudo-collaborator at Harvard, Dr. Jeff Marlow; while we didn't collaborate much during my PhD, I enjoyed going out for drinks occasionally, talking about science or

whatever topic came up.

A big thank you to my other lab mates, including Zhe Zhang, Dr. Steven Edgar, Dr. Jun Park, Dr. Tom Wasylenko, Dr. Mark Kiebler, and Dr. Brian Pereira. Without them, it would have not been the same.

To my undergraduates that I've worked with and supervised: Arica Wyche, Mackenzie Donnelly, and Sarah - thank you! I wish you the best as you pursue your careers and graduate work.

My main hobby while in Cambridge was soccer, and I was captain of the ChemE team for the majority of my time at MIT. I'd like to thank all my team mates: Carlos Siepermann, Steven Brown, Xiao Su, William Ho, Daniel Salem, Bavand Keshavarz, Naveed Bakh, Kosi Aroh, and the many others with whom I've played.

I'd like to thank my family for their support throughout my past 28 years. Without them, who knows if I would have come this far? My brother, Dow, has always been a metric for which I measured myself. He also was also the threshold I always wanted to surpass; call it friendly or brotherly competition. This competition was easy to measure in high school, and at the beginning of college (as we both went to Penn State). But our pathways quickly diverged as he pursued a different "doctorship", and moved south to North Carolina to pursue that dream. I'm proud of what he has achieved towards that goal, and feel closer to him now even though we live far away.

I'm proud to say that my personality was shaped by my mom's (Tracy) support and teachings. At a young age, we lost my dad in an unfortunate vehicle accident. Despite it all, my mom has always kept us moving forward; kept us pursuing our dreams and making the most of ourselves. With young twins, and a demanding job, this could not have been easy. However she has always kept a smile on her face and pushed through. I know my mom always says she is proud of me; I'm also proud of her. Recently, my mom has remarried to Peter Howland; Pete has always been a friend, and while he can never fill the role of father, I'm happy to have him as part of our family. The same goes for Curran and Alex, whom I'm happy to call step-brother.

Finally, I'd like to thank and dedicate this thesis to my dad, Dow Eldon Emerson III (or Duff to those that knew him). You could say I followed in his foot steps, as

we both attended Penn State for Chemical Engineering. While he left us at a young age, I will always remember the positive influence he had on shaping my brother and I. He'd always tell us: "It matters not how you act in front of others, it matters how you act when no one is looking."

Contents

List of Figures

List of Tables

Chapter 1

Introduction

1.1 Limitations in converting gases into fuels and chemicals

Gas fixation serves a crucial role in the carbon cycles of Earth, for which the two main gases are carbon dioxide (CO_2) and methane (CH_4) [1, 2]. Yet the past 100 years of industrialization and development destabilized this cycle, increasing the concentration of atmospheric greenhouse gases and resulting in climate change. Humans release substantial quantities of CO_2 each year; the amount released and the atmospheric concentration continue to rise [1]. Many researchers are interested in capturing and sequestering these gases [3], yet there is little economic or political incentive [4]. One might consider CO_2 fixation in current industrial processes, however these processes only consume 120 megatons as compared to the 9 gigatons released [5, 1]. Another possibility is enhanced oil recovery. Operators are incentivized with higher yields while the CO_2 is also stored underground. Yet enhanced oil recovery has a key limitation; one must consider cost to transport the gas to the well site [6, 7]. Moreover, increasing quantities of CO_2 are released by 2nd and 3rd world nations for whom there is little incentive for CO_2 capture or transportation to sequestration sites [1, 8].

Methane also contributes substantially to climate change [9, 10, 11]; while methane

burns cleaner than other fossil fuels, as a gas it is more difficult to handle and transport. This can be seen in a variety of methane leak sources. For instance, between 4 to 8% is released during shale gas production [12]. During transportation to the end user, more is released from small leaks such as in cities across the USA [13].

Another example is the flaring of methane in the Bakken Shale region of North Dakota, as it was better to burn it to CO_2[1] than harvest that energy on-site or transport it to the market. Yet, due to incomplete combustion, some methane was still released [14]. For North Dakota in 2011, approximately 32% of the produced methane was flared as a waste gas, highlighting the need for technologies to harvest this methane [15]. Yet like CO_2 fixation, there is little economic incentive to implement current technologies for methane fixation of these flared gases; however there is substantial interest in developing these technologies [16, 17].

For these reasons, this introduction and thesis will focus on technologies that valorize gas fixation, their limitations, and efforts to overcome those limitations. Technologies with economic incentive are more likely for implementation, particularly in 2nd and 3rd world nations, than those subsidized through legislation.

When speaking of gas fixation, photosynthesis and CO_2 fixation by plants and algae remains the most prominent in nature; but scientists only considered their industrial use for CO_2 fixation after climate change became a political issue. Work is ongoing to improve photosynthetic systems [18, 19]. Industrially, gas-to-liquid (GTL) technologies were dominated by the Fischer-Tropsch (FT) process. Under specific economic and political conditions[2], the FT process was used for the conversion of coal or CH_4 to synthesis gas (CO, H_2, and CO_2), and then to a range of oils. However, these processes require large scales and high energy inputs, and thus weren't viable for many applications, such as the fixation of CO_2 [23, 17, 16].

Only recently has the importance of gas fixation emerged as a generally appli-

[1]By mole, CO_2 has a smaller greenhouse gase contribution than CH_4 [10].

[2]In the World Wars, Germany needed liquid fuels to power tanks and other gears of war, but only had coal after they were cut off from the Middle East. After World War II, FT-GTL phased out because the technology could not compete with refined crude oil [20, 21]. Gasification and Fischer-Tropsch made a small resurgence in the 1970s and 1980s due partly to the oil crisis of 1973 and partly to the international oil embargo on coal rich Apartheid South Africa [22].

cable technology for the production of valuable chemicals from CO_2 and CO [24], and CH_4 [17]. However, current biological gas fixation has key limitations, including slow growth rates and biomass titers in defined media [25, 26, 27], low product titers [28], and a limited range of products [29]. Work is ongoing to address these limitations through intelligent substrate selection, strain engineering, and bio-reactor process design. This introduction focuses on these limitations, and how they may be overcome.

1.2 Prominent gas fixation pathways in the environment and industry

1.2.1 Improving photosynthesis efficiency and productivity

Photosynthesis is the predominant pathway for CO_2 fixation, where energy from the sun produces O_2, while reducing CO_2 into sugars with RuBisCO and the Calvin-Benson cycle. While plant biomass production absorbs 3 gigatons of carbon [1] each year, there is little possibility for terrestrial carbon removal through plant growth because of land requirements, fertilizer costs, and the impact on food production [30]. Though there is interest in improving crop photosynthesis for the purpose of global food demand [31], the current overall energy efficiency is around 1 to 7% [32, 33, 18].

Another photosynthetic alternative is algae [34], whom have comparatively faster biomass productivies (by 30 times) [35] and can be cultivated in waste water [36]. However, algal systems also have fundamental limitations. First, like plants, algae are directly limited by surface area. The design of photobioreactors must be carefully considered, balancing efficiency with costs. For instance, raceway ponds are cheap to build and operate, however, there are regions of the pond with low efficiency resulting in heat dissipation or the generation of reactive oxygen species (at the surface), or there are light limitations resulting in cell starvation (in the depths) (**Figure** 1-1**A**) [37]. While this problem can be solved with substantial investment, the process must remain cheap for widespread adoption.

A second major limitation is the wavelengths which chlorophyll can absorb; they are limited to the visible range, between 400 to 500 nm, and 600 to 700 nm (**Figure 1-1B**) [38]. In comparison, the sun emits substantial energy above 700 nm, up to about 2400 nm; solar cells have the advantage of harvesting energy from these infrared regions [39, 40]. Scientists are interested in expanding the harvesting band of chlorophyll [41], and this can be done either by genetic engineering [33] or isolating new strains [42].

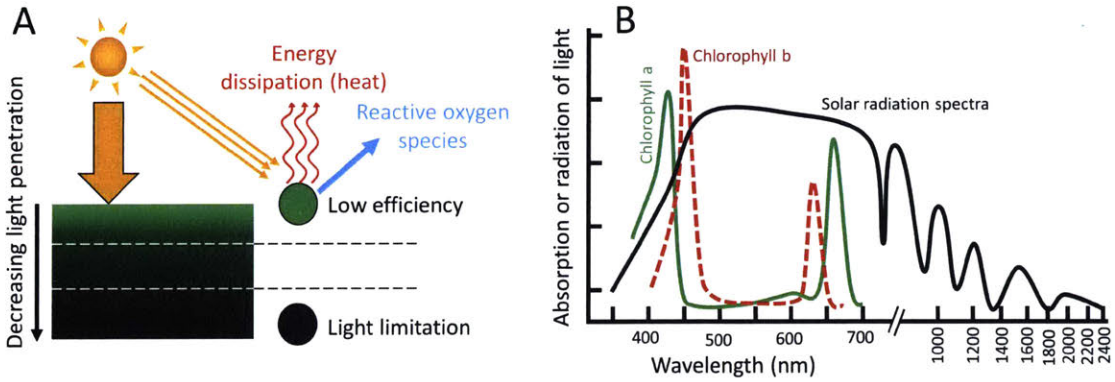

Figure 1-1: Limitations for photosynthesis in algal photobioreactors. (A) Depth and algal concentration affect efficiency of photosynthesis and light starvation. (B) Chlorophyll absorb only certain wavelengths of light, some regions are under utilized. (A) modified from [37].(B) generalized from [38].

1.2.2 Aerobic CO_2 fixation with the Calvin-Benson cycle

The merits of CO_2 fixation with algae must also be compared to photovoltaics and other organisms. For instance, recently, an artificial photosynthetic process was developed that had an efficiency (10%) greater than that of natural photosynthetic systems during rapid growth phases (5 to 7%) [43]. In this process, water was split into H_2 and O_2 with electricity that could be derived from current photovoltaics ($Efficiency = \eta_{solar} = 18\%$). These gases were then fed to *Ralstonia eutropha*, and CO_2 was fixed to biomass and polyhydroxybutyrate (a bioplastic) with the Calvin-Benson cycle. Despite the higher efficiency, titers remained in the $mg\ L^{-1}$ scale, with growth occuring over the course of 6 days. Higher productivities and titers will be

necessary prior to implementation, and there is precidence for reaching those titers and productivities during autotrophic growth with carefully designed reactor systems to ensure safety [44].

Much like plants and algae, which also operate the Calvin-Benson cycle for CO_2 fixation, chemolithoautotrophs like *R. eutropha* require substantial quantities of ATP to reduce CO_2 into biomass and other metabolites (**Table** 1.1), as compared to the Wood-Ljungdahl pathway (WLP). The 3HP/4HB cycle and reductive TCA cycle are the same. For *R. eutropha* and other aerobes, ATP is produced by O_2 respiration [45, 46]. While the Calvin-Benson cycle does require more ATP to fix CO_2, O_2 respiration sufficiently provides this ATP resulting in industrially relevant titers and productivities [44].

The issue, instead, is the lower yield. Ultimately for aerobic CO_2 fixation, the H_2 used in O_2 respiration is lost, resulting in efficiencies less than 57%, and this has important implications on the economics.

Take for instance, CO_2 fixation to acetate with H_2 generated electrolytically. Acetate could then be fermented aerobically with *Yarrowia lipolytica* into lipids, a diesel alternative, at high yields (0.16 g lipid per gram acetate) and productivities ($0.8\ g\ L^{-1}\ hr^{-1}$) [28, 47]. The cost of the H_2 directly determines the break even price of the bio-diesel based on the H_2 yield of each fixation pathway (**Table** 1.1). In **Figure** 1-2, the larger the slope, the more one must charge per gallon for diesel; if this price is higher than that of the market price from oil and gas, the proposed process can not compete.

If the price of H_2 can be brought to 1 \$ kg^{-1} (a reasonable target) [48], the break even price for the canonical Calvin-Benson cycle (5.03 \$ gal^{-1}) [3] remains well above that of max diesel price between 2016 and May 2018 (3.29 \$ gal^{-1}, USA diesel prices, EIA) (**Figure** 1-2). Conversely, the highly efficient WLP was below this threshold (2.87 \$ gal^{-1}), and the reductive TCA cycle was slightly higher.

Despite the simplification, which did not account for other processing costs, the discrepancy in these break even prices clearly indicates that the Calvin-Benson cycle

[3] Assumes a diesel density of 0.832 $kg\ L^{-1}$

and 3HP/4HB cycle require either very low H_2 costs, very high diesel prices, or substantial CO_2 fixation subsidies. Currently, it is un-clear if any of these scenarios will occur. In this case, lipids or diesel would not be an ideal product. Instead, the organism should be engineered to produce a more valuable product [49]. However, the market size of that product must be considered for its potential to remediate gigatons of CO_2 yearly, as well as the theoretical yields that could be achieved [50]. There are few products with a market size in the gigatons per year [51].

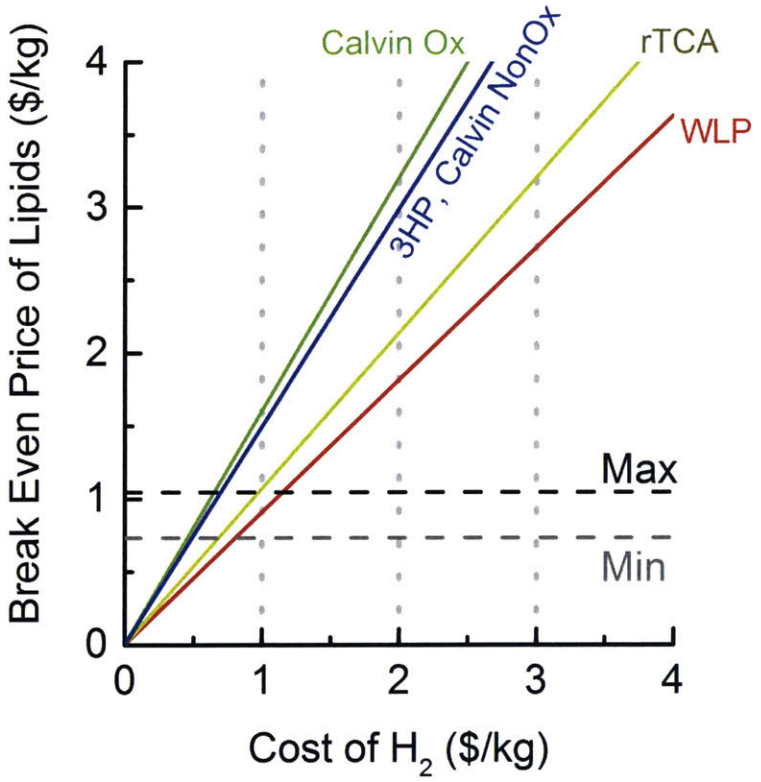

Figure 1-2: Break even price for lipids produced via CO_2 fixation by various pathways, and aerobic lipid accumulation, at given H_2 costs. This break even cost was based on the H_2 yield of each pathway to produce acetate (**Table** 1.1 and an experimental lipid yield of 0.16 $g_{lipid}\ g^{-1}_{acetic\ acid}$ by *Yarrowia lipolytica* [47]. The minimum and maximum diesel price were plotted from between 2016 and May 2018 (EIA).

Table 1.1: CO_2 fixation pathways, and the ATP and H_2 cost to produce 1 mole of acetate, and the H_2 efficiency. Adapted from [52, 46, 18]. H_2 efficiency is calculated from the reducing equivalents in acetate (4 mol) divided by the total H_2 to fix CO_2 and generate ATP. For aerobes, this H_2 is lost. (a) There is net production of ATP during CO_2 fixation, as high energy electrons on reduced ferredoxin are transferred to NAD^+, generating net proton motor force to drive ATP production [53]. (b) Unlike the other pathways, H_2 is not directly oxidized to generate ATP; experimental value given (**Table** 2.8). (c) Assumes biomass is also a product. (d) The Calvin-Benson cycle is assumed to generate glyceraldehyde 3-phosphate (G3P) [54]; oxidative glycolysis converts this first to pyruvate and then acetyl-CoA by pyruvate dehydrogenase, losing 1 mole of CO_2 per acetyl-CoA. (e) Non-oxidative glycolysis is a theoretical bypass that converts all the carbon of G3P into acetyl-CoA and decreases the overall ATP cost per acety-CoA; (f) the enzymes required to do this are not included in this number as it is dependent on the organism [55].

	Requirements for the production of 1 Mol Acetate				
Pathway	**Mol Reducing equivalent**	**Mol ATP**	**Total Mol H_2**	**Number of Enzymes**	**H_2 Efficiency**
WLP	2 NADPH + 2 Fd_{red}	-0.63 [a]	4.25 [b]	8	100% [c]
3HP/4HB cycle	4 NADPH	5	7	13	57%
Reductive TCA cycle	4 NADPH	1	5	8	80%
Calvin-Benson cycle (OxGly)	4 NADPH	6 [d]	7.5	10	53%
Calvin-Benson cycle (NonOxGly)	4 NADPH	5 [e]	7	10 [f]	57%

1.2.3 Challenges for the functional expression of MCR from anaerobic methanotrophs

Sources of methane are substantially different than that of CO_2. Excluding automobiles, CO_2 point sources are generally concentrated at industrial facilities; this makes harvesting and fixing CO_2 more convenient than methane. Methane is produced from large geological formations that span large regions of Northern Appalachia, Texas, and North Dakota [4]. The distributed nature of methane raises substantial problems for harvesting and fixing it into useful liquid products. This is the first important limitation; processes for methane fixation must consider the scale of operation and how to connect that operation with others in the area. Other limitations include low theoretical yields and low productivity achieved experimentally to date.

Small scale FT-GTL technologies are being developed, yet they still require relatively high flow rates ($1,000\ Mscf\ d^{-1}$ or $2.8x10^4\ std\ m^3\ day^{-1}$) [16]. While this would be sufficient for high flow rate wells, there are also substantial reserves of methane whose location or flow rates and pressures are too low for economic production (70%) [56]. Researchers believe biology can fill this niche [17], and there is theoretical evidence that simple reactor design, coupled to those low flow rate wells ($66\ Mscf\ day^{-1}$ or $1869\ std\ m^3\ day^{-1}$) [57] could provide sufficient mass transfer to biologic or inorganic catalysts. This, however, assumes that sufficient rate targets are met by those catalysts. This theoretical analysis is covered in **Chapter** 4. From this analysis, it was clear that further engineering was necessary to meet those targets. The DOE previously recognized this market potential and thus offered $ 30 million as part of the ARPA-e REMOTE program [58] [5]. Work is also ongoing to optimize production of shale reserves across large production regions for liquefaction or FT-GTL [59, 60]; such analysis must also be performed for the proposed biological processes [61].

There are two classes of methanotrophs that can convert methane into fuels and

[4] To name only the most widely known regions in the USA

[5] Advanced Research Projects Agency-energy; Reducing Emissions using Methanotrophic Organisms for Transportation Energy

chemicals. The first, Aerobic methanotrophs, utilize methane monooxygenase (particulate, pMMO; or soluble, sMMO) and O_2 for the conversion methane into methanol, requiring stoichiometric reducing equivalents, resulting in a maximal energy efficiency of only 50% [62]. Like seen above for the Calvin-Benson cycle, this loss in yield would greatly impact the economics and thus researchers are interested in developping other, more efficient pathways for methane fixation [17]. For this reason and because there is substantial literature on aerobic methanotroph engineering [63, 64, 65], aerobic methanotrophy won't be considered here.

The second class of methanotrophs grows anaerobically, activating methane with MCR (methyl-coenzyme M reductase) and the disulfide-linked coenzymes CoM-S-S-CoB. While the exact mechanism is unknown, the pathway is thought to operate in reverse of the canonical methanogenesis pathway, at least in part [66, 67]. Energy is conserved by sodium (Na^+) translocation across the cell membrane [66] and coupling metabolism to an electron acceptor like sulfate [27], nitrate [68], nitrite [6] [69], iron [70], etc.

Large strides have been made in understanding the biochemistry of these organisms in the past 5 years, including discovering the synthesis pathway for F430 [7] [71], elucidating the activating complex for MCR [72], and verifying the radical mechanism for methane oxidation [73]. Biochemistry for higher order alkane activation has also been discovered [74, 75]. A significant number of post-translational modifications have also been discovered which vary by organism [76], as well as an enzyme that generates one of those modifications [77]. Despite these large strides in understanding the mechanism and biochemistry, there are fundamental limitations to engineering these organisms and utilizing them to fix methane.

Until recently, little engineering has been applied to increasing methane fixation by anaerobic methanotrophs (ANME), despite our better understanding of the fundamental biology. Generally, ANME were studied as part of sea-floor sediment in which

[6] Researchers actually think nitrite-linked anaerobic methane oxidation (AOM) proceeds with pMMO by generating O_2 intracellularly [69].

[7] F430 is a key co-factor required by MCR for methane activation.

they are found, with media meant to mimic the ocean [8], and cold temperatures (4 to 15°C). It is no surprise that methane uptake and growth rates were generally slow, on the order of 0.1 *to* 380 $\mu mol\ gDW^{-1}\ day^{-1}$ [78, 27, 79, 80] [9]. Recently, researchers have transitioned ANME consortia from sediment to carbon cloth, removing a relative unknown (sediment) and also growing them at higher temperatures [81].

To-date, no pure culture has been generated for ANME; they remain as a consortia despite multi-year isolation experiments [27, 82]. Because of this, metabolic engineering and synthetic biology can not be used. Researchers have turned to expressing MCR in standard heterologous hosts (i.e. *E. coli*), also with little success. Instead, researchers have opted to express the complicated MCR enzyme [10] in methanogens with some degree of success [84, 85]. Preliminary results showed acetate production (10 mM) with iron (Fe^{+3}) reduction and methane consumption [84]. Further strain engineering or process design enabled production of lactate [86] or electricity from methane [87].

Regardless of these results, yield and productivity remain a contentious issue. Take for instance the hypothetical anaerobic production of butanol from methane. Since little ATP can be derived from sulfate reduction, sulfate reducing AOM (anaerobic oxidation of methane) results in low theoretical yields (40% with aldehyde:ferredoxin oxidoreductase (AOR) butanol pathway), less than that of aerobic methanogens (> 50%) [62]. This, however, did not take into account maintenance energy, that is necessary for activating MCR and maintaining the active site's degree of reduction. Indeed, when accounting for maintenance energy from experimental results, the yield dropped from 40% to 4%, even though the predicted maintenance energy was 2 orders of magnitude lower than that of *E. coli* on a biomass basis [62]. By providing a different electron acceptor (nitrate) and replacing the sodium-ion gradient methyltransferases with soluble methyltransferases (sMTR) [11], the yield could be vastly

[8] If not directly using ocean water.

[9] Quantifying and normalizing methane uptake rate on a cellular basis is difficult, as the cells are generally associated with the sediment. Researchers instead use volatile suspended solids, or total suspended solids. Regardless, comparing results is difficult between experiments.

[10] MCR is a homo-dimer of a hetero-trimer [83], requires 3 cofactors (F430, CoM, and CoB), and post-translational modification which are non-standard for most host cell lines.

[11] The cell wall associated methyltransferase transfers methyl from CoM to tetrahy-

improved (80%). However, the rates that could be achieved with such a system must be questioned; the sMTR reaction has a positive $\Delta G = 30\ kJ\ mol^{-1}$, hence the ratio of reactant:product must be kept above 180,000:1 for thermodynamic feasibility [62]. Perhaps, other electron acceptors with more negative ΔG^0 could be utilized to power the cell wall associated methyltransferase instead of nitrate (NO_3^-; $\Delta G = -463\ kJ\ mol^{-1}$), such as iron ($Fe^{+3}$; $\Delta G = -780\ kJ\ mol^{-1}$) or manganese ($Mn^{+4}$; $\Delta G = -1134\ kJ\ mol^{-1}$). Indeed, a methane and Fe^{+3} microbrial fuel cell produced electricity with a coulumbic efficiency of 90 ± 10% [87].

1.3 Non-photosynthetic CO_2 fixation with the Wood-Ljungdahl pathway

The Wood-Ljungdahl pathway (WLP) and the most historically prominent acetogen, *Moorella thermoacetica* [12], were first described in 1942 [88] and was recognized for its near 100% carbon recovery from glucose in the form of acetate (85%) and biomass (5%). This was a significant discovery, as canonical anaerobic glucose fermentation (by *E. coli*) could only achieve carbon recoveries of 67% due to lost CO_2 during pyruvate decarboxylation. Indeed, it was later discovered that acetogens were able to re-assimilate the lost CO_2 with the WLP [89]. Other than synthetic pathways [55], no other pathway in nature is known to have this high efficiency.

In the past 76 years, there have been significant contributions to the field regarding the biochemistry of this pathway [90], even though not every detail has been resolved [53] (**Figure** 1-3). However, only recently has this pathway risen to prominence for the WLP's ability to convert H_2+CO_2 or CO into acetate and other valuable products. This was in part due to the development of genetic tool kits for these organisms, and an economic and political climate that valorizes the remediation of waste gases (CO_2 and CO). Surprisingly, despite a published transformation protocol [91, 92, 93], *M. thermoacetica* has by and large fallen to the wayside due in part to other researchers

dromethanopterin. This is powered by a Na^+ gradient; which is generated with ATP hydrolysis.

[12] *M. thermoacetica* was previously named *Clostridium thermoaceticum*.

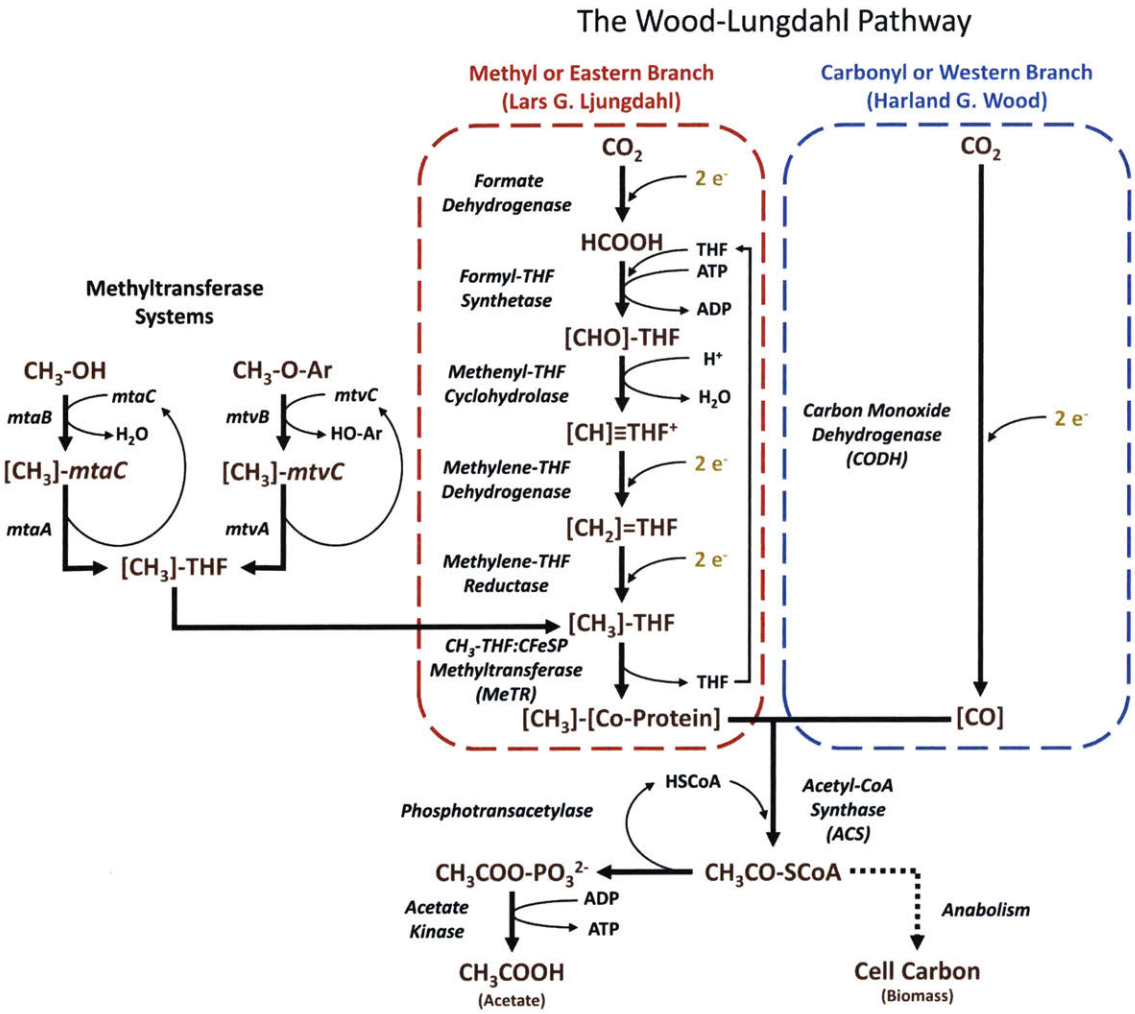

Figure 1-3: The Wood-Ljungdahl pathway was discovered by Lars Ljungdahl and Harland Wood. The methyl branch reduces CO_2 to a methyl group, whereas the carbonyl branch reduces CO_2 to CO. The methyltransferase system for methanol and aromatic (Ar) *O*-methyl esters transfers the methyl group onto THF (tetrahydrofolate). Reducing equivalents are generalized as 'e^-' since they vary between acetogens [53].

inability to replicate Kita et. al.'s results, despite extensive efforts [62]. *Clostridium ljungdahlii* [94], *Clostridium autoethanogenum* [95], and *Acetobacterium woodii* [96] have been widely adopted instead.

Despite the low ATP costs of CO_2 fixation (**Table** 1.1), or perhaps because of the low ATP costs, acetogens generally grow slowly and to lower overall optical densities; this is especially true when yeast extract (YE) was excluded from the media [13]. For instance, the doubling time of *M. thermoacetica* on H_2+CO_2 in defined media was 16 hours and cell density was only 40 mgDCW/L (DCW: dry cell weight) [26]. Growth of *C. ljungdahlii* in similar media with 0.1 g/L YE was faster, with a doubling time of 14.4 $\pm$ 0.8 hours, yet cell density remained low at 56 $\pm$ 4 mgDCW/L (**Table** 2.1). Evolutionary adaptation and optimal media design from an elemental balance can have a substantial impact on growth, increasing cell density 3.75-fold, though surprisingly productivities did not increase [97]. One should also be careful not to add to much nutrients, like nicotinic acid, as they can also have a deleterious affect on growth titer [98]. Reactor design can also have a larger impact on cell titer; growth of *Clostridium autoethanogenum* on H_2+CO_2 in defined media with a continuous stirred tank and cell recycle reached cell density of 1,800 mgDCW/L and productivities of 1.5 and 1.3 $g\ L^{-1}\ hr^{-1}$ for acetate and ethanol, respectively [99].

Despite these seemingly drastic improvements, product titers and cell density remain much less than observed for aerobic autotrophs. Take *Alcaligenes eutrophus* for instance, which can grow to high densities and produce at high titers (91 gDCW/L and 62 $g_{poly-3HB}$/L) and fast rates (1.6 $g\ L^{-1}\ hr^{-1}$) [44] on mineral media containing no YE [100].

1.3.1 Respiration on other electron acceptors in tandem with CO_2 reduction

One reason for high aerobic rates is the respiration of O_2 that powers ATP production. Conversely, anaerobic autotrophic acetogens are ATP starved, which greatly limits

[13] Almost all researchers provide 1 $g\ L^{-1}$ of YE; some provide up to 10 $g\ L^{-1}$.

the titers of acetate that can be achieved [101]. We wondered if a secondary source of ATP production could be utilized by acetogens, in tandem with CO_2 reduction. One such possibility would be respiration with an electron acceptor other than O_2 (**Equations** 1.1 to 1.3). One such electron acceptor, nitrate, has a ΔG close to that of O_2 [102], but seemingly prevents activity of the WLP [103, 104]. The mechanism for deactivation of the WLP in *M. thermoacetica* is currently unknown [105]. Based on the work presented in this thesis, while *M. thermoacetica* can not respire on nitrate while reducing CO_2 with the WLP, *C. ljungdahlii* can. Nitrate improves growth rate, biomass titers, and increases the ATP/ADP ratio and the acetyl-CoA pool size within the cell (**Chapter** 2).

$$O_2 + 2H_2 \rightleftharpoons 2H_2O \qquad \Delta G^{0'} = -237\ kJ\ mol_{H_2}^{-1} \qquad (1.1)$$

$$NO_3^- + 4H_2 + 2H^+ \rightleftharpoons NH_4^+ + 3H_2O \qquad \Delta G^{0'} = -150\ kJ\ mol_{H_2}^{-1} \qquad (1.2)$$

$$SO_4^{-2} + 3H_2 + 2\,H^+ \rightleftharpoons S + 4H_2O \qquad \Delta G^{0'} = -41\ kJ\ mol_{H_2}^{-1} \qquad (1.3)$$

Other researchers have demonstrated similar increases in growth rates on CO rich gases, at least, with the addition of arginine which provides ATP through substrate level phosphorylation (SLP) [106]. However, under autotrophic conditions, acetate production was abolished. Yet this wasn't the greatest limitation of utilizing arginine for ATP synthesis. Instead it is the cost; utilizing arginine for ATP synthesis would cost an order of magnitude greater than that of H_2+NO_3^- or H_2 based on theoretical yields (**Table** 1.2).

While nitric acid is more expensive than sugars for the production of ATP, one should also consider that nitric acid would also act as both nitrogen source and acid for pH balancing. The produced ammonium could also be harvested, then sold, or recycled to nitrate. These processing costs must be considered for future implementation.

Table 1.2: The cost to generate ATP from common WLP substrates. Prices determined from theoretical yields [53] and bulk lab scale prices from Sigma-Aldrich and Airgas. CO_2 was assumed to be free. Minimal O_2 concentrations require more expensive and purer H_2. The cost basis was 9.58 $ per mol arginine (Sigma, 10kg); 0.86 $ per mole nitric acid (Sigma, 70% purity, 6x 2.5L); 0.33 $ per mol H_2 (Airgas, 260 std ft^3, Ultrahigh purity); 1.72 $ per mol fructose (Sigma, 25kg); 0.11 $ per mol methanol (Sigma, 200L).

Substrate	**Theoretical ATP Produced**	$\frac{\$}{mol\ ATP}$
1 Arginine	1.00	9.6
4 $H_2 + HNO_3$	1.50	1.2
4 H_2	0.63	0.5
1 Fructose	4.63	0.4
4 Methanol	2.50	0.2

1.3.2 Mixotrophy with sugars or methanol

Regardless, from the costs listed above, sugars are the cheapest source of ATP. They have also been proposed to improve yields of acetogens through mixotrophy, where sugars and gases are consumed simultaneously [107, 108, 109]. Jones et al [108] and Maru et al [109] showed that adding H_2 to sugar fermentations decreased CO_2 evolution of acetogens, but did not increase yields beyond theoretical values. Nor did they show that exogenous CO_2, i.e. from sources other than the sugar, could be fixed. Jones et al also showed substantial increases in yields when syngas ($CO:CO_2:H_2:N_2$, 55:10:20:15) was added to the headspace instead of N_2. These yields were calculated by dividing product metabolites with consumed sugar molecules and thus did not account for CO and H_2 consumption for which the cost is non-zero.

The inverse is also true; small quantities of sugars can greatly improve CO_2 fixation. Unpublished work from the Stephanopoulos lab has shown that slowly feeding sugar to *M. thermoacetica* growing autotrophically on H_2+CO_2 can greatly improve titers, productivities, and CO_2 fixation rates in *M. thermoacetica* [110]. For instance, CO_2 fixation rates were approximately 4-fold greater when only 10% of electrons were derived from glucose; this also coincided with peak acetate productivity.

Another option, discussed in **Chapter** 3, would be using another source of elec-

trons other than H_2 for the reduction of CO_2. One such option would be methanol, which would be the cheapest theoretical source of ATP. Despite the relatively higher ATP yield, cell density remains much less than that of cultures grown on sugars (**Figure** 2-29 and **Figure** 3-7). Perhaps metabolic engineering of this pathway could alleviate some of this limitation. However no in vitro biochemical evidence has been published elucidating the *mtaABC* cascade from methylotrophic acetogens; though there is precedence for in vitro studies about the aromatic demethylation pathway in *M. thermoacetica* [111].

1.3.3 Electrosynthesis to bypass electron bifurcation of H_2

During growth on H_2+CO_2, one limitation on ATP production is the bifurcation of electrons between reduced ferredoxin (Fd^{-2}) and NADPH [112]; only Fd^{-2} can drive proton motive force (PMF) with the RNF complex and ATP production [53], as the electrons of NAD(P)H are not at a high enough energy. For this reason, and because CO reduction only produces Fd^{-2}, ATP yields and growth rates are higher on CO than H_2 [29, 26].

Take for instance the scheme proposed earlier where H_2 would be produced electrolytically, perhaps by solar power (**Table** 1-2). If instead, the electricity was directly fed to acetogens, for the reduction of ferredoxin, ATP yields would approach that observed with CO. Proof of concept microbrial electrosynthesis (MES) has been developed for a variety of acetogens for the production of acetate and other organic compounds [113, 114, 115].

Currently, there is no proof of electron transfer to ferredoxin in whole cells, though purified ferredoxin from *C. pasteurianum* could be electrochemically reduced [116]. Alternatively, the electrons could be delivered to the RNF complex by another mechanism, though this remains speculative [117] and the effect of MES on the energetic state of the acetogenic cell has not been studied [113].

1.4 Thesis overview and objectives

The objective of this thesis was to explore methods of improving microbrial gas fixation. This includes improving autotrophic cellular energetics (nitrate respiration by *C. ljungdahlii*), understanding assimilation pathways (methanol consumption by *M. thermoacetica*), and modeling low cost reactor designs (methane mass transfer in natural gas wells). We aim to develop technologies that valorize gas fixation, though each chapter is a self-contained analysis of gas fixation from various perspectives and applications.

Chapter 2 focuses on utilizing nitrate as a secondary electron acceptor for the production of ATP. When the substrate was H_2, nitrate improved cellular energetics (such as ATP/ADP ratio), growth rates, cell density, and acetate productivity. Simultaneous CO_2 fixation and nitrate reduction were verified by ^{13}C labeling and a mass and electron balance. The effect of nitrate on the transcriptome is discussed, as well as the impact on metabolites of central carbon metabolism and amino acids. Theoretically, nitrate was shown to improve yields for heterologous products, and this was confirmed experimentally.

Chapter 3 explored the pathway for assimilation of methanol by the acetogen, *M. thermoacetica* that reduces CO_2 simultaneously. While the genes involved in methanol metabolism of *M. thermoacetica* have been annotated, we show through RNAseq that these annotations were likely incorrect. Previous literature for this organism showed that methanol dehydrogenase was the enzyme utilized for methanol assimilation (methanol $\rightarrow$ formaldehyde); recent annotations contradicted this result, that methanol is assimilated via methyltransferases. Labeling studies with deuterated methanol (CD_3OD) confirm that the 3-component methlytransferase is likely the main method for methanol assimilation.

Chapter 4 analyzes a theoretical reactor design for the conversion of methane to liquid fuels and chemicals at the well head. We explore the mass transfer limits of such a system, and then calculate a minimum consumption rate necessary for full conversion of methanol (for biological or inorganic catalysts). We then determine the

affect of process parameters on conversion of methane, such as diameter, concentration of inert gases, and the gradual loss of well pressure.

Chapter 2

Enhancing autotrophic growth of *Clostridium ljungdahlii* through nitrate supplementation

2.1 Introduction

FERMENTATION of syngas (H_2, CO, CO_2) by autotrophic acetogenic bacteria has received considerable attention as a platform for the renewable production of fuels and chemicals [24, 28]. These organisms use electrons derived from four molecules of H_2, to fix two molecules of CO_2 into acetyl-CoA through the Wood-Lungdahl pathway (WLP). Conversion of acetyl-CoA to acetate provides ATP to fuel cellular growth. Some acetogens further convert acetate to ethanol, motivating commercial ventures to produce ethanol from waste steel mill gas [118]. The advent of genetic tools for the model acetogen *Clostridium ljungdahlii* [94] provided an opportunity to divert flux away from acetate to more valuable molecules through metabolic engineering. To date, acetogens have been engineered to produce a variety of chemicals, including butanol [94], butyrate [119], lactate [93], and acetone [108, 96].

In all reports to date, however, the productivities, titers, and yields have been too low to support a commercially viable process when the substrate is syngas. This

is primarily due to energetic considerations. The WLP operates near the thermodynamic limit of life [53], such that H_2-dependent CO_2 fixation to acetate is associated with a small Gibbs free energy change [102]:

$$\begin{aligned} &4\,H_2 + 2\,CO_2 \rightleftharpoons \text{Acetate} + 2H_2O \\ &\triangle G_0 = -24\ kJ\ mol^{-1}H_2 \end{aligned} \tag{2.1}$$

Functionally, this means that each mol of acetate produced supports the generation of only 0.2 to 0.6 mol ATP [53], leading to low growth yields (0.048 g Biomass/g Acetic Acid (this work)) and slow growth rates (t_d > 20 hrs on defined medium [25, 26]). Any diversion of acetyl-CoA flux away from acetate imposes a further ATP penalty on the cell, thus the maximum yield of any heterologous product is therefore constrained by the ATP demands of the cell. Simple calculations of the maximal theoretical yield for butanol, for example, suggest an upper limit of 0.2 mol per 100 mol H_2[46]. Also, at high cell density, the need to produce ATP leads to depletion of the acetyl-CoA pool and a collapse of metabolism [101].

We hypothesized that cell growth, productivity, and carbon yield in acetogens could therefore be improved by providing a cheap, complementary source of ATP. Indeed, recent work in the related acetogen *Clostridium autoethanogenum* showed that arginine supplementation increased growth rate but completely abolished acetate production during autotrophic growth, by enabling additional ATP production from the conversion of arginine to ornithine [106]. However, arginine is an expensive co-substrate (9.58 \$ mol^{-1}) (Sigma-Aldrich, 99 % FCC FG), motivating our search for a cheaper alternative. *Clostridium ljungdahlii* contains a complete set of genes required for nitrate (NO_3^-) assimilation, and heterotrophic growth on fructose with nitrate as the electron acceptor has been experimentally demonstrated [120]. Nitrate is a more favorable electron acceptor than CO_2 [102]:

$$4H_2 + 2H^+ + NO_3^- \rightleftharpoons 3H_2O + NH_4^+$$
$$\triangle_r G'_0 = -150\ kJ\ mol^{-1}H_2 \tag{2.2}$$

We therefore reasoned that a controlled redistribution of the electrons from H_2 between CO_2 for carbon fixation and nitrate for energy generation could improve growth.

Previous literature on nitrate metabolism in acetogens paints a confusing picture. In *Moorella thermoacetica* and *Moorella thermoautotrophica*, nitrate has been shown to abolish acetogenesis by the WLP for C1 substrates such as CO, formate, methanol+CO_2, vanillate+CO_2, syringate+CO_2, and H_2+CO_2 [121, 103]. Growth was only possible in the presence of 1000 mg/L yeast extract (YE), yet the biomass generated was at most 49 mg/L, hence the fixed carbon was potentially derived from YE. Once YE was removed from the media, growth in the presence of nitrate and a C1 substrate was limited to vanillate+CO and syringate+CO. The impact of nitrate on oxalate and glyoxalate metabolism in *M. thermoacetica* has also been studied [122], with similar results. Thus, definitive co-metabolism of nitrate and CO_2 has not been documented in an acetogen.

While simultaneous use of two electron acceptors has been reported in other organisms, e.g. the co-metabolism of nitrate and fumarate by *Wolinella succinogenes* [123], many bacteria carefully regulate their electron flux to one acceptor. For example, *Escherichia coli* uses oxygen (O_2) as its preferential electron acceptor, while down-regulating the oxidoreductases of other electron transport chains. Once oxygen is depleted, nitrate reductases are expressed allowing electrons to flow to nitrate. Only when O_2 and nitrate have both been depleted does *E. coli* switch to the less favorable acceptors (DMSO, TMAO, and fumarate) [124]. It is therefore possible that acetogens employ a similar regulatory mechanism. Nitrate has been shown to down-regulate the expression of the WLP enzymes in cultures of *C. ljungdahlii* grown heterotrophically on fructose [120], but the impact on autotrophic growth has not been studied. We thus set out to test the ability of *C. ljungdahlii* to co-metabolize

nitrate and CO_2, additionally employing transcriptomics to examine the regulation of these two processes. From our findings, we hypothesize that *C. ljungdahlii* indirectly respires nitrate while allowing CO_2 fixation with the WLP (Figure 2-1).

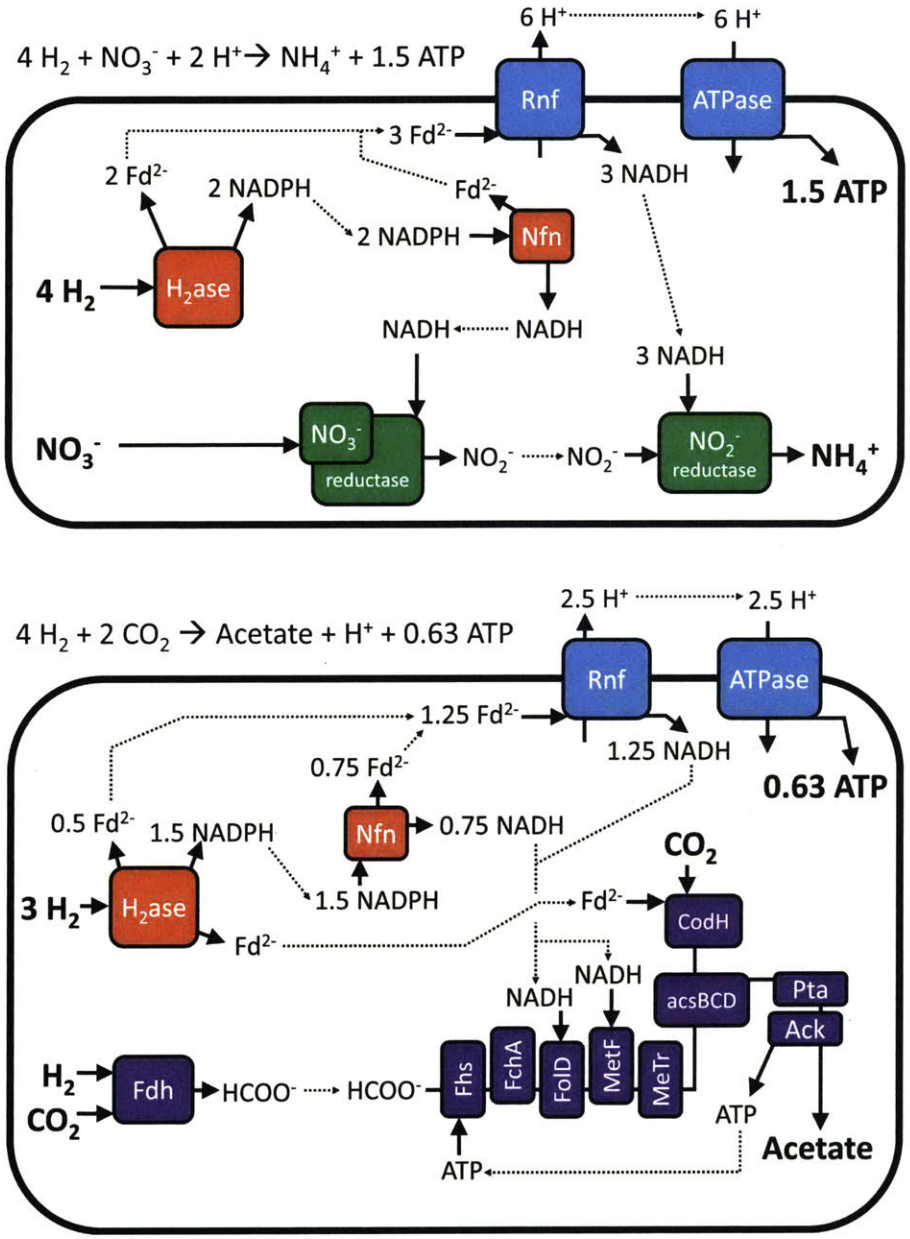

Figure 2-1: Enzymes and reducing equivalents necessary for H_2 energy conservation and ATP production in *C. ljungdahlii* with nitrate (top) or CO_2 (bottom) as the reducing equivalent. Nitrate is proposed as an electron sink for reducing equivalents from the RNF complex, but is not directly involved in ATP generation.

2.2 The Effect of Nitrate on Autotrophic Growth for Various Acetogens

To evaluate the potential of nitrate to improve autotrophic growth, we inoculated parallel cultures of *C. ljungdahlii*, *Acetobacterium woodii*, and *M. thermoacetica* with a headspace of H_2+CO_2, with or without 15 mM sodium nitrate. In accordance with previous literature [103], nitrate inhibited autotrophic growth of *M. thermoacetica* even though it was growth supportive in the presence of YE (**Table** 2.1 and **Figure** 2-9). *A. woodii* did not metabolize nitrate and served as a negative control. To our gratification, autotrophic growth of *C. ljungdahlii* on H_2+CO_2 was greatly improved in the presence of nitrate, increasing growth rates, and biomass yields.

2.2.1 Nitrate Improves Autotrophic Growth of *C. ljungdahlii* on H_2

When nitrate was supplemented to *C. ljungdahlii* growing on H_2+CO_2, the culture grew robustly, with simultaneous acetate and formate production and stoichiometric conversion of nitrate to ammonium (**Figure** 2-2**A,B**). Growth was associated with nitrate depletion and a rise in pH from 6.0 to about 7.3. After 52 hrs, nitrate was depleted, leading to a halt in metabolic activity and a significant drop in optical density. After another 100 hrs, growth resumed in unison with the onset of formate consumption and resumption of acetate production. During this time, pH declined with acetate production. Nitrate-dependent growth was robust and continued after several subcultures (**Figure** 2-14), confirming the phenotype was not due to carry-over from the inoculum.

Interestingly, the nitrate-supplemented culture significantly outperformed the un-supplemented control, in terms of growth rate (0.084 ± 0.002 vs 0.048 ± 0.003 hr^{-1}), and final OD_{660nm} (0.323 ± 0.001 vs 0.148 ± 0.011). Moreover, the cellular yield per acetate ($Y_{C/A}$) was also greatly increased to 0.48 ± 0.03 mol cell carbon per mol acetate with nitrate from 0.11 ± 0.01 without nitrate (Table 2.1). Since autotrophic

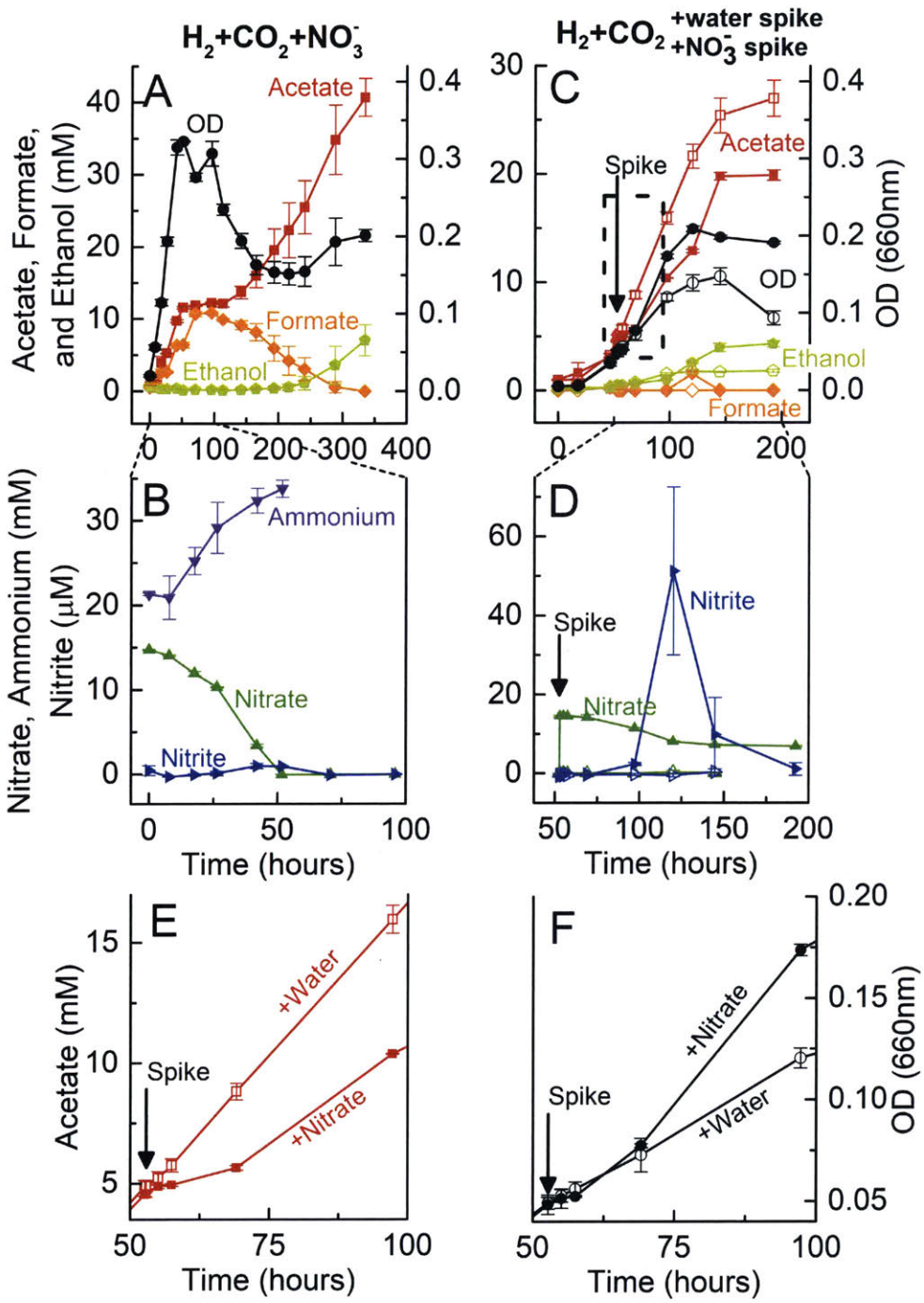

Figure 2-2: Metabolite concentrations and optical density of *C. ljungdahlii* grown with H_2 and CO_2 as the electron and carbon source. Cultures either contained nitrate throughout (A, B) or received a spike of nitrate (closed symbols) or water (open symbols) at 52 hrs (C, D). RNA was extracted 5 minutes before and 2 hrs after this spike. Acetate (E) and OD_{660nm} (F) are given for 50 hrs after the spike from panel (C). Black circle, OD_{660nm}; red square, acetate; orange diamond, formate; yellow pentagon, ethanol; green up-arrow, nitrate; blue right-arrow, nitrite; purple down-arrow, ammonium. Metabolite units are in mM, except nitrite which is in μM. Standard deviation given for three biological replicates.

growth is ATP-limited, the increased $Y_{C/A}$ implies additional ATP is generated from nitrate reduction. Despite the increased growth rate, nitrate supplementation led to a decrease in the WLP cell specific productivity (0.28 ± 0.02 vs 0.45 ± 0.02 mmol C hr^{-1} $mmol^{-1}$ $C_{biomass}$), as determined by acetate and biomass production rate (mM/hr) divided the average biomass concentration (mM). However, due to the higher growth rate and optical density, volumetric productivity was increased (0.47 ± 0.01 vs 0.38 ± 0.02 mmol C hr^{-1} L^{-1}) (**Figure** 2-3).

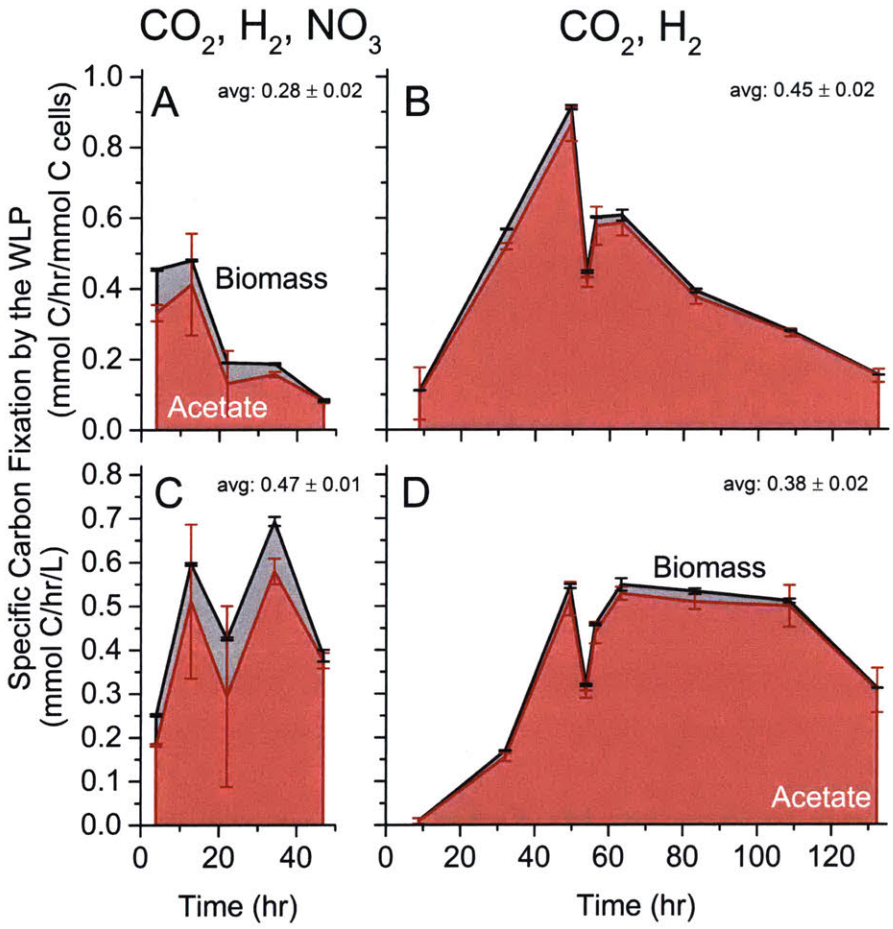

Figure 2-3: The specifc rate of carbon fixation to either acetate (red) or biomass (black) was determined for *C. ljungdahlii* from the data presented in Figure 2-2 when grown autotrophically with (A,C) and without nitrate (B,D). Formate was excluded as this is an early intermediate of the Wood-Ljungdahl pathway. While specific carbon fixation per biomass (A,B) was lower in the presence of nitrate, the carbon fixation per volume (C,D) is comparable, if not higher, due to the faster growth rate and higher final optical density. The productivity during growth was averaged and is presented in the upper right corner of each panel. The drop in productivity in B and D occurs after those cultures received a spike of water as a control for the nitrate spiking experiment. Cell specific productivity (mmol C/hr/mmol C cells) was determined by dividing the acetate and biomass production rate (mM C/hr) by the average biomass concentration between those time points (mM C). Standard deviation given for three biological replicates.

Table 2.1: Carbon and nitrogen balances for cultures during growth phase. Values were determined by subtracting the initial time point from the concentration at peak OD; this time is indicated under the substrate. Negative values imply consumption. Biological constants necessary to calculate mM C biomass from OD_{660nm} are given in Table SII. The nitrogen balance was calculated by dividing the nitrogenous products by the nitrate consumed. The total C and N that could be derived from YE are given in the bottom row. Standard deviation given in parentheses for three biological replicates.

		ΔBiomass (mM C)	ΔAcetate (mM)	ΔEthanol (mM)	ΔFormate (mM)	ΔTotal C (mM C)	ΔNO_3^- (mM)	ΔNO_2^- (mM)	ΔNH_4^+ (mM)	ΔBiomass (mM N)	Nitrogen Balance
	H_2+CO_2	1.62	15	0.6	0.00	32.8	—	—	—	—	—
C. ljung	(97 hr)	(0.13)	(0.6)	(0.8)	(0.00)	(2.0)	—	—	—	—	—
	H_2+CO_2+NO_3^-	4.30	9.02	-0.29	5.8	27.6	-11.3	5x10-4	11	1.07	107%
	(42 hr)	(0.24)	(0.21)	(0.07)	(0.4)	(0.6)	(0.2)	(7x10-4)	(1.5)	(0.08)	(13%)
	CO+CO_2	4.42	19.1	0.63	0.03	42.6	—	—	—	—	—
C. ljung	(70 hr)	(0.19)	(0.1)	(0.14)	(0.04)	(0.3)	—	—	—	—	—
	CO+CO_2+NO_3^-	1.32	1.07	0.39	0.31	3.76	-3.3	3x10-2	6.5	0.33	208%
	(116 hr)	(0.18)	(0.35)	(0.12)	(0.07)	(0.73)	(0.8)	(1x10-2)	(0.1)	(0.04)	(52%)
	H_2+CO_2	1.95	43.0	0.00	0.00	87.9	—	—	—	—	—
M. therm	(96 hr)	(0.08)	(0.5)	(0.00)	(0.00)	(1.1)	—	—	—	—	—
	H_2+CO_2+NO_3^-	1.49	0.61	0.00	0.00	2.72	-6.6	1.77	1.8	0.37	56%
	(96 hr)	(0.22)	(0.21)	(0.00)	(0.00)	(0.33)	(0.5)	(0.05)	(1.3)	(0.06)	(20%)
A. woodii	H_2+CO_2	4.23	100.3	0.01	8.3	213	—	—	—	—	—
	(70 hr)	(0.09)	(4.5)	(0.14)	(0.9)	(9)	—	—	—	—	—
YE		3.34	—	—	—	—	—	—	—	0.80	—
(0.1g/L)		(0.05)	—	—	—	—	—	—	—	(0.01)	—

Constants		$\frac{gDCW}{L * OD_{660nm}}$	$\frac{gC}{gDCW}$	$\frac{gN}{gDCW}$
	H_2+CO_2	0.377	0.448	0.128
C. ljung		(0.021)	(0.015)	(0.004)
	H_2+CO_2+NO_3^-	0.385	0.454	0.132
		(0.016)	(0.007)	(0.002)
YE			0.401	0.113
			(0.006)	(0.002)

2.2.2 Nitrate Worsens Autotrophic Growth of *C. ljungdahlii* on CO

Considering the advantage nitrate provides to growth on H_2, growth on CO+NO_3^- was the obvious next substrate to test. In the absence of nitrate, growth on CO by acetogens is normally faster than on H_2. This is due to higher ATP yields per acetate (1.5 on CO vs. 0.63 on H_2) [29]. The higher ATP yield is directly related to the moles of reduced ferredoxin produced per mole of electron source (CO or H_2), as only reduced ferredoxin can power proton translocation with the RNF complex. Reduction of 4 CO to CO_2 results in 4 reduced ferredoxin. Conversely, Reduction of 4 H_2 to 8 H^+ results in 2 reduced ferredoxin and 2 NADH [53].

The direct consequence is that CO grown cultures have shorter doubling times. For instance, the doubling time of *M. thermoacetica* on minimal media is [26]:

- 6 hours on Glucose
- 10 hours on CO
- 25 hours on H_2+CO_2

A more prescient implication is the effect of ATP yields on product yields [29] (**Table** 2.7). This is in part the cause for excitement for the results of *C. ljungdahlii* grown on H_2+CO_2+NO_3^-. The ATP yield per electron is predicted to be similar between CO and nitrate (**Section** 2.4.3), and so there was curiosity as to whether nitrate would also improve growth on CO, as it did on H_2.

C. ljungdahlii was grown on semi-defined media with 0.1 g/L YE and 20 psig of a mixture of CO and CO_2 (80%:20% on a molar basis). When nitrate was supplemented, *C. ljungdahlii* grew slower, and to lower OD_{660nm}'s (**Figure** 2-4). During this time, little to no acetate or ethanol was produced (1.07 $\pm$ 0.35 and 0.39 $\pm$ 0.12 mM, **Table** 2.1). Instead, nitrate was reduced, and ammonium was produced. In stark contrast with H_2 cultures, there was substantial nitrite production within the first 45 hours with a high of 163 μM and an average of 131 $\pm$ 40 μM. The N balance was also a

quandary; at 208 ± 52%, more ammonia was produced than could be derived from nitrate alone (N in ammonium and biomass produced divided by nitrate consumed, **Table** 2.1). To better understand why *C. ljungdahlii* grew poorly on nitrate and CO, the toxicity of nitrite was determine. Next, $^{15}NO_3^-$ and $^{15}N_2$ was used to determine the source of the excess ammonium .

Nitrite is known to inhibit bacterial growth in a variety of organisms at a variety of concentrations, up to 5 mM [125, 126, 127, 128]. In one article, isolates of a soil *Pseudomonas* grew poorly at concentrations of 2.9 mM nitrite when in an anaerobic environment, even though nitrate is a substrate of this isolate. The most relevant example is *Clostridium botulinum*, whose iron-sulfur proteins react with nitrite, destroying the iron-sulfur cluster and forming iron-nitric oxide complexes [128]. The WLP contains numerous enzymes that require iron-sulfur clusters, such as the CodH, CoFeSP, and AcsBCD [89, 129, 130]. Whether nitrite concentrations 0.15 mM and below were poisoning iron-sulfur clusters was unclear, as *M. thermoacetica* can grow in the presence of 5 mM nitrite and oxalate with the WLP [131, 132]. For this reason, a kill curve was generated by growing *C. ljungdahlii* at varying concentrations of nitrite and fructose. Fructose was chosen as the substrate instead of H_2+CO_2 so as to separate the direct effect of nitrite from the low energy environment of H_2.

At low concentrations of nitrite (0.15 mM), there were measurable differences in the onset of growth. Regardless, these cells were able to grow to comparable cell density (approximately 1 OD_{660nm}) with a delay of approximately 24 hours (**Figure** 2-5). Higher concentrations, greater than 1.5 mM, completely arrested growth. Perhaps at the lower concentrations (0.15 mM), the cell culture re-mediated nitrite by reducing it to ammonium, though this is conjecture as the nitrite and ammonium concentrations were not measured in this experiment. From these results, nitrite could indeed negatively impact growth at the concentrations measured in the original experiment (**Figure** 2-4**A**). However this is likely not the main factor, as nitrite concentrations dropped below 40 μM after the original spike in concentration of nitrite.

The other avenue of inquiry was the nitrogen balance, which suggested a second source of nitrogen other than nitrate. In **Figure** 2-4, 3.8 mM of nitrate was consumed,

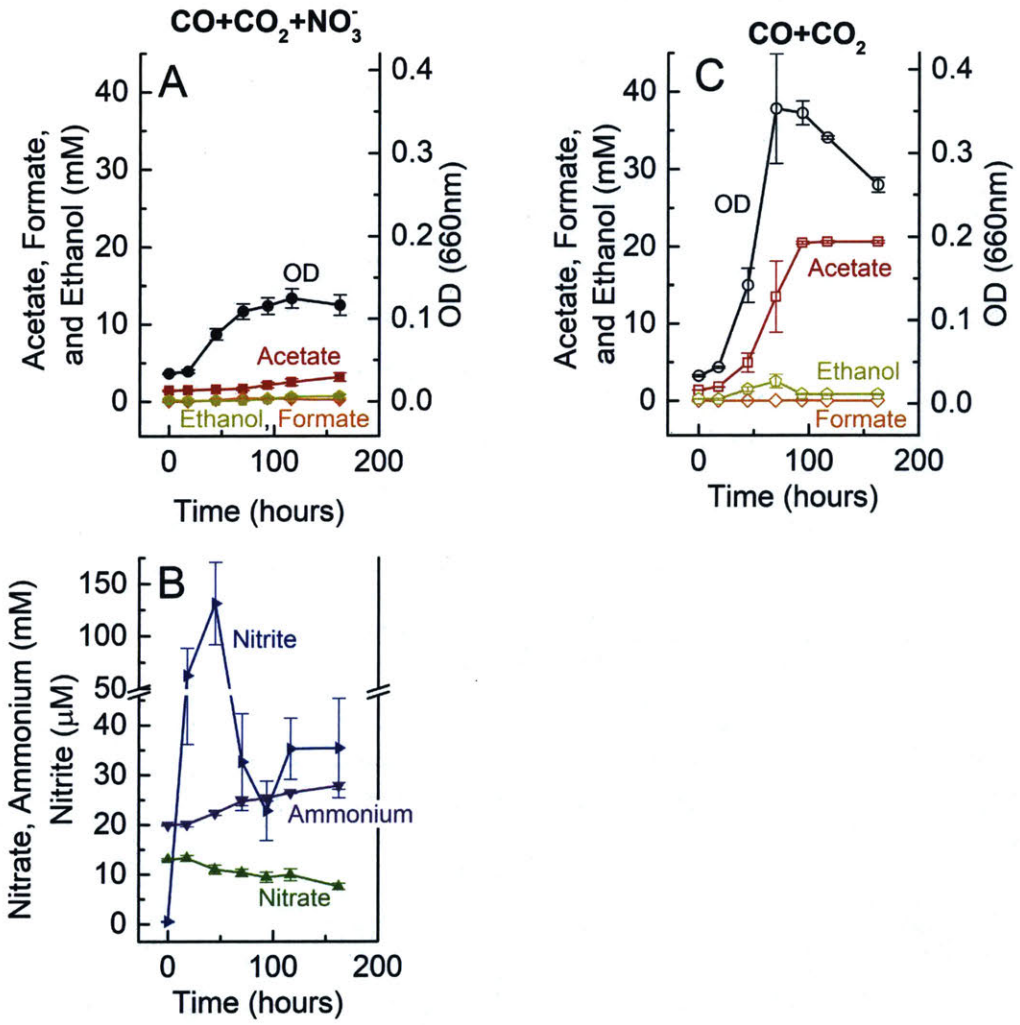

Figure 2-4: Metabolite concentrations and optical density of *C. ljungdahlii* grown with CO and CO_2 as the electron and carbon source, with (A, B) and without (C) nitrate. Black circle, OD_{660nm}; red square, acetate; orange diamond, formate; yellow pentagon, ethanol; green up-arrow, nitrate; blue right-arrow, nitrite; purple down-arrow, ammonium. Metabolite units are in mM, except nitrite which is in μM. Standard deviation given for three biological replicates.

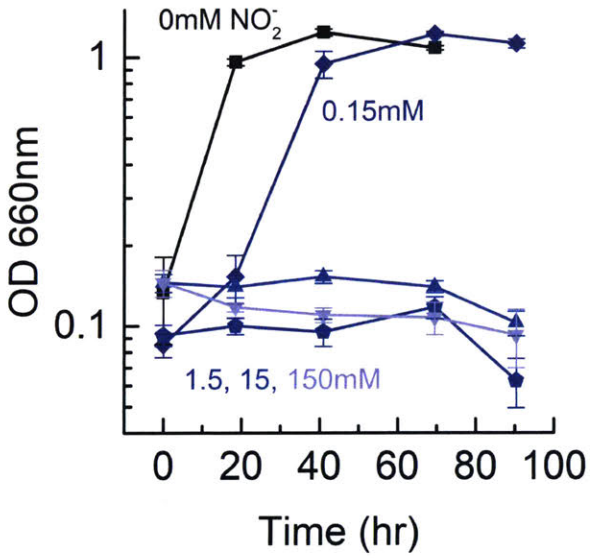

Figure 2-5: Inhibition of growth of *C. ljungdahlii* by nitrite; the carbon substrate was fructose and YE was present at 0.1 g/L. Nitrite concentrations: 0 mM, square; 0.15 mM, diamond; 1.5 mM, pentagon; 15 mM, up-triangle; and 150 mM, down-triangle. Standard deviation given for three biological replicates grown in hungate tubes.

and 6.5 mM of ammonium was generated; this was an excess of 2.7 mM of ammonium. Taking into account the culture volume (50 mL media and 107 mL headspace), this was 0.14 mmol ammonium. Within the media, there are 3 other possible sources, YE, N_2, and cysteine. The absolute quantity of each was: 0.04 mmol N in YE (**Table** 2.1), 5.4 mmol N in N_2 (1 atm), and 0.1 mmol N in cysteine (reducing agent). Based on the poor growth, we at first hypothesized that *C. ljungdahlii* was inexplicably fixing N_2, as amino acid deamination of arginine in the highly similar *C. autoethanogenum* resulted in ATP generation and improved growth rates [106]. Furthermore, *C. ljungdahlii* contains the genes necessary for N_2 fixation, and this has been experimentally shown when fructose was the substrate [133]. To test this hypothesis, a variety of conditions were tested in an attempt to improve ammonium generation, or abolish it.

The original growth conditions from **Figure** 2-4**A** contained approximately 1 $atm_{absolute}$ N_2 from the glovebox headspace, 19 mM NH_4Cl, and 1.36 atm_{gauge} of $CO+CO_2$ at a molar ratio of 80% to 20%. The original experiment is listed as 'A' or '2017' in the table of **Figure** 2-7. A design of experiments (DOE) was developed to abolish or improve the hypothesized N_2 fixation. For instance, removing N_2 from the headspace should prevent N_2 except that dissolved in the media. Another hypothesis to test was concerning the electron source (CO) and subsequent intracellular electron acceptor (reduced ferredoxin). Considering N_2 would be unnecessary with the presence of ammonium and nitrate; we hypothesized that the cells were using nitrogenase to remediate high concentrations of reduced ferredoxin. To test this, acetate was added, as acetate reduction to ethanol via AOR requires reduced ferredoxin [94]. Conversely, adding more N_2 and removing ammonia might improve N_2 fixation. The following conditions were used in the DOE:

A Original experiment from **Figure** 2-4 **A**

B Control to match 'A'

C -N_2: N_2 degassed from headspace with $CO+CO_2$ for 10 minutes

D +15 mM acetate: acetate added as a sink for ferredoxin

E $+N_2$: higher pressure of N_2 will increase mass transfer and the dissolved concentration

F $-NH_4^+$: NH_4^+ removed from media

G $+N_2$-NH_4^+: combination of 'E' and 'F'

C. ljungdahlii was grown on $CO+CO_2$ in PETC media with 0.1 g/L YE and 19 mM NH_4Cl. At late log phase, the culture was spun down and resuspended in media containing no NH_4^+, and inoculated in the conditions listed above. The growth and metabolite curves are found in **Figure** 2-6, while the nitrogen balance on nitrate and ammonium is presented in **Figure** 2-7. For most cultures (B, E, F, G), there was a substantial lag phase during the first 70 hours, after which growth resumed to a final OD_{660nm} less than 0.1 after 143 hours. In some cultures, growth continued after this plateau; the cultures that continued to grow also produced substantial acetate. When N_2 was flushed from the headspace, there was no lag phase, but growth was arrested by 0.051 ± 0.000 OD_{660nm}. Conversely, the culture containing acetate had no lag phase, but grew to the highest OD_{660nm} (0.137 ± 0.004) after 143 hours; after 429 hours, the OD_{660nm} was 0.300 ± 0.015. Perhaps acetate ameliorated the stressed conditions of the culture, however there was little change in the acetate concentration within the first 143 hours, dropping by 0.92 ± 0.07 mM; moreover, ethanol concentration only increased by 0.32 ± 0.09 mM. When compared to the change in concentration of nitrate and ammonium (5.8 ± 1.1 and 8.0 ± 3.5, respectively), acetate likely does not serve as a sink for ferredoxin on the same order of magnitude as nitrate. Instead, acetate likely served as a source of fixed carbon, as compared to CO or CO_2. This is supported by the carbon balance in **Table** 2.1; *C. ljungdahlii* grown on $CO+CO_2+NO_3^-$ fixed only a little more carbon than could be potentially derived from YE.

While the nitrogen balance was decreased from the original experiment (**Figure** 2-7**A** condition 'A' vs. 'B'), the DOE N balances indicated that there was another source of N other than nitrate. Mirroring the no growth phenotype of the $-N_2$ condition, little to no nitrate was reduced or ammonium generated within the first 143 hours. After

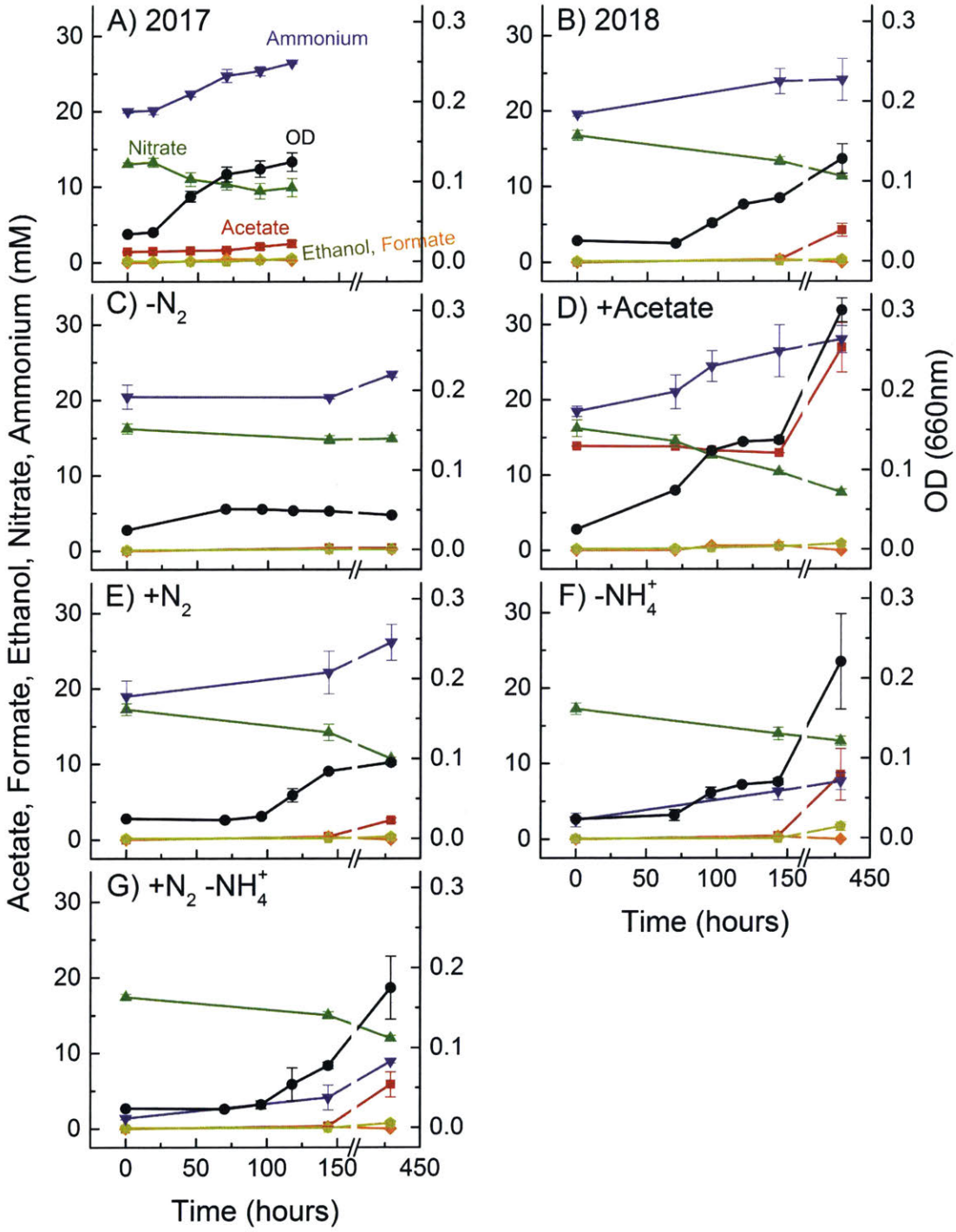

Figure 2-6: Growth and metabolite curves of *C. ljungdahlii* grown on $CO+CO_2+NO_3^-$ under a variety of conditions listed in **Figure** 2-7. Black circle, OD_{660nm}; red square, acetate; orange diamond, formate; yellow pentagon, ethanol; green up-arrow, nitrate; blue right-arrow, nitrite; purple down-arrow, ammonium. Metabolite units are in mM. Standard deviation given for three biological replicates.

Table 2.2: Experimental conditions for $^{15}N_2$ labeling experiment, including available electron sources and sinks.

	Gas Substrate (20 psig)	$^{15}N_2$ (psig)	$^{14}NO_3^-$ (mM)	$^{15}NO_3^-$ (mM)
A	$CO+CO_2$	2		
B	$CO+CO_2$		15	
C	$CO+CO_2$	2	15	
D	$CO+CO_2$	2		15

429 hours this was not the case; one possible explanation was incomplete flushing, as N_2 remained dissolved in the media despite flushing the headspace.

While the results suggested N_2 fixation, the best method to verify this was through $^{15}N_2$ labeling. A recent method was published for derivatizing NH_4^+ with phenol to produce indophenol [134], which can be measured via LC-MS. *C. ljungdahlii* was grown similar to 'F' of **Figure** 2-7; ammonium was removed from the media, the headspace was evacuated with a vacuum pump, and 2 psig of $^{15}N_2$ was added to the headspace. Cells were grown horizontally in balch tubes with 10 mL of media, so as to decrease the cost of labeled $^{15}N_2$.

Against expectations, there was no labeling of ammonium from $^{15}N_2$ in the experimental condition after growth (**Figure** 2-8**A**, $^{15}N_2$+$^{14}NO_3^-$+CO+CO_2). Instead, the only observable ^{15}N labeling was derived from $^{15}NO_3^-$. In this culture, the un-labeled ammonium was not carry-over from the inoculation (**Figure** 2-8**B, C**). Despite the absence of a positive control for $^{15}N_2$ fixation, the previously un-accounted for N was likely derived from either the yeast extract, or cysteine ($C_3H_7NO_2S$) which were present in the media. As cysteine de-amination was the likely cause, and because cysteine is comparatively expensive (27.63 $/mol, Sigma Aldrich, 5kg, 97% FG), inquiry into this phenotype was halted.

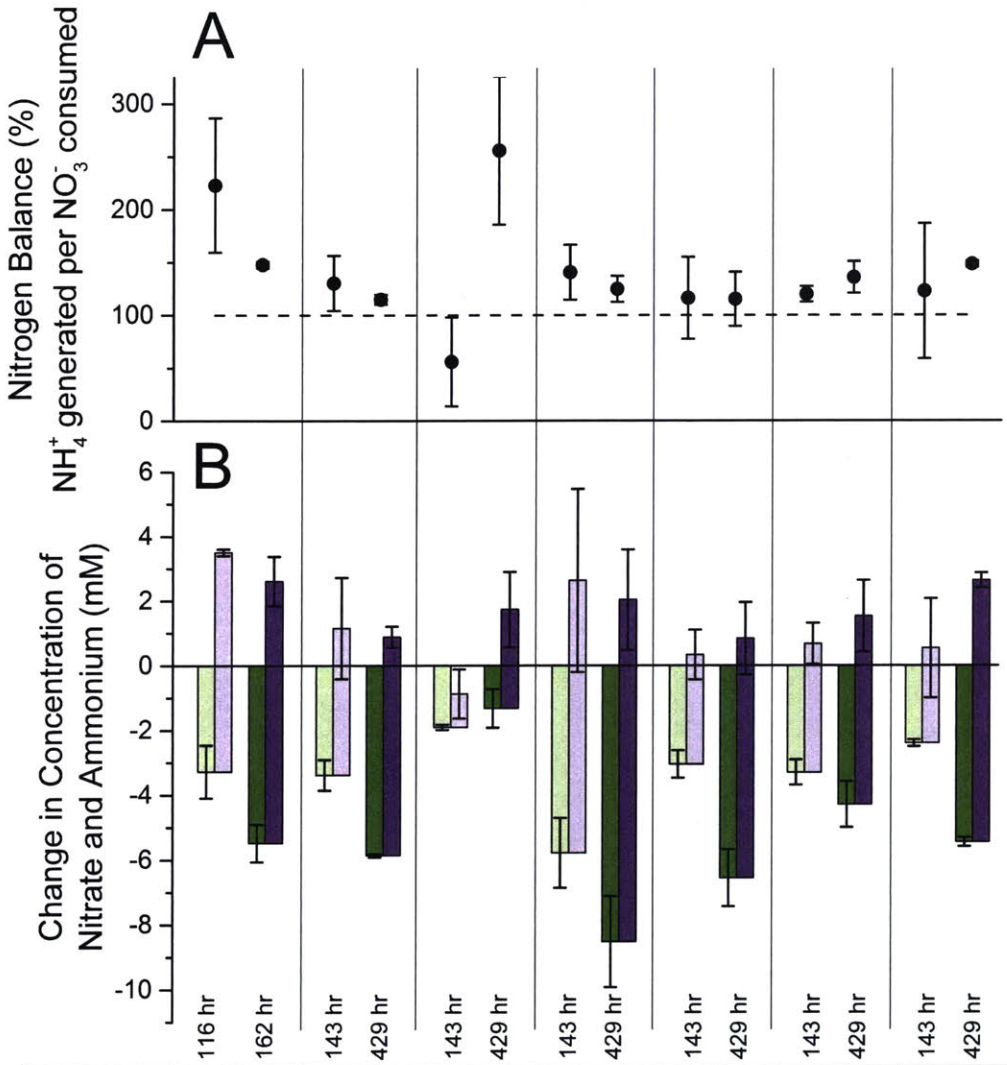

	A	B	C	D	E	F	G
Experiment	2017	2018 DOE					
N2 psig	1	1	~ 0	1	10	1	10
NH4 mM	19	19	19	19	19	--	--
Headspace flush	--	--	10 min	--	--	--	--
Acetate mM	--	--	--	15	--	--	--

*Cells washed once prior to subculture so '--' represents approx. zero. Media contains 0.1 g/L YE

Figure 2-7: DOE nitrate and ammonium balances of *C. ljungdahlii* grown on CO and NO_3^-.(A) the N balance was calculated by dividing the ammonia and $N_{biomass}$ generated by the nitrate consumed. (B) Change in concentration of ammonium and nitrate was taken between inoculation and the specified time listed below figure. Nitrate consumption (green) results in a decrease. Ammonium synthesis (purple) results in an increase. The difference was presumed to be fixed from a source other than nitrate. Standard deviation given for three biological replicates.

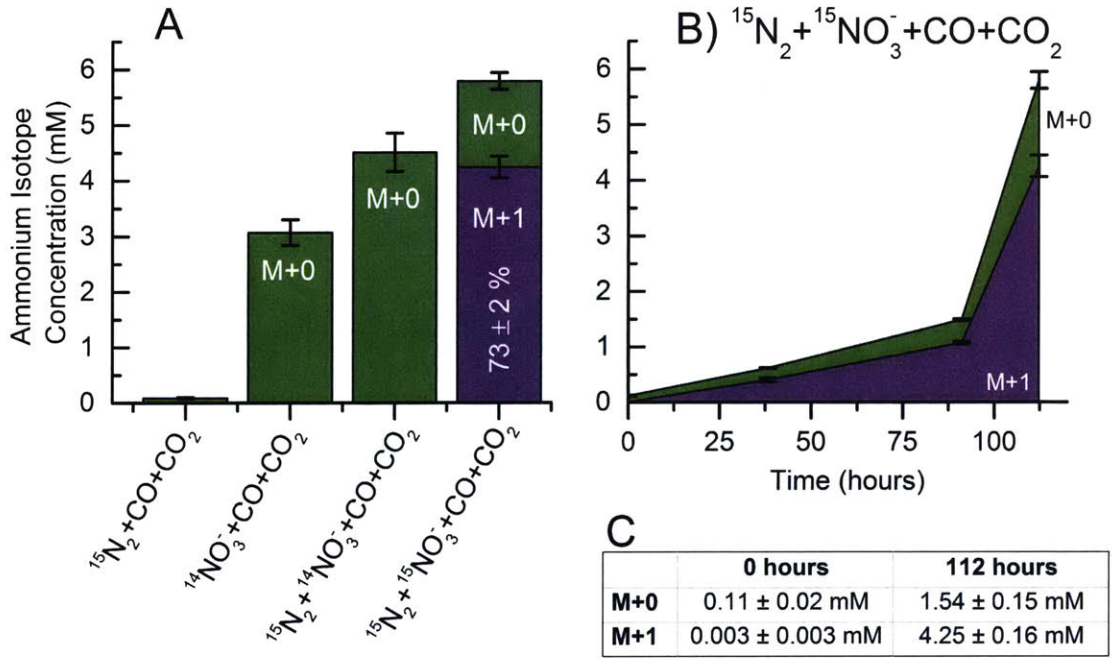

C

	0 hours	112 hours
M+0	0.11 ± 0.02 mM	1.54 ± 0.15 mM
M+1	0.003 ± 0.003 mM	4.25 ± 0.16 mM

Figure 2-8: Labeling pattern of soluble ammonium (NH_4^+) after growth of *C. ljungdahlii* on CO+CO_2, and $^{15}N_2$ or $^{15}NO_3^-$. (A) Concentration of ammonium isotopes after 123 hours for conditions listed in **Table** 2.2. (B) Time course of labeling pattern of $^{15}N_2$+$^{15}NO_3^-$+CO+CO_2. (C) Ammonium isotope concentration at the beginning and end of the $^{15}N_2$+$^{15}NO_3^-$+CO+CO_2 culture. All cultures were in stationary phase by 112 hours. Isotope labeling corrected for natural abundance. Standard deviation given for three biological replicates.

2.2.3 Nitrate does not Improve Autotrophic Growth of *M. thermoacetica* and *A. woodii* on H_2

As seen in literature [103], *M. thermoacetica* was able to grow in the presence H_2 and nitrate, however this appeared dependent on YE. For instance, the carbon found in the biomass and acetate (2.72 ± 0.33 mM) was less than the carbon available as YE (3.34 ± 0.05 mM). It was unclear if this flux of carbon was solely due to the YE or partially derived from CO_2. Furthermore, growth rate and final OD_{660nm} were decreased in the presence of nitrate. Substantial nitrite was produced from nitrate, reaching 1.8 ± 0.0 mM by stationary phase. These large concentrations of nitrite likely exacerbated the slow growth phenotype, as nitrite can be toxic [126]. This was observed with *C. ljungdahlii* (**Figure** 2-5), though *M. thermoacetica* was expected to grow in the presence of nitrite concentrations of at least 5 mM [131, 132]. Another 2.1 ± 1.3 mM of nitrate was converted to either ammonium or biomass, resulting in the nitrogen balance closing only to 59 ± 20 % (Table 2.1).

The difference in response to nitrate between *M. thermoacetica* and *C. ljungdahlii* was striking. The key differences between these organisms is the reducing equivalents required for various steps of the WLP [53], and the nitrate reductase system. *M. thermoacetica*'s nitrate reductase was putatively annotated as cell wall associated, like *E. coli*'s, and would use the cytochromes to mediate net proton motive force to power ATP production from nitrate. Researchers have yet to identify cytochromes or quinols in *C. ljungdahlii*, and the nitrate reductase was putatively annotated to be cytosolic based [120]. It was unclear if this was a key factor in nitrate repressing the WLP, or if transcriptional down-regulation was key.

As expected from literature [103], *A. woodii* was unable to metabolize nitrate autotrophically on H_2 (**Figure** 2-9) or heterotrophically on fructose. In the presence of fructose, after 45 hrs, nitrate was not consumed ($\Delta NO_3^- = 0.0 \pm 1.1$ mM) and the final OD_{600nm} was not substantially different than in the absence of nitrate (1.96 ± 0.03 mM without nitrate vs. 1.91 ± 0.07 mM with nitrate). This negative control was partially to ensure other factors were not resulting in the observed phenotype

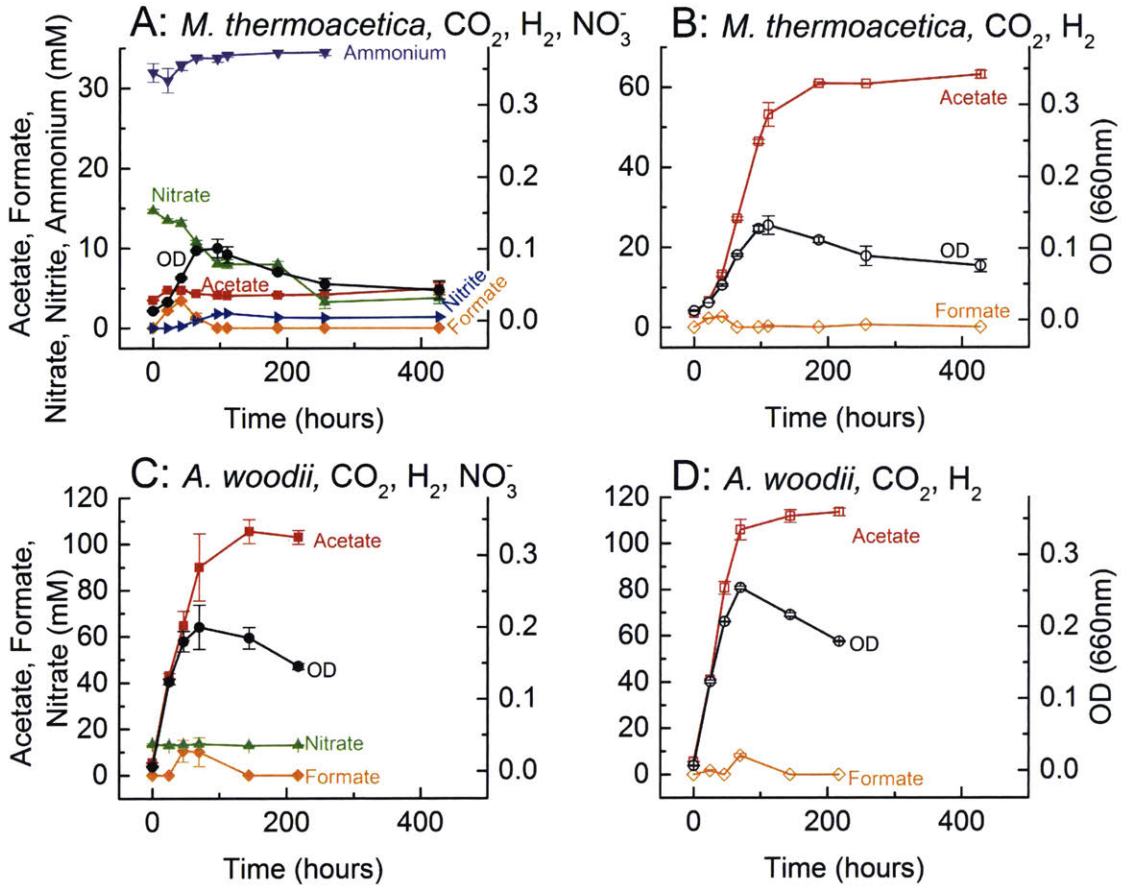

Figure 2-9: Metabolite concentrations and optical density of *M. thermoacetica* (A,B) or *A. woodi* (B,C) grown with H_2 and CO_2 as the electron and carbon source; with (A,C) and without (B,D) nitrate. Black circle, OD_{660nm}; red square, acetate; orange diamond, formate; yellow pentagon, ethanol; green up-arrow, nitrate; blue right-arrow, nitrite; purple down-arrow, ammonium. Metabolite units are in mM. Standard deviation given for three biological replicates.

of *C. ljungdahlii*. That there was no major impact of nitrate on *A. woodii*'s growth was surprising, as the Na^+-translocating F_1F_0-type ATPase was inhibited by 10 mM nitrate [135]. Perhaps without a transporter, nitrate could not enter the cell and thus could not inhibit the ATPase.

2.2.4 Chemical Mutagenesis of *M. thermoacetica* did not Remove Nitrate Repression of WLP

Despite *C. ljungdahlii* having the desired phenotype (utilization of the WLP in the presence of nitrate reduction), there would be benefits of adding this same ability to *M. thermoacetica*. Originally, the acetogen of choice for research and gas fermentation was *M. thermoacetica*; much of the research about the WLP was performed on isolates of *M. thermoacetica* as it was the only acetogen available to laboratories for study from the 1940's to 1960's [90]. There are also industrial benefits for growing the thermophilic *M. thermoacetica*. For instance, sterility is easier to maintain at these higher temperatures (55°C). Another important benefit is *M. thermoacetica*'s ability to grow on methanol and fix CO_2 in the process. The other methylotroph acetogen, *A. woodii*, does not metabolize nitrate and thus can not fulfill this role.

Rationally engineering the simultaneous utilization of nitrate and the WLP was desirable, yet two key bottlenecks existed, an efficient transformation protocol and the mechanism of repression of the WLP by nitrate. While a transformation protocol has been reported for *M. thermoacetica* [136, 91, 92, 93], our lab was not able to replicate there results. Transformation would occur, occasionally, but at low efficiencies and with little reproducibility ([62]). Even if the transformation protocol was effective, the method by which nitrate represses the WLP was unknown. Hence there were no targets for rational engineering. The alternative was random chemical mutagenesis, with the hope that sufficient stress and selective pressure would result in a strain of *M. thermoacetica* capable of utilizing nitrate and the WLP simultaneously. The mutagen chosen here was methylnitronitrosoguanidine (MNNG), which Alkylates G and T nucleotides, leading to transition mutations (G $\rightarrow$ A or T $\rightarrow$ C).

The protocol for mutagensis was modified from a protocol to mutagenize *Clostridium acetobutylicum* [137]. In brief, *M. thermoacetica* was first grown on methanol (100 mM) in a defined media containing no YE. At late log phase, cells were mutagenized for 5 minutes at 1, 10, and 100 μg/mL MNNG, washed, and then allowed to recover for 24 hours in a semi rich media (1 g L^{-1} YE and 4 g L^{-1} glucose). The cells were

washed once to remove the glucose and YE, and then inoculated into defined media under selective pressure with the substrates listed in **Table** 2.3. Two sources of energy were chosen, H_2 and methanol. H_2 was selected as it mirrored the successful results seen in *C. ljungdahlii.* Methanol was also included because growth rates and titers are greater than growth on just H_2+CO_2.

Assuming that the mutagensis results in only 1 viable cell per serum bottle (able to grow on CO_2 and NO_3^-), the time for an observable OD_{600nm} change (0.1) can be approximated from the expected growth rate (approximately 0.0295 hr^{-1} when *M. thermoacetica* was grown on methanol) and a cell to OD conversion ($Cells/mL = (OD_{600nm})(8 * 10^8)$). The expected time was approximately 26 days.

$$t = \frac{\ln\left(\frac{0.1\ OD_{600}}{\left(\frac{1\ cell}{50\ mL}\right)\left(\frac{1\ OD600}{8*10^8\ \frac{cell}{mL}}\right)}\right)}{0.0295\ hr^{-1}} = 26\ days \tag{2.3}$$

Table 2.3: Growth substrates provided to mutagenized *M. thermoacetica* after recovery. (-) indicates no expected growth, (+) growth to OD_{600nm} 0.2, (++) growth to OD_{600nm} 0.6 (+++) growth to OD_{600nm} 1.0. The nitrogen source is provided either as ammonium sulfate at 19 mM or sodium nitrate at 15 mM.

	Growth Substrate	N Source	Methanol	Glucose
Neg Control	(-) CO_2+NO_3^-	-NH_3,+NO_3^-	—	—
Pos Control	(+++) Glucose+NO_3^-	-NH_3,+NO_3^-	—	4 g/L
	(++) Methanol+CO_2	+NH_3,-NO_3^-	100 mM	—
	(+) H_2+CO_2	+NH_3,-NO_3^-	—	—
Selective Pressure	Methanol+CO_2+NO_3^-	-NH_3,+NO_3^-	100 mM	—
	H_2+CO_2+NO_3^-	-NH_3,+NO_3^-		—

In defined media with H_2+CO_2, *M. thermoacetica* was expected to grow to about 0.1 OD_{660nm}, hence growth and respiration on nitrate should improve the final biomass titer, much like it did when the organism was *C. ljungdahlii.* Even after extended recovery time (approximately 160 days), there was no substantial signs of growth under selective pressure (the presence of nitrate, **Figure** 2-10), beyond that of the 0.1 OD_{660nm}. There was also no substantial nitrate or methanol consumption: nitrate concentrations only decreased from 15.7 ± 0.2 to 14.1 ± 0.5 mM and methanol de-

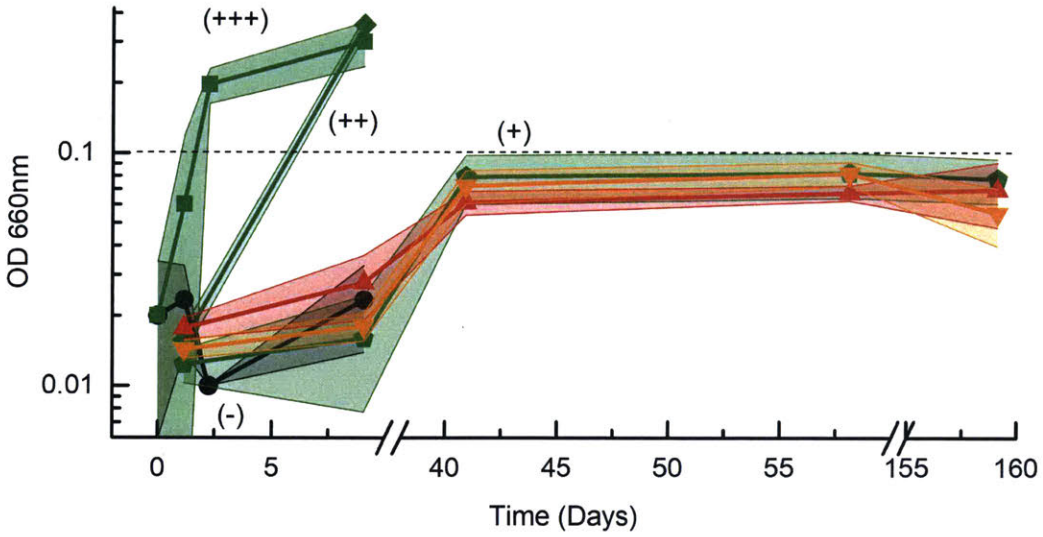

Figure 2-10: After chemical mutagenesis, *M. thermoacetica* was grown on defined media and the supplements mentioned in **Table** 2.3. For each selective condition, there was one 50 mL culture per mutagen concentration. The average under the selective condition was plotted. For instance, the curve for (++) was the average of cultures recieving either 1, 10, or 100 μg/mL of MNNG. Black circle, CO_2+NO_3^-; green square, glucose+No_3^-; green diamond, methanol+CO_2; green pentagon, H_2+CO_2; red up-arrow, methanol+CO_2+NO_3^-; orange down-arrow, H_2+CO_2+NO_3^-.

creased insignificantly from 102 $\pm$ 2 to 100 $\pm$ 2 mM. Moreover there was negligible acetate production. In comparison, the no nitrate controls grew well, except H_2+CO_2. This indicated that the concentration of MNNG used did not kill the culture.

This unsuccessful attempt suggests a more rational approach may be necessary to engineer *M. thermoacetica* to operate the WLP in the presence of nitrate. At this time, however, that mechanism of repression is unknown. If the mechanism was transcriptional regulation, chemical mutagenesis may be able to disable the key sensor or regulator. However if the repression is enzymatic in nature, such as inhibition/ deactivation of key enzymes (formate dehydrogenase or CODH), random mutagenesis likely won't disrupt the phenotype.

2.3 Confirming CO_2 Fixation in the Presence of Nitrate

2.3.1 The Role of Yeast Extract for Autotrophic Growth with Nitrate

Yeast extract (YE) is commonly used in acetogen research and other non-standard organisms to ensure robust and reproducible growth, usually at 1 g L^{-1}. This is conspicuously true for non-standard growth substrates such as gases (H_2). Even when elimination of this YE is desirable, researchers are unable. For instance, 0.05% YE (0.5 g L^{-1}) was necessary to ensure reproducible initiation of growth for *A. woodii* grown on methanol and methylated aromatics [138]. This is not surprising, as autotrophic growth operates at the thermodynamic limit [53]; any available fixed carbon as amino acids or sugar metabolites decreases the burden on energy metabolism (acetate secretion). While the addition of YE ensures reproducible and robust growth, the presence of YE can obfuscate results. As mentioned in Section 2.2.3, acetate and biomass generated during growth of *M. thermoacetica* on H_2+CO_2+NO_3^- could be derived from YE (Table 2.1). Further complicating matters, YE is a 'black box' and contains a variety of compounds. Since these compounds are generally un-defined, the compounds impact on a bacterial culture is unclear. To address this, researchers have even fractionated YE to determine which key compounds improve growth rates [139].

For this research, removing YE was desirable so as to minimize variables that could affect the conclusions drawn; in particular, that CO_2 fixation was occurring with the WLP in the presence of nitrate, instead of derived from YE. Moreover, the necessity of YE adds a large economic burden if these processes are implemented at an industrial scale. This can be clearly be seen by comparing the cost of YE to sugar; the cost of YE[1] is 230.26 \$ kg^{-1} whereas the cost of glucose[2] is 9.56 \$ kg^{-1}. While

[1]The cost of BD Bacto Yeast Extract was 11,513.22 \$ per 50 kg; accessed 2/26/2018 (VWR).
[2]The cost of D-(+)-Glucose ($\geq$ 99.5% (GC)) 239 \$ per 25 kg, accessed 2/26/2018 (Sigma-Aldrich).

attempts to remove YE were made, they resulted in low reproducibility, particularly for cultures grown on just H_2+CO_2. Furthermore, slight perturbations might result in interrupted growth.

To determine what concentration of YE to use, 3 concentrations of YE were added to the media (approximately 1, 0.1, and 0.01 g L^{-1}). This was achieved in different ways, first a culture was grown on H_2+CO_2+NO_3^- and 1 g L^{-1} YE, then:

1. Culture inoculated with a 10x dilution into media with no YE (> 0.1 g L^{-1} YE)
2. Cells washed twice (1 mL per mL) with media containing no YE, and inoculated with a 10x dilution
   (a) Spent media added back at either a 10x or 100x dilution (> 0.1 or 0.01 g L^{-1} YE)
   (b) Fresh YE stock solution (10 g L^{-1}) added at either a 100x or 1000x dilution (0.1 or 0.01 g L^{-1} YE)

These variations can be found in **Table** 2.4. Washing the media and adding either spent media back or fresh YE would account for any molecules secreted and present in the inoculum, which could power growth and CO_2 reduction. At the peak OD_{660nm}, the fixed carbon was determined from acetate, formate, and biomass (little to no ethanol was fermented). When 1 g L^{-1} of YE was provided (Inoculum, **Figure** 2-11), the carbon fixed was the same or less than the carbon provided in the form of YE; hence it was unclear whether there was CO_2 fixation. Conversely, the fixation of CO_2 in the presence of nitrate was substantially greater than that provided in YE, when the YE concentration was 0.1 g L^{-1} or less (A - D, **Figure** 2-11). When cells were washed, there was a decrease in fixed carbon between culture A and C (A: 0.422 $\pm$ 0.042 vs. C: 0.286 $\pm$ 0.025), likely due some form of stress during anaerobic centrifugation and resuspension. Curiously, there was not a substantial difference between receiving fresh YE or spent media when approximately 0.1 g L^{-1} YE was provided (B: 0.313 $\pm$ 0.026 vs. C: 0.286 $\pm$ 0.025), even if some of the YE was likely consumed from the spent media in the inoculum. This trend was also true at the

lower YE concentration of 0.01 g L^{-1}. This suggests that YE did play a role during H_2+CO_2+NO_3^- metabolism, yet it was not substantial.

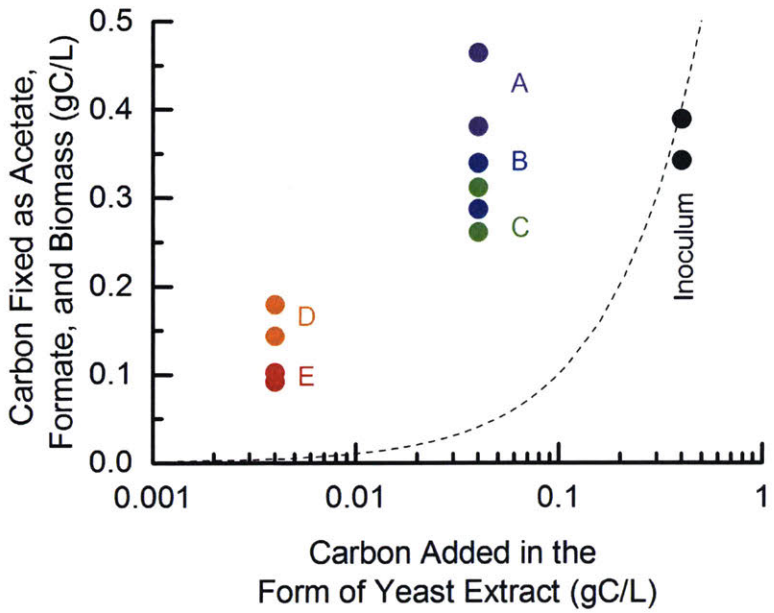

Figure 2-11: Carbon fixed into acetate, formate, and biomass, plotted against carbon present in the inoculum in the form of yeast extract. *C. ljungdahlii* was grown with H_2+CO_2+NO_3^-. The culture designations are given in **Table** 2.4. Each point represents a single biological replicate. Any points above and to the left of the dotted line indicate fixed carbon that could not be attributed to the YE.

To ensure that YE was not necessary for growth on H_2+CO_2+NO_3^-, the components of YE were first determined and then selectively added to a defined media containing no YE. The general components of YE were found in literature [139]: 0.63g free amino acids and peptides per g YE, 0.10g sugars per g YE, and 0.07g nucleic acids per g YE; the remaining mass was minerals, vitamins, or unreported. The composition of amino acids and peptides was determined from *Saccharomyces cerevisiae* [140]. Fructose and glucose were chosen as the sugar, and an equimolar mixture of dNTP's was chosen for the nucleic acids. If 0.1 g L^{-1} YE was fully replaced with a defined replacement, the resulting concentrations would be approximately those listed in **Table** 2.5.

To media containing no YE, a variety of supplements were added (**Table** 2.5). *C. ljungdahlii* was then grown on H_2+CO_2+NO_3^-, and the OD_{600nm} was measured

Table 2.4: Constituents of media prepared with varying concentrations of YE. The approximate concentration of YE present in the media is given in mg L^{-1}

				Resuspension after washing			
Culture	Fresh (mL)	Nitrate, 1M (mL)	YE, 10g/L (μL)	Spent (mL)	Fresh (mL)	YE (mg/L)	Notes
Inoculum	45	0.75	5000			1000	
A	44.25	0.75		5		<100	No Wash
B	43.75	0.75	500		5	100	Wash 2x
C	44.25	0.75		5		<100	Wash 2x
D	44.2	0.75	50		5	10	Wash 2x
E	44.25	0.75		0.5	4.5	<10	Wash 2x

after 100 hrs using a modified Ultrospec 10 (**Figure** 2-12). For instance, '+YE' indicates the presence of 0.1 g/L YE (the control). 'AA + NA + Sugars' indicates all components were added (63 mg/L amino acids, 0.07 mg/L nucleic acids, and 10 g/L sugars) to replace YE. Based on growth after 100 hrs, there was no substantial difference between the various conditions even if no supplements were added ('-YE'). This indicates that while YE was necessary for reproducibility of growth on H_2+CO_2, YE was not necessary for the observed growth improvements on H_2+CO_2+NO_3^-. This has important implications, as the improvements in growth rate of H_2+CO_2+NO_3^- over H_2+CO_2 will likely increase as YE is eliminated from the media.

2.3.2 Mass Balances and $^{13}CO_2$ Labeling Confirm CO_2 Fixation

While carbon balances in Table 2.1 indicate substantial CO_2 fixation in the presence of nitrate, other sources of C were present in the media, particularly L-cysteine hydrochloride which was added at around 0.3 g/L (1.9 mM or 5.7 mM C) as a reducing agent to scavenge for oxygen. Furthermore, prior to constructing a metabolic model and calculating ATP yields from nitrate reduction, there was a necessity to confirm that the predominant electron (or energy) source was H_2 and the only electron acceptors were CO_2 and nitrate. Other sources and sinks would greatly affect this calculation.

Table 2.5: Composition of supplements in media when provided in place of yeast extract. Concentrations are those present within the growth media. For instance, AA + Sugar indicates that 63 mg AA per L and 10 mg Sugar per L replaced YE.

Amino Acids	**mg/L**
Alanine	2.76
Arginine	16.68
Asparagine	0.67
Aspartic acid	5.06
Citrulline	3.00
Glutamic acid	17.48
Glutamine	6.67
Glycine	0.78
Histidine	0.97
Isoleucine	0.40
Leucine	0.25
Lysine	0.65
Methionine	0.38
Ornithine	1.65
Phenylalanine	0.40
Serine	1.71
Threonine	1.98
Tryptophan	0.39
Tyrosine	0.24
Valine	0.90
Amino Acid Total	**63**

Sugars	**mg/L**
Gluose	5
Fructose	5
Sugars Total	**10**

Nucleic Acids	**mg/L**
Equimolar dNTP's	0.07

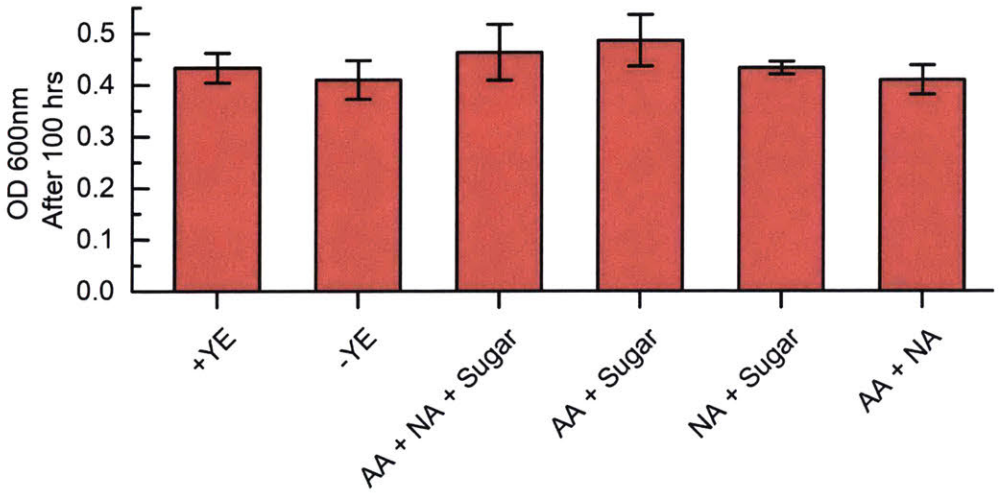

Figure 2-12: The effect of YE and its theoretical components was determined by measuring growth of *C. ljungdahlii* on H_2+CO_2+NO_3^- after 100 hrs. To a defined media that did not contain YE ('-YE'), YE or a mimicking synthetic blend was added (**Table** 2.5). Parts of the synthetic blend were removed to determine the effect on growth. For instance, AA + NA + Sugar implies all 3 supplements replaced YE, whereas AA + NA implies that only amino and nucleic acids were added. No specific component played a signficant role. Cells were grown horizontally in Balch tubes and OD_{600nm} was determined with a modified handheld ultraspec. Standard deviation given for three biological replicates.

To further verify that CO_2 was reduced and fixed to acetate by *C. ljungdahlii* in the presence of nitrate, $^{13}CO_2$ was provided to the headspace. Both cultures (H_2+$^{13}CO_2$ and H_2+$^{13}CO_2$+NO_3^-) exhibited significant labeling of acetate as M+1 and M+2 (**Figure** 2-13A,B). For H_2+$^{13}CO_2$ there was 43% M+1 and 29% M+2, whereas for H_2+$^{13}CO_2$+NO_3^- there was 34% M+1 and 21% M+2. This includes the unlabeled acetate present in all cultures after inoculation at approximately 2 mM C. The no $^{13}CO_2$ control (**Figure** 2-13C) exhibited growth and acetate production up to 11.4 ± 0.1 mM C which corresponds closely with the unlabeled carbon in the other cultures (**Figure** 2-13A,B). These unlabeled carbons could be attributed to either the unlabeled bicarbonate, the YE, or the inoculum. Based on the media formulation and ideal gas law, bicarbonate was the likely source as bicarbonate accounts for 49.3% of the available carbon in $^{13}CO_2$ and $H^{12}CO_3^-$.

This validates that CO_2 is indeed fixed in the presence of nitrate, and suggests that the nitrate inhibitory mechanisms predicted in *M. thermoacetica* [105] were not operating in *C. ljungdahlii.* Moreover, the presence of labeling as M+2 (both carbons in acetate) indicate neither the methyl or carbonyl branch of the WLP was blocked.

To ensure that only H_2+NO_3^- were responsible for the increase in growth yield, a detailed H_2 balance was performed by comparing changes in headspace pressure and concentration, and metabolite concentrations for cultures seen in **Figure** 2-14. These cultures were grown in serial batch to verify that there were minimal changes to the H_2 balance over time.

Other than H_2, YE (0.1 g/L) and L-cysteine HCl (0.3 g/L or approximately 32 mM) could provide reducing equivalents. The reducing equivalents that could be derived from YE were calculated from the experimentally determined molecular formula; based on degree of reduction, at most 6.15 mM H_2-equivalents were available in 0.1 g/L YE. For the standard 50mL culture volume used here, this was 0.31 mmol (**Section** A.1). The possible contribution of YE to the predicted H_2 consumption was plotted in **Figure** 2-13D as a dashed line.

The measured values of H_2 consumption matched closely with those determined theoretically and was closed to 80 ± 4% for the H_2+CO_2 cultures, and 91 ± 4% for

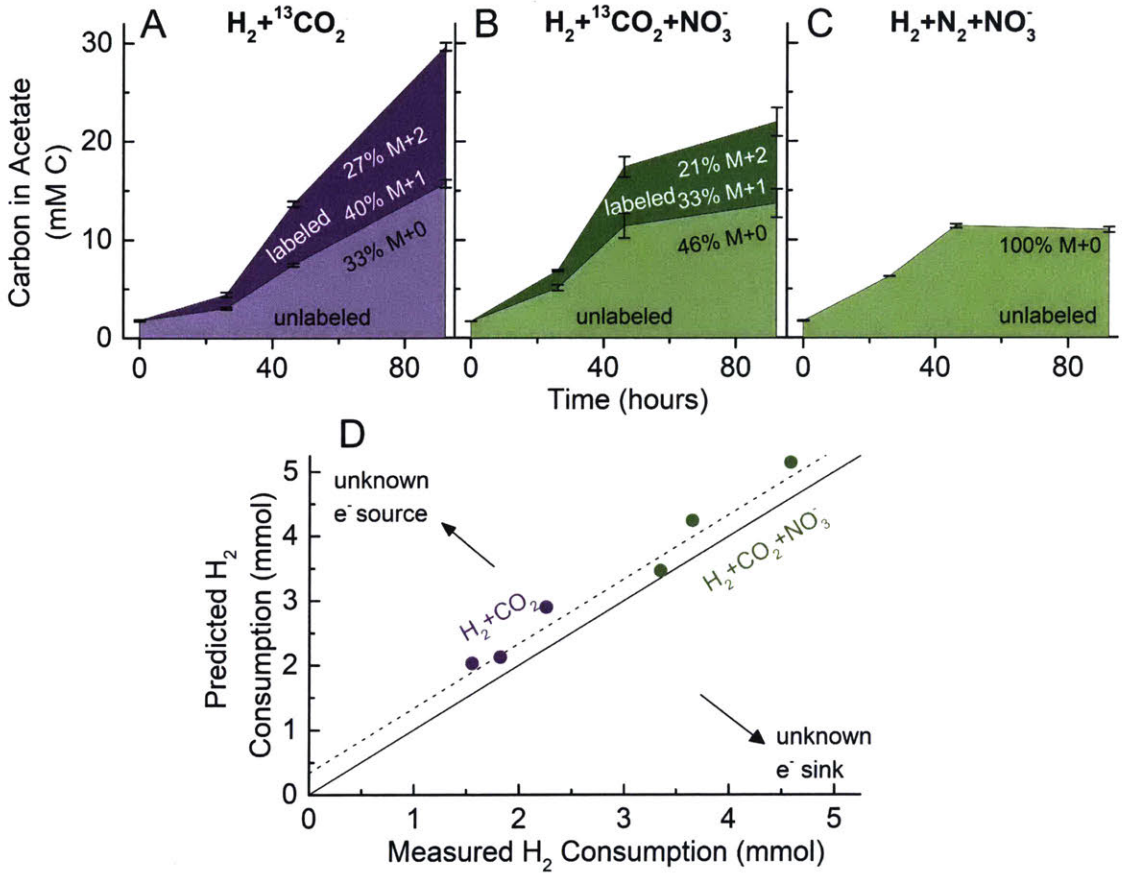

Figure 2-13: Labeling from $^{13}CO_2$ confirms CO_2 fixation and the H_2 balance confirms H_2+NO_3^- was responsible for improved yields and rates. Labeled carbon was detected in derivatized acetate produced during growth of *C. ljungdahlii* on (A) H_2+$^{13}CO_2$, (B) H_2+$^{13}CO_2$+NO_3^-, and (C) H_2+N_2+NO_3^-. (C) Unlabeled carbon was likely derived from bicarbonate or YE, as seen in the no $^{13}CO_2$ control. Labeling pattern of acetate is given at the final time point as a percentage. Labeled carbons determined from the M+1 and M+2 pool of acetate; labeled carbon = 1*(M+1) + 2*(M+2). (D) In a subsequent experiment, measured H_2 consumption was compared to predicted H_2 consumption; the prediction was based on reduction of CO_2 to acetate, formate, and cells or nitrate to ammonium and cells. Each point is a single culture. The possible contribution of YE is accounted for with the dashed line. Arrows indicate why data would fall on either side of this line. Standard deviation given for two (A,B,C) biological replicates.

H_2+CO_2+NO_3^- cultures (**Figure** 2-13D, **Table** 2.6). This indicates that almost all electron donors and acceptors are accounted for in these experiments; the discrepancy of excess reducing equivalents could be attributed to YE, as designated by the dashed line in **Figure** 2-13D. This implies that nitrate reduction was directly responsible for the increase in growth yield; by extension nitrate reduction was coupled to ATP production. With this known, approximate ATP yield could be calculated from metabolite and biomass balances.

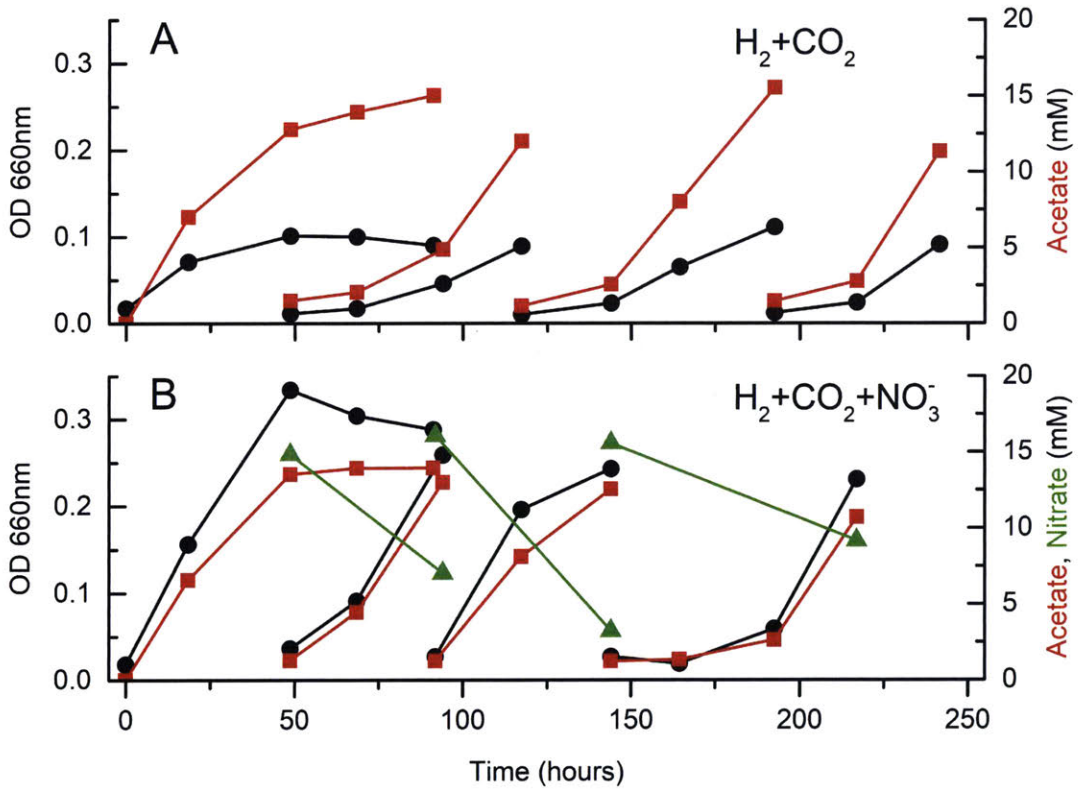

Figure 2-14: Growth of *C. ljungdahlii* on (A) CO_2+H_2 or (B) CO_2+H_2+NO_3^-. This growth was robust and continued after multiple subcultures. In the presence of nitrate (B), growth (black circles) occurred simultaneous to acetate production (red squares) and nitrate reduction (green up-triangles). Each drop in OD indicates a subculture by approximately 10x dilution. The carbon and hydrogen balance is provided in **Table** 2.6. Nitrate is present in all sub-cultures of panel B, but not measured for the first culture. H_2 balances were determined from the final 3 cultures from each condition, at the last time point.

Table 2.6: Change in metabolite and cellular concentrations determined at inoculation and after subculture for growth curve in **Figure** 2-14. The predicted consumption of H_2 was determined by the reduction of CO_2 to carbon products and nitrate to ammonium. Measured H_2 consumption was determined from changes in volume, pressure, and H_2 concentration of the headspace. A total bottle volume of 157 mL was assumed. Changes in liquid volume due to sampling, and changes in pressure of headspace due to measuring pressure were accounted for in the balance (**Section** A.2).

	$CO_2 + H_2$			$CO_2 + H_2 + NO_3^-$			
Culture:	**A**	**B**	**C**	**A**	**B**	**C**	**units**
ΔOD	0.00375	0.00487	0.00384	0.0110	0.0108	0.0099	OD 660nm * L media
ΔCells	0.053	0.068	0.054	0.160	0.157	0.143	mmol Cellular Carbon
ΔAcetate	0.505	0.691	0.481	0.580	0.564	0.458	mmol Acetate
ΔFormate	0.001	0.000	0.000	0.062	0.043	0.102	mmol Formate
ΔNitrate	—	—	—	0.385	0.633	0.310	mmol Nitrate
ΔH_2	2.13	2.90	2.03	4.24	5.14	3.46	mmol H_2 (predicted)
Liquid Volume	49.5	49.5	49.5	50.3	50.3	50.3	mL (initial)
	41.5	46.5	47.5	43.3	43.3	37.3	mL (final)
Pressure	21.36	20.97	21.81	21.48	21.28	22.20	psig (initial)
	10.22	6.93	12.58	3.78	0.44	5.60	psig (final)
H_2 %	72.0	71.4	72.7	72.9	72.2	74.7	mol/mol total (initial)
	72.8	78.9	75.2	70.2	64.2	70.2	mol/mol total (final)
ΔH_2	1.82	2.26	1.56	3.65	4.58	3.35	mmol H_2 (measured)
H_2 Balance	86%	78%	77%	86%	89%	97%	

2.4 A Proposed Model for Nitrate-dependent ATP Production in *C. ljungdahlii*

That nitrate reduction was coupled to ATP production was surprising, since this pathway in *C. ljungdahlii* was predicted to be assimilatory, and typically assimilatory nitrate reduction is not energy conserving because it occurs in the cytoplasm [141]. The other two known nitrate reduction systems, respiratory and fermentative, are energy conserving [141, 142]. Respiratory nitrate reduction involves a Q loop to couple nitrate reduction to ATP generation, for example as seen in *E. coli* [143]. Fermentative nitrate reduction redirects carbon flow to pathways with substrate level phosphorylation, by providing a non-fermentative electron acceptor [142]. *M. thermoacetica* is predicted to respire nitrate, as its genome contains genes similar to *E. coli*s membrane-bound nitrate reductase [144] and has the genes necessary to synthesize cytochromes and quinones. *C. ljungdahlii*, on the other hand, does not contain the genes necessary for cytochrome or quinone synthesis [94] and thus is not predicted to respire nitrate. Further, energy conservation by fermentative nitrate reduction is inconsistent with our experimental results, since carbon flux is not redirected from ethanol to acetate under the conditions tested (**Table** 2.1). Thus, nitrate-dependent ATP production in *C. ljungdahlii* likely occurs by a novel mechanism.

During autotrophic growth, energy conservation in *C. ljungdahlii* is mediated by the Rhodobacter Nitrogen Fixation (Rnf) complex, which catalyzes the highly exergonic transfer of electrons from reduced ferredoxin to NAD^+, using the free energy released to electrogenically translocate protons across the cell membrane. These protons are then imported through an ATPase, leading to the production of ATP. It therefore seemed likely that the Rnf complex plays a role in ATP generation from nitrate reduction. **Figure** 2-1 shows a hypothetical pathway for the Rnf-dependent generation of ATP from nitrate reduction. In this pathway, four molecules of H_2 are oxidized by an electron-bifurcating hydrogenase, reducing two molecules each of $NADP^+$ and ferredoxin [99]. The electron-bifurcating transhydrogenase (Nfn) converts two NADPH into NADH and reduced ferredoxin. The three reduced ferredoxin

are subsequently re-oxidized at the Rnf complex, leading to the formation of three additional molecules of NADH, and the extrusion of six protons. The protons are re-imported through the ATPase, generating 1.5 molecules of ATP. Meanwhile, the four NADH molecules are re-oxidized in the cytosolic reduction of nitrate to ammonium. The net stoichiometry is [102]:

$$\begin{aligned} &4H_2 + 2H^+ + NO_3^- + 1.5ADP + 1.5P_i \rightleftharpoons 4H_2O + NH_4^+ + 1.5ATP \\ &\triangle_r G'_0 = -138\ kJ\ mol^{-1}H_2 \end{aligned} \tag{2.4}$$

The proposed mechanism relies on electron bifurcation by the hydrogenase to couple nitrate reduction to ATP production without the need for a membrane-bound nitrate reductase. Though this mechanism is hypothetical, there is precedent from caffeate reduction in *A. woodii*, which also increases growth yields and produces 1 mol of ATP per mol of caffeate by a similar RNF-dependent mechanism [145, 146, 147].

Importantly, the proposed mechanism is completely independent of carbon metabolism, and provides significantly more ATP than the production of acetate from H_2 (1.5 vs 0.63) by allowing ferredoxin oxidation to be coupled to energy conservation, rather than to CO_2 reduction to CO. These theoretical predictions were broadly consistent with our experimental data averaged during growth phase, where 0.296 ± 0.005 mol ATP per mol acetate was produced by the WLP and 0.801 ± 0.023 mol ATP per mol of nitrate by nitrate reduction (see **Section** 2.4.1). The difference between theoretical and experimental ATP yields can be attributed to a maintenance coefficient, as well as other factors that affect ATP generation and change during the stages of growth. These include pH and acetate concentration [101].

2.4.1 Mathematical Modeling of Stoichiometric Pathways and Determination of ATP Yields

Mathematical models were assembled in MATLAB to predict ATP yields and the theoretical yields for the production of various potential products [148]. The stoi-

chiometric equations used to model the WLP are given in **Equation** 2.5 to 2.18 [53]. While some metabolic models equate all electron carriers [24], this can impact the accuracy of the model due to the importance of electron bifurcation for these pathways and organisms [149, 112]. Take for example the hydrogenase and formate dehydrogenase of *Clostridium autoethanogenum*, which are key steps of the WLP and have specific electron donors and acceptors [112]. The electron-bifurcating hydrogenase co-reduces NADP+ and oxidized ferredoxin, but reduces neither in isolation (**Equation** 2.13). The formate dehydrogenase (complexed to the electron-bifurcating hydrogenase) reduces CO_2 with H_2 directly (**Equation** 2.6). For this reason, all reducing equivalents were treated independently [53].

In **Equation** 2.17, the ATP required to produce a carbon mole of biomass is determined from an approximate gram cell per C mol cell and the biomass produced per mol of ATP. Here we use values characteristic for clostridia; 26 $gCell\ mol^{-1}_{cellularcarbon}$ and 10.7 $gBiomass\ mol^{-1}_{ATP}$ [24]. The biomass molecular formula chosen was $CH_{2.08}O_{0.53}N_{0.24}$ [24, 46], which matched closely with the biomass composition determined for *C. ljungdahlii* via CHNS (**Figure** A-1, $CH_{1.76}N_{0.25}S_{0.02}$).

Nitrate assimilation in *C. ljungdahlii* was proposed [94] to be similar to that of the *Clostridium perfringens*-like fermentative nitrate reductases [150]. Though others [120] have noted similarities to the nitrate reduction system of *Nautilia profundicola* [151], even if *C. ljungdahlii* contains neither cytochromes nor a periplasm. Fermentative nitrate reduction is different than assimilatory and respiratory nitrate reduction, as fermentative nitrate reduction is considered to be linked to energy conservation by substrate-level phosphorylation by redirecting electron flux to reactions that provide substrate level phosphorylation such as acetate, butyrate, lactate, and ethanol [142]. Based on arguments presented previously, nitrate reduction in *C. ljungdahlii* was likely not fermentative nor respiratory (with cytochromes and quinols). Instead we hypothesize the mechanism involves soluble nitrate reductases and was indirectly linked to ATP production through the RNF-complex (**Figure** 2-1). As this model was not verified, we instead chose a more generalized equation for nitrate dependent ATP production.

Nitrate reduction occurs with four major steps, 1) nitrate uptake, 2) reduction of nitrate to nitrite, 3) reduction of nitrite to hydroxylamine, and finally 4) reduction of hydroxylamine to ammonium [120]. How and at which step energy is conserved is unknown; if the proposed model were correct, no step was directly related to ATP production (**Figure** 2-1). Hence the intake and reductions have been combined for a generic ATP generation term (X) in Equation 2.18. This would include the potential cost of importing and exporting nitrate and ammonium. While the genes necessary for cytochrome production are not present in *C. ljungdahlii*, this does not preclude other electron transport systems other than the RNF-complex. Moreover, the electron carrier utilized during nitrate reduction is also unknown; here we use the equivalent electrons as derived from H_2, acknowledging that the specific electron carrier may affect the energetics of metabolism and the theoretical ATP yield. For instance, if reduced ferrodoxin is necessary for nitrate reduction, ATP can't be produced with the proposed mechanism.

The WLP, on the other hand, can produce at most 0.63 ATP per acetate because 1 reduced ferredoxin was required to form the carbonyl group of acetyl-CoA [53]. However the cost would likely be lower due to maintenance, higher ATP cost of biomass, and other losses. Hence we introduced an efficiency for ATP production by the WLP (N in **Equation** 2.16).

Denitrification to N_2 was also possible, as *C. ljungdahlii* was known to fix N_2 [133]. The proton translocating RNF-complex was implicated to play a necessary role during N_2 fixation and hence could be involved in energy metabolism. However, based on the provided elemental nitrogen balances, the majority of nitrate was converted to either ammonium or biomass and denitrification likely plays little to no role here (**Table** 2.1).

$$CO_2 + Fd_{red} \rightleftharpoons CO + Fd_{ox} \tag{2.5}$$

$$CO_2 + H_2 \rightleftharpoons Formate \tag{2.6}$$

$$Formate + ATP \rightleftharpoons CHO\text{-}THF + ADP + Pi \tag{2.7}$$

$$CHO\text{-}THF \rightleftharpoons CH\text{-}THF + H_2O \tag{2.8}$$

$$CH\text{-}THF + NADH \rightleftharpoons CH_2\text{-}THF + NAD^+ \tag{2.9}$$

$$CH_2\text{-}THF + NADH \rightleftharpoons CH_3\text{-}THF + NAD^+ \tag{2.10}$$

$$CH_3\text{-}THF + CO \rightleftharpoons Acetyl\text{-}CoA \tag{2.11}$$

$$Acetyl\text{-}CoA + ADP + Pi \rightleftharpoons Acetate + ATP \tag{2.12}$$

$$2H_2 + Fd_{ox} + NADP^+ \rightleftharpoons Fd_{red} + NADPH \tag{2.13}$$

$$2NADPH + NAD^+ + Fd_{ox} \rightleftharpoons 2NADP^+ + NADH + Fd_{red} \tag{2.14}$$

$$2Fd_{red} + 2NAD^+ + 4H^+_{in} \rightleftharpoons 2Fd_{ox} + 2NADH \tag{2.15}$$

$$N\,ADP + N\,Pi \rightleftharpoons N\,ATP + 4H^+_{in} \tag{2.16}$$

$$Acetyl\text{-}CoA + 2.43ATP + 0.3NADH \rightleftharpoons Biomass + 2.43ADP + 2.43Pi \tag{2.17}$$

$$NO_3^- + 4H_2 + X\,ADP + X\,Pi \rightleftharpoons NH_4^+ + X\,ATP \tag{2.18}$$

The system of equations were solved for the substrates H_2+CO_2 to determine N in **Equation** 2.16 using experimental data from **Figure** 2-2 and **Table** 2.1. This provided an ATP yield averaged during the whole growth phase. No accumulation of intermediates was assumed including electron carriers (NADH, NADPH, and ferredoxin) and ATP [148]. By setting acetate and biomass production, the efficiency for ATP production was calculated with the MATLAB solver function. The result was lower than expected and this can be attributed to averaging throughout growth phase. For instance, during growth on H_2+CO_2 instantaneous ATP yields drop from 0.52 $\pm$ 0.02 at 32 hrs to 0.10 $\pm$ 0.01 mol ATP per mol acetate at 132 hrs (**Figure** 2-15).

$$N_{C.\ ljungdahlii} = 0.470 \pm 0.008 \ or \ 0.296 \pm 0.005 \frac{ATP}{acetate} \tag{2.19}$$

Assuming the ATP yield on biomass and acetate remain approximately the same when grown on H_2+CO_2 or H_2+CO_2+NO_3^-, the ATP derived from nitrate reduction (X) was calculated from the carbon and nitrogen balance for cells grown on H_2+CO_2+NO_3^- after 42 hrs (**Figure** 2-2 and **Table** 2.1). During this time 9.0 ± 0.2 mM acetate was produced, contributing ATP to growth as defined previously. Also within this time frame, nitrate was converted stoichiometrically to ammonium and biomass, within error, with a closure of 107 ± 13 %. For this reason, all nitrate was assumed to be converted to ammonium. From this, X was calculated with the MATLAB solver function to be 0.801 ± 0.023 ATP per mol nitrate. This was indicative of significant ATP production per nitrate or per H_2. This value was lower than the predicted theoretical value for indirect nitrate respiration with the RNF complex (1.5). However, this can similarly be attributed to averaging throughout the growth phase. The instantaneous ATP yield from nitrate peaked at 1.5 ± 0.1 at 22 hrs and drops to 0.51 ± 0.04 mol ATP per mol nitrate at 34 hrs (**Figure** 2-15). Note that the earliest measurement was likely not reliable to due the small changes in acetate, nitrate, and biomass after inoculation.

$$X_{C.\ ljungdahlii} = 0.801 \pm 0.023 \frac{ATP}{nitrate} \tag{2.20}$$

Growth of *M. thermoacetica* on nitrate occurred in the absence of substantial acetate production, hence *M. thermoacetica* likely produced ATP during nitrate reduction (in agreement with literature). A similar analysis was performed to determine the ATP derived from nitrate by *M. thermoacetica*. The ATP yield based on the proton gradient for growth on H_2+CO_2 was 0.132 ± 0.006 mol ATP per mol Acetate. As for nitrate respiration by *M. thermoacetica*, 0.65 ± 0.11 mol ATP per nitrate was produced.

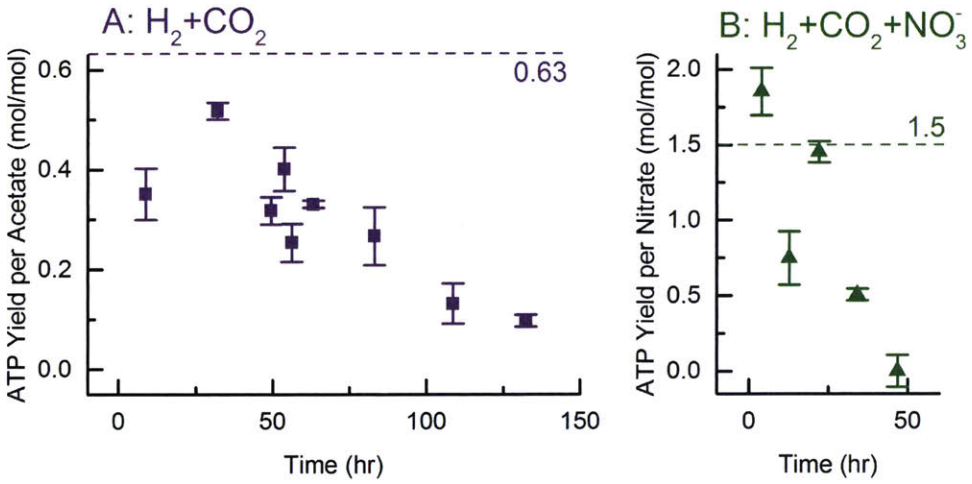

Figure 2-15: Instantaneous ATP yields calculated for the production of (A) acetate or reduction of (B) nitrate, by *C. ljungdahlii*. Cultures were grown on (A) H_2+CO_2 or (B) H_2+CO_2+NO_3^-. The ATP yield from acetate was calculated from the H_2+CO_2 culture, and then used to calculate the ATP yield from nitrate with the H_2+CO_2+NO_3^-. The theoretical maxima were denoted with dashed lines (A: 0.63 and B: 1.5). Over time as the culture grew, the ATP generally decreased.

$$N_{M.thermoacetica} = 0.132 \pm 0.006 \frac{ATP}{acetate} \tag{2.21}$$

$$X_{M.thermoacetica} = 0.65 \pm 0.11 \frac{ATP}{nitrate} \tag{2.22}$$

2.4.2 Ionophore corroborates proton motive force couples ATP synthesis to nitrate reduction

The proposed model for coupling ATP production to nitrate reduction involves the Rnf complex, which pumps protons out of the cell during electron transfer from reduced ferredoxin to NAD^+. The cell utilizes this proton motive force (PMF) to generate ATP with an ATPase that imports those protons. To determine if PMF was the central mechanism for ATP production coupled to nitrate reduction, two options were available. The first was generating an Rnf complex knockout [133]. The second was utilizing ionophores that can disrupt proton motive force. Each had positive and negative aspects; the knockout would be definitive, but would take substantial

time to generate. The ionophore required no genetic engineering, though only narrow conclusions could be drawn from these experiments; the ionophore would disrupt all ATPases and the RNF complex. In both cases, the cell would likely be sickly. In the preliminary experiments below, the ionophore was utilized to corroborate the hypothesis that nitrate reduction was associated to ATP production via PMF. Genetic knockouts are necessary to verify this hypothesis.

Ionophores are chemicals used to permeablize hydrophobic membranes to ions. Protonophores are ionophores that permeablize cellular membranes to protons (H^+), allowing them to pass freely through the membrane. Different organisms have different sensitivities to ionophores. For instance, *C. ljungdahlii* was sensitive to a proton ionophore (TCS, 3,3',4',5-Tetrachlorosalicylanilide) but not to a sodium ionophore (ETH2120) [133]; that experiment implicated the RNF complex of *C. ljungdahlii* was H^+ dependent. This was in juxtaposition to *A. woodii* which has a sodium dependent RNF complex and ATPase [147, 152, 153]. As high protonophore concentrations are toxic, separating the affect of ATP production via PMF from cellular health was difficult. For this reason, three separate experiments were conducted. First, the concentration sensitivity of *C. ljungdahlii* was determined from 5 to 5000 nM. Then swimming speed was determined at varying concentrations of TCS as a gauge of cellular health. Finally, the cellular yield (biomass per fructose) was used as a proxy to determine if TCS disrupts ATP production via PMF.

TCS was prepared in methanol at 5 μM, then diluted again with methanol to 1000x the desired concentration; methanol was added to the control. TCS was added to PETC media, but with 1 g/L YE and 5 g/L fructose. Fructose was chosen, as PMF would be required for any growth on gases (CO or H_2). Instead, *C. ljungdahlii* can generate ATP from both substrate level phosphorylation (SLP) and PMF with fructose. The change in OD was measured after 18 hours and the results clearly indicated that TCS concentrations above 300 nM were toxic to *C. ljungdahlii* (**Figure 2-16A**). Interestingly, from 5 to 80 nM, there was an apparently linear correlation between growth and TCS concentration which could be a result of both cellular health or ATP yields from the substrate fructose. Based on these results, a concentration

range from 0 to 160 nM was selected and supplemented to PETC media with 1 g/L YE and 5 g/L fructose with biological triplicates (**Figure** 2-16**B, C**). The change in OD_{660nm} and the change in fructose concentration were measured as a proxy of ATP yield from fructose metabolism. This is discussed further on.

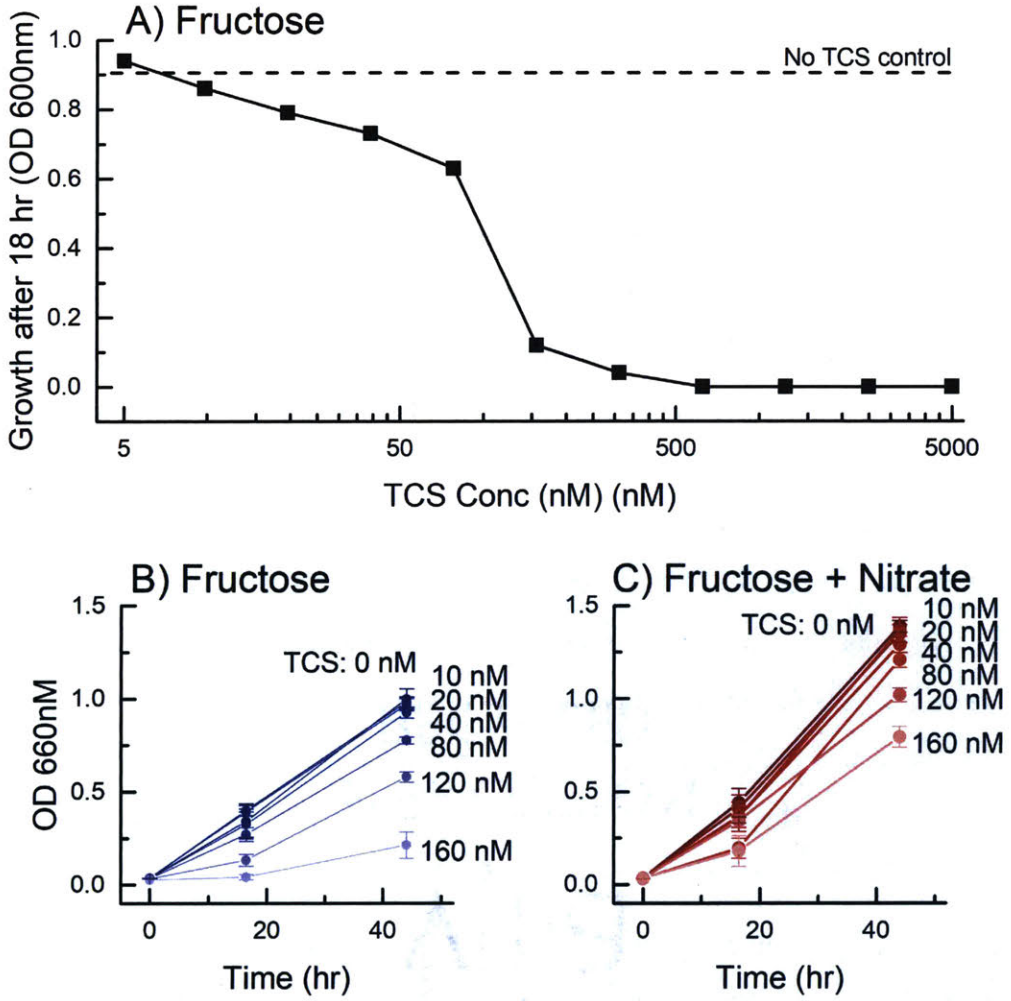

Figure 2-16: Growth of *C. ljungdahlii* on fructose and varying concentrations of TCS, a protonophore. (A) Preliminary kill curve was generated by inoculating hungate tubes at 0.1 OD_{600nm} and measuring the change in OD after 18 hours with a handheld UV-Vis spectrophotometer. (B, C) Based on these results, a variety of concentrations of TCS were added to cultures grown on fructose (B) or fructose+NO_3^- (C).

Motility (swimming plates) was used as a proxy for cellular health in the presence of TCS, as motility is also driven by ATP and PMF [153]. As TCS was added, the cell would expend extra ATP to maintain the PMF necessary for motility. As observed here, even after motility was lost, growth was still possible but at very low yields

(biomass per fructose).

Briefly, agar plates containing PETC with 1 g/L YE, 0.4 g/L fructose, and 3 g/L agar (0.3%) were prepared. The lower concentration of fructose was meant to promote swimming, as the substrate would be depleted prior to reaching stationary phase. These plates were spotted the next day with 5 μL of a healthy culture of *C. ljungdahlii*, and allowed to grow in a 37°C incubator within an anaerobic chamber. After 5 days, the agar plates were removed from the glovebox and the swimming halo was imaged to ascertain the swim area. The images were collated, and analysed with ImageJ [154]; the images can be seen in **Figure** 2-17. Qualitiatively, there was a decrease in swimming area as TCS was increased. By 160 nM, there was no measurable colony on the fructose plates. The same decrease occured for the fructose+nitrate plates, however, the change was not as significant, and there was still a measurable colony at 160 nM. There was an interesting difference in morphology of the swimming halo between cultures grown with and without nitrate. Two un-edited plates (TCS concentration of 0 nM) were representative of this, as seen in **Figure** 2-17. The fructose halo was concentrated only at the stab location, with a relatively dilute halo. Conversely, the fructose+nitrate halo did not spread as far, but was much more concentrated in that area. For instance, the fructose halo was approximately 2.4x greater in size, but the intensity of the fructose+nitrate halo was 1.6x greater on average (as determined from ImageJ). The reason the nitrate grown cells swam less was unknown. Perhaps it was in part due to an increase in growth rate and yield because of the nitrate.

Quantitatively for the fructose plates, swimming decreased steadily with increasing concentrations of TCS **Figure** 2-18**B**. By 80 nM, swim area had decreased by 3.5 $\pm$ 0.9 fold, but was still substantial. At 120 nM, swim area had decreased by 12.9 $\pm$ 2.9 fold; by 160 nM, there was no measurable halo or colony. Conversely, there was no change in the swim area of the fructose+nitrate plates until after 120 nM. As discussed previously, at low TCS concentrations, fructose+nitrate swam less than fructose plates. However, fructose+nitrate was able to maintain the initial swim area for substantially longer.

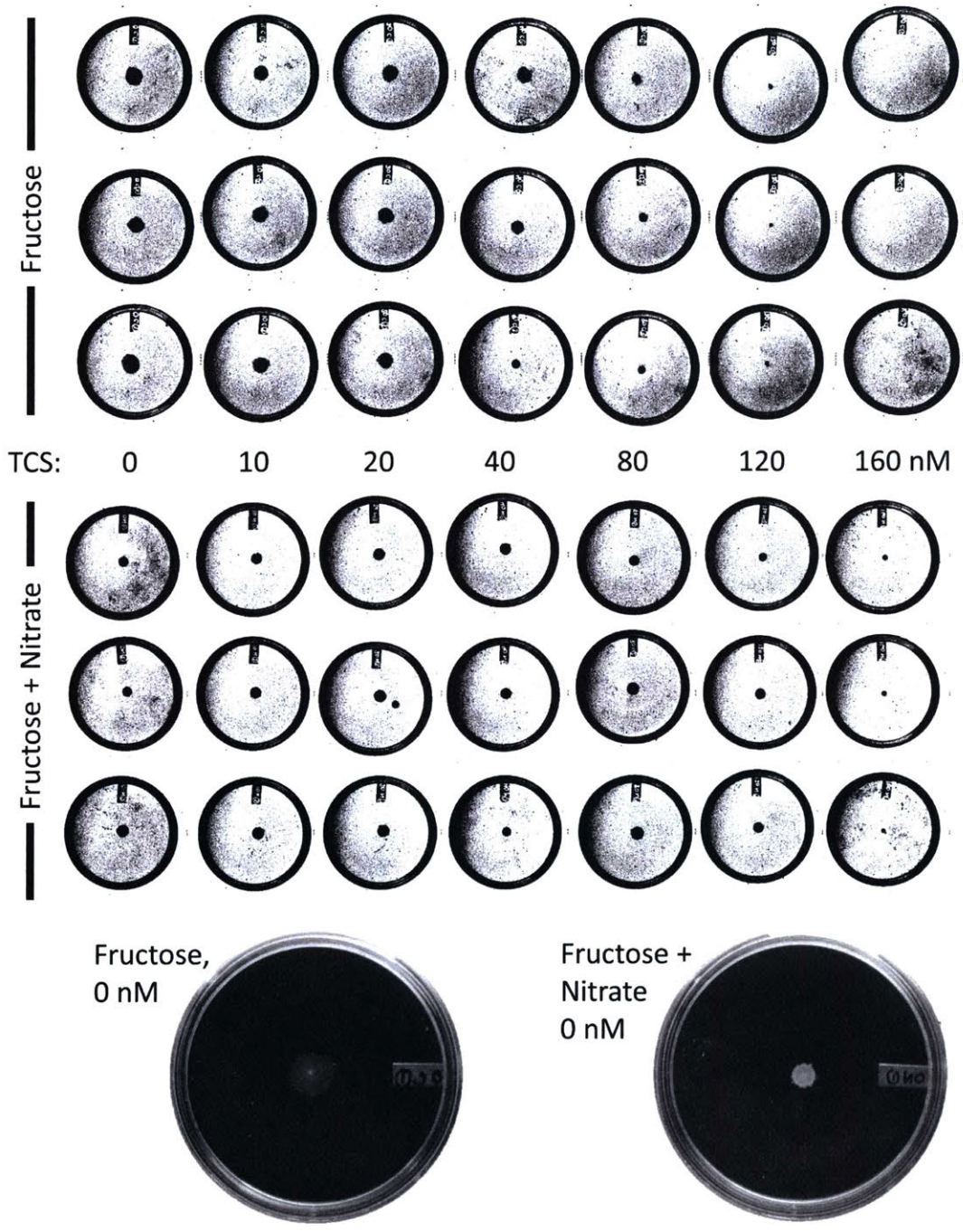

Figure 2-17: Swimming plates of *C. ljungdahlii* grown on fructose or fructose and nitrate, and varying concentrations of TCS. Bottom, un-edited image of plates with fructose or fructose+nitrate, and no TCS.

Next, the biomass yield per fructose was calculated as a proxy for ATP yield from fructose. This is a generally appropriate assumption that simplifies metabolism to the most important reactions; any excess ATP is assumed to result in biomass production[148]. These equations and assumptions were in line with those presented in **Section** 2.4.3. The maintenance coefficient was ignored in these calculations and analysis, even though the role it might play would only increase as the concentration of TCS increases. Calculating the maintenance coefficient would be prohibitively difficult for this proof of concept experiment. When the equations are simplified and combined, they reduce to:

$$Fructose \rightleftharpoons 2Acetate + 2CO_2 + 4ATP + 8e^- \tag{2.23}$$

$$8e^- + 2CO_2 \rightleftharpoons Acetate + 0.63ATP \tag{2.24}$$

$$8e^- + NO_3^- \rightleftharpoons NH_4^+ + 1.5ATP \tag{2.25}$$

$$Acetate + 3.43ATP \rightleftharpoons Biomass \tag{2.26}$$

$$\tag{2.27}$$

ATP production in Equation 2.23 is from SLP during glycolysis, whereas **Equation** 2.24 and 2.25 is from PMF via the RNF complex (**Equation** 2.25 was hypothesized to be via the RNF complex). Under normal circumstances, i.e. when PMF was operational, at most 4.63 ATP can be derived from 1 mole of fructose in the presence of CO_2, and approximately 1.34 moles of biomass (just **Equation** 2.23 and 2.24). If PMF is blocked by TCS, this drops to 4 ATP per fructose and 1.16 moles biomass. The same is true in the presence of nitrate and functional PMF, this would be 5.5 ATP per fructose and 1.60 moles biomass; if PMF is blocked this would drop to 4 ATP per fructose and 1.16 moles biomass.

The expected theoretical changes to biomass yield, were compared to experimental data (**Figure** 2-18**A**, dashed line "1" and "2" for fructose, and dashed line "3" and "4" for fructose+nitrate). For instance, dashed line "3" was an extension of the biomass yield at 0 nM TCS. Dashed line "4" was the expected biomass yield if no

ATP was produced via PMF ((Line "3")*(4/5.5)).

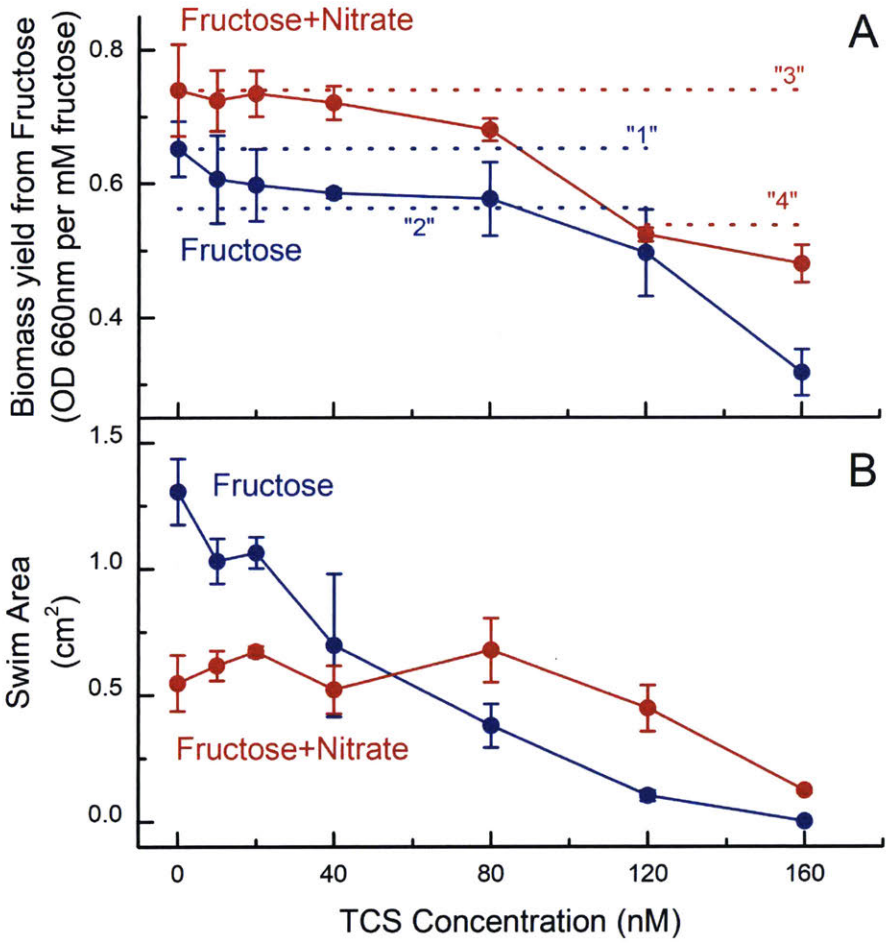

Figure 2-18: Biomass yield from fructose and swim area of *C. ljungdahlii* at varying concentrations of TCS. (A) The biomass per fructose was calculated for cultures grown in **Figure** 2-16**B, C**. Dashed line "1" and "2" indicate the initial biomass yield for fructose, and the predicted yield if ATP could not be produced via proton motive force. Dashed line "3" and "4" indicate the same for fructose+nitrate. (B) The swimming area calculated from **Figure** 2-17 with ImageJ. Red, fructose; blue, fructose+nitrate. Standard deviation given for biological triplicates.

Only after 80 nM of TCS was added, was there a change to the biomass yield for the fructose+nitrate cultures. Conversely, there was a substantial drop in biomass yield of the fructose cultures to the expected yield (dashed line "2"). By 120 nM, both conditions were at or slightly below the expected yields. This plateaued for the fructose+nitrate cultures but continued to plummet for the fructose cultures. Clearly

the fructose culture was unhealthy at 160 nM, even if the biomass yield was non-zero. The data suggests that the presence of nitrate allowed *C. ljungdahlii* to better stabilize its membrane potential at higher concentrations of TCS; PMF was abolished at 40 nM for the fructose culture, but 120 nM for the fructose+nitrate culture. This trend was also observed for the swimming area, even though the fructose+nitrate had a smaller swimming area at lower TCS concentrations.

At 160 nM TCS, there was a substantial difference in the biomass yield, as the fructose culture dropped to approximately 48% of its peak yield. This drop was likely associated with an increase in the maintenance coefficient; the cell was utilizing ATP to maintain the proper membrane potential necessary for growth and metabolism. This was not seen in the nitrate cultures, which matches the higher sensitivity threshold for TCS.

That the ATP yield of the fructose+nitrate did decrease to that predicted (dashed line "4") by 120 nM of TCS, while maintaining cellular health and swimming, corroborates that PMF was the method by which nitrate was coupled to ATP synthesis. This same trend was seen for the fructose cultures, as they dropped to the expected value by 40 nM TCS.

The results corroborate the hypothesis that ATP production in the presence of nitrate was dependent on PMF. Moreover, nitrate appears to improve the ability of the cell to maintain PMF and the membrane potential. Further work will be necessary to verify that the RNF complex was implicated in ATP production in the presence of nitrate. A RNF complex knockout has been generated in the past and could answer this question [133].

2.4.3 Nitrate assimilation improves theoretical yield of acetyl-CoA-derived products

ATP limitation was the leading hypothesized cause of the low yields reported for production of heterologous chemicals through syngas fermentation [46]. We therefore asked whether supplementation of nitrate to boost ATP production could lead to

higher yields of these products, by reducing the amount of acetyl-CoA that must be converted to acetate. To probe this question, we calculated the theoretical yield of various chemicals (**Equations** 2.28 to 2.37) [29] produced from H_2+CO_2, with and without nitrate, using the experimentally determined ATP yields for *C. ljungdahlii*. The yields are shown in **Table** 2.7 and the stoichiometries are shown in **Table** 2.8.

The WLP, nitrate reduction, and biomass production were modeled with **Equation** 2.5 to 2.18. The production pathways for a variety of chemicals were modeled with the simplified reaction equations:

$$Acetyl\text{-}CoA + 2NADH \rightleftharpoons Ethanol \tag{2.28}$$

$$Acetyl\text{-}CoA + NADH + Fd_{red} \rightleftharpoons Ethanol + ATP \tag{2.29}$$

$$2Acetyl\text{-}CoA + NADH \rightleftharpoons S\text{-}3HB \tag{2.30}$$

$$2Acetyl\text{-}CoA + NADPH \rightleftharpoons R\text{-}3HB + ATP \tag{2.31}$$

$$3Acetyl\text{-}CoA + 2NADH + 3ATP \rightleftharpoons Isoprene + CO_2 \tag{2.32}$$

$$Acetyl\text{-}CoA + CO_2 + Fd_{red} + NADH \rightleftharpoons Lactate \tag{2.33}$$

$$Acetyl\text{-}CoA + CO_2 + 2NADH \rightleftharpoons Lactate \tag{2.34}$$

$$2Acetyl\text{-}CoA + 2Fd_{red} + NADH \rightleftharpoons 2,3\text{-}Butanediol \tag{2.35}$$

$$Acetyl\text{-}CoA + Acetate \rightleftharpoons Acetone + CO_2 \tag{2.36}$$

$$2Acetyl\text{-}CoA + Acetate + ATP \rightleftharpoons Isobutene + 2CO_2 \tag{2.37}$$

For every product examined, both the hydrogen yield (Y_H) and the carbon yield (Y_C) improved significantly with the supplementation of nitrate. The greatest benefit was realized in pathways where significant amounts of additional ATP was required for product biosynthesis. For instance, when producing isoprene from H_2+CO_2 alone, Y_C was only 14%; the rest of the carbon was diverted to acetate for ATP synthesis. When nitrate was present, however, acetate production was not theoretically necessary for energy generation, and Y_C was 96%, a 6.9 fold increase of the theoretical Y_C. Furthermore, adding nitrate (as nitric acid) decreased the calculated cost per

mole of product, due to lowering the H_2 and CO_2 requirement per mole of product (as determined from lab scale quantities). For these reasons, nitrate respiration could greatly improve CO_2 fixation and autotrophic chemical production by H_2. However, controlling electron flux between nitrate and CO_2, and ensuring high expression of the WLP are key considerations in future research.

The importance of controlling electron flux can be broadly explained for any product: too much nitrate reduction would result in high ATP production and carbon wasted on growth. Alternatively, too little nitrate reduction would result in cells increasing acetate production to compensate for ATP demands.

This can also be seen by comparing the experimental mass balance (**Table** 2.1) with the optimal mass balance (**Table** 2.8) for growth on H_2+CO_2+NO_3^-. Take for instance a situation where biomass was the product. Our theoretical model assumed that no acetate production was necessary for ATP production, hence the Y_C was 100% (**Table** 2.8). However, this was not experimentally observed; 9 mM of acetate was produced along with 11.3 mM nitrate consumed (**Table** 2.1). On a basis of 1 mol biomass, that was 2 mol acetate and 2.6 mol nitrate.

Since ATP generation from nitrate reduction results in higher growth rates (0.084 $\pm$ 0.002 vs 0.048 $\pm$ 0.003 hr^{-1}) and yields (**Table** 2.7), one might expect the cell to depress acetate production beyond that used for biomass generation. This was observed when arginine deiminase was the source of ATP production during autotrophic growth [106], but this was not observed here. Instead, electrons were split between carbon fixation (59 $\pm$ 6%) and nitrate reduction (41 $\pm$ 6%) as determined from the carbon and nitrogen balance in **Table** 2.6. The reason for why *C. ljungdahlii* maintains acetate production was unclear; unless there was no direct regulation by nitrate.

2.4.4 Nitrate improves the autotrophic production of 3HB

Based on common understanding of bacterial metabolism, cells will preferentially consume the better substrate, in this case nitrate. Despite the secretion of acetate (**Figure** 2-2), nitrate greatly improved growth rate of *C. ljungdahlii*, and this was connected to more efficient ATP production per H_2, and higher ATP/ADP ratio

Table 2.7: Theoretical carbon yield, hydrogen yield, and lab scale cost for producing chemicals autotrophically with and without nitrate. A basis of 1 mole of product was chosen. Depending on the condition, acetate was produced or nitrate consumed to generate the necessary ATP (shown in moles). When nitrate was supplied, no acetate production was assumed as this results in the highest theoretical yield. Products were listed with the number of carbons in the molecule along with the pathway of production. A full metabolite balance is presented in **Table** 2.8, showing the CO_2 and H_2 consumed. Y_C represents the theoretical maximum carbon yield, as determined by the carbon present in the product divided by the carbon dioxide fixed. Y_{H_2} represents the H_2 electrons present in the product per total consumed. The cost of the substrate per mole of carbons in the product was given (\$ $molC^{-1}$). For instance, the substrate cost for 1 mol of isobutene (4 carbons) was 34.40 \$. The cost basis was 0.86 \$ per mole nitric acid (Sigma, 6x 2.5L), 0.33 \$ per mol H_2 (Airgas, 260 std ft^3, Ultrahigh purity), and 0.82 \$ per mol CO_2 (Airgas, 260 std ft^3, Research grade). If CO_2 can be acquired at no cost, production with nitrate remains cheaper than without for all products.

	Substrates:	**H_2+CO_2**				**H_2+CO_2+NO_3^-**			
Products (#C)	**Pathway**	**\$ $molC^{-1}$**	**Acetate**	**Y_{H_2}**	**Y_C**	**\$ $molC^{-1}$**	**Nitrate**	**Y_{H_2}**	**Y_C**
Biomass (1)		29.09	9.29	6%	5%	9.01	-3.41	14%	100%
Acetate (2)	**Acetate kinase**	1.57	1.00	94%	95%	—	—	—	—
Ethanol (2)	**Acetaldehyde DH**	5.05	2.13	41%	31%	2.74	-0.78	64%	95%
	AOR	1.93	0	94%	93%	—	—	—	—
S-3HB (4)		6.13	6.07	27%	24%	2.86	-2.23	49%	95%
R-3HB (4)		3.91	3.06	41%	39%	2.25	-1.12	65%	95%
Isoprene (5)	**Mevalonate**	12.80	18.55	16%	14%	4.79	-6.80	34%	96%
Lactate (3)	**NADH-dependent**	4.91	3.40	30%	22%	2.47	-1.25	53%	93%
	Bifurcating LDH	3.58	2.60	36%	27%	2.25	-0.95	59%	93%
2,3-Butanediol (4)	**Acetolactate**	6.59	6.47	29%	23%	3.10	-2.37	53%	95%
Acetone (3)	**Acetoacetate**	4.54	2.80	41%	41%	2.53	-1.03	64%	96%
Isobutene (4)	**Acetone,3-OH-isovalerate**	8.60	9.07	25%	25%	3.70	-3.33	47%	97%

Table 2.8: Theoretical carbon, hydrogen, and nitrate balance for producing chemicals autotrophically with and without nitrate. Products were listed with the number of carbons in the molecule along with the pathway of production. A basis of 1 mole product was assumed, with the production/ consumption of all other products/ reactants participating in the balances reported in moles. Biomass production was set at 5 % of the carbons in the product, hence the difference between each product, but the same between each substrate.

		Substrates:	**H_2+CO_2**			**H_2+CO_2+NO_3^-**		
Products (#C)	**Pathway**	**Bio**	**CO_2**	**H_2**	**Acetate**	**CO_2**	**H_2**	**Nitrate**
Biomass (1)		1.00	-19.59	-39.48	9.29	-1.00	-15.93	-3.41
Acetate (2)	**Acetate kinase**	0.11	-2.11	-4.25	1.00	—	—	—
Ethanol (2)	**Acetaldehyde DH**	0.10	-6.37	-14.76	2.13	-2.10	-9.36	-0.78
	AOR	0.15	-2.15	-6.35	0.00	—	—	—
S-3HB (4)		0.20	-16.33	-33.73	6.07	-4.20	-18.36	-2.23
R-3HB (4)		0.20	-10.33	-21.71	3.06	-4.20	-13.95	-1.12
Isoprene (5)	**Mevalonate**	0.25	-42.35	-88.77	18.55	-5.25	-41.79	-6.80
Lactate (3)	**NADH-dependent**	0.15	-9.95	-19.94	3.40	-3.15	-11.33	-1.25
	Bifurcating LDH	0.15	-6.35	-16.74	2.60	-3.15	-10.16	-0.95
2,3-Butanediol (4)	**Acetolactate**	0.20	-17.13	-37.33	6.47	-4.20	-20.95	-2.37
Acetone (3)	**Acetoacetate**	0.15	-8.75	-19.54	2.80	-3.15	-12.45	-1.03
Isobutene (4)	**Acetone,3-OH-isovalerate**	0.20	-22.34	-48.75	9.07	-4.20	-25.77	-3.33

(**Figure** 2-21). We wished to test this theoretical analysis to determine if nitrate could in fact increase yield and productivity of autotrophic chemical production.

For this reasons, the plasmid pCL2pta3HB131 from Woolston et. al. [62, 155] was characterized for the autotrophic production of 3-hydroxybutyrate (3HB), with and without nitrate. The pCL2 backbone [156] plasmid was constructed in *E. coli* and later transformed into *C. ljungdahlii.* The 3HB operon (*phaA* and *tesB*) was codon optimized, and the RBS motif was optimized. The operon was driven by the constitutive but putative PTA promoter [119]. As richer media improves titer and productivity [62], unless otherwise stated, the YE concentration in the medium was increased from 0.1 to $1gL^{-1}$.

Prior to transformation of the plasmid into *C. ljungdahlii*, a new antibiotic kill curve was generated for *C. ljungdahlii* on thiamphenicol (thi), as previous researchers only used thiamphenicol under heterotrophic conditions (fructose) [94, 99]. There was worry that autotrophic growth would limit the cells ability to resist high levels of antibiotic, and would prevent growth even with the resistance genes. Moreover, a lowered antibiotic concentration would be less stressful to the cell and could improve production of 3HB. To answer this question, thiamphenicol (dissolved at 1000x in DMSO and stored aerobically) was titrated from 0.16 to 5 $\mu g\ mL^{-1}$ into PETC media containing 0.1 $g\ L^{-1}$ YE. Cultures were grown horizontally in balch tubes, and the OD_{600nm} was measured daily.

The kill curve (**Figure** 2-19) indicated that atleast 5 $\mu g\ mL^{-1}$ was necessary to prevent growth of *C. ljungdahlii* on H_2+CO_2+NO_3^-. On the other hand, thiamphenicol was even more effective on *C. ljungdahlii* grown on H_2+CO_2, preventing growth by 1.58 $\mu g\ mL^{-1}$. For this reason, 5 $\mu g\ mL^{-1}$ of thiamphenicol was used for subsequent experiments. Curiously, nitrate had a large impact on countering the antibiotic effects at lower concentrations, allowing substantial growth even at 1.58 $\mu g\ mL^{-1}$, a concentration deadly for *C. ljungdahlii* grown on H_2+CO_2. This was reminescent of the results from the protonophore experiments (**Figure** 2-18).

With the optimum antibiotic concentration chosen, the 3HB strain could be characterized. Preliminary results were peculiar, in that either the pathway, the antibi-

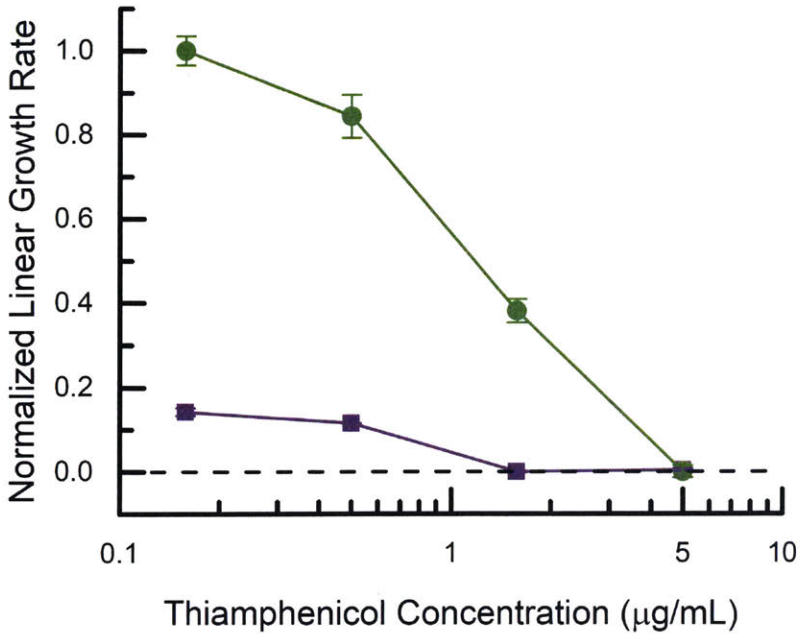

Figure 2-19: Thiamphenicol kill curve for *C. ljungdahlii* grown autotrophically with H_2+CO_2 or H_2+CO_2+NO_3^-. Standard deviation given in parentheses for two biological replicates.

otic, or another variable was greatly impairing *C. ljungdahlii*'s ability to consume nitrate autotrophically. Mutagenesis of the transformed strain was ruled out, as re-transformation into fresh competent cells generated the same phenotype (i.e. little to no nitrate consumption). Newly prepared media, nor decreasing the YE concentration affected the lack of nitrate consumption.

Next, the antibiotic was tested. As previously mentioned, stocks of thiamphenicol were dissolved in DMSO and stored aerobically at -20°C. To account for and remove the oxygen, prepared media was shaken for 2 hours prior to inoculation so that cysteine could scavenge for oxygen. The strain was first acclimated to growth on H_2+CO_2+thi or H_2+CO_2+NO_3^-+thi. After reaching approximately 0.2 OD_{660nm}, the cultures were sub-cultured to the respective media either with or without antibiotics. In this way, thiamphenicol and DMSO were largely reduced in half the cultures, except that which remained from the 10x dilution.

Regardless of condition (with or without nitrate, with or without theiamphenicol), the cultures grew at approximately the same rate and to approximately the same final

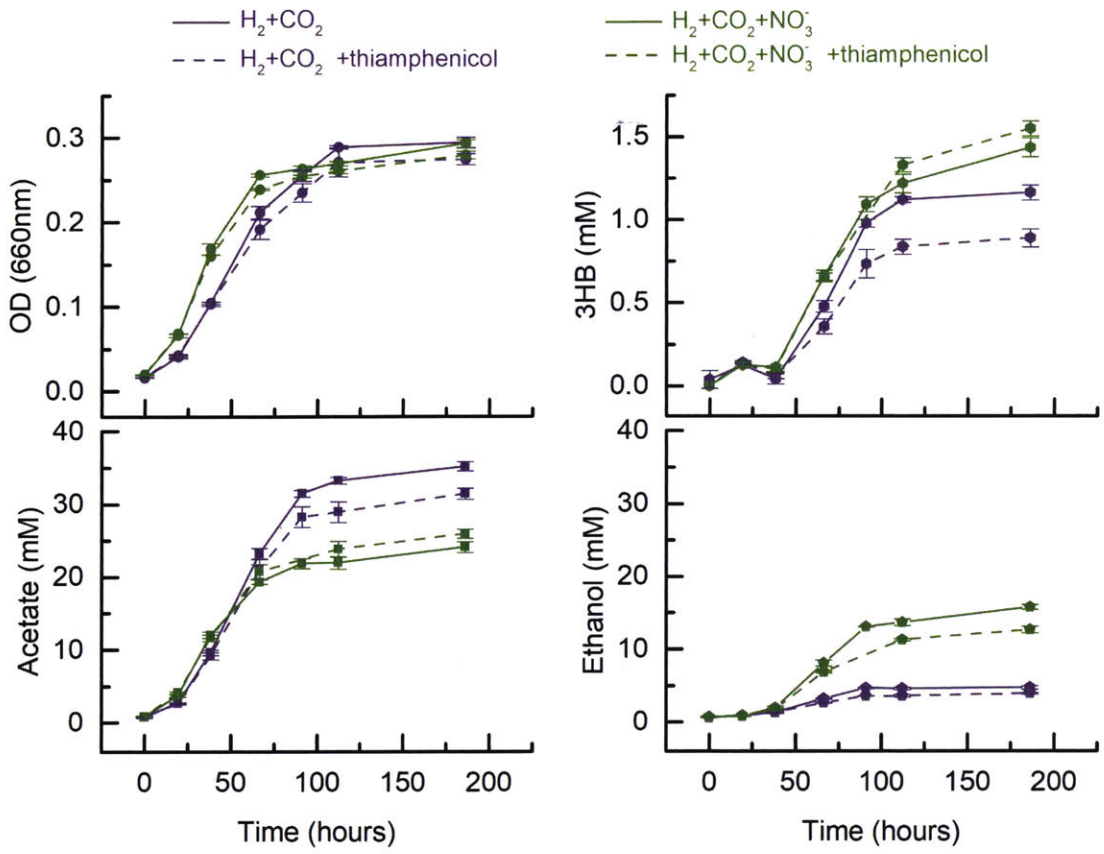

Figure 2-20: Growth and extracellular metabolites of a 3HB producing *C. ljungdahlii* strain with and without NO_3^-. Standard deviation given in parentheses for three biological replicates.

optical density. Production of acetate was reduced in cultures containing nitrate, however this coincided with increased ethanol production. 3HB production was higher in cultures containing nitrate, reaching 1.55 ± 0.04 mM (+nitrate and -thiamphenicol). This corresponed to a carbon yield of 7.4% (+nitrate and -thiamphenicol), as compared to 4.8% in the absence of nitrate (-nitrate and -thiamphenicol).

While the yield and titer increased, they remain far from the predicted theoretical limits. Part of the issue is pathway control; acetogens have evolved to produce acetate and redirecting flux from acetate to heterlogous products has proven difficult for researchers [155]. Substantially more work would be necessary to reach the targets presented in **Table** 2.7, however we believe this is only a matter of time.

2.5 Nitrate Increases ATP/ADP Ratio and Acetyl-CoA Pool Size when the Electron Source was H_2

To further investigate the increase in ATP production from nitrate metabolism, intracellular metabolites were measured at mid-log phase for *C. ljungdahlii* grown on fructose+CO_2, H_2+CO_2, or CO+CO_2, with and without nitrate. Of significant importance were the ATP/ADP ratio and the acetyl-CoA pool size (**Figure** 2-21), since the former informs on the energetic state of the cell, and the size of the acetyl-CoA pool has been linked to metabolic collapse in energetically limited cells [101]. The ATP/ADP ratio increased in the presence of nitrate when the electron source was fructose or H_2. For fructose, this was small at only an increase of 1.3 ± 0.3-fold. For the H_2+CO_2 culture, this was a 5.3 ± 0.9-fold increase, and the ATP/ADP ratio approached that of the fructose culture. Conversely, when *C. ljungdahlii* was grown on CO+CO_2+NO_3^-, the ATP/ADP ratio fell 2.7 ± 1.5-fold, as compared to growth on CO+CO_2. This either explained, or was symptomatic of the poor growth on CO+CO_2+NO_3^- (**Figure** 2-4).

The acetyl-CoA (AcCoA) pool size only increased in the presence of nitrate when the substrate was H_2+CO_2, again to levels comparable to the fructose-grown culture (a 2.8 ± 0.9-fold increase). When the electron source was either fructose or CO, the presence of nitrate decreased the acetyl-CoA pool size by 2.1 ± 1.3-fold and 2.8 ± 0.9-fold, respectively. This was rational, as nitrate negates the necessity of operating the WLP when grown on fructose, functionally decreasing acetate production rates by about 30%. On the other hand, growth was poor on CO+CO_2+NO_3^-, and part of the cause was likely low levels of acetyl-CoA, and the inability of the cell to maintain a high ATP/ADP ratio.

Taken together, the ATP/ADP and acetyl-CoA data suggest that nitrate significantly enhanced the energetic state of the cell during growth on H_2, by increasing the supply of ATP as well as acetyl-CoA. The opposite was true when the electron

source was CO.

Other intracellular metabolites were measured, including from gluconeogenesis and different amino acid biosynthesis pathways. Generally, nitrate had little affect on glycolysis/gluconeogenesis when the electron source was fructose.

When the electron source was H_2, though, the intracellular concentration of many metabolites along gluconeogenesis were increased, except for pyruvate for which there was a 1.9-fold decrease. The lower metabolites of the gluconeogensis increased by 2-fold (1.9 ± 0.6 for PEP (phosphoenolpyruvic acid); 1.8 ± 0.4 for 3PG (3-phosphoglyceric acid); 1.3 ± 1.0 for DHAP (dihydroxyacetone phosphate)) approaching the concentrations present when grown on fructose. The concentration of the metabolites of upper gluconeogenesis were also increased substantially, from 1.7- to 5.3-fold for FBP (fructose 1,6-bisphosphatase, 5.3 ± 0.8), F6P (fructose 6-phosphate, 3.0 ± 0.4), and G6P (glucose 6-phosphate, 1.7 ± 0.9). R5P (ribose 5-phosphate) was also increased by 2.7 ± 0.1-fold, rising to a concentration twice that present in the fructose grown culture. These increased pool sizes could be related to the significant increase in growth rate and titer observed during growth on H_2+CO_2+NO_3^-. While pool size can not be related to metabolic flux, one can expect that the increased growth rate would also correspond to an increased flux through these pathways for the synthesis of cellular building blocks (amino acids, nucleotides, ribonucleotides, etc).

Unlike the metabolites of gluconeogenesis, the various measured amino acids generally decreased in concentration when the substrate was H_2+CO_2+NO_3^- (vs. H_2+CO_2). The most apparent was lysine, which decreased by 5.1 ± 1.4-fold. This concentration was 30 ± 4-fold less than that observed in the fructose grown culture. Of the measured amino acids, only arginine and glutamate increased in concentration, though the increase was moderate (2.2 ± 1.4 and 1.4 ± 0.2-fold, respectively). This depletion could be explained by a higher growth rate requiring the amino acids for protein synthesis. Moreover, addition of these key metabolites to the media may have marked improvements on the growth rate and titer; especially lysine which was essentially depleted.

The most striking change was that of αKG (α-ketoglutaric acid) when grown on

$CO+CO_2+NO_3^-$. Intracellular concentrations for aKG when grown on $CO+CO_2$ were already comparable to that when grown on fructose. When nitrate was added, there was a 4.7 $\pm$ 2.1-fold increase in concentration. α KG is part of the branched TCA cycle present in *C. ljungdahlii* [94, 157]. This result could not be explained by cellular metabolism of cysteine - a media component, and the predicted source of excess ammonium. Instead, accumulation could result from the stresses placed onto the cell.

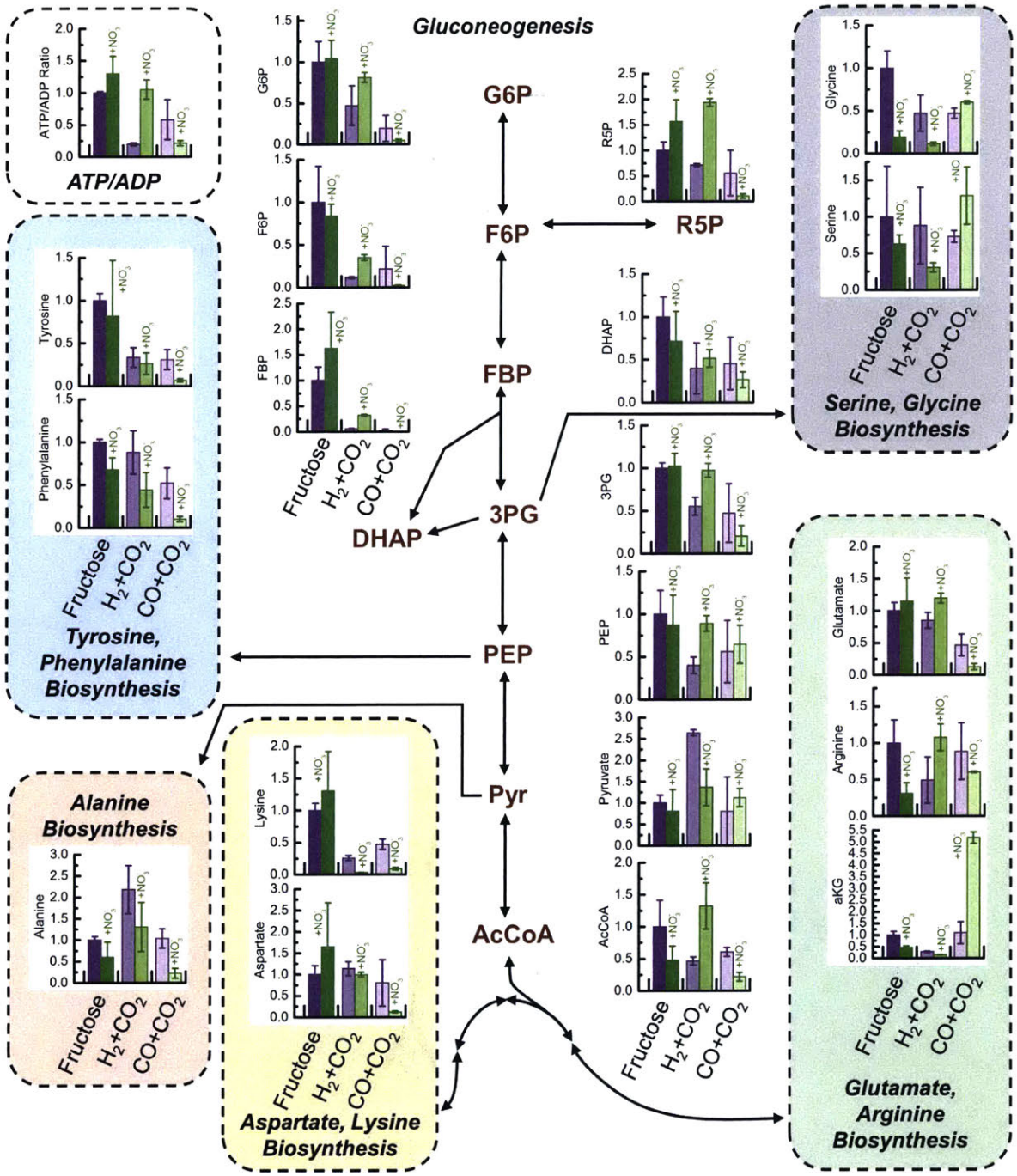

Figure 2-21: Normalized intracellular metabolite concentration of *C. ljungdahlii* were measured during mid-log phase while grown on fructose, H_2+CO_2, or CO+CO_2, with and without nitrate. Metabolites from gluconeogenesis and amino acid biosynthesis are shown. Samples were normalized to the levels of fructose alone. 3PG, 3-phosphoglyceric acid; AcCoA, acetyl-CoA; DHAP, dihydroxyacetone phosphate; F6P, fructose 6-phosphate; FBP, Fructose 1,6-bisphosphatase G6P, glucose 6-phosphate; PEP, phosphoenolpyruvic acid; Pyr, pyruvate; R5P, ribose 5-phosphate. Standard deviation given for biological triplicates.

2.6 Regulatory Response of *C. ljungdahlii* to Nitrate

Little was known about how nitrate regulated the WLP. Some researchers believed nitrate transcriptionally regulated the WLP of *M. thermoacetica* [104] and *C. ljungdahlii* [120]. This was sensible, as cells generally control which substrates are consumed first [158]. For *E. coli*, nitrate repression/activation occurs at a transcriptional level, and is modulated by four genes, *narQ*, *narX*, *narL*, and *narP* [158]. The gene products, NarQ and NarX are independent transmembrane sensor-transmitters. NarL and NarP are the response regulator that, when phosphorylated [159], binds to DNA [160] and activates or represses specific metabolic pathways.

We originally theorized the presence of similar regulation by nitrate on the WLP. For *M. thermoacetica*, acetate production was abolished, which indicated either stringent regulation of the WLP or chemical inhibition of key WLP enzymes. The current mechanism remains unknown. In comparison, *C. ljungdahlii* still produced acetate when grown on H_2+CO_2+NO_3^-, but at lower yields than in the absence of nitrate (2.1 $\pm$ 0.1 vs. 9.1 $\pm$ 0.8 mol acetate per mol cell carbon growth) (**Table** 2.1). Understanding how the cell controlled the electron flux would help future efforts in regulating these pathways.

2.6.1 Resolving the Time Necessary for *C. ljungdahlii* to Respond to a Nitrate Stimulus

A preliminary experiment was conducted to determine the appropriate time scale for measuring transcriptional response to the addition of nitrate into a culture. *C. ljungdahlii* was grown on H_2+CO_2 in the absence of YE (in comparison to other experiments that contained 0.1 g/L YE); at 0.1 OD_{660nm}, nitrate was spiked into half of the cultures. RNA was extracted 6 minutes prior to the spike, 4 min after the spike, and 40 minutes, 1 hour, 3 hours, and 6 hours after the spike. The transcriptional change in key genes of the WLP: Fhs (CLJU_c37650) and RnfC (CLJU_c07070) and

nitrate reduction pathway: nitrate reductase catalytic subunit (CLJU_c23730) and permease (CLJU_c23740) were determined by qRT-PCR. The abundance of 16s RNA and RecA (CLJU_c13280) served as a proxy for the house keeping genes, though they are known to not be the most stable under varying carbon sources or alcohol stresses [161]. Instead, the absolute quantity of mRNA was measured with a standard curve generated via PCR from the *C. ljungdahlii* genome and ranging from 1,000 to 0.0001 pg per reaction, and a water control. Efficiency on a given PCR plate ranged from 80 to 100%, with standards run for every plate. The primers used can be found in **Table** A.1.

After absolute quantification (copies per pg of total RNA), the time course was normalized to the average copies per pg of total RNA for all cultures immediately prior to the nitrate spike. The change in expression level was plotted in **Figure** 2-22. Within the first 30 minutes, there was substantial up-regulation of the annotated nitrate pathway genes when nitrate was spiked into the cultures. The nitrate reductase catalytic subunit was up-regulated by 188 ± 127 fold and the permease was up-regulated by 326 ± 216 fold.

Conversely, there was little change in the WLP genes, Fhs and RnfC, in comparison to the water spike control. Even after 6 hours, Fhs and RnfC transcripts only decreased by 2.4 ± 0.6 fold and 2.5 ± 0.5 fold, respectively. In fact, immediately after the spike, there was a small increase in mRNA level of Fhs and RnfC for all cultures by approximately 3 fold. This may be related to a stress response to small quantities of oxygen in the spike, or heat shock during the sampling and spiking. Even if there was no clearage of enzymes within this time frame, 30 minutes is sufficient for substantial mRNA degradation, let alone 6 hours. For this reason, it was unlikely *C. ljungdahlii* actively down-regulates the WLP in the presence of nitrate by preventing transcription.

While the expression level of the 16sRNA remained unchanged, the addition of nitrate resulted in a 2.45 ± 0.09 fold increase in RecA four minutes after the spike; after 6 hours though, RecA mRNA levels decreased 7.7 ± 0.4 fold from the initial time point. Conversely, the other cultures that did not recieve nitrate also had an

initial increase in RecA levels (4.6 ± 2.7 fold), and these heightened levels remained throughout the time course.

RecA is a homologous recombinase and is involved in stress response of a bacteria by allowing for SOS mutagensis, and thus evolution in response of the stress. While this was not studied in acetogens, it is well known in *E. coli* [162, 163]. The initial increase of RecA levels were likely due to heat shock and culture manipulation during sampling and spiking. The substantial fold decrease in relative RecA mRNA levels in the presence of nitrate implies a decrease in recombination necessity and perhaps a less stressful environment. This corroborates the results from **Section** 2.4.2.

2.6.2 Resolving nitrate regulation of metabolism with RNAseq

We next employed transcriptomics to analyze global gene expression in *C. ljungdahlii* during growth on H_2+CO_2, with or without nitrate. Samples were taken at multiple time points, in an effort to better understand how electron flux was partitioned between nitrate and CO_2. To probe quasi-steady state expression profiles, cultures were grown with or without nitrate and RNA samples were taken during mid-exponential growth phase, and the $\log_2$ fold change was quantified between the nitrate and the no-nitrate samples. For the dynamic transcriptome change, cultures were grown without nitrate. At approximately 1/3 the final expected OD (0.05 OD_{660nm}), an RNA sample was extracted. Then 5 min later, the cultures received either a nitrate spike or water control spike (**Figure** 2-2C). RNA was then extracted 2 hrs after, and the $\log_2$ fold change was quantified between the two time points for a given culture. The experimental outline can be seen in **Figure** 2-23. The $\log_2$ fold change in expression for the WLP genes and putative nitrate reduction pathway genes for each condition is shown in **Figure** 2-24. Principal Component Analysis (PCA) and MA-plots (mean expression vs. log fold change) are given found in **Figures** A-3 to A-8.

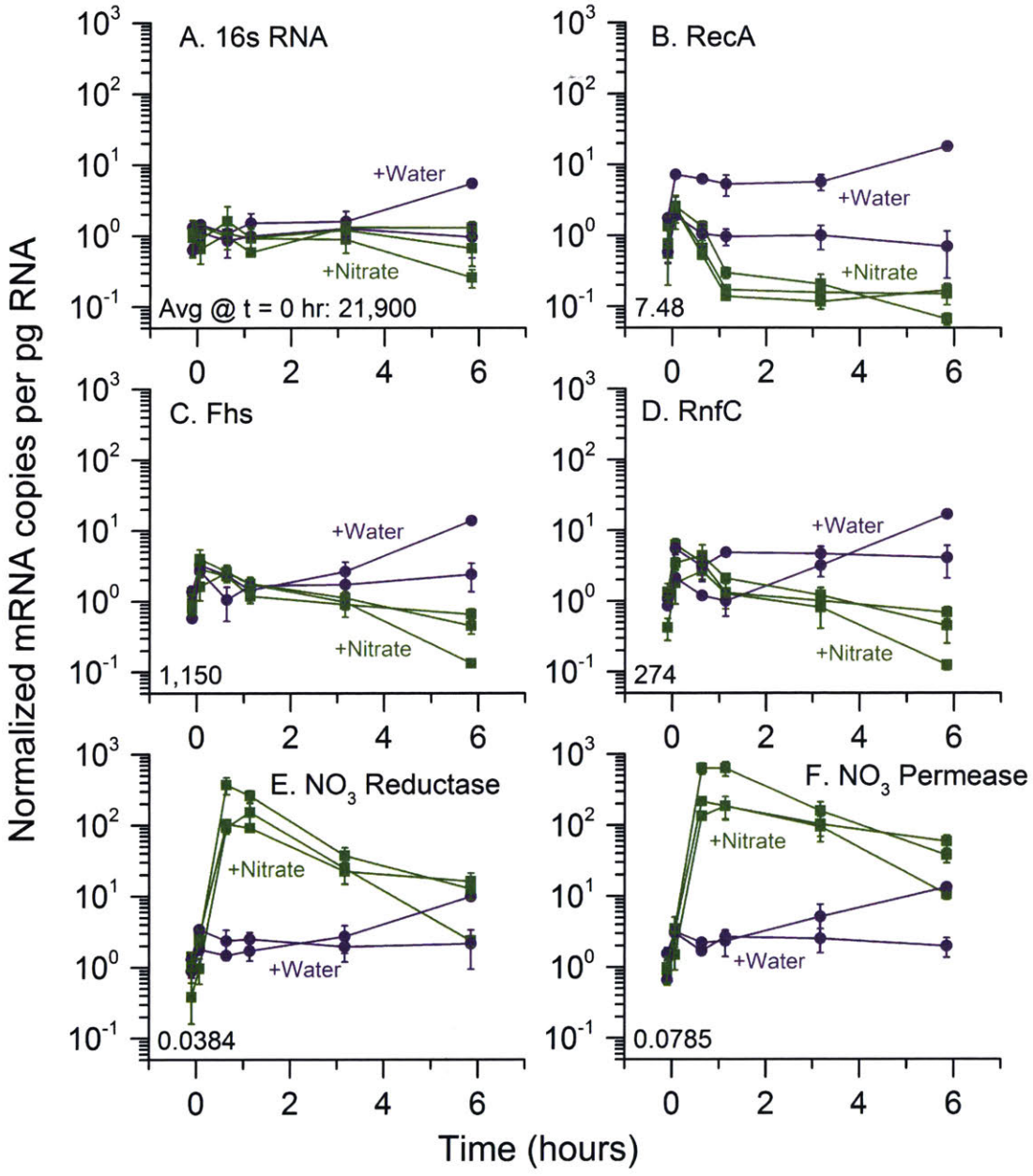

Figure 2-22: Change in mRNA expression levels over time after *C. ljungdahlii* cultures were spiked with nitrate. RNA was sampled immediately prior to, and following the spike at intermittent time points. Normalized expression level was calculated by first averaging the copies per pg total RNA for all samples, and dividing each time point by this average. This average copies per total pg RNA prior to spiking can be found in the lower left corner of each panel. Purple circle, water spike (n=2); green square, nitrate spike (n=3). One 'water spike' culture did not grow and hence was not analyzed. Standard deviation given in parentheses for three technical replicates and a no RT control. Individual biological replicates are plotted. Standard deviation given for technical triplicates.

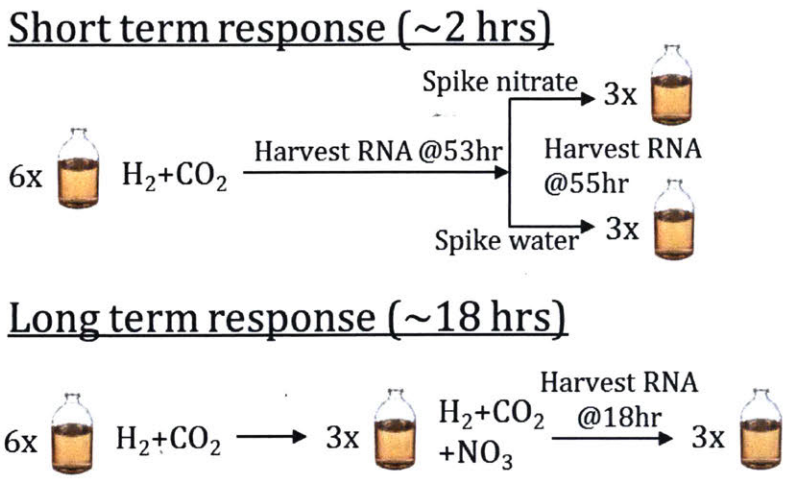

Figure 2-23: Experimental plan to asses transcriptional response to nitrate after short (2 hr) or long (18 hr) time periods.

2.6.3 Reconstructing un-aligned reads confirms lack of contamination

The first priority was confirming the absence of biological contamination, which could be used to explain the observed phenotype and refute the proposed mechanism. Reads that were un-aligned with the *C. ljungdahlii* genome could be from other organisms. For this reason, the un-aligned reads of sufficient quality were re-constructed into large fragments with Trinity [164], and the putative gene was determined with nucleotide BLAST. Those un-aligned reads were mapped to the large fragments and sorted by FPKM, with the top hits given in **Table** 2.9. The results from the first nitrate grown culture were representative of all samples and is presented below.

Depending on the replicate, between 2 and 51% of reads were not mapped or were unaligned to the *C. ljungdahlii* genome due to low quality or sequence variation. Data from the first biological replicate grown on H_2+CO_2+NO_3^- was representative of all the replicates and 20% of the reads were not mapped; of this, 40% were of sufficient quality for re-construction.

Of the unaligned fragments with sufficient quality, 99.7% mapped to ribosomal-like transcript fragments that were highly similar to those found in *C. ljungdahlii*, *Bacillus subtilis*, and *E. coli* (16s, 23s, etc.). The final 0.3% were highly similar to

various regions of *C. ljungdahliis* genome. The large presence of rRNA fragments was expected, as rRNA removal was part of the sample processing with Illumina RiboZero. The important conclusion, despite substantial un-aligned reads, was the absence of genes from other organisms, confirming that nitrate reduction and ATP production were performed by *C. ljungdahlii.*

2.6.4 Transcriptomic response to nitrate

Within 2 hrs of receiving the nitrate spike, transcripts related to nitrate metabolism rose dramatically (**Figure** 2-24, middle boxes) (e.g. 8.2 $\log_2$ fold for the nitrate reductase, NO_3^- red). Curiously, levels of WLP transcripts were unchanged during this time. During quasi-steady state growth on nitrate (**Figure** 2-24, right boxes), genes involved in nitrate metabolism were highly up-regulated compared to the no-nitrate control (e.g. 6.2 $\log_2$ fold for NO_3^- red). By contrast, genes involved in the WLP were significantly down-regulated (e.g. 2.9 $\log_2$ fold for the acetyl-CoA synthase, acsBCD), which is consistent with the lower specific flux through the WLP discussed earlier.

After receiving the nitrate spike (**Figure** 2-2**E,F**), growth and acetate production did not substantially change within 2 hrs, similar to the WLP transcripts. After 5 hrs acetate production slightly diverged; only after 15 hrs was this divergence substantial. Growth only diverges after 44 hrs.

Comparing the time-dependent change in transcripts and metabolism after the addition of nitrate can provide clues to the mechanism involved. Within 2 hrs there was no change in WLP transcripts in response to nitrate, hence nitrate likely does not directly repress WLP transcription with a sensor/regulator; 2 hrs was sufficient time for significant RNA transcript turnover if WLP transcripts were tightly repressed [165, 166] (**Figure** 2-25). For instance, the smallest apparent half-life was 35 minutes, for a radical SAM domain protein (CLJU_c22770). Other genes included a putative transcriptional regulator (41 min, CLJU_c22780) and a hypothetical protein (55 min, CLJU_c22610)

Conversely, the quick up-regulation of the nitrate reduction system indicates con-

Table 2.9: Prevalence in FPKM of fragments reconstructed from reads un-aligned to the *C. ljungdahlii* genome. The top BLAST result for each fragment is given, along with the corresponding organism. The top fragments are presented in this table, accounting for 99.9% of all FPKM.

FPKM	Overlapping function	Organism	Coverage	Identity
273630	23s rRNA	*Escherichia coli*	0.98	100%
255857	16s rRNA	*Escherichia coli*	0.99	99%
248259	23s rRNA	*Escherichia coli*	1	99%
209418	23s rRNA	*Escherichia coli*	1	100%
178239	23s rRNA	*Escherichia coli*	0.96	100%
80522	16s rRNA	*Bacillus subtilis*	1	100%
68096	16s rRNA	*Bacillus subtilis*	1	100%
29078	23s rRNA	*Bacillus subtilis*	0.99	100%
27789	16s rRNA	*Bacillus subtilis*	0.93	100%
10317	23s rRNA	*Bacillus subtilis*	0.86	100%
10204	23s rRNA	*Clostridium ljungdahlii*	0.93	100%
7263	23s rRNA	*Clostridium autoethanogen*	0.73	99%
6942	23s rRNA	*Bacillus subtilis*	0.98	99%
3193	16s rRNA	*Clostridium ljungdahlii*	0.86	100%
2351	16s rRNA	*Clostridium ljungdahlii*	0.79	100%
1979	23s rRNA	*Bacillus subtilis*	0.98	90%
606	dnaA	*Clostridium ljungdahlii*	1	100%
603	23s rRNA	*Escherichia coli ECC-1470*	0.92	98%
592	23s rRNA	*Clostridium ljungdahlii*	0.77	100%
504	23s rRNA	*Clostridium ljungdahlii*	0.93	100%
404	23s rRNA	*Escherichia coli strain K*	0.92	99%
355	CLJU_c04840	*Clostridium ljungdahlii*	0.94	100%
286	Elongation factor Tu	*Clostridium autoethanogen*	0.98	100%
258	CLJU_c10110	*Clostridium ljungdahlii*	0.95	100%
241	CLJU_c33770	*Clostridium ljungdahlii*	0.92	99%
239	23s rRNA	*Clostridium ljungdahlii*	0.85	100%
222	meTr	*Clostridium ljungdahlii*	0.93	100%
208	16s rRNA	*Clostridium autoethanogen*	0.79	100%
192	cdd cytidine deaminase	*Clostridium ljungdahlii*	0.99	100%
156	30S ribosomal protein	*Clostridium ljungdahlii*	0.86	100%
154	CLJU_c02220	*Clostridium ljungdahlii*	1	100%
152	guaA GMP synthase	*Clostridium ljungdahlii*	0.93	100%
144	30S ribosomal protein	*Clostridium ljungdahlii*	0.96	99%
142	tRNA-Asp-GTC	*Clostridium ljungdahlii*	0.75	100%
137	23s rRNA	*Clostridium ljungdahlii*	0.99	98%
122	23s rRNA	*Clostridium ljungdahlii*	0.73	99%
110	Unannotated gene, between CLJU_c08260 and CLJU_c08270	*Clostridium ljungdahlii*	0.91	99%
107	rplJ	*Clostridium ljungdahlii*	1	100%
100	predicted cell wall binding protein	*Clostridium ljungdahlii*	1	100%

trol by a sensor/regulator system. Because acetate production only slightly diverges after 5 hrs, enzyme inhibition or competition was likely not a key mediator even though some formate dehydrogenases are inhibited by nitrate [167, 168, 169, 170]. Instead, the substantial divergence of acetate production at 15 hrs corresponds closely to WLP transcript down regulation (**Figure** 2-24, right boxes) and the time frame of bacterial protein turnover (approximately 20 hrs) [171, 172]. One possibility is that changes in the cellular redox environment cause this shift in metabolism [173]. Other mechanisms are also possible, such as nitrate repressing the production of a protein that up-regulates WLP transcription. Further experimentation will be required to fully understand how electron flux is partitioned between CO_2 and nitrate.

Gene Set Enrichment Analysis (GSEA) [174] was calculated to determine how the presence of nitrate impacts genome-wide expression on sets of genes (i.e. pathways), and whether they were correlated to the phenotoype; in this case, the phenotype was growth on H_2+CO_2, either with or without nitrate. The algorithm calculates an enrichment score (ES) for gene sets to determine if the genes within the gene set are represented at the top or bottom of a ranked list of genes. The ES is normalized (NES) to account for differences in gene set sizes and correlations between gene sets in the data set. The statistical significance (false discover rate, FDR) is then calculated by 'scrambling' the phenotype labels, and determining the likelihood that the results were derived by chance. The pathways with a FDR less than 15% were plotted in **Figure** 2-26.

As expected, the pathways with the largest negative NES (down-regulation) was the WLP. This was followed by histidine and selenocompound metabolism. For histidine metabolism, the pathway from 5-Phosphoribosyl 1-pyrophosphate (PRPP) to histidine was largely down-regulated, while the pathway from histidine to glutamate was generally up-regulated. Selenocompound metabolism down-regulation was logical, as selenocompounds are important for key enzymes of the WLP, such as the formate dehydrogenase [89]. The relative up or down-regulation for each gene in the gene set (or pathway) is given in **Figures** A-10 to A-27.

Perhaps surprising, was the down regulation of gluconeogenesis in the presence of

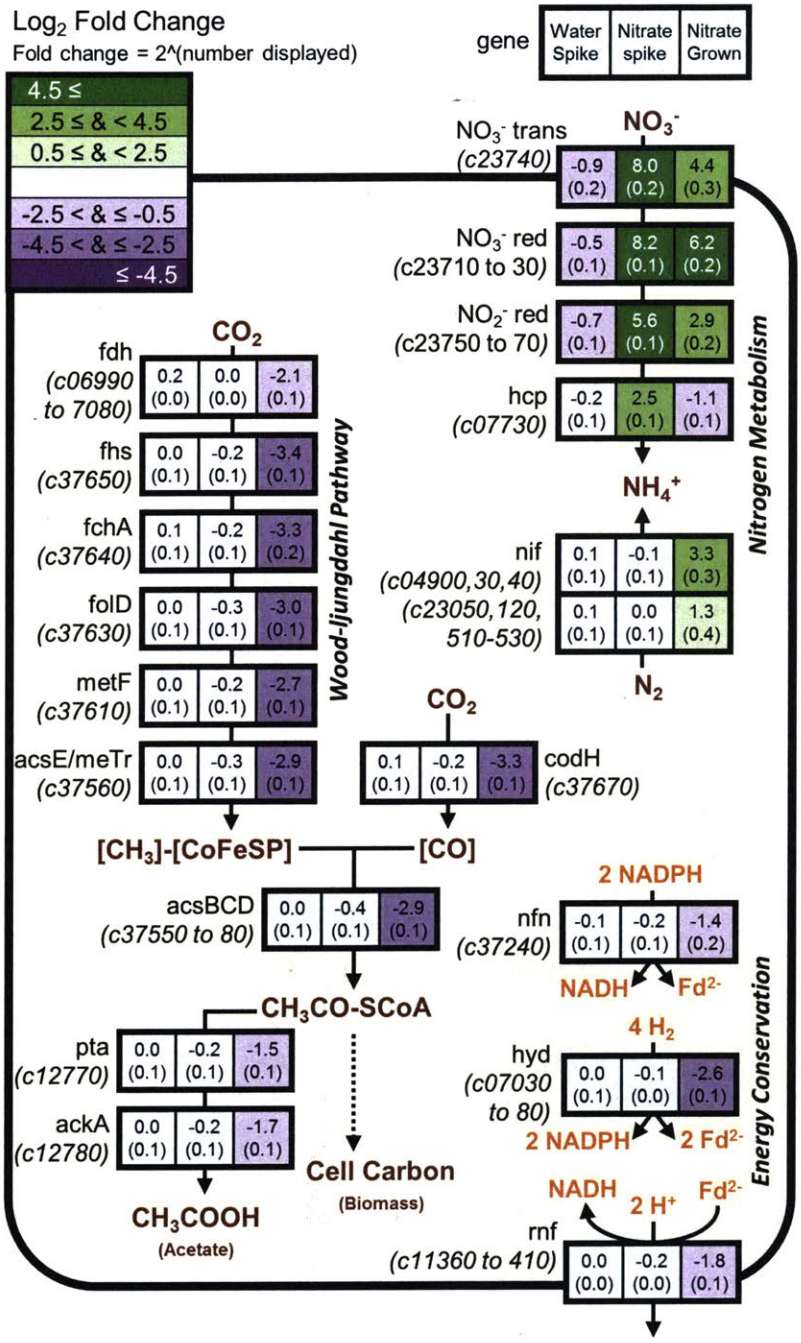

Figure 2-24: Log_2 fold change in expression for RNA transcripts in *C. ljungdahlii* related to the WLP, nitrogen, or energy metabolism. The left-most and middle box is the change after receiving a water and nitrate spike, respectively. The right-most box is the fold increase of cultures grown on nitrate vs. those grown without. The fold change of spiked cultures compares 2 hrs after vs. 5 minutes before the spike. Green indicates an increase in transcript levels in the presence of nitrate, whereas purple indicates a decrease. For enzymes with subunits, an average is given. Standard deviation given in parentheses for three biological replicates.

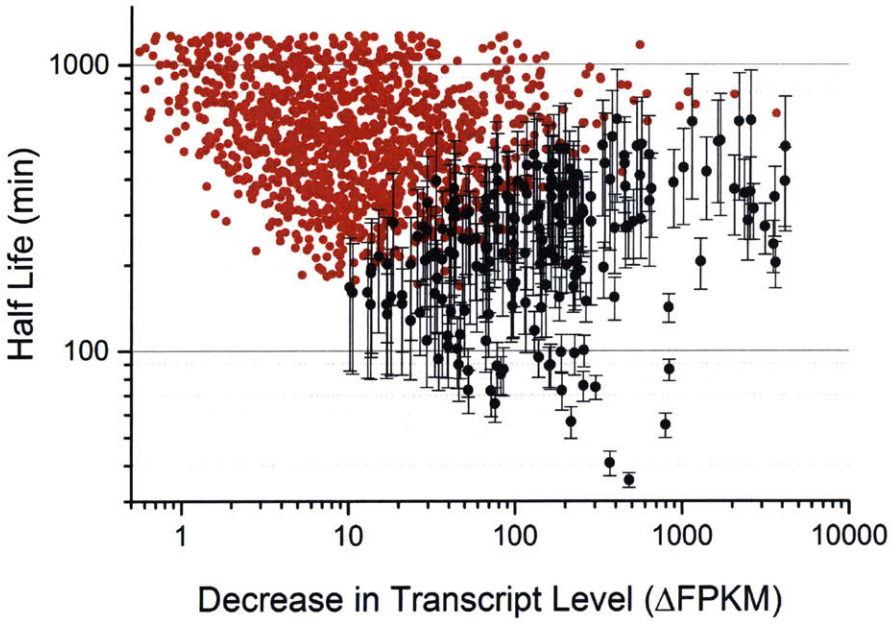

Figure 2-25: Observed half-life of mRNA transcripts as determined from samples taken before and 2 hrs after a nitrate spike. Only transcripts with log2fold change < -0.1 were plotted. Half-life was calculated for all transcripts that decreased in expression level assuming exponential decay over those 2 hrs. Black points had a relative error less than 50%; red points had a greater error. The two transcripts with the smallest half-life were a radical SAM domain (CLJU_c22770) and a putative transcriptional regulator (CLJU_c22780). Standard deviation given for three biological replicates.

nitrate. Genes that were highly down-regulated included glyceraldehyde-3-phosphate dehydrogenase, pyruvate kinase, phospho-glycerate kinase, and 6-phosphofructokinase. Conversely, adhE1 and adhE2 (aldehyde/alcohol dehydrogenase) were up regulated. These results were surprising because the normalized metabolite pool sizes in gluconeogenesis were generally elevated in the presence of nitrate, with the exception of pyruvate (**Figure** 2-21; center 2 bars in each figure). Similarly, the pentose phosphate pathway was down-regulated, whereas R5P levels were elevated in the presence of nitrate.

While the genes for amino acid biosynthesis were generally up-regulated, those involved in phenylalanine biosynthesis were down-regulated; which was evidenced by a decrease in intracellular phenylalanine pool sizes. On the other hand, despite up-regulation of lysine biosynthesis genes, intracellular concentrations decreased.

2.6.5 Implications of metabolism regulation on future strain engineering

For practical implementation, control of the WLP and nitrate reduction are important. As discussed in **Section** 2.4.3, controlling the flux of electrons between CO_2 and NO_3^- would be important for achieving the yields theorized in **Table** 2.7. Moreover, high flux must be maintained through the WLP for product synthesis. For these reasons, we studied how nitrate regulates the WLP as well as other key pathways in *C. ljungdahlii.*

There was down-regulation of the WLP in the presence of nitrate, and this in part resulted in a decrease in cell specific productivity of biomass and acetate (**Figure** 2-3). Yet, acetate was still produced in significant titers. Conversely, despite the significant up regulation of the nitrate reductase sub-units, this respiration pathway was un-able to compete for all of the available high energy electrons (NADH, NADPH, or reduced ferredoxin). The best method to engineer a high yield strain would be fully de-coupling the transcription of the WLP and nitrate reduction from the presence of nitrate. Once de-coupled, the relative expression level of each should be systematically

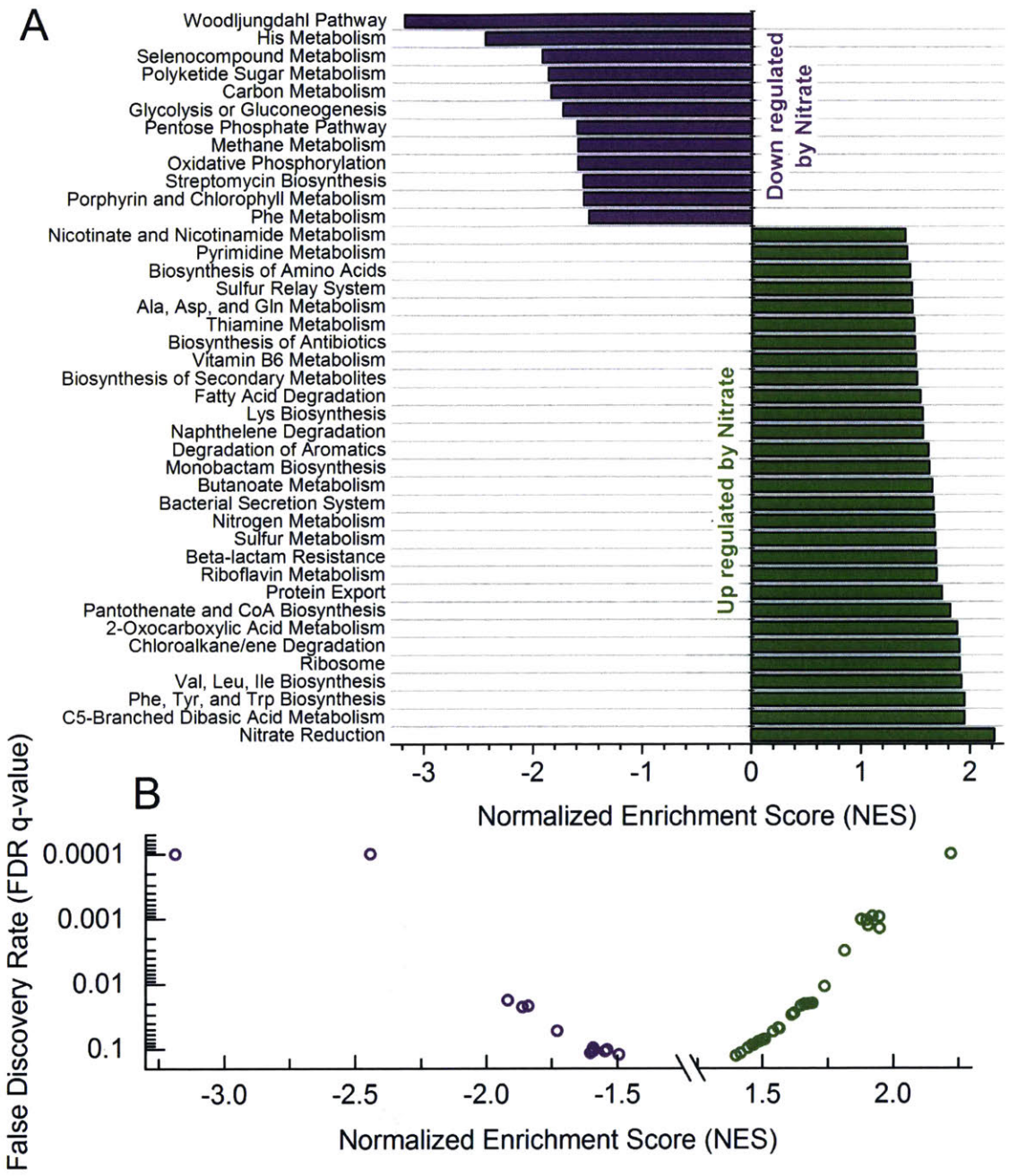

Figure 2-26: GSEA pathway analysis of RNAseq data comparing growth on H_2+CO_2 vs. H_2+CO_2+NO_3^-. Only gene sets with less than 15% false discovery rate (FDR) were plotted. (A) Normalized Enrichment Score (NES) for each pathway. (B) NES plotted against FDR.

titrated to optimize either productivity or yield.

The best method for de-coupling either pathway's expression level from the presence of nitrate is unclear. For the nitrate reduction pathway, there very likely is a sensor regulator system. Potential targets can be found from the RNAseq data, as sensor-regulator concentration can have an impact on binding occupancy of control sites, and thus degree of regulation [175, 176]. Predicted sensors, regulators, and DNA binding proteins were listed that were either highly up-regulated or down-regulated by the addition of nitrate (**Table** 2.10). When comparing the $\log_2$ fold change for a given gene, there was sometimes positive correlation (CLJU_c23620), however this was generally not the case. For instance, after 2 hours in the presence of nitrate, there was no transcriptional response for CLJU_c34900, CLJU_c14970, and CLJU_c18890. Yet, after long term growth, these 3 predicted regulators were highly up-regulated.

These candidates could be knocked out, and those strains which are insensitive to nitrate would likely be directly involved in regulating nitrate metabolism. While generating knockouts in *C. ljungdahlii* is not as fast as in *E. coli*, they have been performed in the past [133, 177].

Table 2.10: Log_2 fold change of predicted regulators and DNA binding proteins. The fold change was either grown with or without nitrate, and 2hrs after vs. before receiving a nitrate spike. Genes that were highly up or down regulated are shown. Top candidates are given for each condition.

Gene	Annotation	Nitrate Spike	Nitrate Grown
CLJU_c23620	putative nucleic-acid binding protein containing a Zn-ribbon	2.16 ± 0.37	2.63 ± 1.19
CLJU_c07750	transcriptional regulatory protein	1.65 ± 0.31	0.27 ± 0.41
CLJU_c23300	predicted transcriptional regulator	0.97 ± 0.17	-0.99 ± 0.22
CLJU_c39160	predicted transcription regulator	-0.83 ± 0.19	-2.96 ± 0.24
CLJU_c29600	predicted two-component response regulator	-0.90 ± 0.26	-1.29 ± 0.26
CLJU_c22780	putative transcriptional regulator	-2.95 ± 0.29	0.13 ± 0.18
CLJU_c34900	predicted transcriptional regulator	0.01 ± 0.15	6.37 ± 0.88
CLJU_c14970	predicted two-component response regulator	0.00 ± 0.32	5.20 ± 0.52
CLJU_c18890	predicted transcriptional regulator	0.30 ± 0.31	4.67 ± 0.24
CLJU_c08900	predicted zinc finger containing protein	0.31 ± 0.35	4.14 ± 0.28
CLJU_c19400	predicted transcriptional regulator	-0.27 ± 0.10	-3.79 ± 0.19
CLJU_c10870	predicted two-component sensor histidine kinase	-0.43 ± 0.22	-3.83 ± 0.35
CLJU_c32950	predicted transcriptional regulator with 2 HTH motifs	0.23 ± 0.12	-4.92 ± 0.21

2.7 Future experiments and preliminary work

Once the energy metabolism is controlled, and expression strains are generated, the next step is fermentation of those strains in bubble columns. All results previously presented were derived from either serum bottles and balch tubes, shaken within incubators. Culturing in serum bottles and balch tubes have 4 key limitations:

1. Mass transfer: in serum bottles, k_La is low and the driving force is high compared to bubble columns

2. Nitrate limitations: in almost all serum bottle fermentations, nitrate (15mM) is fully consumed, resulting in stationary and death phase (**Figure** 2-2)

3. pH limitations: pH increases substantially during nitrate reduction from an optimal 6 to upwards of 7.5

4. Ammonium concentrations: high levels of ammonium may be toxic; all serum bottle fermentations start with 19 mM to maintain consistency with 'no nitrate' controls

These considerations can generally be addressed by scaling up to bubble column bioreactors, with a nitric acid feed to balance pH rise. The preliminary results are presented here to show, approximately, what would result during autotrophic fermentation of *C. ljungdahlii* WT on H_2+CO_2 in the presence of nitrate. For these experiments, the YE concentration was changed from 0.1 $g\ L^{-1}$ to 1 $g\ L^{-1}$. The reactor set-up can be seen in **Figure** 2-27.

Based on the pH change of the culture grown in a serum bottle (**Figure** 2-28**A**), pH greatly increases during nitrate reduction. Based on the ratio of reduction of nitrate and oxidation of acetate, it was determined that a pure feed of nitric acid was undesirable, as it would result in large increases of nitrate concentration, instead of keeping pH and nitrate at a steady state concentration. To maintain a steady state, the acid feed was set at 1 mole of nitric acid to 0.7 mole hydrochloric acid (1:0.7). While the concentration of nitrate was steady, the pH fluctuated substantially

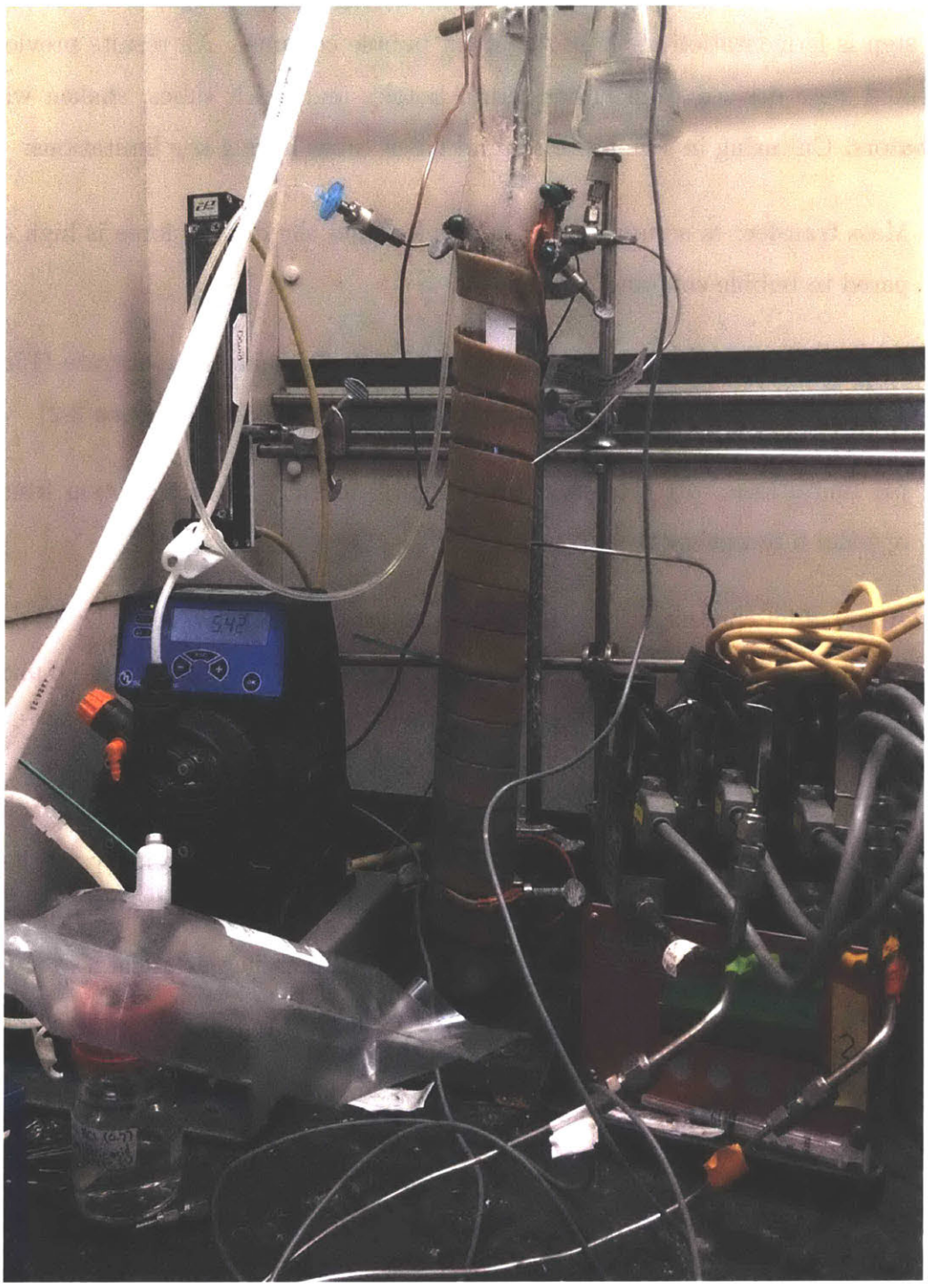

Figure 2-27: Bubble column bioreactor set-up.

throughout the experiment, so the acid feed was then lowered from 5 M to 1 M at the same ratio of acids. Moreover, the growth was not qualitatively different than that observed in the serum bottle, so the flow rate of gas was increased from 125 to 1000 sccm, by switching from the digital flow controller to a rotameter.

$$NO_3^- + 4\ H_2 + 2H^+ \rightleftharpoons NH_4^+ + 3\ H_2O \tag{2.38}$$

$$2\ CO_2 + 4\ H_2 \rightleftharpoons \text{Acetate} + H^+ + 2\ H_2O \tag{2.39}$$

The results of these modifications was a substantial improvement of growth and acetate productivity; the OD and acetate titer would likely be even higher if nitrate was not depleted at 39 hr, despite the nitric acid feed. Immediately prior to this was the greatest specific productivity of 0.56 $g\ acetic\ acid\ gDCW^{-1}\ hr^{-1}$, 3 times greater than in serum bottles (**Table** 2.11). This acetate formation rate is substantial considering the flux of electrons redirected to nitrate. While volumetric productivity must still be improved for industrial relevance, the large increases in acetate production on a cell basis were promising, and are on the order of magnitude for those seen in *C. ljungdahlii* grown under similar conditions with fructose (**Table** 2.11, **Figure** 2-29). The decrease in acid feed resulted in a steady reactor pH, however the high flow rotameter was erratic due to changes in pressure in the gas tank regulator.

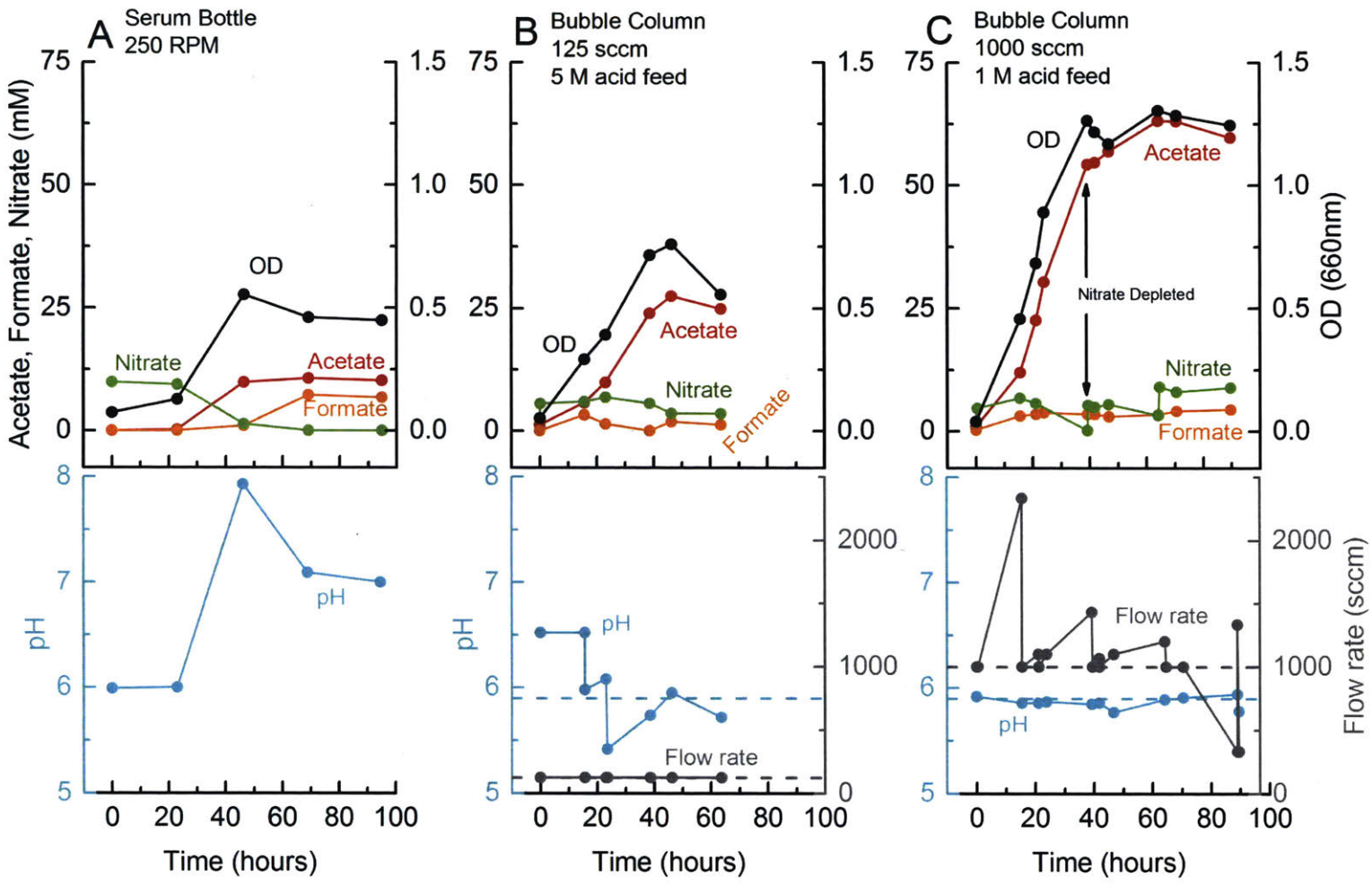

Figure 2-28: Growth curve and metabolites of *C. ljungdahlii* grown on H_2+CO_2+NO_3^- in a serum bottle or bubble column bioreactors. (A) Growth in a serum bottle. (B) Growth in bubble column bioreactor with a flow rate of 125 sccm and an acid feed of 5 M. (C) Growth in bubble column bioreactor with a flow rate of approximately 1000 sccm and an acid feed of 1 M; nitrate was added sporadically to maintain a constant nitrate concentration. Black, optical density; red, acetate; orange, formate; green, nitrate; light blue, pH; gray, gas flow rate. Each figure was a biological replicate, as a proof of concept experiment. The concentration of YE for all conditions was 1 $g\ L^{-1}$.

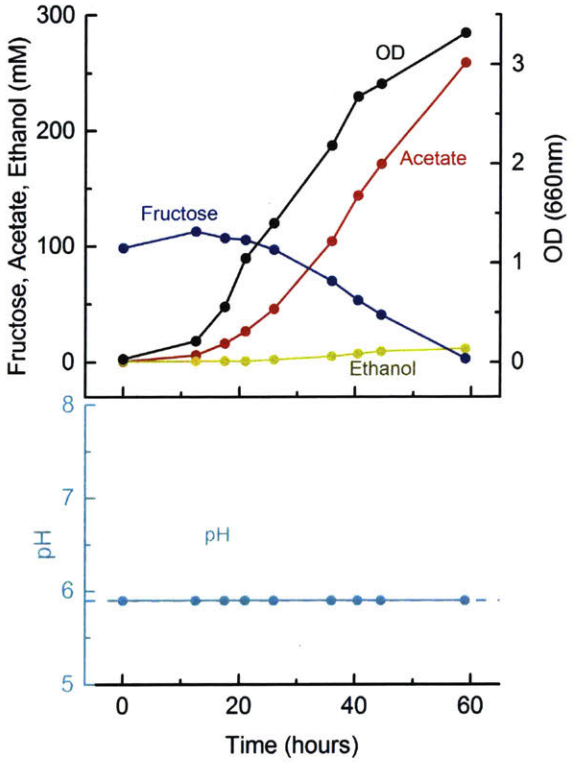

Figure 2-29: Growth curve and metabolites of *C. ljungdahlii* grown on fructose in a stirred tank reactor. Black, optical density; red, acetate; dark yellow, ethanol; blue, fructose; light blue, pH; gray, gas flow rate. The concentration of YE was 1 $g\ L^{-1}$ and ammonium chloride was added at 4 $g\ L^{-1}$.

Table 2.11: Max productivity of acetate production by *C. ljungdahlii* grown on H_2+CO_2+NO_3^-, in serum bottles or bubble column bioreactors. Data corresponds with growth curves from **Figure** 2-28. The fructose culture sparged with CO_2, and did not contain nitrate.

Serum Bottle 250 RPM H_2+CO_2+NO_3^-	**Bubble Column 125 sccm H_2+CO_2+NO_3^-**	**Bubble Column 1000 sccm H_2+CO_2+NO_3^-**	**Stirred Tank Fructose+CO_2**	**Units**
0.19	0.25	0.56	0.80	$\frac{gAceticAcid}{gDCW\ hr}$
0.025	0.054	0.17	0.52	$\frac{gAceticAcid}{L\ hr}$

2.8 Conclusion

In this work, we showed that, unlike other studied acetogens, *C. ljungdahlii* was able to simultaneously reduce CO_2 and nitrate, with electrons derived from H_2. Cultures supplemented with nitrate grew faster, and to higher optical densities, than those without, as verified via carbon and hydrogen balance, and ^{13}C labeling. Based on these balances, we further showed that nitrate reduction was coupled to ATP generation, and this was corroborated by measurements of the ATP/ADP ratio. We proposed a mechanism that accounts for the energetic coupling, even though the nitrate reductase from *C. ljungdahlii* was not membrane-bound. Specific flux through the Wood-Ljungdahl pathway was decreased in the presence of nitrate, owing to the reduced demand for acetate production to fuel ATP production. Transcriptomic analysis of steady state cultures suggests the reduction in flux was partially mediated by downregulation of the associated enzymes, but the absence of transcriptional changes in 2 hrs of a nitrate spike indicated transcriptional regulation was not direct. The ability to decouple ATP production from the WLP during autotrophic growth has important implications for improving selectivity of products produced with this organism, as well as redirecting carbon flux from acetate to desirable product, as shown by theoretical calculations. This discovery has significant implications for current industrial autotrophic fermentations when the product is not ethanol or acetate. To take full advantage of this novel metabolic capability, future work will be directed at elucidating and controlling of electron flow between nitrate and CO_2.

2.9 Materials and Methods

2.9.1 Gases and Chemicals

The gases purchased from Airgas (Ma) included research grade H_2 (> 0.5 ppm O_2) and a mix of CO_2 and H_2 (20% and 80% by mole, respectively). The anaerobic chamber (Coy Laboratories, Mi) atmosphere was 5% H_2, 10% CO_2, and 85% N_2.

2.9.2 Bacterial, media, and culture conditions

All cultures were grown anaerobically in 125 mL serum bottles with butyl rubber stoppers and aluminum crimp seals (Chemglass Life Sciences, NJ). The handling of all live cultures was performed in an anaerobic chamber (Coy Laboratories) and growth was monitored at OD_{660nm}, and a media blank was used to correct for the absorbance of resazurin. When hungate tubes were used, OD_{600nm} was measured with an Ultrospec 10 UV/Vis spectrophotometer (Amersham Biosciences). The headspace was charged to 137.9 kPa (gauge) (20 psig) with 80% H_2 and 20% CO_2 by mole. Alternatively, the headspace was 137.9 kPa (gauge) with 80% CO and 20% CO_2 by mole. If the electron source was fructose, the headspace was 137.9 kPa (gauge) of 100% CO_2.

Clostridium ljungdahlii ATCC 55383 (ATCC, Manassas, VA) was grown at 37°C, pH 6.0, and shaking at 250 RPM. The base media for *C. ljungdahlii* contained 2 g $NaHCO_3$, 1 g NH_4Cl, 0.1 g KH_2PO_4, 0.1 g KCl, 0.2 g $MgSO_4 \cdot 7\,H_2O$, 0.8 g NaCl, 0.02 $CaCl_2 \cdot 2\,H_2O$ per 970 mL. To this 10 mL of Vitamin Supplement (ATTC), 10 mL of Trace Mineral Supplement (ATTC), and 0.5 mL of resazurin stock solution (0.2 % by weight in water) was added.

Moorella thermoacetica ATCC 39073 (ATCC, Manassas, VA) was grown at 55°C, pH 6.6, shaking at 200 RPM. The base media composition for *M. thermoacetica* was modified from Pierce [132] and contained A) 7.5 g $NaHCO_3$, B) 7 g KH_2PO_4, 5.5 g K_2HPO_4, C) 2 g $(NH_4)_2SO_4$, 0.5 g $MgSO_4 \cdot 7\,H_2O$, 0.02 $CaCl_2 \cdot 2\,H_2O$. Solution A was dissolved in 200 mL of water, B in 200 mL, and C in 570 mL. To prevent precipitation, solution B was added slowly to C, then A was added slowly to B and C. To this 10 mL of Vitamin Supplement (ATTC), 10 mL of Trace Mineral Supplement (ATTC), and 0.5 mL of resazurin stock solution was added.

Acetobacterium woodii DSMZ 1030 (DSMZ, Braunschweig, Germany) was grown at 30°C, pH 7.4, shaking at 250 RPM. The base media composition for *A. woodii* was modified from Bache [138] and Straub [178], and contained 10 g $NaHCO_3$, 1 g NH_4Cl, 0.33 g KH_2PO_4, 0.45 g K_2HPO_4, 0.16 g $MgSO_4 \cdot 7\,H_2O$, 0.1 $CaCl_2 \cdot 2\,H_2O$ per

970 mL. To this 10 mL of Vitamin Supplement (ATTC), 10 mL of Trace Mineral Supplement (ATTC), and 0.5 mL of resazurin stock solution was added.

The media was filter sterilized (0.22 μm PES; Corning, Ny) and then transferred into an anaerobic chamber. 10 mL of 3 % by weight sterile cysteine stock solution was added, and media was used when fully reduced. Bacto^{TM} yeast extract (BD, Md) was added as designated from 10 g/L stock solution; the stock was prepared in the respective media and filter sterilized. The Trace Mineral Supplement contained per liter 0.5 g EDTA, 3 g $MgSO_4 \cdot 7\,H_2O$, 0.5 g $MnSO_4 \cdot H_2O$, 1 g NaCl, 0.1 g $FeSO_4 \cdot 7\,H_2O$, 0.1 g $Co(NO_3)_2 \cdot 6\,H_2O$, 0.1 g $CaCl_2$ (anhydrous), $ZnSO_4 \cdot 7\,H_2O$, 0.01 g $CuSO_4 \cdot 5\,H_2O$, 0.01 g $AlK(SO_4)_2$ (anhydrous), 0.01 g H_3BO_3, 0.01 g $Na_2MoO_4 \cdot 2\,H_2O$, 0.001 g Na_2SeO_3 (anhydrous), 0.01 g $Na_2WO_4 \cdot 2\,H_2O$, 0.02 g $NiCl_2 \cdot 6\,H_2O$. The Vitamin Supplement contained per liter 2 mg Folic acid, 10 mg Pyridoxine hydrochloride, 5 mg Riboflavin, 2 mg Biotin, 5 mg Thiamine, 5 mg Nicotinic acid, 5 mg Calcium pantothenate, 0.1 mg Vitamin B_{12}, 5 mg pAminobenzoic acid, 5 mg Thioctic acid, 900 mg Monopotassium phosphate. All other media components were prepared anaerobically by sparging with Argon for 20 min, including water and 1 M sodium nitrate in water.

2.9.3 Cellular density and composition

The correlation to gDCW/L was determined by harvesting 50 mL of late-log phase cells with Whatman membrane filters (nylon, 0.2 μm pore size, 47 mm diameter) and a vacuum pump. The cells were rinsed twice with 10 mL of millipure water, then dried for 48 hrs at 60°C, along with a no-cell control. The elemental composition (C, H, N, S) of biomass and yeast extract was determined with an Elementar Vario EL Cube CHNS. Approximately 5 mg of cell biomass were prepared (in triplicate) and dried by lyophilization. The CHNS (as defined by Elementar) was operated under default parameters and standardized with sulfanilamide.

2.9.4 Metabolite analytical methods

The HPLC to measure formate, acetate and ethanol was run with a mobile phase of 14 mM sulfuric acid running at 0.7 mL/min with an Agilent 1260 Infinity separations module equipped with an Aminex HPX-87H ion exclusion column, and an Agilent 1260 Infinity refractive index detector. The temperature of the system was 50°C. Nitrate was assayed [179] by adding 40 μL salicylic acid stock to 5 μL of supernatant and mixed by vortexing. The acid solution was neutralized with 955 μL of 2 M NaOH. The final solution was measured on a Molecular Devices (Ca) SpectraMax M2e plate reader at 410 nm. The salicylic stock was prepared fresh with 50 mg of salicylic acid per 1 mL of H_2SO_4 (95 to 98 % pure). Nitrite was assayed [180] by first diluting the supernatant such that expected nitrite concentration was between 40 μM and 2 μM. To a sample volume of 200 μL, 4 μL of a sulfanilamide solution was added, mixed thoroughly and let to react for 4 min. This was quenched quickly with 4 μL of a N-(1-Naphthyl)-ethylenediamine dihydrochloride (NNEDA) solution and mixed thoroughly; after 10 min the absorbance was measured at 543 nm. The sulfanilamide solution was prepared by mixing 25 mL of HCl and 150 mL of water. To this, 2.5 g of sulfanilamide was added, and diluted to 250 mL. The NNEDA solution was prepared by dissolving 0.2 g of NNEDA in 100 mL of water. Ammonia was measured enzymatically with the Ammonia Assay Kit (Sigma-Aldrich).

2.9.5 Metabolite labeling, derivatization, and measurement by LC-MS

Acetate and formate were derivatized with the following method. To 2 mL of 50/50 water/acetonitrile, 12.25 mg of 2-nitrophenyl-hydrozine hydrochloride (NPH) was dissolved. To 2 mL of water, 95.88 mg of 1-ethyl-3-(3-dimethylaminopropyl)carbodiimide hydrochloride (EDC) was dissolved. The EDC solution was combined in equal parts with 3 %v/v pyridine in ethanol. Samples were diluted such that the concentration of carboxylic acid was less than 5 mM. To 50 μL of diluted sample, 200 μL of EDC/pyridine was added, followed by 100 μL of the NPH solution. Samples were

mixed by vortexing and incubated at 60°C for 20 min. Derivatized samples were diluted 10x prior to analysis by LC/MS/MS with an Agilent 1100 separations module equipped with an Agilent Zorbax 300SB-C18 column, and an API 4000 LC/MS/MS. The mobile phase was: 0 to 15 min, 5%v/v acetonitrile in water; 15 to 25, 100%; and 25 to 30, 5% running at 0.3 mL/min and the temperature of the system was 50°C. Ammonia was derivatized to indophenol and measured via LC/MS/MS [134].

2.9.6 RNA isolation and RNAseq

When the culture had reached mid-log phase, 5 mL of culture was anaerobically collected by centrifugation (13,400 RPM for 10 min at 25°C) and RNA was immediately extracted with an RNeasy Mini Kit (Qiagen). Cell pellets were re-suspended in 100 °L of lysozyme/TE buffer (20 mg/mL lysozyme, 10 mM Tris, 1 mM EDTA, pH 8), vortexed for 10 sec and incubated for 10 min at 37°C, with frequent mixing. RNA was then harvested using the standard RNeasy Mini Kit (Qiagen). DNA in the sample was digested with the standard DNase I (NEB) protocol for 10 min at 37°C. The RNA was re-purified with the RNeasy Mini Kit, eluted in RNase free water, and stored at -80°C. RNAseq was performed by the BioMicroCenter (MIT), including QC of RNA with a BioAnalyzer (Agilent) and removal of ribosomal RNA with the Ribo-Zero rRNA Removal Kit (Bacterial, Illumina).

Samples were sequenced with an Illumina MiSeq, with paired end reads of 75 bp. Data analysis was performed with the Galaxy Web platform (https://usegalaxy.org/) [181]. Raw data was processed with FASTQ Groomer and aligned with Bowtie2 [182]. Aligned reads were mapped with htseq-count to the genome and annotation from EnsemblBacteria (http://ensemblgenomes.org/) [183]. Un-aligned reads were re-constructed with Trinity [164] to ensure the absence of biological contamination (**Table** 2.9). Differential expression of aligned reads was determined with DESeq2 [184, 185]. The workflow for the Galaxy Web platform is given in **Figure** A-9.

2.9.7 qRT-PCR analysis

For qRT-PCR, RNA was isolated in a similar method as mentioned in **Section** 2.9.6, except DNase was not used to digest genomic DNA, and the second purification to remove DNase was not performed.

qRT-PCR was performed as seen in [155], with commercially available kits, QuantiTect Reverse Transcription (Qiagen) and RT2 SYBR Green qPCR Master Mix (Qiagen), following the provided protocol. Primers used for RT-PCR analysis are shown in **Table** A.1, and were designed with PerlPrimer [95]. Reactions were carried out in 96-well PCR plates (VWR) and sealed with BioRad Microseal B seals. For each biological replicate, there were 3 technical replicates and 1 minus RT control. qPCR cycles were performed on a BioRad iCycler using iQ3 software. The raw data was analyzed in BioRad iQ5 to determine the Ct number; the Ct number was quantified as copies/pg total RNA with a logarithmic standard curve generated from linear DNA fragments of the gene of interested. These linear fragments contained the whole gene of interest, were generated by PCR, purified with gel electrophoresis and quantified with a NanoDrop. The standard curve allowed for the calculation of the qPCR primer efficiency, which was generally greater than 90%. Melt curves were generated after each qPCR reaction cycle to ensure the specificity of the primers to the target gene.

2.9.8 Hydrogen and carbon dioxide headspace gas analysis

Hydrogen concentrations were determined using an Agilent Technologies model 7890A gas chromatograph equipped with a thermal conductivity detector (TCD) and CP-MolSieve 5A capillary column (25 m x 0.320 mm, film thickness 30 micron; Agilent Technologies). A 500 μL gas sample was injected using a split mode inlet (split ratio: 10:1) set at 50^{o}C. The inlet temperature was held for 1.5 mins following injection and then increased to 250^{o}C at a rate of 100^{o}C/min. Ultra-high purity (UHP) helium was used as the carrier gas, and was set at a flow rate of 5 mL/min. Column temperature was programmed from 40 to 250^{o}C at a rate of 40^{o}C/min with 1.5 and 3 minute holds at the lower and upper temperatures, respectively. The TCD temperature

was set at 300°C, and the polarity of the filament was reversed to ensure positive peaking of hydrogen with the helium carrier. Standards were prepared with UHP helium and high purity hydrogen to span the range of sample concentrations. A 1mL aliquot of 18.2 mOhm water was added to each standard to mimic the treatment of the samples. A full calibration curve was performed prior to sample injection ($R^2 > 0.9999$), and additional standards were interspersed within the sample run for further quality assurance and control.

Carbon dioxide concentrations were determined using an Agilent Technologies model 7890A gas chromatograph equipped with an Agilent Technologies 5975 inert XL mass selective detector (MSD) and GS-GasPro capillary column (60m x 0.320 mm; Agilent Technologies). A 250 μL gas sample was injected using a split mode inlet (split ratio: 100:1) set at 50°C. The inlet temperature was held for 2 minutes following injection and then increased to 200°C at a rate of 100°C/min. Ultra-high purity helium was used as the carrier gas, and was set at a flow rate of 2.0 mL/min. Column temperature was programmed from 40 to 75 at a rate of 15°C/min, then from 75 to 250 at a rate of 50°C/min with 3, 1, and 3 minute holds at the low, moderate, and high temperatures, respectively. The MSD utilized electron impact ionization with an ionization energy of 69.9 eV. Temperatures were set at 150°C for both the source and quadrupole mass filter. Standards were prepared with UHP helium and high purity CO_2 to span the range of sample concentrations. A 1mL aliquot of 18.2 mOhm water was added to each standard to mimic the treatment of the samples, and then this water was acidified with 25 μL of 50 % phosphoric acid per 5mL of prepared volume to ensure minimal dissolution of the CO_2 in the water. A full calibration curve was performed prior to sample injection ($R^2 > 0.995$), and additional standards were interspersed within the sample run for further quality assurance and control.

2.9.9 Measurement of Intracellular Metabolites by LC-MS

During mid-exponential phase, 3 to 5 mL of culture was quickly transferred from serum bottles to 0.2 μm nylon membrane filters using syringes within an anaerobic environment. Immediately after vacuum filtration, the filters were washed with two vol-

umes of water precooled at 4°C and transferred to a 40:40:20 methanol/acetonitrile/water with 0.1 M formic acid solution on ice. The samples were then kept at -20°C for 20 min for cell lysis and metabolite extraction. The filters were subsequently washed and the solution containing the metabolites was transferred to Eppendorf tubes preloaded with 100 μL 15% ammonium bicarbonate. After 10 min of centrifugation at 4°C, the supernatant was dried under nitrogen and resuspended in 40 μL MiliQ water for LC-MS analysis.

Metabolites were quantified with a Dionex UltiMate 3000 UPLC system (Thermo) coupled to a QExactive orbitrap mass spectrometer (Thermo) by electrospray ionization. A ZIC-pHILIC (5 μm polymer particle) 150 2.1 mm column (EMD Millipore) was used with solvent A being a 20 mM ammonium carbonate and 0.1% ammonium hydroxide solution, and solvent B being acetonitrile. The flow rate was 0.150 ml/min using the following gradients: 80% B to 20% B between 0 and 20 mins; 20% B to 80% B between 20 and 20.5 mins; constant 80% B from 20.5 to 28 mins. The column and autosampler tray were kept at 25°C and 4°C respectively. The mass spectrometer was operated in polarity switching mode scanning from 70 to 1,000 m/z. Total ion counts for each metabolite were extracted and processed using MAVEN software [186] and natural abundance of atomic isotopes were accounted for and corrected using IsoCor software [187]. All measurements were normalized to the control cultures (fructose and CO_2 only).

2.9.10 Chemical Mutagenesis

M. thermoacetica was grown to OD 660nm of approximately 0.5 on 100 mM methanol and 10 psig of CO_2 in 30 mL of semi-rich N-SCM (1 g/L YE). Cells were harvested anaerobically by centrifugation for 20 min at 3800 rpm and 4°C. Cells were re-suspended in fresh N-SCM semi-rich media with 100 mM methanol to an OD 660nm of approximately 2.5 (6 mL media). This 6 mL was split into 3 hungate tubes, 2 mL to each tube. Each tube was treated with a final concentration of 1, 10, or 100 μg/mL NTG (N-methyl-N-nitro-N-nitrosoguanidine, also called methylnitronitrosoguanidine (MNNG)) from 1 mg/mL (7mM) stock in 100 mM citrate buffer at pH 5.5. This

stock was stored at -80C.

Cells were incubated with NTG for 5 minutes at 55°C, and then collected by centrifugation at 3800 rpm and 4°C for 20 min. The cell pellet was re-suspended with 2 mL of fresh N-SCM semi-rich media. Cells were washed again, and then re-suspended 0.5 OD 660nm with approximately 10 mL of fresh N-SCM semi-rich media (containing 100 mM methanol), and transferred to balch tubes. The headspace was charged with pure CO_2 to 10 psig.

Cells were allowed to recover in non-selective media (N-SCM semi-rich media) for 24 hours at 55°C, after which cells were collected by centrifugation at 3800 rpm at 25°C for 20 min. The cell pellet was re-suspended in 10 mL of defined N-SCM media and provided with the growth substrates listed in **Table** 2.3.

2.9.11 Motility Assay

Motility was assayed with swim plates [188, 189] containing 3 g/L agar (0.3%). Molten agar medium was prepared in the glovebox by combining 64 mL of preheated water (to boiling, containing 0.24 g of agar) with 16 mL of 5x PETC containing fructose and YE preheated to 60°C; the final concentration were 0.4 g/L fructose and 1 g/L YE. For the indicated plates, nitrate was added up to 20 mM from 1 M stock. Then 80 μL of TCS stock was added. The agar medium was mixed, and 25 mL was aliquoted per petri dish; the agar medium was allowed to solidify, and used within 48 hrs. TCS stock solutions were prepared in a range of concentrations from 0 to 160 μM in methanol. When no TCS was added, 80 μL methanol was added to maintain consistency.

From a late-log phase culture, 1 μL of culture was withdrawn in to a pipette tip; the tip was stabbed half-way into the agar but no culture was ejected from the pipette tip. If the stab touched the plastic petri dish, the stab was re-performed on a fresh plate. Swim plates were incubated for 5 days and photographed aerobically.

Images were processed with ImageJ [154] following the protocol outlined by Morales-Soto et.al. [190].

2.9.12 Bubble Column Bioreactor Operation

The anaerobic bubble column was generally operated as described by Hu et. al. [28]. The reactor and tubing lines were first sterilized with 70% ethanol, and the ethanol solution was removed through the sampling port; the ethanol was removed by rinsing with sterile water until the remaining water (approximately 5 mL) contained less than 1 mM ethanol.

C. ljungdahlii was grown in a glass bubble column (G. Finkenbeiner Inc., Waltham, MA) with an inner diameter of 4.5 cm, a height of 80 cm, and a culture volume of 1 L. The media use was that described in **Section** 2.9.2, but containing 1 g/L YE instead of 0.1 g/L, and containing 2x the concentration of Trace elements. Ammonium chloride and sodium bicarbonate were excluded from the reactor media, but not that of the inoculum. Nitrate was added at 15 mM. The media was filter sterilized and added to the reactor via peristaltic pump and sterile tubing.

Temperature was controlled at 37°C with heating tape and a temperature controller. pH was controlled by the addition of an acid feed containing nitric acid and hydrochloric acid at a molar ratio of 1:0.7. The concentration of the acid was provided in **Figure** 2-28. The pH controller was an Etatron DLX pH/ORP pump control system with a submersible pH electrode. The pH controller was calibrated prior to each reactor run and sterilized with 70% ethanol. The gas composition was 80% H_2 and 20% CO_2. When the gas flow rate was 125 sccm, the flow rate and composition was controlled with 2 AALBORG digital mass flow controllers with a cut off of 100 sccm per controller; 'Research grade' H_2 and CO_2 were used from Airgas. When the gas flow rate was 1000 sccm, the flow rate was controlled with a 150 mm Cole Parmer rotameter containing a glass float (Cole Parmer Number: 03217-20). The appropriate scale reading was determined from the calibration provided and the difference between the specific gravity of air and a mix of H_2+CO_2; a premixed gas was used in this instance, as mentioned in **Section** 2.9.1.

After the media was added to the reactor, oxygen was removed by sparging anaerobic N_2 overnight, at which point cysteine was added and the gas was switched to

the H_2+CO_2 mix. Once the media was anaerobic, the reactor was inoculated with 5% vol/vol from cultures grown on H_2+H_2+NO_3^- in mid to late-log phase of growth. Nitrate was assayed periodically; in the case of depletion, anaerobic sodium nitrate solution was added.

Chapter 3

Elucidating Methanol Metabolism and CO_2 Fixation in Acetogens

3.1 Introduction

CARBON dioxide fixation with H_2 is limited by thermodynamics; the first reduction to formate or a carbonyl has a positive ΔG [53, 112]. Nitrate respiration was shown to increase growth rates and acetate productivities in the previous chapter as it provided an alternative for ATP production; cells grown autotrophically were generally ATP deficient [99, 108, 101].

However, an important consideration was that nitrate would divert a significant flux of electrons away from CO_2 fixation and acetate production. We wondered if other cheap co-substrates could serve a similar role, increasing growth rates without compromising CO_2 fixation. Of the reported growth substrates for acetogens, methanol was a promising alternative due to the volume of its production and the metabolic stoichiometry [105]. Moreover, the ATP yield per acetate was substantially increased in comparison to H_2 (**Equation** 3.1 to 3.3) [53, 29], though it remained less than CO. However, this was not surprising as CO_2 fixation would have an impact on ATP yield; here we've reported a range from 2.5 to 4 mol ATP per 3 mol acetate and the actual value would be dependent on intracellular reducing equivalent balances [191]. The expected ATP yield for *M. thermoacetica* would be 2.5 mol ATP

per 3 mol acetate [53]. These higher yields correspond to faster growth rates and higher optical density titers [25, 26]. For this reason, we wanted a better understanding of how acetogens consumed methanol so as to inform future engineering of these strains. However not much is known about methanol metabolism by acetogens, with discrepancies in the literature.

$$4\ CH_3OH + 2\ CO_2 \rightleftharpoons 3\ \text{Acetate} + 2.5\ ATP + 2\ H_2O \tag{3.1}$$

$$12\ CO + 6\ H_2O \rightleftharpoons 3\ \text{Acetate} + 6\ CO_2 + 4.5\ ATP \tag{3.2}$$

$$6\ CO_2 + 12\ H_2 \rightleftharpoons 3\ \text{Acetate} + 1.5\ ATP \tag{3.3}$$

Methanol has been a substrate for bacterial and yeast fermentations for some time, in the production of heterologous proteins [192] and food supplements [193]. While not comparable to glucose, methanol is a rational feedstock for biotechnology, due to the large scale of its production. Researchers have even proposed methanol as a basis for the next generation of the energy economy, replacing oil and natural gas [194]. Currently, methanol is produced from synthesis gas (CO, H_2, CO_2) via the low-pressure methanol process (5-10 MPa) [195]. This synthesis gas can be generated via methane [196]. Alternatively, methanol can be generated from CO_2+H_2 or CO_2+electricity [197, 198]. Work is ongoing to improve these types of systems [196].

There are three main routes for methanol metabolism in nature (based on the first oxidation step or methyltransfer), of which only two are well studied (**Figure** 3-1). The first and most prevalent is aerobic methylotrophy [199] in organisms such as *Pichia pastoris* [200], where methanol is oxidized to formaldehyde before assimilation via the serine or RuMP cycle. The oxidation to formaldehyde immediately sets an upper carbon efficiency threshold to about 62% due to lost electrons, with lost carbon released as CO_2 [201, 202]. There are a variety of aerobic methylotrophs, with their key differences being the cofactor used by the methanol dehydrogenase and the assimilation pathway. For instance, the type of methanol dehydrogenase affects energy conservation and ATP yields(NAD, PQQ, or AOX-dependent). There is currently

substantial interest in the heterologous expression of these enzymes to generate an *E. coli* methylotroph [203]

The second type of methylotroph is anaerobic methanogens; they utilize a set of either insoluble [204] or soluble [205, 206, 207] methyltransferases with methane as the ultimate end product. For the soluble methyltransferase such as those found in *Methanosarcina barkeri* [208], the methyl group is first transferred onto a cobalimin [209] co-factor (MtaC) by the methyltransferase (MtaB) [205]. The methyl is subsequently transferred to coenzyme M (CoM) [210] by MtaA [207]. While interesting from a biological stand point, these organisms are not as useful when the methanol was derived from methane [1] [211]. Moreover, some of the methane must be oxidized fully to CO_2 to power methanogenesis, resulting in maximum carbon yields of 75% [210].

The final type of methanol metabolism joins directly with the WLP and produces acetate as a product, and is the pathway targeted by this thesis chapter, as seen in *Moorella thermoacetica* [105] and *Acetobacterium woodi* [138]. While the mechanism of methyltransfer was theorized to be similar to anaerobic methylotrophic methanogens (ie. a 3-component soluble methyltransferase) [144], no in vitro evidence has confirmed this hypothesis. The most extensive research to date was on vanillate metabolism in *M. thermoacetica*; the individual enzymes of the soluble MtaABC cascade were purified to apparent homogeneity and verified with in vitro assays [111]. In conflict with these results, earlier research found that methanol metabolism in *M. thermoacetica* and *M. thermoautotrophica* occured via methanol oxidation by a PQQ-dependent methanol dehydrogenase [212, 213]. Through $^{13}CH_3OH$ and CD_3OD labeling, we wish to resolve the mechanism by which methanol is metabolized in *M. thermoacetica*, and then determine the genes likely involved via RNAseq.

While the yields are high for acetogenic methylotrophs due to CO_2 fixation (150%) [214], the growth rates are lower than that of aerobic methanotrophs (growth rates of 0.08 vs 0.5 hr^{-1} [25, 214, 201]). While this type of methylotrophy has potential because it can fix CO_2, improvements must be made to increase cell titers and

[1] This would result in a futile cycle; methane → methanol → methane [196])

productivities.

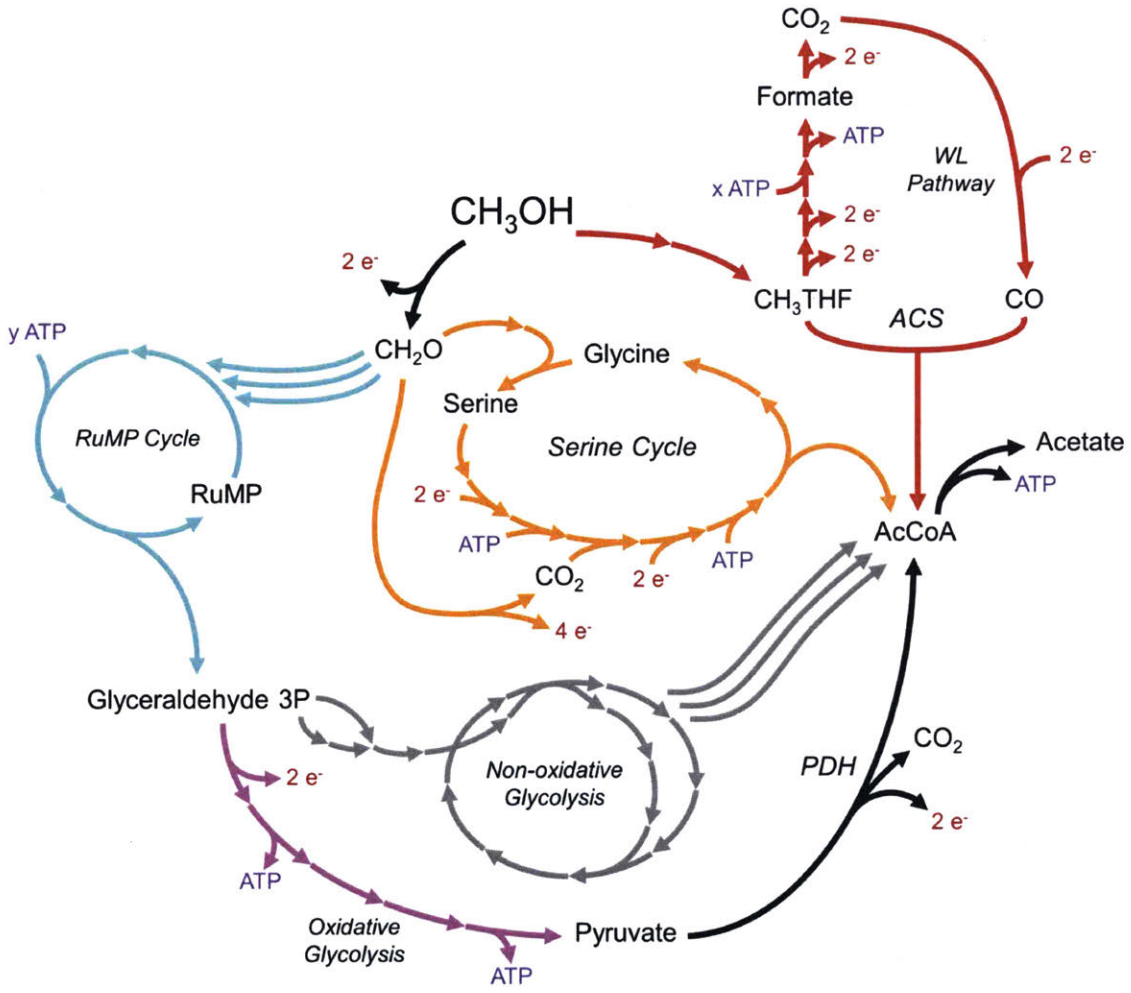

Figure 3-1: Pathways for methanol assimilation in bacteria and yeast. Aerobic methylotrophy begins with oxidation to formaldehyde; these electrons are used to reduce O_2 and are thus lost. Formaldehyde is then metabolized via the serine cycle or RuMP cycle. Anaerobic methylotrophs (acetogens) first transfer the methyl to a cobalamin active site, where it is subsequently transfered to tetrahydrofolate (THF), before assimilation into the WLP. Non-oxidative glycolysis is a proposed pathway for bypassing CO_2 loss during pyruvate dehydrogenation [55]. PDH, pyruvate dehydrogenase; WL, Wood-ljungdahl; RuMP, ribulose monophosphate pathway. All pathways are depicted to have a similar product, acetate, for ease of comparison.

3.2 Determining the type of methyltransferase by $^{13}CH_3OH$ labeling

First, we set out to determine the method of methyl assimilation by *M. thermoacetica* and *A. woodii*, whether it was via methanol dehydrogenase or the 3-component methyltransferase system. After removal of sugars from the media, *M. thermoacetica* grew on methanol with lag phases of less than 3 days. On the other hand, *A. woodii* required substantial time for acclimitization, generally 15 to 30 days; preparation of cryo stocks negated this acclimitization. This behaviour has been reported in literature in the past [138, 215], and for these reasons, *A. woodii* was maintained during experimentation by repeated subculturing for at most 2 months at a time.

Based on growth yields (141 $\pm$ 3% mole carbon in acetate produced per mole carbon in methanol consumed, (**Figure** 3-3, *M. thermoacetica* CH_3OH), we were unable to determine between these two possibilities. The electrons from methanol dehydrogenation could be shuttled to CO_2 reduction, and the formaldehyde (CH_2O) could spontaneously react with THF, thus entering the WLP [216]. For this reason, deuterium labeled methanol (CD_3OD) was fed to both *M. thermoacetica* and *A. woodii*. The presence of M+3 labeled acetate would indicate that methanol was not reduced first to formaldehyde (**Figure** 3-2). ^{13}C labeled methanol ($^{13}CH_3OH$) was used as a control to determine how much of the methyl group was incorporated into acetate.

After acclimitization, growth of *M. thermoacetica* and *A. woodii* were robust, and methanol consumption coincided with acetate production with yields approaching if not exceeding the theoretical yield (150%). The excess acetate could be derived from the yeast extract (YE) present at 0.5 $g\ L^{-1}$. Generally, *M. thermoacetica* grew at faster rates, but to lower optical densities. Furthermore, despite the same inoculum for each set of substrates (un-labeled vs. labeled methanol), there were statistically significant differences in growth. This could be related to the kinetic isotope effect [170, 217].

At mid-log phase (approximately when acetate concentrations reached 25 mM),

the supernatant was diluted and then the acetate was derivatized and measured on an LC-MS-MS. The ^{13}C methanol labeled 40% of the acetate in carbon in *M. thermoacetica* (Moth $^{13}CH_3OH$), which may seem surprising based on a stoichiometry of 4 methanol and 2 CO_2 per acetate (**Equation** 3.1 and **Figure** 3-4). Instead, one mole of methanol was oxidized to CO_2 and would not likely be incorporated back into acetate due to dilution with unlabeled CO_2 (**Equations** 3.4 and 3.5) [105]. Therefore, the theoretical labeling pattern would be 50% or less; the discrepancy can be related to the reversibility of the WLP steps as seen in the deuterium labeled acetate. Moreover, some un-labeled acetate was present upon inoculation of these cultures.

$$CH_3OH \rightleftharpoons CO_2 + 6\ e^- \tag{3.4}$$

$$3\ CH_3OH + 3\ CO_2 + 6\ e^- \rightleftharpoons 3\ \text{Acetate} \tag{3.5}$$

Deuterated methanol was incorporated substantially as M+3, as well as M+2 and M+1 for both organisms. This indicates that the 3-component methyltransferase system plays a role in methanol metabolism for both *M. thermoacetica* (MoTh CD_3OD) and *A. woodii* (Acwo CD_3OH), not methanol dehydrogenase. The presence of M+1 and M+2 has two possible causes. The first and likely explanation would be the reversibility of the WLP; based on the equations presented above, the WLP must operate in reverse for the generation of 6 electrons. Alternatively, if there was activity from a methanol dehydrogenase, M+1 isotopes would be enriched. While this possibility can not be refuted, we have verified that the methanol was assimilated at the methyl level by these organisms; likely this is catalyzed by the 3-component methyltransferase that has been hypothesized in literature [144].

The cause for differences in labeling between *M. thermoacetica* and *A. woodii* was not clear. Assuming the absence of methanol dehydrogenase activity, the likely cause was differences in the fluxes of methanol oxidation to CO_2 versus assimilation into acetate. This could be resolved with flux balance analysis of the WLP. For *A. woodii*, the substantial labeling of acetate as M+3 and greater than 50% labeling

overall could indicate another source of reducing equivalents provided in the culture, as less methanol was reduced to CO_2 than required (**Equations** 3.4 and 3.5). Perhaps cysteine served as the reducing source, however this was not experimentally verified.

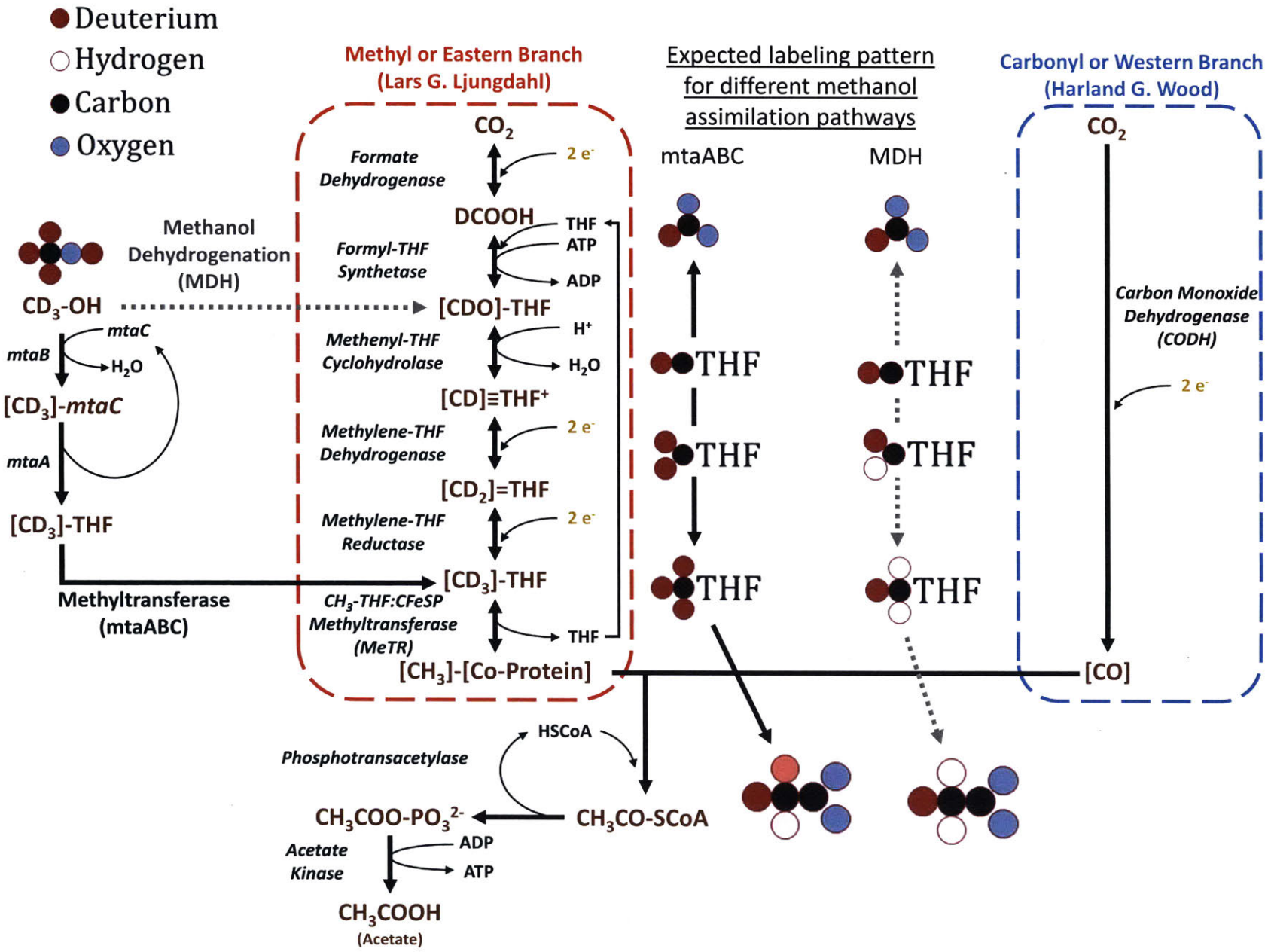

Figure 3-2: Depending on the mechanism of methanol assimilation, acetate will have different levels of deuteration. For MtaABC, there is expected to be a mixture of M+3 to M+0 labeling depending on the reversibility of the WLP. If MDH oxidizes methanol to formaldehyde, only M+1 or M+0 labeling should be possible.

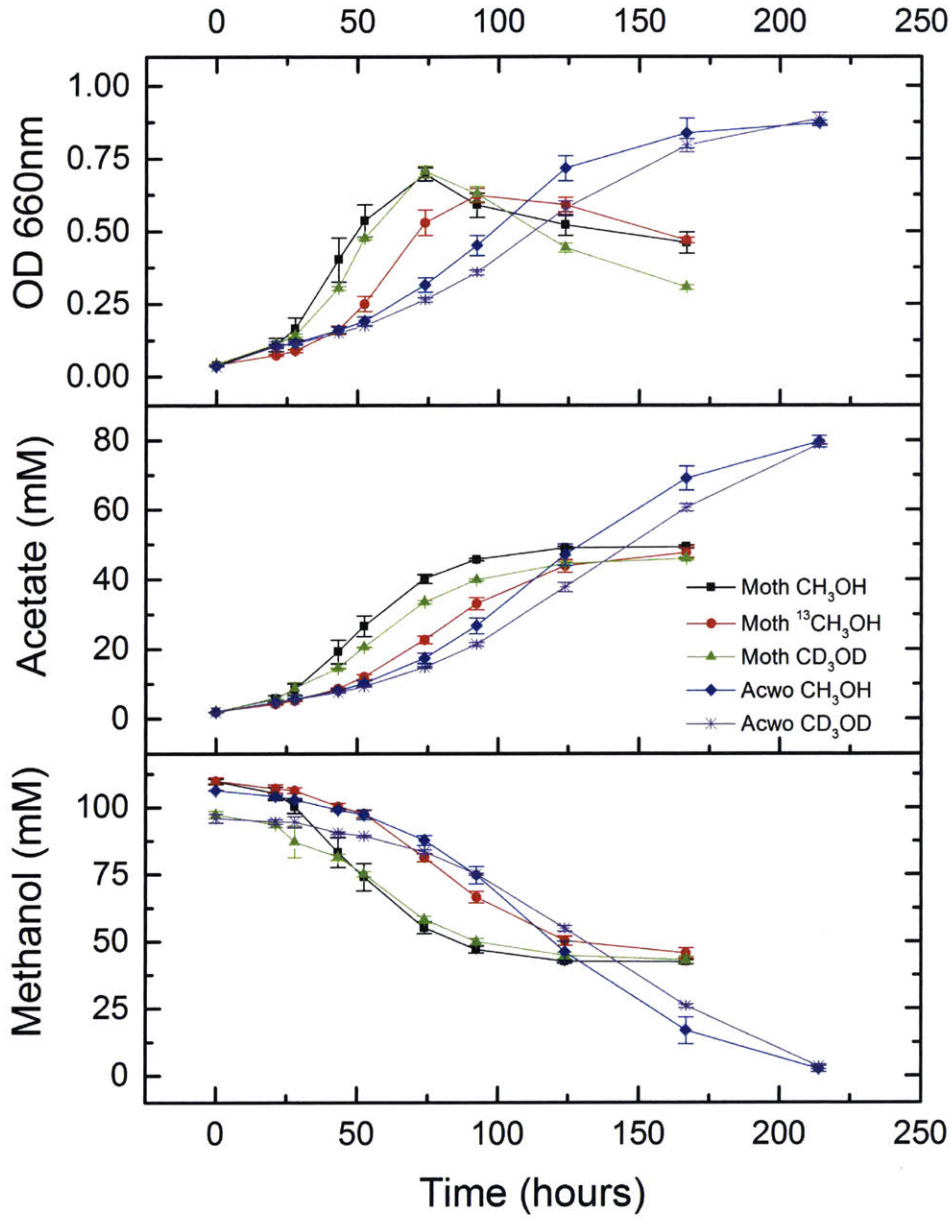

Figure 3-3: Growth of *M. thermoacetica* and *A. woodi* on un-labeled and labeled methanol. Black square, *M. thermoacetica* CH_3OH; red circle, *M. thermoacetica* $^{13}CH_3OH$; green triangle, *M. thermoacetica* CD_3OD; blue diamond, *A. woodii* CH_3OH; purple asterik, *A. woodii* CD_3OD. Standard deviation given for biological triplicates.

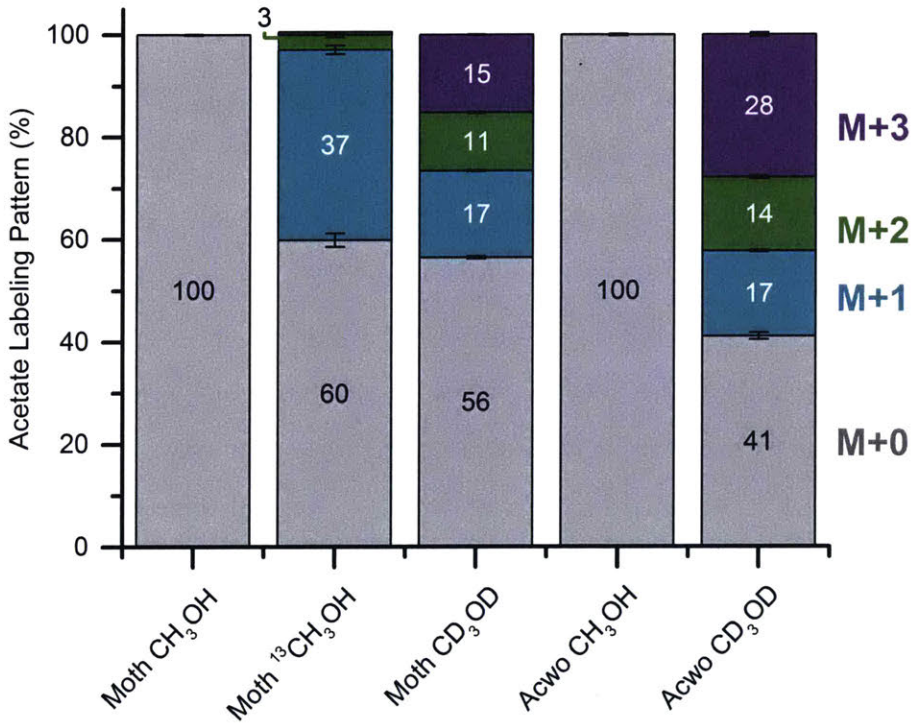

Figure 3-4: Labeling pattern of acetate when *M. thermoacetica* and *A. woodi* were grown on un-labeled and labeled methanol. Gray, M+0; blue, M+1; green, M+2; purple, M+3. Standard deviation given for biological triplicates.

3.3 Identification of putative methanol methyltransferases with RNAseq

While production of acetate from methanol was highly efficient, other products could add greater value to this process, and would create a larger incentive for CO_2 fixation. However this would require genetic engineering. While transformation protocols have been reported for *M. thermoacetica* [136, 91, 92], our lab has not been successful in replicating their protocol reproducibly [62]. Instead, the genes responsible for methanol assimilation could be expressed in a similar acetogen with a more tractable genetic tools such as *C. ljungdahlii* [94].

When *M. thermoacetica* was originally sequenced, most of its metabolic pathways were putatively annotated, including those involved in methanol and vanillate consumption [144]. However, putative annotations are often wrong, and so we wished to verify or determine those genes involved in methanol metabolism. To do this, *M. thermoacetica* was grown on glucose (5 $g\ L^{-1}$) or methanol (100 mM) in media containing 0.1 $g\ L^{-1}$ YE. RNA was harvested at mid-log phase (**Figure** 3-5) and transcript abundance was determined with RNAseq.

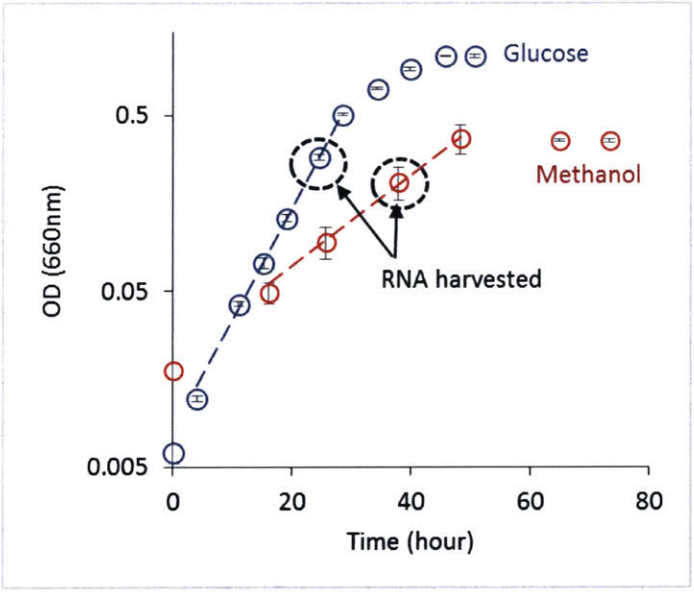

Figure 3-5: Growth of *M. thermoacetica* for RNA extraction. Blue, glucose; red, methanol. Standard deviation given for biological triplicates.

When methanol and CO_2 were the sole carbon substrate, those genes involved in methanol metabolism and the WLP would likely be up-regulated, thus providing higher translation of those enzymes. For instance, while the WLP was in operation during growth on glucose, the WLP played a far more important role when the substrate was methanol. This can be seen in two genes involved in the WLP, CODH and AcCoA synthase (Moth_1202, 1203); transcript levels increased by 4 fold in the presence of methanol (**Figure** 3-6).

The annotated *mtaB* (Moth_1208) and *mtaC* (Moth_1209) were also highly upregulated by methanol, and had high expression in an absolute sense (12,000 and 16,000 FPKM or fragments per kilobase of transcript per million reads). Conversely, the annotated *mtaA* genes (Moth_1447, 2100, 2102, 2346) had small fold increases in expression (3.3) and were barely expressed (200 FPKM). This suggests that these genes were not responsible for methanol metabolism. Other methyltransferases may instead catalyze the final methyl transfer of mtaA, such as Moth_2115 or 2116. These were both upregulated 22-fold and 29-fold, respectively, and had expression levels of 3,600 and 4,700 FPKM. Future experimentation would be necessary to verify the metabolic role of these enzymes by expression in *E. coli* or *C. ljungdahlii*, and verification with in vitro assays. Similar assays have been performed with the methyltransferases of *M. barkeri* expressed in *E. coli* [205, 206, 207].

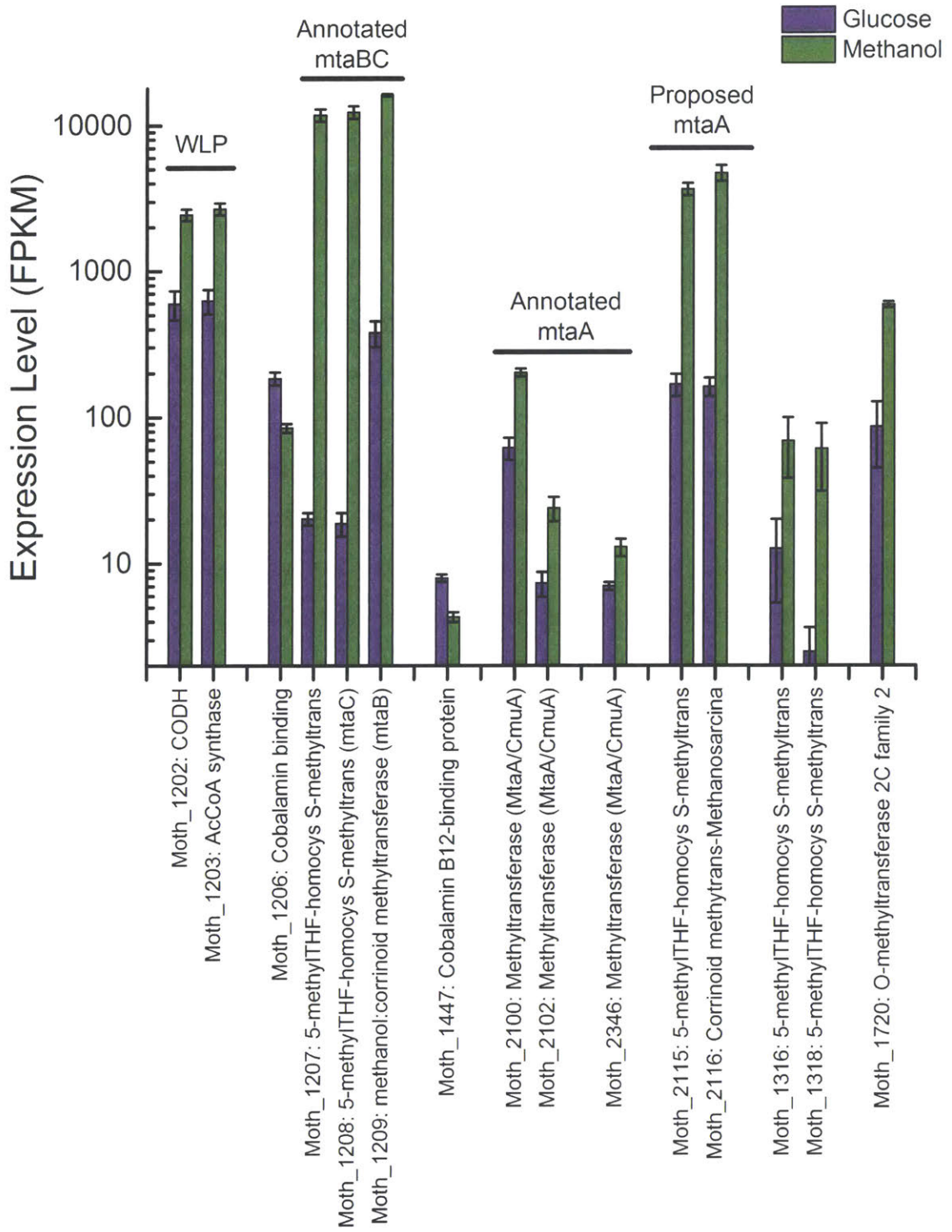

Figure 3-6: Transcript abundance of methyltransferase genes in *M. thermoacetica* grown on methanol versus glucose. Purple, glucose; green, methanol. FPKM, fragments per kilobase of transcript per million reads. Standard deviation given for biological triplicates.

3.4 Improving acetate productivity and titers from methanol

While growth on methanol was robust and reached higher optical densities than growth on gases, these optical densities and growth rates were still lower than that of sugars. Indeed, the per cell productivities were sufficient, yet biomass accumulation was not. For this reason, we explored some simple methods to improve biomass titers.

Preliminary work during cultivation for methanol labeling and RNA extraction was conducted with 0.1 $g\ L^{-1}$ YE and resulted in growth to approximately 0.658 $\pm$ 0.023 OD_{660nm} (*M. thermoacetica*, **Table** 3.1). When YE was removed entirely, optical density and acetate titer dropped to 0.538 OD_{660nm} and 30.8 mM, respectively (**Figure** 3-7**A**). pH adjustment and feeding of methanol in a stirred tank bioreactor did not drastically alleviate the low titers (**Figure** 3-7**B**).

By increasing the YE concentration to 0.5 $g\ L^{-1}$, adjusting the pH in late log phase, and feeding methanol, optical density and acetate titers approached 1 OD_{660nm} and 60 mM (**Figure** 3-7**A**). We next transitioned to a stirred tank bioreactor, as the changes in pH in late log phase could impact productivity and growth. The results, however were not promising as optical density was less, 0.574 OD_{660nm}, even though acetate concentration was slightly increased at 63.6 mM (**Figure** 3-7**B**).

We then transitioned to introducing nutrient supplements (YE) to improve growth and productivity, as most researchers use upwards of 10 $g\ L^{-1}$ when cultivating these organisms to high optical densities [218, 28]. While this would not be industrially feasible due to costs, it provides a metric for what could be possible. Future media optimization would then remove the YE while maintaining high titers and productivities [97]. For instance, key amino acids can be supplemented instead [219].

Adding YE substantially improved maximum optical density to 1.48 $\pm$ 0.08 OD_{660nm}, and acetate titers reached 147 $\pm$ 12 mM, a 2.4-fold increase (**Figure** 3-7**C**).

To account for the YE that was used to grow and produce acetate, a 'no methanol' control was included, the result of which was surprising. In the absence of methanol, there was virtually no growth or acetate production. Acetate reached titers of only

7.7 ± 0.1 mM, whereas yeast extract at 10 $g\ L^{-1}$ could provide atleast 300 mM C (**Table** 2.1). This indicated that YE served as a source of secondary metabolites and cellular building blocks such as amino acids; *M. thermoacetica* did not metabolize the YE as a source of ATP synthesis.

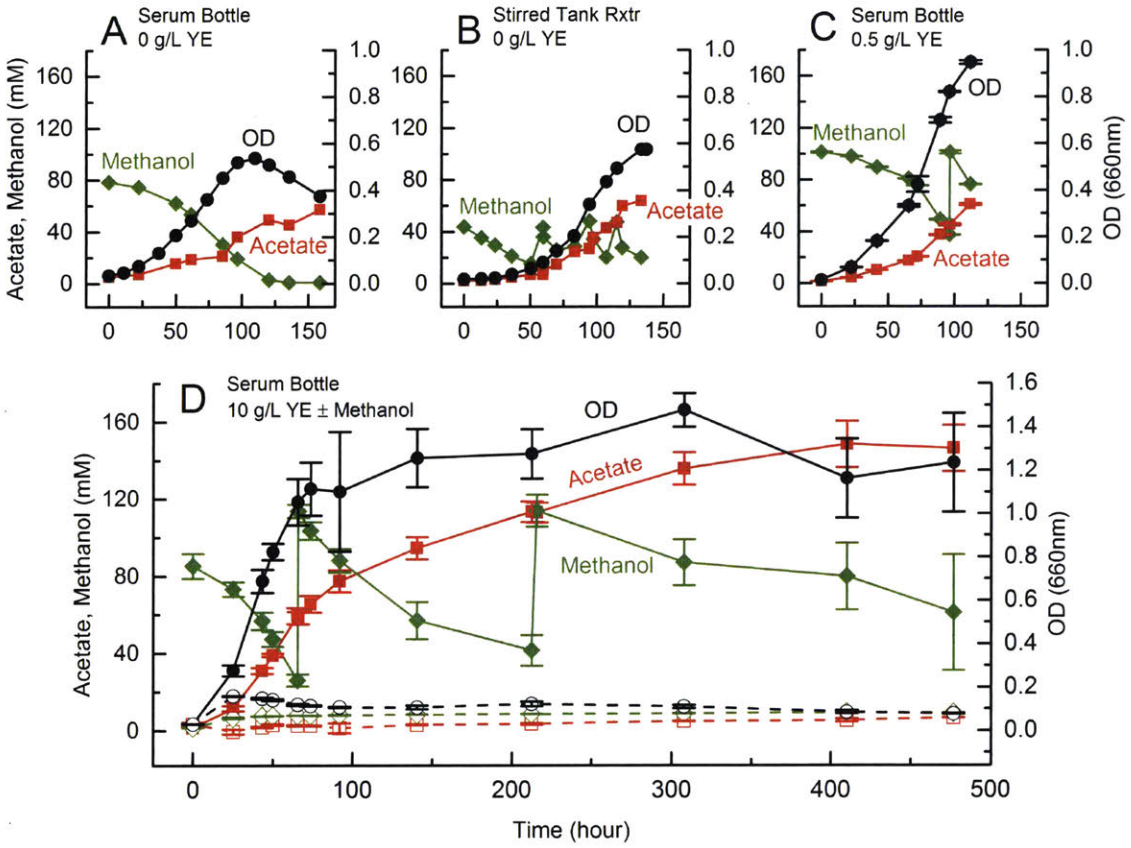

Figure 3-7: Growth of *M. thermoacetica* on methanol and production of acetate. The cultivation environment and nutrient supplements were varied to increase biomass and acetate titer. (A) serum bottle, 0.5 $g\ L^{-1}$ YE. (B) stirred tank reactor, 0.5 $g\ L^{-1}$ YE. (C) serum bottle, 10 $g\ L^{-1}$ YE, with and without methanol; pH adjusted to 6.8 after each addition of methanol. Standard deviation given for biological duplicates (A) and triplicates (C).

3.5 Conclusion

The mechanism and the genes involved in methanol metabolism in acetogens was not completely understood and there were conflicting reports in the literature on how methanol was metabolized in *M. thermoacetica*. Here we've verified that methanol is

Table 3.1: Max optical density, methanol consumption, acetate secretion, and carbon yield

Experiment	**Figure**	**Max OD_{660nm}**	**Methanol (mM)**	**Acetate (mM)**	**Carbon Yield (%, Acetate per Methanol)**
Moth CH_3OH 0.1 $g\ L^{-1}$ YE	3-3	0.658 ± 0.023	67.3 ± 1.1	47.4 ± 0.5	141 ± 3
Moth $^{13}CH_3OH$ 0.1 $g\ L^{-1}$ YE	3-3	0.584 ± 0.026	64.1 ± 2.3	45.7 ± 1.5	142 ± 7
Moth CD_3OD 0.1 $g\ L^{-1}$ YE	3-3	0.663 ± 0.018	54.2 ± 1.9	43.9 ± 0.3	162 ± 6
Acwo CH_3OH 0.1 $g\ L^{-1}$ YE	3-3	0.837 ± 0.010	103.8 ± 1.1	77.7 ± 1.6	150 ± 4
Acwo CD_3OD 0.1 $g\ L^{-1}$ YE	3-3	0.854 ± 0.020	92.5 ± 2.0	77.0 ± 1.1	166 ± 4
Serum 0 $g\ L^{-1}$ YE	3-7A	0.538	77.5	52.0	134
Reactor 0 $g\ L^{-1}$ YE	3-7B	0.574	—	63.6	—
Serum 0.5 $g\ L^{-1}$ YE	3-7C	0.947 ± 0.008	88.7 ± 1.2	59.5 ± 0.9	134 ± 3
Serum 10 $g\ L^{-1}$ YE + Methanol	3-7D	1.48 ± 0.08	166 ± 15	147 ± 12	178 ± 8
Serum 10 $g\ L^{-1}$ YE - Methanol	3-7D	0.123 ± 0.011	—	7.7 ± 0.1	—

incorporated into the WLP at the methyl- level through $^{13}CH_3OH$ and CD_3OD labeling in *M. thermoacetica* and *A. woodii*. The distribution between the various isotopes (M+3 to M+1) was an indication of how reversible the WLP was in both acetogens. Most of the labeling was recovered (44% and 59%), as compared to the theoretical expectation (50%). The M+3 percentage was much higher in *A. woodii* than *M. thermoacetica*, and the overall labeling was higher than theoretically possible. The reason for this was unknown. RNAseq data from *M. thermoacetica* showed that the methyltransferases *mtaBC* were correctly annotated, and *mtaA* was incorrectly annotated, when the genome was originally sequenced. Generally the fold change and overall transcript abundance was low when grown on methanol vs. glucose. Of the other annotated methyltransferases, Moth_2115 and 2116 were both highly up-regulated in the presence of methanol. Hence, these were proposed to likely serve the metabolic function of MtaA. Increasing the growth rates and titers was desirable. Preliminary experiments indicated that yeast extract had the largest impact on titer and acetate productivity, as compared to increasing key vitamins and minerals. However yeast extract would be undesirable within industrial processes, and hence a more in depth media optimization must be conducted to eliminate yeast extract, while maintaining high titers and yields.

3.6 Materials and Methods

3.6.1 Bacterial, media, and culture conditions

M. thermoacetica and *A. woodii* were grown in the media and culturing conditions presented in **Section** 2.9.2, with the following modifications: yeast extract was present in the media at 0.5 $g\ L^{-1}$, unless otherwise stated, and the gas headspace was charged with pure CO_2.

3.6.2 Metabolite analytical methods

The methanol and acetate were measured as discussed in **Section** 2.9.4.

3.6.3 Methanol labeling, derivatization of acetate, and measurement by LC-MS

Labeled methanol was aquired from Cambridge Isotopes (Tewksbury, MA). Labeled acetate was derivatized and measured via LC-MS as discussed in **Section** 2.9.5.

3.6.4 RNA extraction and sequencing

RNA was extracted and sequenced with the protocol in **Section** 2.9.6.

3.6.5 Methanol bioreactor operation

A 1 L reactor was run with a 0.5 L culture volume at a temperature of 55^{o}C and an impeller speed of 200 RPM. YE was excluded from the media. The pH was controlled at 6.6 by feeding of 5 M HCl. Anaerobic CO_2 was sparged into the reactor at a flow rate of approximately 100 sccm to maintain anaerobicity. Methanol was periodically added to maintain a concentration between 60 and 20 mM.

Chapter 4

Theoretical Analysis of Natural Gas Recovery from Marginal Wells with a Deep Well Reactor

Portions of this chapter were first modeled in [220] **and later expanded in** [221].

Technology plays a key role in gas fixation. As most gases are sparingly soluble in liquid, transfer of that gas into the liquid phase is non-trivial. Moreover, high conversion of that gas in biological processes is generally not considered, as the gas being transferred is oxygen. Any un-used gas can be directly vented to the atmosphere after filtration.

Waste gas fermentation is different. Instead, high conversions are desired, while maintaining industrially relevant flow rates and productivity. If possible, capital costs should also remain low if the product is fuel.

The following chapter analyzes a theoretical reactor design for the conversion of methane into fuels or chemicals. The goal was determine if such a design could be used for small scale gas-to-liquid conversions, and what reaction rates would be required for biological and inorganic catalysts.

Current natural gas harvesting technologies are only economically viable at high gas flow rates. Subsequently, a significant quantity of gas remains unused in aban-

doned wells. Methanotrophic organisms are under development to capitalize on this resource given their preference for ambient conditions, however capital and methane mass transfer costs must be minimized. We propose using the well as the bioreactor negating capital costs, and leveraging the gas pressure for mass transfer. We evaluated the Deep Well Reactors feasibility by developing mathematical models that simulated mass transfer and explored how operating parameters impacted ethanol production. The results showed sufficient mass transfer for 100% conversion, despite minimal complexity. Current aerobic methanotrophs and inorganic catalysts could provide sufficient reaction rates. Conversely, anaerobic methanotrophs rates must be improved by 1200-fold. With an appropriate catalyst, this technology allows the recovery of methane at flow rates an order of magnitude lower than current technologies.

4.1 Introduction

ONLY 30.3% of total worldwide natural gas reserves are proven, i.e. can demonstrate with reasonable certainty to be recoverable in future years from known reservoirs under existing economic and operating conditions" [56]. As the majority of reserves are currently inaccessible, developing new cost-effective technologies to harvest them is important[222, 223]. Toward this aim, we focus here specifically on abandoned and marginal wells. Natural gas wells generally produce to the limit of economic feasibility, and are then capped and abandoned. At the time of abandonment, these so-called marginal wells have a flow rate of about 1869 $std\ m^3\ day^{-1}$ (or 66 $Mscf\ day^{-1}$)[57]. Extending the economic cutoff from $1.9x10^3$ to 187 $std\ m^3\ day^{-1}$ would increase the total gas harvested by 15% [57, 224, 225]. Further, with an estimated 2.3 million abandoned wells in the onshore U.S., (200,000 in Pennsylvania alone [226]), monetizing this gas is of great interest, as the infrastructure is in place, the wells have little economic value, and pose an environmental concern due to emissions [227].

Harvesting from such wells, which are too dispersed to be economically connected

to pipelines, is difficult because the low energy density of natural gas necessitates liquefaction or chemical conversion to a liquid prior to transportation; processes which are too expensive to be implemented for low-capacity wells. With liquefied natural gas (LNG), this cost is associated with large storage and regeneration facilities, incompatible with small or intermittent markets [228]. For chemical conversion, the Fischer-Tropsch gas-to-liquid (FT-GTL) process is a mature technology, but has historically been complex, capitally intensive, and only viable at the largest scale [23, 229] and comparatively high oil prices. For example, FT-GTL projects in the US have been placed on hold, including those from Shell [230] and Sasol [231] due to the precipitous drop in oil prices at the end of 2014, from $ 100 (Sept 2014) to $34 per bbl (Jan 2016). Development of miniaturized FT-GTL technologies that reduce the capital cost of conversion has surged in importance for these reasons [17], yet many of these solutions currently require flow rates in excess of $2.8x10^4\ std\ m^3\ day^{-1}$ [16], an order of magnitude greater than those available in marginal wells. While tradition FT-GTL cannot process lower flow rates, biology may be able to fill this niche.

Methanotrophs have been proposed as an alternative to FT-GTL. One consideration for natural gas wells is the absence of oxygen. Even though aerobic methanotrophs are well studied, the energy required to operate a compressor for delivering sufficient air to the bottom of the Deep Well would cost at least 10% of the effective methane flow rate to generate. Hence, weve focused on anaerobic methanotrophs as they have also been proposed for harnessing methane from marginal wells [17, 232], and efforts are underway to enrich and purify the native consortia reponsible [27], understand the underlying biology [68, 69], and engineer organisms for anaerobic conversion of methane to targeted compounds [84, 233]. This analysis can later be extended to include aerobic methanotrophs. While bio-GTL has the benefit of a higher theoretical efficiency and product selectivity, there are key operational limitations. In many biological systems, the slow transfer of a gaseous substrate to the liquid phase limits the overall process rate [234]. The power input required to achieve this mass transfer is also significant; this is about $1\ kW\ m^{-3}$ for standard reactors [235], corresponding to 13% of the energy input from the effective methane flow rate

in this case study. To reach economic viability, Bio-GTL must achieve significantly higher transfer rates at minimal power input and reactor cost. One such method is to use the pressure of the gas at the bottom of the well to enhance mass transfer, by using the existing well casing as the bioreactor. In addition to reducing the power requirement, this could also decrease the capital expense by reducing material costs.

To evaluate the feasibility of this approach, we constructed a preliminary mathematical model of a small scale GTL reactor which utilizes the wells pre-existing concrete structure as a high aspect ratio bubble column reactor (BCR) for conversion into liquid fuels or chemicals. By utilizing a pre-built structure, otherwise abandoned, much of the capital cost can be relegated while maintaining a high reactor volume. As we are most interested in the application of this technology to marginal wells, we chose for this case study a gas production rate of 1869 $std\ m^3\ day^{-1}$ (F_{Std}), the current cut-off for a marginal well. This results in an effective flow rate two orders of magnitude smaller than other small scale FT-GTL systems mentioned previously [16, 236]. In comparison to other BCR models, our model is different in two key ways: First, the high aspect ratio of this system imposes a significant pressure gradient from top to bottom, whose impact on the mass transfer rate must be accounted for. Second, the potency of methane as a greenhouse gas [227] requires its complete conversion in the reactor. This is typically not required in the design of BCRs because of the energy input required to reach such transfer rates [58]. We therefore use the model to assess the attainable mass transfer rates, to determine the biological reaction rate required to fully convert the methane, and to calculate the associated reactor productivity. We conclude with an assessment of how achievable these rates are, and how this affects the feasibility of the proposed reactor system.

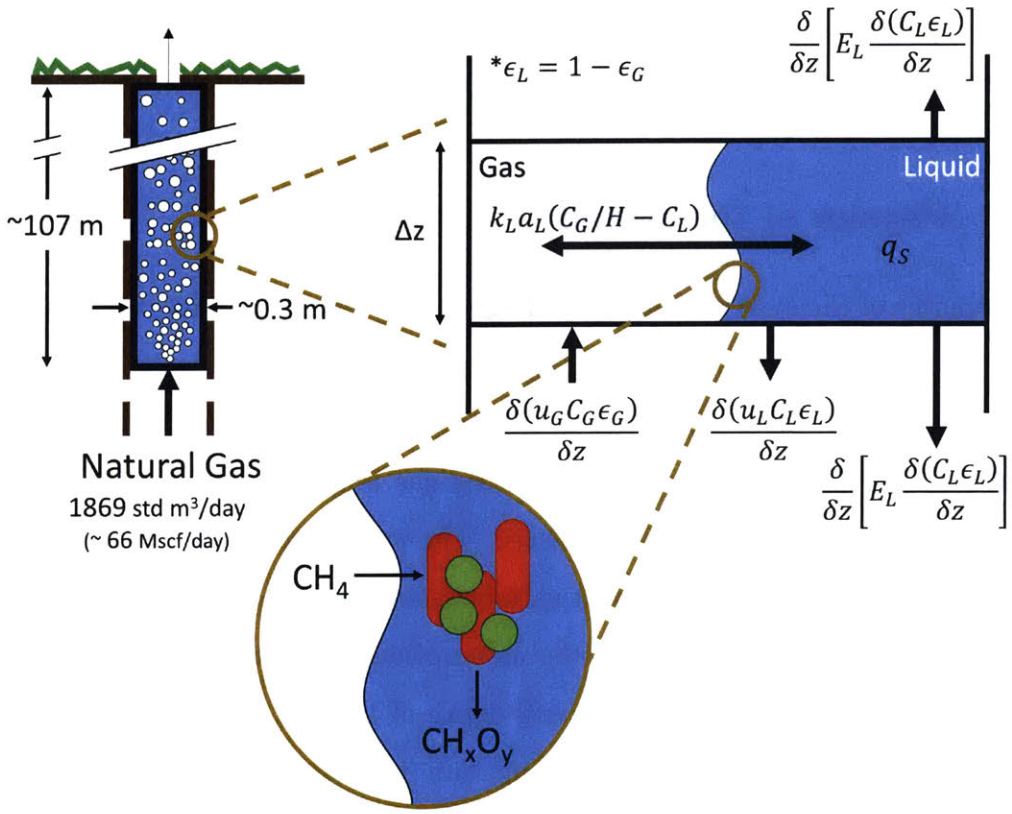

Figure 4-1: Geometry of the Deep Well Reactor bubble column. In the case study, the diameter was 0.305 m and the length was 107 m. The inset depicts a discreet element of the gas and liquid phase where gas rises through the column, is transported into the liquid phase, and reacts by biological or inorganic catalysts. The terms acting on each phase are shown along with arrows to indicate directionality, but not magnitude. The base case flow rate was 1869 $std\ m^3\ day^{-1}$ at 1.14 MPa.

4.2 Model Development

The performance of the Deep Well Reactor was modeled and simulated under different conditions with gas and liquid phase differential mass balances with MATLAB®. Mass transfer between these phases was modeled by the two film theory. Due to the length of the column, a hydrostatic pressure gradient is imposed along the column. In the base case, the inlet gas is assumed to be pure methane. All variables are defined at the end of the article.

4.2.1 Physics of the system

The geometry of the system is shown in **Figure** 4-1, where a pre-existing natural gas well is used as a reactor by installing a faceplate and sparger at the desired depth within the column. The maximum height of the water column (**Equation** 4.1) is specified by the well bottom pressure, as the gas pressure must always be greater than that of the liquid hydrostatic pressure. The well bottom pressure for a depleted well is calculated from standard well variables, including a well bottom pressure of a marginal well approximated from the assumption of an initial well head pressure of 9.798 $kPa\ m^{-1}$ [237], a maximum well depth of 1600 m, a well diameter of 0.305 m, and initial flow rate of $2.8x10^4\ std\ m^3\ day^{-1}$ at the time of initial production [238]. By relating flow rate and pressure with Darcys law, the initial pressure would decrease from 15.68 MPa to P = 1.14 MPa at a flow rate of 1869 $std\ m^3\ day^{-1}$. Here standard temperature and pressure are defined as 288.15 K and 101.325 kPa. The diameter of the well plays an important role as this cannot be modified in the field and greatly affects the reactor volume, as seen in **Section** 4.3.5.

$$L = \left[\frac{P - P_a}{\rho_L g}\right]\left[\frac{101325\ Pa}{1\ atm}\right]\left[\frac{\frac{kg}{m\ s^2}}{Pa}\right] = 107m \tag{4.1}$$

The flow rate of gas through the liquid is defined by the gas hold-up (ϵ_G), hence decreasing the flow rate through the column from 1869 $std\ m^3\ day^{-1}$ to an effective flow rate of only 152 $std\ m^3\ day^{-1}$. As the gaseous phase rises through the column,

methane is transported to the liquid phase based on the conservative Akita model [239, 240], where it is consumed at a specified uptake rate (q_S). In determining the productivity of the system, ethanol is used as a model compound. While other fuel molecules with better properties could be envisioned, the choice here is arbitrary as the goal of this work is to explore the mass transfer potential of the system.

4.2.2 Modeling design equations

The model equations detail a dynamic continuous reactor system in both liquid and gas phases. The set of design equations are given below as **Equations** 4.2 to 4.4. **Equation** 4.2 defines the pressure gradient, implying that the gas concentration is linear and at a pseudo-steady state. This does not imply that the total flow rate of gas is independent of time. **Equation** 4.3 is the gas phase mass balance, including convective and mass transfer terms. **Equation** 4.4 is the liquid phase mass balance and includes reaction (r_L) along with convection and mass transfer. Empirical models, described in the following sections, were used to determine the gas holdup and mass transfer coefficient (**Equation** 4.10 and 4.11). The effect of back mixing by dispersion (E_L) in **Equation** 4.6 was ignored because of its negligible effect due to the high aspect ratio, as discussed in **Section** 4.2.3. The generalized reaction rate (r_L) is defined as a value averaged throughout the system (q_S), and not dependent on methane concentration since such dependencies are unknown at this time. The reaction rate is defined so as to not exceed the maximal mass transfer rate (**Equation** 4.5).

$$C_G = \frac{P_a}{RT} + \frac{\rho_L g}{RT}(L - z) \tag{4.2}$$

$$\frac{\delta(C_G \epsilon_G)}{\delta t} = -\frac{\delta(u_G C_G \epsilon_G)}{\delta z} - k_L a_L \left(\frac{C_G}{H} - C_L\right)(1 - \epsilon_G) \tag{4.3}$$

$$\frac{\delta(C_L(1 - \epsilon_G))}{\delta t} = -\frac{\delta(u_L C_L(1 - \epsilon_G))}{\delta z} + \left[k_L a_L \left(\frac{C_G}{H} - C_L\right) - r_L\right](1 - \epsilon_G) \tag{4.4}$$

$$r_L = \begin{cases} q_S & \text{if } C_L > 0 \\ k_L a_L \frac{C_G}{H} & \text{if } C_L = 0 \end{cases} \tag{4.5}$$

More complicated models have been used in the past, incorporating bubble size distributions in a computational fluid dynamic model for different flow regimes [241]. However, this added complexity is not expected to greatly increase accuracy because the gas holdup and mass transfer coefficient empirical equations used here were developed over a wide range of conditions including homogenous and heterogeneous bubble flow regimes, as determined from the expected transitional superficial velocity [240, 242].

4.2.3 Back mixing

The complete mass balance within the liquid phase is presented as **Equation** 4.6. **Equation** 4.6 differs from **Equation** 4.4 by including the back mixing term, E_L. Solving **Equation** 4.6 would be computationally expensive, unless back mixing could be neglected. The back mixing term (E_L) is empirically related to diameter and superficial gas flow rate, and generally depresses the liquid methane concentration at the bottom of the well due to desorption. For the conditions in the base case with a batch liquid phase, the $k_L a_L$ dominates over that of back mixing because of the large aspect ratio (350:1) and low flow superficial flow rate (u_G). For these reasons, back mixing has been neglected in this study as discussed in below.

$$\begin{aligned} \frac{\delta\left(C_L\left(1-\epsilon_G\right)\right)}{\delta t} = & -\frac{\delta\left(u_L C_L\left(1-\epsilon_G\right)\right)}{\delta z} + \left[k_L a_L\left(\frac{C_G}{H} - C_L\right) - r_L\right]\left(1-\epsilon_G\right) \\ & + \frac{\delta}{\delta z}\left[E_L \frac{\delta\left(C_L\left(1-\epsilon_G\right)\right)}{\delta z}\right] \end{aligned} \tag{4.6}$$

Mixing of the liquid phase can have an important contribution to the reactor dynamics, through various phenomena including turbulent vortices, liquid entrainment by rising bubbles, liquid circulation, etc. To account for this, a simple axial dispersion model (ADM) has been incorporated into the model equations. ADM is appropriate

for tall columns [243] and is widely used when computational fluid dynamic simulation is undesirable due to complexity and costs. ADM is a semi-empirical model accounting for longitudinal diffusion of the gas (E_g) and liquid (E_L). Semi-empirical laws are available to estimate these coefficients (**Equation** 4.7 and 4.8); while feasible in many cases, there is uncertainty whether such models will correctly predict this phenomena [240]. These coefficients appear in the system design equations (**Equation** 4.6).

$$E_L = 0.35\ D^{\frac{4}{3}}\ (g u_G)^{\frac{1}{3}} \tag{4.7}$$

$$E_G = 50\ D^{\frac{3}{2}}\ (u_G)^{\frac{1}{3}} \tag{4.8}$$

Back mixing by diffusivity in the gas phase (E_G) can be neglected when the Bodestein number (**Equation** 4.9) is greater than 10, and the gas phase can be approximated as plug flow [240]. This assumption is valid for this case study as $Bo = 93$, due to the height of the column which is greater than 100 m.

$$Bo = \frac{u_G L}{\epsilon_G E_G} \tag{4.9}$$

The model equations are computationally expensive, particularly when back mixing is included (E_L), partially due to an incomplete set of steady state boundary conditions at the well bottom including the liquid concentration of methane (C_L). Hence model simplification was desired, where appropriate, so that the important parameters can be tested and analyzed. This simplification centers around two major regimes, the ideality of longitudinal mixing (back mixing coefficient, E_L) and whether the liquid phase operates in continuous mode (liquid velocity, u_L). To determine the importance of back mixing, we compare whether the back mixing terms plays an important role in comparison to that of the mass transfer term. On the other hand, the operation of the liquid phase continuously is an operational decision that usually centers on productivity and economics. We show that under the base case conditions, non-ideal back mixing in the deep well bioreactor is negligible due to the high aspect ratio of the reactor. Furthermore, the feasibility of a continuous liquid phase is shown

to be dependent on economics, as there is no major change in productivity.

The second derivative term for back mixing results in the greatest increase of computational complexity when solving **Equation** 4.6, if only because the steady state boundary conditions are not known a priori. This is due to the possibility of desorption of methane from the liquid phase in the case that an element of liquid has a greater concentration than that of the saturated element as calculated from Henrys law. Take for instance a batch non-reacting system, under ideal conditions (no back mixing), the liquid concentration profile (C_L) coincides with that of saturation. When the back mixing term is included, this no longer holds true, and the liquid concentration at the inlet is depressed due to desorption. This effect is negligible in the base case and only becomes important if the mass transfer coefficient is depressed by at least 100 fold (**Figure** 4-2). Similarly, increasing the liquid phase reaction rate (r_L) will have the same effect, compounding with the mass transfer term. Physically this implies that, despite desorption, the high mass transfer term is able to transfer the methane back to the liquid phase. Two main phenomena contribute to this; first gas expansion within the column maintains a high gas hold up, and thus a high $k_L a_L$. Second, the one component assumption helps maintain a very high driving force throughout the column. The effects of having other inert compounds is explored later with a simpler system. For these reasons, the second derivative back mixing term is expected to negligibly affect the base case system. Hence, the back mixing term is not included for the subsequent results.

4.2.4 Gas hold up and transition between flow regimes

Most bubble column models have been applied to systems with aspect ratios of approximately 5 and use depth averaged values. Here, the aspect ratio is approximately 350. Consequently, many parameters must be considered as functions of depth within the column, including the superficial velocity (u_G) and gas hold-up (ϵ_G); furthermore, flow regimes may also change as a function of height. To account for this, correlations from literature are used that can account for these variations. The one presented in **Equation** 4.10 was developed by Akita from a system with an aspect ratio of 26,

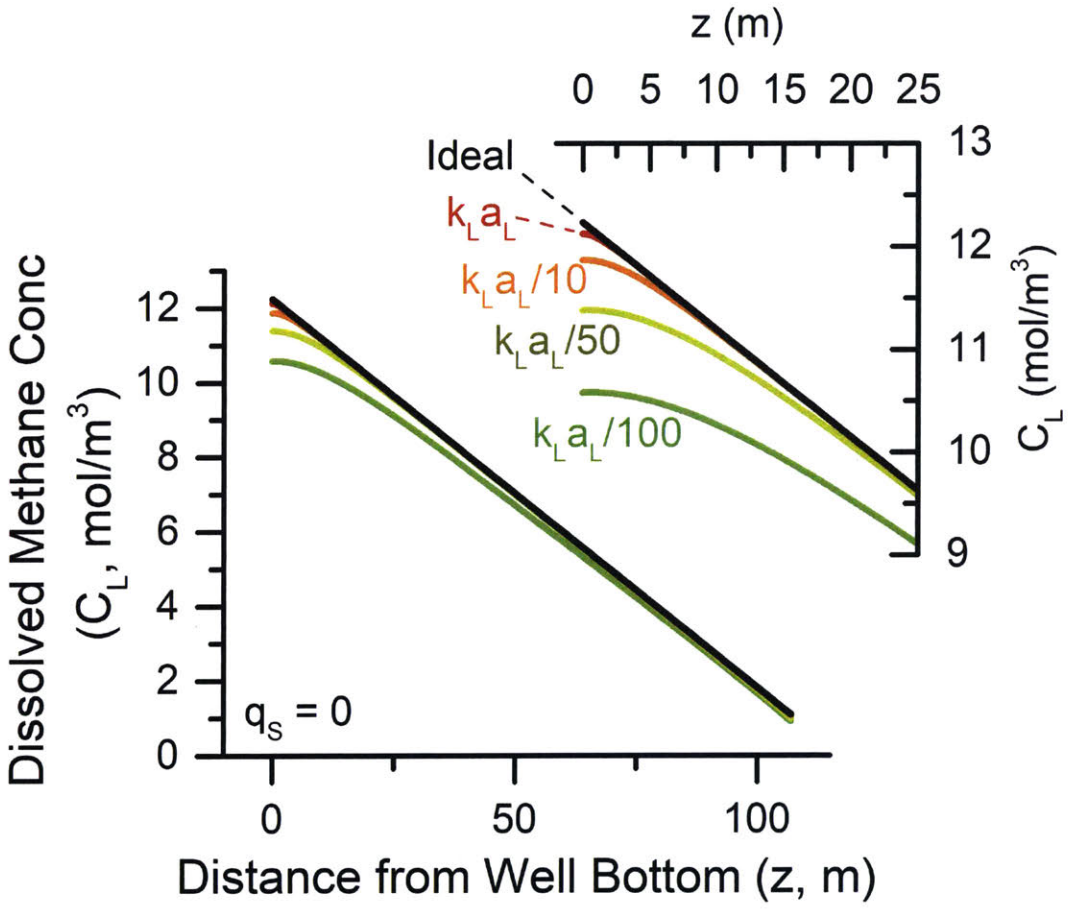

Figure 4-2: Liquid concentration profiles in the Deep Well Reactor when modeled with back mixing but no liquid phase reaction and no liquid flow rate (inset highlights the bottom 25 m of the column). Different curves represent the ideal reactor (black, no back mixing), and the real reactor with varying degrees of mass transfer. Mass transfer was artificially reduced by 1 (red), 10 (orange), 50 (yellow), and 100 times (green) at each discretization. Model approaches steady state after approximately 5 hours (model time).

a single 5 mm hole gas sparger [239] and generally provides a conservative estimate of gas holdup [241]. While Akitas model (**Equation** 4.10) does not explicitly differentiate between bubble flow regimes, the model was developed under laminar and turbulent gas flow regimes, as accounted for with the denominator to the fourth power. While there is a discrepancy in aspect ratio between Akitas model and this case study, extrapolation is possible. One can imagine multiple Akita columns stacked in series creating discreet elements that are accurately modeled. As the volume of an individual discreet reactor decreases, the resulting model approaches that of the differential balance presented in this study.

$$\frac{\epsilon_G}{(1-\epsilon_G)^4} = 0.25\left(\frac{D^2\rho_L g}{\sigma}\right)^{\frac{1}{8}}\left(\frac{D^3\rho_L^2 g}{\mu_L^2}\right)^{\frac{1}{12}}\left(\frac{1}{Dg}\right)^{\frac{1}{2}} u_G \tag{4.10}$$

Due to variations of gas flow rate and pressure within the column, gas flow regimes may vary with height. To differentiate between the flow regimes, Krishna et. al. developed a method to describe the transition from bubble flow (homogenous) to churn turbulent regime (heterogenous) [244], as described in **Appendix** B.1.1.

4.2.5 Mass transfer coefficient

For the two film theory, mass transfer within the liquid phase film controls the rate of gas-liquid mass transfer [245]. This mass transfer rate can be further affected by reactions happening in that phase, as is the case for this system. However, since this is difficult to model, many researchers limit their studies to absorption models only, with the understanding that such models are more applicable to slow reaction models as is the case here. The mass transfer coefficient ($k_L a_L$) is defined by the liquid properties, solid concentration, gas sparger, and operating conditions. In particular, the gas sparger chosen can greatly influence the mass transfer at low superficial gas velocities ($< 0.15 ms^{-1}$) [243], which is the case for the base case model. Regardless, these effects arent considered here, in favor of a conservative empirical model tested at various temperatures, column diameters, and liquid and gas phases [242].

$$\frac{k_L a_L D^2}{D_{CH_4:L}} = 0.6 \left(\frac{D^2 \rho_L g}{\sigma_L}\right)^{0.62} \left(\frac{D^3 \rho_L^2 g}{\mu_L^2}\right)^{0.31} \left(\frac{\mu_L}{\rho_L D_{CH_4:L}}\right)^{0.62} \epsilon_G^{1.1} \tag{4.11}$$

The physical parameters of the system are calculated at the temperature (K) indicated, by curve fitting the data from CRC Handbook of Chemistry and Physics [246] or with published interpolations [247]. Density was fit using a second order polynomial with temperature, viscosity was fit with the Andrade equation [248], and surface tension found by interpolation [247]. Despite the depth of the well, these properties will remain approximately constant at these moderate pressure and temperatures. The equations for each physical property are found in **Appendix** B.1.2. Natural gas is predominantly methane (76 to 98%) [249, 250], with other gases primarily composed of longer hydrocarbons, CO_2, CO, N_2, and O_2. The effect of impurities on mass transfer is small and thus the feed is assumed to be pure methane, as discussed in **Section** 4.3.5. The diffusivity of methane was calculated from published experimental data [251, 252] and fit with an activation energy and pre-exponential factor (**Appendix** B.1.3) [251]. The Henrys Law coefficient was found from an empirical correlation for methane and water (**Appendix** B.1.4) [246]. The solubility of methane is higher in ethanol than water [253]; for simplicity the Henrys Law coefficient for water-ethanol mixtures is assumed to be that of pure water providing a conservative dissolved methane concentration. For this study, 328.15 K (55^oC) was chosen as this is the optimal growth temperature for *Moorella thermoacetica*, an organism currently of interest in our lab for gas-to-liquid bioprocessing [218, 28]. Temperature gradients within the ground determine the cost of maintaining this temperature. Since the focus of the paper is on mass transfer and reaction rate, the effects of the ground temperature are ignored and will be incorporated in future economic analysis.

4.2.6 Calculating Conversion for the Base Case

Reaction rates and mass transfer limits are best determined and understood for the steady state system ($\delta/\delta t = 0$) with a batch liquid phase ($u_L = 0$), resulting in **Equation** 4.12. The difference between a batch and continuous liquid phase, and the

presence of inert gases was deemed negligible, as discussed in the Results and Discussion, and **Section** 4.3.4 and 4.3.5. With the other terms deemed also negligible, reaction rate and mass transfer are balanced (**Equation** 4.13). Typically, the reaction rate is modeled using functions of concentrations (C_L) and these relationships can be important for accurately analyzing and scaling a reactor. For instance, biological systems are often modeled using the Monod equation [254]. Despite the benefit of such reaction models, they have not been incorporated in this analysis because they are unknown at this time. For this reason, the reaction rate term is generalized to an average volumetric reaction rate (q_S in **Equation** 4.5). This simplification is a shortcoming of the model, as there is high variation in liquid phase methane concentration along the vertical axis due to the high aspect ratio. Regardless, important information is still derived from such a model, laying the ground work for studying the feasibility of the technology and setting a base line volumetric reaction rate that must be achieved for stipulated reactor volumes or productivities.

$$\frac{\delta\left(u_G C_G \epsilon_G\right)}{\delta z} = -k_L a_L \left(\frac{C_G}{H} - C_L\right)\left(1 - \epsilon_G\right) \tag{4.12}$$

$$k_L a_L \left(\frac{C_G}{H} - C_L\right) = q_S \tag{4.13}$$

Assuming a one-component system, **Equation** 4.12 is integrated along the length of the column, generating **Equation** 4.14. Here, Z is the percent of methane transported to the liquid phase, and the volume of liquid can be substituted for the cross sectional area and integrated gas holdup. The molar flow rate of methane (i) and uptake rate (j) are next normalized to their maximal values (**Equation** 4.15 and 4.16), where $F_{G,max}$ is the maximum achievable molar flow rate in the column and $q_{S,max}$ results in 100% transfer at the maximum flow rate.

$$Z = \frac{F_{G0,mol} - F_{G,mol}}{F_{G0,mol}} = \frac{q_S A \int_{z=0}^{z=L}\left(1 - \epsilon_G\left(@z\right)\right)\delta z}{F_{G0,mol}} = \frac{q_S V_L}{F_{G0,mol}} \Rightarrow Z = \frac{j}{i} \tag{4.14}$$

$$i = \frac{F_{G0}}{F_{G,max}} \text{ where } \qquad F_{G,max} = F_{G,std}\epsilon_G\,(@z = 0) = 0.07464\frac{mol}{s} \tag{4.15}$$

$$j = \frac{q_S}{q_{S,max}} \text{ where } \qquad q_{S,max} = \frac{V_L}{F_{G,max}} = 0.009633\frac{mol}{m^3 s} \tag{4.16}$$

Table 4.1: Variables used in the model are provided below along with their unit and description. Values are provided for the base case ($F_S td = 1869\ std\ m^3\ day^{-1}$ and $q_S = 9.633x10^{-3}\ mol\ m^{-3}\ s^{-1}$). When the values are dependent on depth, they are reported at the bottom of the water column ($z = 0$).

Variable	**Value**	**Units**	**Description**
z	0 to 107	m	Depth into the column
L_{well}	1600	m	Total length of well
L	107	m	Water column height (base case)
t	0 to 18,000	s	Time
D	0.305	m	Diameter of column (base case)
A	0.0731	m^2	Well cross sectional area (base case)
V_{rxtr}	7.82	m^3	Volume of reactor (base case)
V_L	7.66	m^3	Volume of liquid in reactor
P	11.21	atm	Well bottom pressure of gas
P_a	1	atm	Atmospheric pressure
T	328.15	K	Reactor temperature
R	$8.206x10^{-5}$	$\frac{m^3\ atm}{K\ mol}$	Gas constant
g	9.81	$\frac{m}{s^2}$	Gravitational constant
X_l	$1.77x10^{-5}$	$\frac{mol}{mol}$	Mole fraction of gas dissolve in water at 1atm
H	38.33	—	Dimensionless henrys constant

Continued on next page

Table 4.1 – continued from previous page

Variable	Value	Units	Description
C^*_{Li}	10.86	$\frac{mol}{m^3}$	Saturated concentration of i
C_{Li}	10.57	$\frac{mol}{m^3}$	Dissolved concentration of i in the bulk liquid phase
C^*_{Gi}	$\sim$ 416.3	$\frac{mol}{m^3}$	Saturated concentration of i in the gas phase at the gas-liquid interface
C_{Gi}	416.3	$\frac{mol}{m^3}$	Concentration of i in the bulk gas phase
$MW_{methane}$	0.01604	$\frac{kg}{m^3}$	Molecular weight of methane
MW_{H_2O}	0.01802	$\frac{kg}{m^3}$	Molecular weight of water
F_{Std}	1869 or 66,000	$\frac{std\ m^3}{day}$ or $\frac{std\ ft^3}{day}$	Volumetric flow rate of methane assuming std conditions of 288.15 K and 101325 Pa and no water column
$F_{G,mol}$	0.0746 or 5383	$\frac{mol}{s}$ or $\frac{std\ ft^3}{day}$	Effective molar flow rate accounting for gas hold up. Note $F_{G,mol}$ is related to F_{Std} through the gas hold up
u_G	0.0301	$\frac{m}{s}$	Superficial gas velocity
u_trans	0.0413	$\frac{m}{s}$	Transition superficial gas velocity
u_sb	0.2264	$\frac{m}{s}$	Rise velocity of small bubbles (Wilkinson)
u_lb	00.2316	$\frac{m}{s}$	Rise velocity of large bubbles (Wilkinson)

Continued on next page

Table 4.1 – continued from previous page

Variable	Value	Units	Description
ϵ_G	0.0816	$\frac{m^3}{m^3}$	Gas holdup, fraction of total volume
ρ_L	985.7	$\frac{kg}{m^3}$	Water density (at 55°C)
ρ_G	6.677	$\frac{kg}{m^3}$	Gas density
μ_L	$5.07x10^{-4}$	$\frac{kg}{m\ s}$	Water dynamic viscosity (at 55°C)
σ_L	0.0671	$\frac{N}{m}$	Liquid surface tension (at 55°C)
$D_{CH_4:H_2O}$	$3.29x10^{-9}$	$\frac{m^2}{s}$	Liquid phase diffusivity of methane
$A_{CH_4:H_2O}$	$1543x10^{-9}$	$\frac{m^2}{s}$	Pre-exponential factor for methane diffusion in water
$E_{A,CH_4:H_2O}$	16.78	$\frac{kJ}{mol}$	Activation energy for methane diffusion in water
E_L	0.0478	—	Longitudinal diffusion coefficient in liquid
E_G	0.422	—	Longitudinal diffusion coefficient in gas
Bo	93	—	Bodestein number
$k_L a_L$	0.0326	$\frac{1}{s}$	Liquid phase mass transfer coefficient
r_L	$r_L = q_S$	$\frac{mol}{m^3\ s}$	Liquid phase reaction rate
$q_{S,max}$	0.009633	$\frac{mol}{m^3\ s}$	Uptake rate of methane for 100% conversion
q_S	0 to 1.1	$\frac{mol}{m^3\ s}$	Uptake rate of methane
Productivity	0.79	$\frac{g}{L\ hr}$	Productivity of reactor system based on 100% carbon conversion to ethanol. Volume based on total reactor size.

4.3 Results and Discussion

A variety of conditions are studied within this chapter (maximum mass transfer rate, reaction rate required for certain conversion rates, etc.). These are listed in **Table** 4.1, with physical assumptions, explanation of importance, and key conclusions.

4.3.1 Mass transfer performance is comparable to other bubble column reactors

The mass transfer limits of the proposed reactor were found by assuming an infinitely fast biocatalyst ($q_S = \infty$), which corresponds mathematically to a dissolved liquid concentration of zero ($C_L = 0$). Next, the maximum flow rate was found that still allowed complete conversion, as methane release to the environment must be prevented, while maintaining the base case well bottom pressure. The resulting flow rate was $F_{Std,Breakthrough} = 3.55x10^4\ std\ m^3\ day^{-1}$, which represents the maximum flowrate the reactor can accommodate without being mass transfer limited. The corresponding average mass transfer coefficient was $k_L a_{L,avg} = 0.12\ s^{-1}$. This is comparable to other bubble column reactors at similar average flow rates of $u_G = 0.28\ m\ s^{-1}$; Ghandi reviewed a variety of models and most had mass transfer coefficients less than or equal to 0.2 s^{-1} [239, 255]. This is a significant result as this mass transfer coefficients is powered by gas pressure in the geological formation and not a compressor. Hence the operating cost (or energy input) associated with mass transfer is negligible. This mass transfer coefficient can also be increased at higher flow rates, but with diminishing returns and incomplete conversion (**Figure** 4-3**B**).

4.3.2 Minimum reaction rate for full conversion

In accordance with the goal of monetizing marginal wells, we next sought to determine the minimum reaction rate required for full conversion of methane at a flow rate of 1869 $std\ m^3\ day^{-1}$. This rate defines a threshold for microbial and catalytic systems to be used with the Deep Well Reactor. Here, conversion is defined as $Z = j/i$

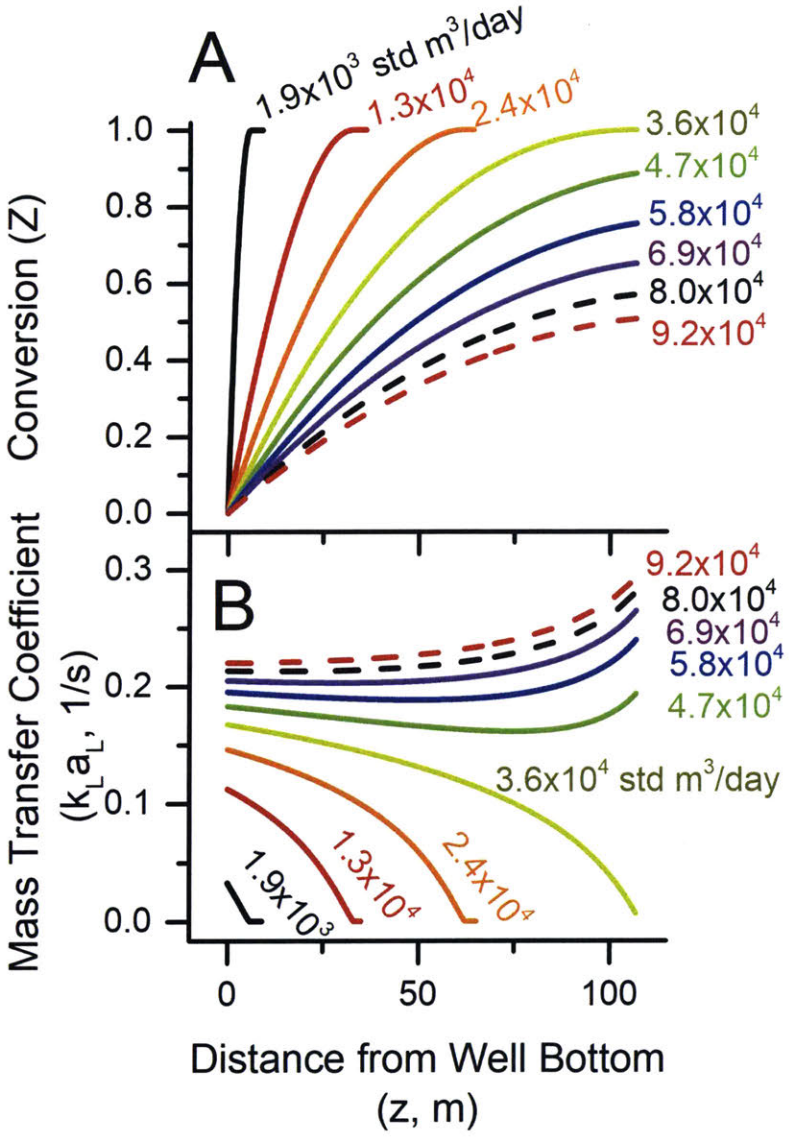

Figure 4-3: The breakthrough flow rate was found by incrementally increasing the standard volumetric flow rate from 1869 (base case) to $9.2x10^4$ *std* m^3 day^{-1} to determine the point at which mass transfer would limit a system with infinite reaction rate ($q_S = \infty$,$C_L = 0$) while maintaining a constant well bottom pressure. The model is at steady state with a batch liquid phase; (A) Conversion and (B) mass transfer coefficient. Numbers in the plot represent the standard volumetric flow rate for that condition.

Table 4.2: List of cases tested, their importance, and key conclusions drawn from their analysis. Units are given the first time a given variable is mentioned, and remain consistent throughout the table.

Cases	Assumptions	Importance	Key Conclusions
Mass transfer performance	$q_S = \infty\ mol\ m^{-3}\ s^{-1}$ $F_{Std} = 1.9x10^3 to$ $9.2x10^4 stdm^3\ day^{-1}$	Determine maximum mass transfer rate possible and flow rate at which the reactor is intrinsically limited by mass transfer.	The flow rate of $1.9x10^3$ is reasonable for the well geometry, allowing full conversion with a suitable catalyst.
Minimum reactor volume and reaction rate for full conversion	$q_S = 0\ to\ 9.6x10^{-3}$ $F_{Std} = 0\ to\ 1.9x10^3 to$ $\Delta V_{rxtr} set for 100\% conv$	Varying q_s and F_{Std} changes the height required for full conversion, affecting productivity. Determine the required q_s for a given F resulting in 100% conversion.	For the base case F_{Std}, current anaerobic methanotrophs consume methane too slowly in bench scale reactors for application in this process. The reaction rates for aerobic methanotrophs and metal catalysts are reasonable; but require pumping of oxygen or co-reactants.
Reaching productivities for economic viability	$q_S = 0\ to\ \infty$ $F_{Std} = 1.9x10^3$	The base case F_{Std} and q_s result in a lower than desirable productivity ($0.8g\ L^{-1}\ hr^{-1}$). Determine the reaction rate and reactor volume required to achieve $2g\ L^{-1}\ hr^{-1}$.	The reaction rate must exceed $2.5x10^{-2}$ $mol\ m^{-3}\ s^{-1}$ to achieve desirable productivities. Assumes stoichiometric conversion to ethanol.
Continuous vs. batch reactors	$q_S = 9.6x10^{-3}$ $F_{Std} = 1.9x10^3$ $F_L = 1.9x10^3$	Determine the if method of operation affects process variables. Determine flow rate of water required to achieve 100 g/L ethanol in the continuous reactor.	Batch and continuous operation do not affect process parameters. Discussion of the pros and cons of both the batch and continuous system are presented.
Flow rate and pressure decay with time	$q_S = 9.6x10^{-3}$ $F_{Std} = 3.7x10^2\ to\ 3.6x10^4$ $\Delta V_{rxtr} \sim \Delta P \sim \Delta F$	As gas is extracted, P and F decrease. With smaller P, less reactor volume is available.	As P and F decrease, $qs = 9.6x10^{-3}$ is not sufficient for full conversion. But this decay is expected to be slow, on the order of years before performance is impacted.

(**Equation** 4.14), where "i" is the normalized flow rate and "j" is the normalized reaction rate. The conversion and height for full conversion ($Z = 1$) have been plotted against "i" and "j" in **Figure** 4-4. For instance, at $i = 0.8$ and $j = 0.5$, $Z = 0.75$. For the base case flow rate of 1869 $std\ m^3\ day^{-1}$, q_S must be greater than $9.633x10^{-3}\ mol\ m^{-3}\ s^{-1}$ to fully utilize the methane. For the breakthrough flow rate of $3.55x10^4\ std\ m^3\ day^{-1}$, 1.1 $mol\ m^{-3}\ s^{-1}$ is required (**Figure** 4-3**A**), an increase of 114 times. This is significantly greater than the increase in flow rate (19 times) due to an increase in the gas flow rate and thus an increase in gas hold up and a decrease in liquid volume. This is not entirely detrimental, as the increased gas hold up translates to higher mass transfer coefficients on average for a flow rate of $3.55x10^4\ std\ m^3\ day^{-1}$ (**Figure** 4-3**B**). Beyond this breakthrough threshold, the flow regime becomes unstable [245] in the upper regions of reactor due to the untransferred gas expanding significantly, with only a small increase in $k_L a_L$ (**Figure** 4-3**B**).

To implement such a technology at a flow rate of 1869 $std\ m^3\ day^{-1}$, catalysts must be found than can approach a rate of $1x10^{-2}\ mol\ m^{-3}\ s^{-1}$. Rates for anaerobic methanotrophic organisms are roughly three orders of magnitude lower than this ($8.1x10^{-6}\ mol\ m^{-3}\ s^{-1}$) [27], emphasizing the biological kinetics as the limitation of this system. However, anaerobic methane oxidation is a relatively new field of study, and our understanding is limited [256, 257, 258], thus it is realistic to expect the volumetric rates to improve substantially as more is learned about the organisms responsible. On the other hand, aerobic methanotrophs such as *Methylococcus capsulatus* (0.02 $mol\ m^{-3}\ s^{-1}$ with 2 $g_{Cell} L^{-1}$) [259] and some catalysts, such as copper and iron containing zeolites (0.01 $mol\ m^{-3}\ s^{-1}$ with 2.7 $g_{Catalyst}\ L^{-1}$) [260] can achieve these volumetric rates. However, aerobic methanotrophs require oxygen for growth. The energy required to operate a compressor for delivering sufficient air to the bottom of the Deep Well would cost at least 10% of the effective methane flow rate to generate (**Appendix** B.2). Similarly, the cited catalysts requires peroxide as a stoichiometric oxidant, and anaerobic methane oxidizers require either nitrate or sulfate, significantly increasing the raw material cost of the operation. The complex

interplay of kinetics, yields, and process will have to be examined in a more complete techno economic analysis. Yet the major finding is that the mass transfer capabilities of the proposed reactor system are unlikely to be a limitation in the development of this technology.

In the base case, q_{Smax} represents the point between mass transfer and reaction control regimes. This is extended along the other conditions in **Figure** 4-4**A**, as the upper left most contour line that indicates the transfer of 100% of the methane and the minimum desired reaction rate for a given flow rate. This contour line is not straight, as might be expected from **Equation** 4.14, because the standard volumetric flow rate (F_{Std}) and initial molar flow rate are related through the gas holdup, and thus are not 1:1 (**Equation** 4.10). Within the upper left region of **Figure** 4-4**A**, the full volume of the reactor is not utilized and the reactor can be shrunk to increase overall productivity as depicted in **Figure** 4-4**B**. For instance, at $i = 0.8$ and $j = 1$, only 72 m of reactor is necessary instead of the full 107 m. The implication is that higher reaction rates can be used to increase productivities by decreasing reactor volume.

4.3.3 Reaction rate required for economic viability

Productivities greater than 2 $g\ L^{-1}\ hr^{-1}$ fuel have been proposed for economically viable processes [17], over 2.5 times greater than that presented in the base case (1869 $std\ m^3\ day^{-1}$, **Figure** 4-6). We therefore examined ways to improve the productivity of the reactor system. In the work that follows, productivity is determined by assuming all carbon from methane is converted to ethanol at 100% efficiency. While such an efficiency is obviously unrealistic, it is a convenient starting point that can be easily calibrated to experimentally determined efficiencies. For a given gas flow rate, the volumetric productivity can be increased by decreasing the fluid volume within the reactor, as mentioned previously (**Figure** 4-4). In accordance, the intrinsic process kinetics (q_S) must be increased. To exceed 2 $g\ L^{-1}\ hr^{-1}$, q_S must surpass $2.5x10^{-2}\ mol\ m^{-3}\ s^{-1}$ (**Figure** 4-5**B**). This value is over 2.5 times greater than the $q_{S,max}$ of $9.633x10^{-3}\ mol\ m^{-3}\ s^{-1}$, required for complete methane conversion. This

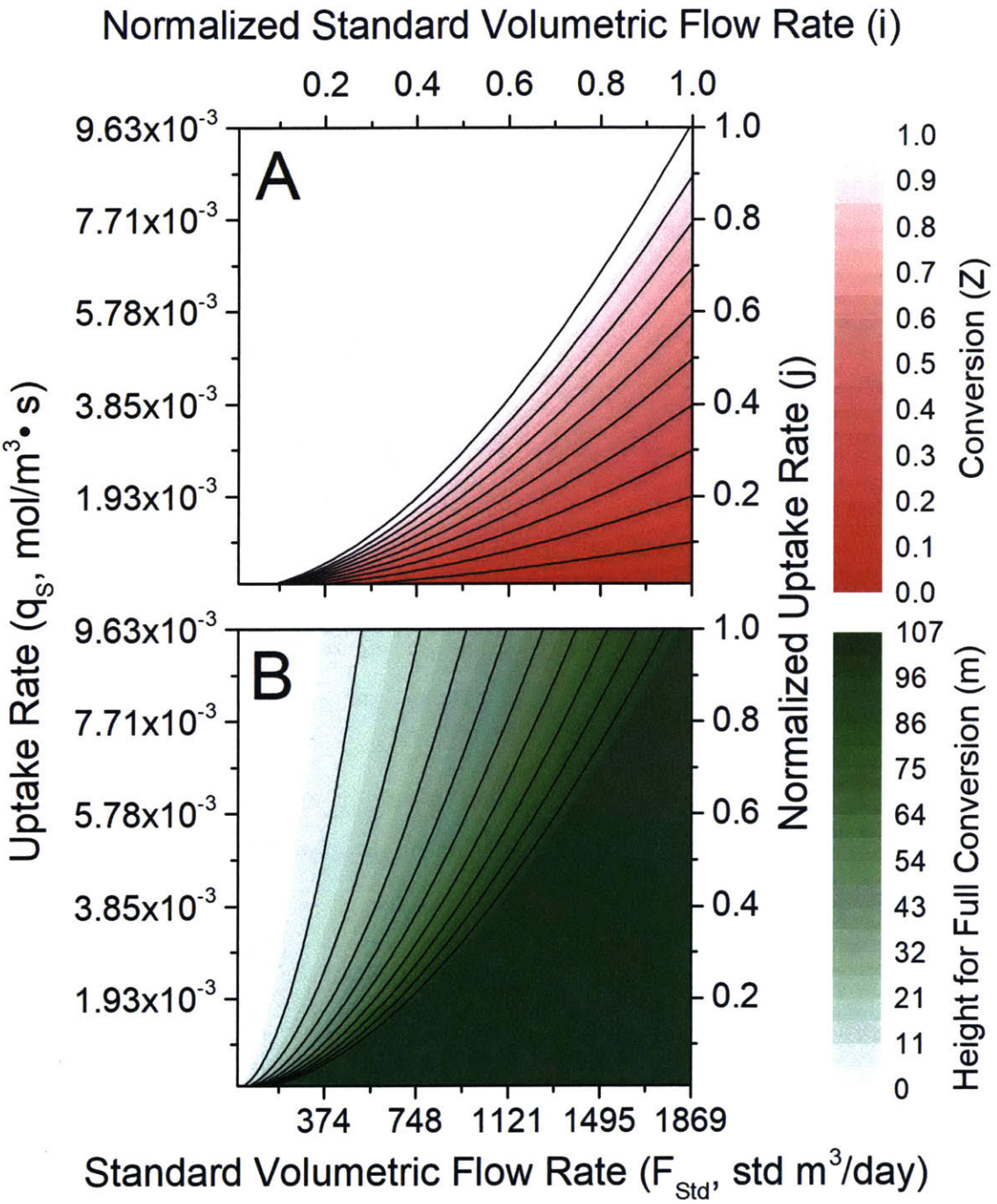

Figure 4-4: The (A) conversion and (B) required column height for full conversion at various flow rates and reaction rates. The model is at steady state with a batch liquid phase. Uptake rate is normalized to $q_{S,max} = 9.633x10^{-3}\ mol\ m^{-3}\ s^{-1}$ and volumetric flow rate to $F_{STD} = 1869\ std\ m^{-3}\ day{-}1$. The maximum height in panel (B) is 107 m at which point conversion decreases, corresponding to the lower right of panel (A). At the top left of (B), the full reactor volume is not need; Contour lines are drawn for each 10% increase of conversion or height, corresponding to the gradients to the right the graph.

results in the active reactor volume shrinking to $3.2m^3$ (or a height of about 43 m) as seen in **Figure** 4-5. At these higher uptake rates, the gas phase remains entirely homogenous, which is not the case for $q_{S,max}$. The maximum productivity under the base case is $11.4g\ L^{-1}\ hr^{-1}$, as limited by mass transfer ($q_S = \infty$). If a sufficiently fast catalyst is found, the proposed reactor can easily reach desirable productivities. Yet, this does not account for the time that may be needed for starting the reactor, an important consideration when the biocatalyst must first grow to reasonable densities.

4.3.4 Continuous operation does not affect reactor performance

One method to minimize the startup time is to operate continuously. Moreover, the mode of operation (batch or continuous liquid phase) must be considered when performing future economic analysis. The continuous reactor was modeled by assuming a continuous downwards flow of liquid (countercurrent) with an inlet concentration of $C_L = 0$. The results of the simulation showed no major impact on reactor variables, such as C_L, $k_L a_L$, driving force, and productivity under continuous operation (**Figure** 4-6). This means the choice of how to operate the reactor can be based entirely on other process demands.

For instance, with the base case and a batch liquid phase ($F_{G,Mol} = 0.0746\ mol\ s^{-1}$ and $V_{rxtr} = 7.82\ m^3$) and a reasonable average gas hold up in a reacting system ($\epsilon_G = 0.0737$, **Figure** 4-6**C**), 6 days are required for all the methane to be converted to 100 $g\ L^{-1}$ of ethanol, assuming 100% conversion. This ignores the growth period for the organism, the efficiency of the pathway, as well as harvesting and restarting the reactor.

The continuous system, at the expense of added complexity and infrastructure, has a few benefits: First, the continuous system can recycle cell matter, which negates much of the start-up time associated with generating biomass for biologic systems. Second, the continuous system does not require emptying and refilling the reactor system, as is the case for the batch system; productivity of the batch system in **Figure**

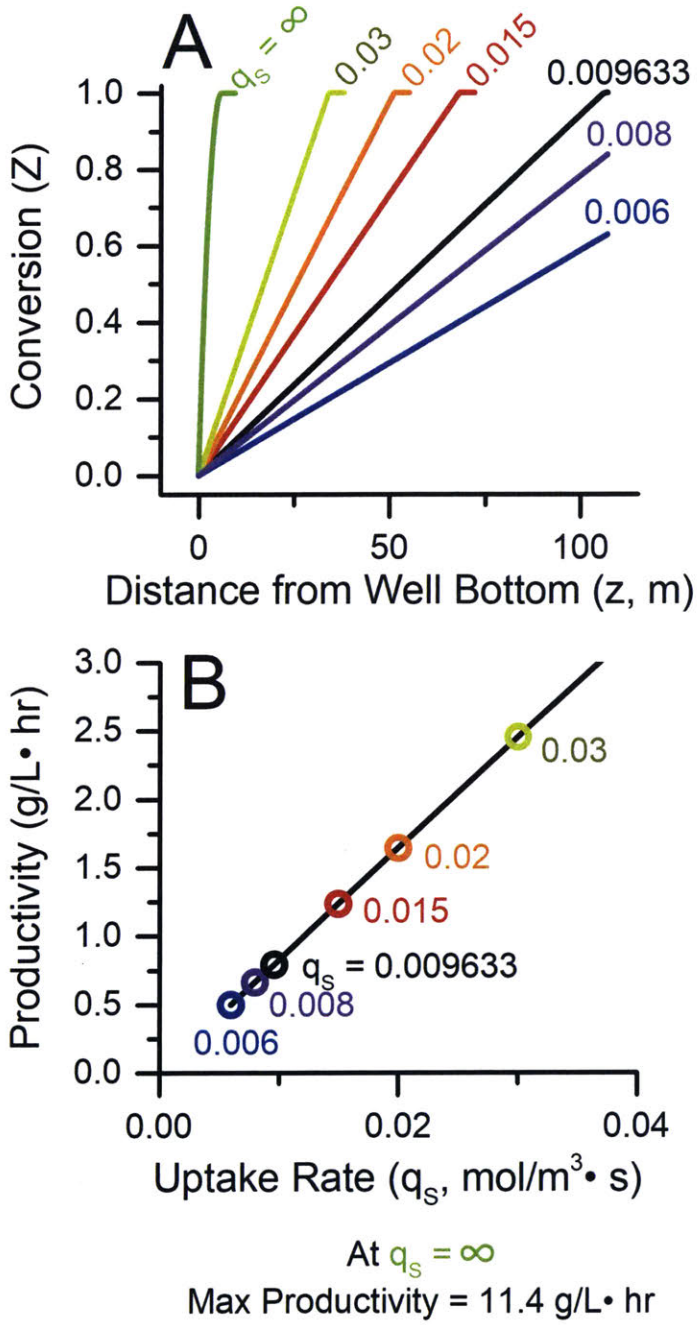

Figure 4-5: Effect of uptake rate (q_S) on productivity for the base case (1869 *std* m^3 day^{-1}), for a batch liquid phase at steady state and no back mixing. By decreasing the utilized space within the reactor (A) productivity can be greatly increased. (A) Conversion and (B) productivity. Numbers in the plot represent the uptake rate for that condition. Productivity based on the assumption of 100% carbon conversion to ethanol as an upper threshold.

4-6**C** does not account for this down time. Finally, the product concentration can be controlled easily, whereas the batch system may exhibit regions of elevated product concentrations that may poison or inhibit the catalyst.

Similarly, through modeling, the liquid flow rate for continuous reactor can be found that results in the same outlet product concentration of 100 $g\ L^{-1}$ (1.6 $m^3\ day^{-1}$), along with the reaction rate needed to achieve 100% conversion (0.01040 $mol\ m^{-3}\ s^{-1}$). The liquid phase is assumed to operate closely to that of a plug flow reactor, where back mixing is expected to negligibly affect the results due to the high $k_L a_L$ and reasonable superficial velocity. Since the back mixing term is negligible, the continuous liquid phase reactor can be judged under steady state conditions. By varying the liquid flow rate, the product concentration can be controlled, with this relationship depicted in **Figure** 4-6**C**, along with an essentially constant overall productivity of 0.86 $g\ L_{reactor}^{-1}\ hr^{-1}$. This is at the lower end of the range reported by Haynes and Gonzalez [17], however the limitation here is not the mass transfer, but the gas flow rate and reaction rate. Indeed, the productivity of the continuous system is only a modest 8.7% greater than that of the batch system, while requiring an 8.2% increase in specific reaction rate to achieve 100% conversion. This is expected, as a majority of gas is transferred and reacted, thus the flow rate of methane into the reactor has much greater control over productivity than liquid flow rate. The slight change in productivity over that of the specific reaction rate can be attributed to the dissolved methane at the entrance region, which is stipulated to enter at a value of 0, shifting this concentration slightly downward (**Figure** 4-6**A** inset). Subsequently, the driving force in the entrance region is greatly increased, and remains at least slightly elevated throughout the column (**Figure** 4-6**B**). Conversely, the superficial gas velocity and the mass transfer coefficient remain virtually unchanged between continuous and batch operation.

While there is no large increase of productivity from batch to continuous operation, other benefits are associated with the continuous system. The effect of poisoning at high product concentrations can be seen in **Figure** 4-6**C**, where the concentration of ethanol at the exit increases greatly as one approaches a flow rate of 0. Note

that in such regimes, back mixing will dominate over the effects of liquid translation, negating some of this effect. The major limitation of the continuous system is the increased complexity and capital cost, including a devoted processing skid or pipeline; if multiple wells could be connected, some of this cost can be negated by economics of scale. Based on the arguments above, without further economic analysis, one cannot determine which system is more feasible for producing a low cost fuel. Yet the continuous and batch reactors exhibit very similar phenomena. For this reason, the liquid phase is assumed to be operated in batch mode, and the conclusions are expected to extend to that of the continuous liquid reactor.

4.3.5 The effect of diameter, inert gases, and Darcys Law on the required reaction rate

As mentioned previously, a goal of this model was to stipulate a reasonable volumetric reaction rate for the system such that the outlet conversion is 100% (from **Figure** 4-4, $q_{S,max} = 9.633x10^{-3}\ mol\ m^{-3}\ s^{-1}$). Diameter will impact this value greatly due to the significant decrease in reactor volume (V_{rxtr}). Conversely, gas hold up is generally independent of diameter when the diameter is greater than 15 cm [242]. The mass transfer coefficient is slightly affected by diameter, yet only to the 0.17 power, so the effect is expected to be negligible. In terms of previously made assumptions, a lower diameter will also correspond to a decreased E_L and less back mixing than that of the base case (**Equation** 4.7). Regardless, diameter plays an important role in the required q_S because we do not expect to have any control over the diameter when building the Deep Well Reactor. This is due to the proposed nature of the technology, re-purposing abandoned natural gas wells. Decreasing the diameter of the well from the base case of $D = 0.305m$ would disproportionately increase the required uptake rate. For instance, the diameter might be as small as 0.15 m [225], half the size of the base case and a quarter of the volume. Since the height is firmly set by the well bottom pressure, maximum height is another uncontrollable variable. To achieve a conversion of $Z = 1$ with a diameter of 0.15 m and base case flow rate, the reaction

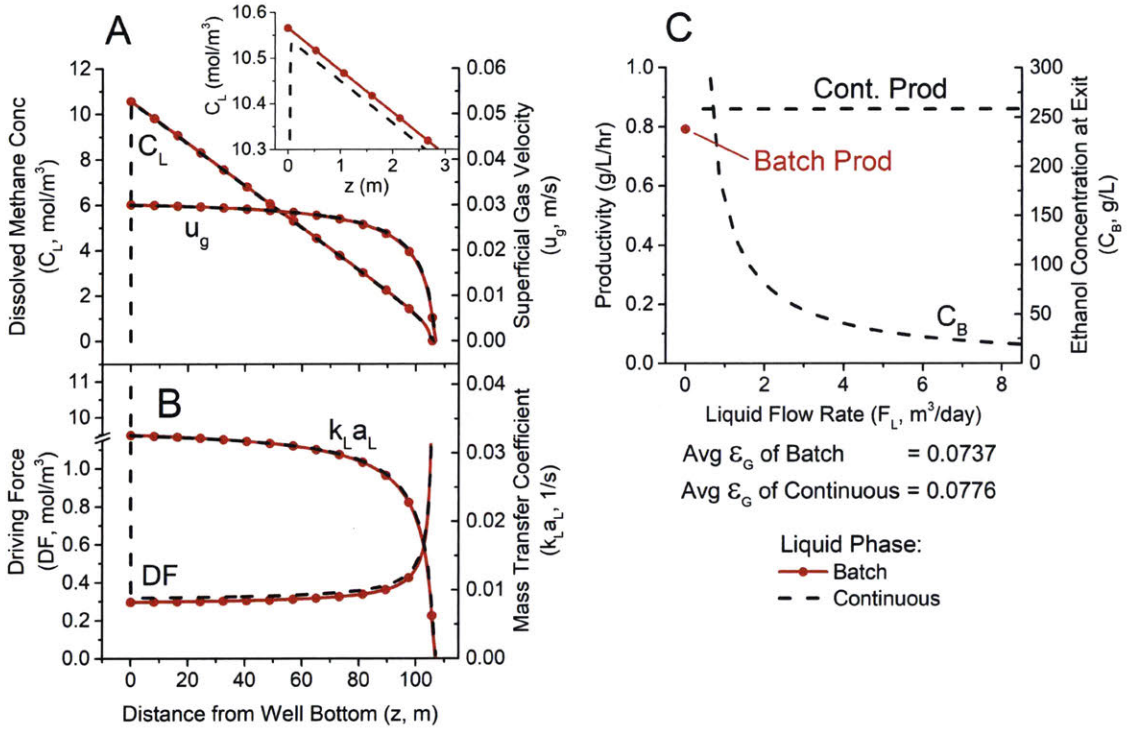

Figure 4-6: Comparison of continuous and batch liquid phase in the Deep Well Reactor for the base case (1869 $std\ m^3\ day^{-1}$). Reaction rate for continuous system chosen to achieve 100% conversion on a carbon mole basis; $1.04x10^{-2}\ mol\ m^{-3}\ s^{-1}$ for the continuous and $9.633x10^{-3}\ mol\ m^{-3}\ s^{-1}$ for the batch system. (A) Dissolved methane concentration and superficial velocity of gas as a function of height in well. Inset shows apex of dissolved methane concentration, and the small difference between the continuous and batch profiles. (B) Mass transfer coefficient and driving force ($C_G/H\ -\ C_L$) as a function of height in well. (C) Outlet concentration and productivity as a function of liquid flow rate for continuous liquid system. Productivity based on the assumption of 100% carbon conversion to ethanol. Productivity for the batch reactor based on an average ethanol concentration of 100 $g\ L^{-1}$ and represented as a single red dot. Productivity reported on a reactor volume basis, with the appropriate gas holdup values reported. Profiles in (A) and (B) taken from continuous reactor producing 100 $g\ L^{-1}$ with a liquid flow rate of $F_L = 1.6\ m^3\ day^{-1}$.

rate must be increased over 10 fold to 0.1026 $mol\ m^{-3}\ s^{-1}$. The reason for the drastic increase in rate over $q_{S,max}$ is due to a 2.4 fold increase in the effective molar flow rate and a 4.6 fold decrease in liquid volume within the reactor. If such a reaction rate cannot be achieved, at the expense of productivity, the effective diameter could be increased by linking neighboring wells in parallel. **Appendix** B.3 briefly analyzes the proximity of abandoned wells in Pennsylvania, where groups of 5 wells can be usually found within 5 to 10 hectares of each other. Alternatively, the standard flow rate could be decreased to match the reactor volume. As mentioned in the introduction, each real world natural gas well has slightly different characteristics and the operating conditions should be tailored to the individual well.

Gas impurities in the feed are another important consideration, as they dilute the driving force and can also potentially compete with methane or poison the catalyst. A reasonable range of impurities for natural gas wells is between 2 to 24 mol%, depending on the formation, including longer chain hydrocarbons (ethane being most abundant after methane), Helium, and Nitrogen [249, 250]. While secondary phenomena (competition and/ or poisoning) are not accounted for in the kinetic models presented here [261], the importance of impurities on dilution can easily be explored. To this end, for a given uptake rate (q_S) and initial molar flow rate ($F_{G,mol}$), inert gas was added so as to maintain the same molar flow rate of methane; subsequently, the standard volumetric flow rate increases in correspondence with the added impurities. For simplicity, all impurities are assumed to be inert in the system. Take for instance the base case; increasing the inert gas from 0 to 25 mol% results in the conversion dropping slightly from 100% to 98.4% (**Figure** 4-7**C**). Indeed, much higher levels of impurities (88 mol%) are required to decrease the overall mass transfer lower than 90%. Much of this decrease can be attributed to lost driving force at the top 25% of the column, with the well bottom having very similar values (**Figure** 4-7**B**). The reason for the small difference in conversion is from the improved mass transfer coefficient (**Figure** 4-7**A**), which increases with the added gas as gas holdup also increases. Again, these effects only play a significant role at the top of the well, once much of the methane has already been depleted.

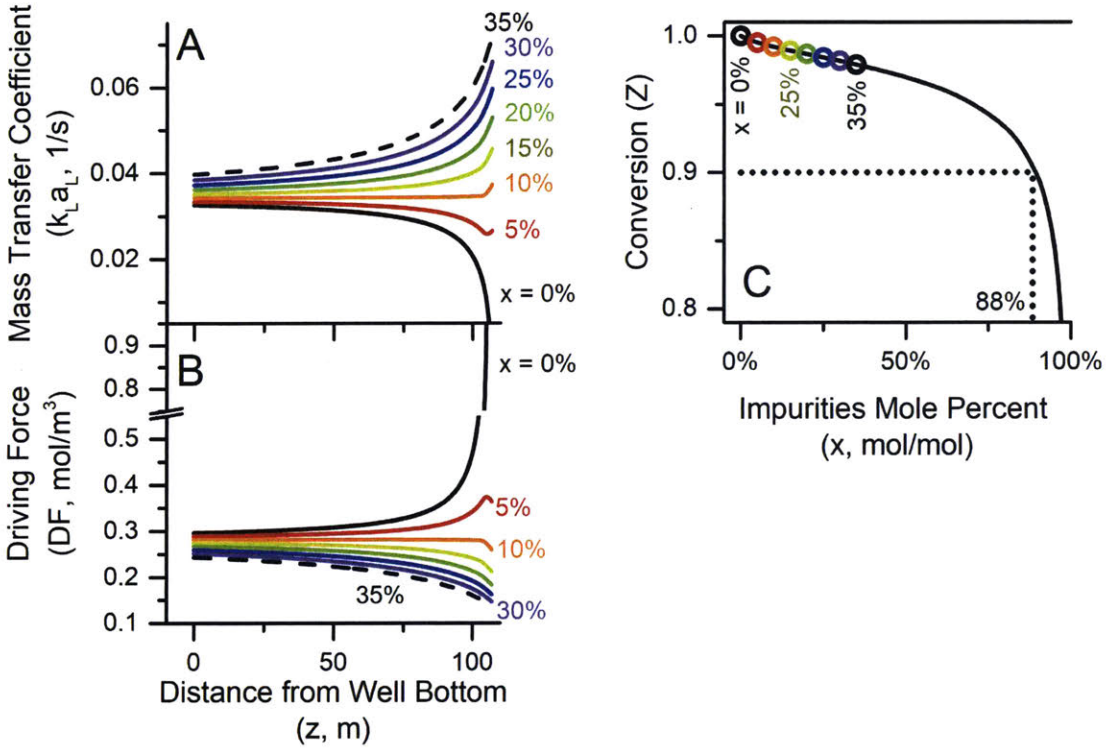

Figure 4-7: Effect of inert gas (impurities) on (A) mass transfer coefficient, (B) driving force, and (C) conversion. The reactor was modeled as a 2 component system with batch liquid phase at steady state. The base case conditions were modified such that an inert was added at the stipulated mole fraction (x) while maintaining a constant initial molar flow rate of methane and well bottom pressure. Numbers in the plot represent the mole fraction of impurities (assumed inert) for that condition. These numbers correspond to the unfilled circles in panel (C).

4.3.6 Higher specific reaction rates are required as the marginal well depletes

Flow rate and pressure are related in natural gas wells, as discussed in the methods, but the temporal effect of well depletion on reactor performance has been ignored in the previous analysis. As the flow rate diminishes, so too does the pressure at the bottom of the well, and thus the maximum reactor volume that can be sustained. This in turn requires higher specific conversion rates to meet the goal of 100% conversion. To better understand this relationship, flow rate and pressure were dependently varied ($\Delta F_{Std} \sim \Delta P$) while maintaining $q_{S,max}$ as the reaction rate and a maximum column height of 1600 m, and the effect on conversion was plotted (**Figure** 4-8**B**). The results of this analysis were promising for flow rates greater than 1869 $std\ m^3\ day^{-1}$, as $q_{S,max}$ was sufficient for complete conversion up to flow rates of $2.8x104\ std\ m^3\ day^{-1}$. This coincides with utilizing the whole well height (1600 m), suggesting higher flowrates could be harnessed at 100% conversion with even deeper wells. For flow rates less than 1869 $std\ m^3\ day^{-1}$, however, there is a significant drop in conversion. By 453 $std\ m^3\ day^{-1}$, the conversion is only 70% and at 312 $std\ m^3\ day^{-1}$, 50%. This is worrisome, as flow rate and pressure will decay while gas is extracted. It is clear that $q_{S,max}$ is not sufficient specific reaction rate when operating the base case well for extended periods of time because conversion will continuously fall with the flow rate. Yet the time required for the flow rate to decay from 1869 to 453 $std\ m^3\ day^{-1}$ is over 9 years, with a reasonable decay rate of 0.15 per year ($F_2 = F_1 e^{-0.15*\text{time}}$) [57].

While the dissolved methane concentration varies significantly with changes in pressure (**Figure** 4-8**A**), both the driving force ($C_G/H - C_L$) and $k_L a_L$ remain approximately the same throughout the column when compared on a height normalized basis (**Figure** 4-8**C and D**). The differences between the flow rates occurs when conversion approaches 100%. Here, driving force sharply increases because the dissolved methane concentration goes to zero and the concentration of methane in the gas phase increases when pressure decreases near the top of the column. Moreover, the mass transfer coefficient goes to zero as the gas is consumed and gas hold-up

volume goes to zero (see **Equation** 4.11). Instead, reactor volume is the key driver of these results, highlighting the importance of the initial pressure of the well for any given flow rate. The larger the initial pressure, the larger the available volume.

The Deep Well Reactor shows significant promise as a practical method for inexpensive mass transfer of methane to the liquid phase. By incorporating the reactor into the pre-existing structure, a substantial reactor volume is available. Based on the analysis presented, this volume is set by the well bottom pressure and plays a significant role in the reaction rate required for high conversion. Furthermore, the Deep Well Reactor benefits from negligible cost associated with powering $k_L a_L$ through gas pressurization and reactor mixing, as the pressure is supplied by the geological formation. The presented model can be easily adapted to account for variations between wells (geometric, gaseous, etc.), however a kinetic model for future biological catalysts would result in more accurate results when preparing pilot testing. With the appropriate biocatalyst, marginal wells can be repurposed to achieve close to 100% conversion. Economic analysis is still required prior to implementation of pilot studies, as downstream separations will have a large impact on economics. That all of the gaseous methane can be transferred to the column at reasonable rates is perhaps surprising, as most BCRs are not operated to conserve the gas phase. In the general application of BCRs, significant flow rates of gas are used to ensure high $k_L a_L$ and thus high productivity at the expense of compression costs. This is not the case for the Deep Well Reactor, which has a large and free mass transfer potential due to the high aspect ratio and large volume.

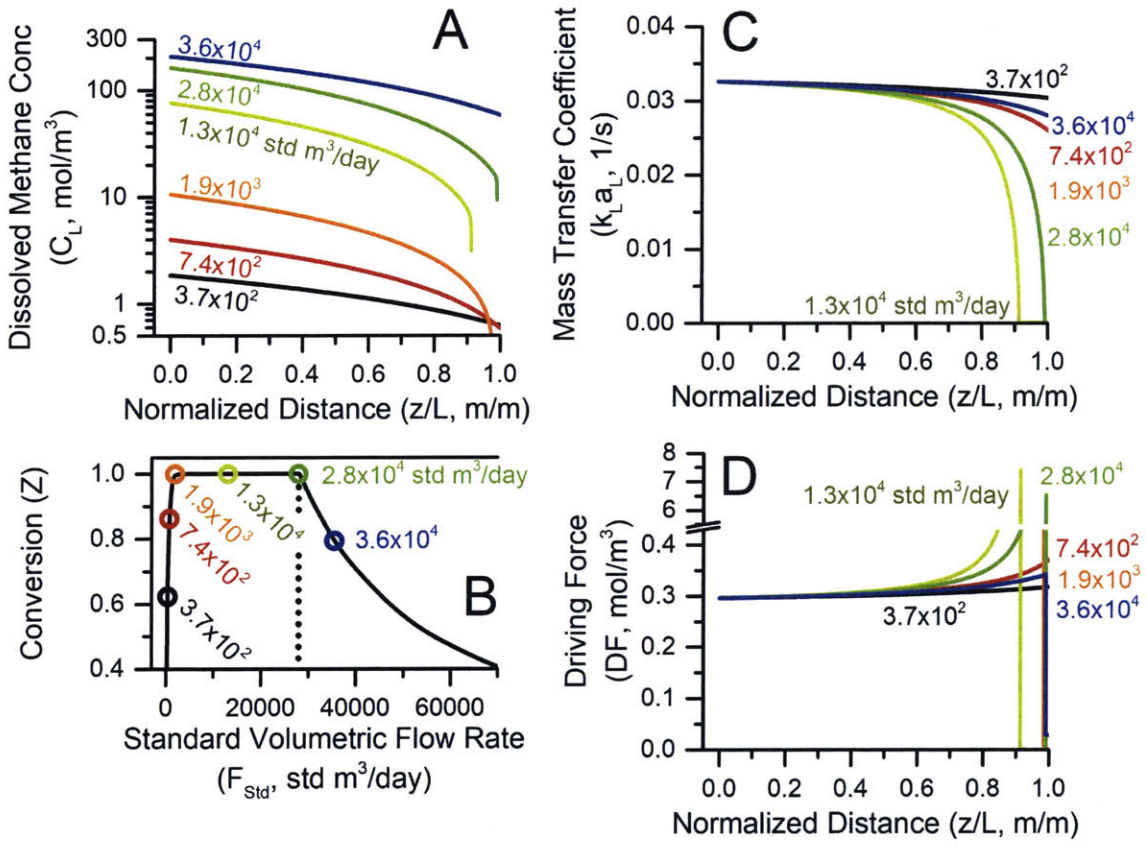

Figure 4-8: The effect of varying flow rate with pressure drop within the reactor. The standard volumetric flow rate and well bottom pressure was dependently increased with Darcys law ($\Delta F_{Std} \sim \Delta P$) while maintaining a constant specific reaction rate is $9.633x10^{-3}$ $mol\ m^{-3}\ s^{-1}$ throughout. The reactor height was scaled such that the hydrostatic pressure matches the well bottom pressure, with a maximum height of 1600 m.

4.4 Conclusion

Marginal natural gas wells constitute an important quantity of methane that currently cannot be economically extracted. Implementation of a low cost gas-to-liquid reactor system at the well head reduces transportation costs and is key attribute for solving this problem. Based on the analysis of the Deep Well Reactor with a conservative mass transfer model, the simple Deep Well Reactor has the required capacity to transfer methane from the gas to liquid phase. This is true even for flow rates orders of magnitude lower than other proposed small scale gas-to-liquid technologies, allowing the Deep Well reactor to operate in a truly distributed manner. The proposed approach could lower capital costs of the reactor by using the pre-existing structure. Furthermore, the power required to drive mass transfer is provided by the well head pressure and is thus negligible. While the system slows the effective molar flow rate of methane, producing liquid fuels or chemicals can add substantial value to the natural gas well. For these reasons, mass transfer does not appear to a major limitation for the implementation of biological catalysts. Despite the optimistic outlook of the reactor technology, biological (or inorganic) catalysts that can achieve the desired reaction rates are still in development and currently do not meet the minimum rates required for reasonable productivities. Thus, increased focus on these catalysts is the most important challenge for the implementation of the Deep Well Reactor, which is otherwise expected to perform well based on this assessment.

Chapter 5

Conclusions and Future Directions

5.1 Thesis Summary

CARBON dioxide fixation by anaerobic acetogens with the WLP is the most efficient on the basis of ATP. Yet, the WLP operates at the thermodynamic limit of life ($\Delta G = 0$). This results in low growth rates, biomass density, product titer, and overall productivity. **Chapter** 2 and 3 focused on ways of improving growth energetics by supplying another electron acceptor (nitrate) or electron donor (methanol).

Chapter (4) was also related to gas fixation, but focused on methane. Within **Chapter** 4, a theoretical reactor system was analyzed for the conversion of stranded methane wells for the production of liquid fuels and chemicals. Currently, small scale catalytic gas to liquid technologies are being developed; the proposed reactor would operate at flow rate orders of magnitude lower than others that have been proposed.

5.1.1 Nitrate and the WLP

At the beginning of my Ph.D., my goal was to understand why nitrate blocked the WLP of *M. thermoacetica*. Once understood, various metabolic engineering techniques could be utilized to allow co-utilization of nitrate and CO_2. Concurrently, another student was developing the transformation protocol for *M. thermoacetica* that would empower that engineering. Luckily for this thesis, though not for his, Ben

was unable to consistently transform *M. thermoacetica*, despite developing a novel and inventive method for optimizing a transformation protocol [62]. As his work shifted to *C. ljungdahlii*, mine did as well. Surprisingly, *C. ljungdahlii* was able to metabolize nitrate while growing on CO_2. And moreover, nitrate reduction corresponded to substantial increases in productivity and titer. Thus the main goal of my thesis shifted; first to verify if the results were credible, second to determine the potential mechanism by which growth rate was improved, and finally whether the addition of nitrate to such processes would be reasonable worthwhile based on yield and economics.

These results were confirmed with mass balances, H_2 balances, and the incorporation of $^{13}CO_2$ into both carbons of the main product, acetate. First, the mass balances of biomass density and acetate titer verified that yeast extract alone could not account for fixed carbon. When nitrate was present, there was 27.6 $\pm$ 0.6 mM C that was fixed into biomass, acetate, and formate; yeast extract was present at 10% of this, only 3.34 $\pm$ 0.05 mM C. These results were confirmed again with $^{13}CO_2$, as labeling patterns approached the theoretical limit when accounting for labeled $^{13}CO_2$ and unlabeled bicarbonate. The measured and predicted values of H_2 consumption were also closed to 91 $\pm$ 4%, verifying that only H_2 and nitrate were responsible for the improved in growth rate and biomass titer.

The yeast extract was also determined to be unnecessary to achieve high biomass density; as excluding it did not affect growth on nitrate and CO_2. Instead, yeast extract was maintained within the media so as to achieve consistent growth behaviour when the substrate was only H_2 and CO_2.

Transcriptomics and metabolomics were further used to understand the changes within the cell. The results indicated that nitrate likely did not directly down-regulate the WLP, as WLP mRNA transcripts remained virtually unchanged within 2 hours of receiving a spike of nitrate. Conversely, the genes responsible for nitrate metabolism were greatly upregulated within 2 hours. The intracellular metabolite pool sizes were also of interest. Most importantly, when the electron donor was H_2, addition of nitrate resulted in higher acetyl-CoA pool sizes and a higher ATP/ADP ratio; both

were important for growth. Despite the higher growth rates, the pool size of most metabolites in gluconeogensis were increased; conversely the amino acid pool sizes were generally lower. Lysine prominently stood out, as it was virtually depleted in the presence of nitrate.

Finally, metabolic models were used to understand the potential yields when producing a variety of products with nitrate and CO_2. If the flow of electrons can be properly controlled, carbon yields could reach 100%, if biomass was included.

5.1.2 Methanol and the WLP

We were also interested in developing technologies for the conversion of methanol into fuels and chemicals. Of the well known acetogens, only *M. thermoacetica* and *A. woodii* can consume methanol. We were interested in transferring *mtaABC* operon, responsible for methanol metabolism, into *C. ljungdahlii*. However these genes were only putatively annotated, thus we wished to determine if the annotations were likely candidates. To do this, we sequenced the mRNA transcriptome when grown on methanol or glucose; our expectation was that genes involved with methanol would be highly up-regulated when grown on methanol. Indeed, the transcriptome confirmed that the annotated genes for *mtaBC* were likely correct but *mtaA* was incorrect. Based on the transcriptome, we proposed other putative methyltransferases for *mtaA*.

Previous literature on methanol growth in M. thermoacetica was inconsistent with recent gene annotations, suggesting a methanol dehydrogenase was present instead of the soluble *mtaABC* cascade. *M. thermoacetica* was grown on deuterated labeled methanol; the substantial presence of M+3 acetate indicated that methanol entered the WLP at the methyl level. From this, we could infer that a methanol dehydrogenase was not the main enzyme activity, even if it could be present within the cell.

5.1.3 The Deep Well reactor

Biology generally operates at slower rates than catalytic systems. We wished to ask whether such slower rates could be conducive for decentralized bio-processing at

methane well sites with slow flow rates. We envisioned the simplest process, with the cheapest capital costs, which resulted in the idea to use the well casing as the bioreactor; no extraneous power input would be required as the pressurized gas would power mass transfer. We wished to know if reasonable mass transfer rates could be achieved and whether complete conversion could be possible. Indeed the unique aspect ratio (very tall and very skinny) resulted in very favorable mass transfer rates. If the catalyst was fast enough, complete conversion would be possible.

While the necessary rates were comparable to aerobic methanotrophs and catalytic systems, these would require addition of oxygen or hydrogen peroxide, respectively. The added cost and complexity of oxygen and hydrogen peroxided would be non-trivial. Conversely, current anaerobic methanotrophs are 1000x to slow for the proposed technology.

5.2 Future directions

5.2.1 Nitrate and the WLP

The results of adding nitrate to cultures of *C. ljungdahlii* were very promising. However, substantial work remains prior to implementation of any future technologies. In particular, the flow of electrons within the cell must be tightly controlled to maintain high yields without sacrificing titers. Perhaps this can be done with controlled feeding of nitrate. Though, if metabolic engineering will be necessary, one must first understand how nitrate regulates the WLP. The exact mechanism could not be directly inferred from the transcriptomic data, yet this transcriptomic data will provide valuable targets in future studies.

Surprisingly, nitrate negatively impacted growth of *C. ljungdahlii* when the substrate was CO instead of H_2. This was very surprising, and the cause of the decreased growth and lack of acetate production is unknown. Future work exploring this result could shine light on how these cells regulate their metabolism, based on substrates, intracellular conditions, etc.

Other electron donors and acceptors must also be studied, beyond nitrate. Because these organisms do no respire oxygen, other pathways must be provided for the production of ATP that do not inhibit CO_2 fixation.

5.2.2 Methanol and the WLP

While the mechanism and putative genes were identified for methanol assimilation in *M. thermoacetica*, these must be confirmed with in vitro enzyme assays, preferable from heterologous strains. Once confirmed, these genes could be transformed into acetogens like *C. ljungdahlii*, which we believe could then directly grow on methanol.

The ability of *M. thermoacetica* to grow and produce acetate from methanol is also of industrial interest. Yet, growth rates, biomass density, and acetate titers remain lower than desired. The limitations of growth on methanol must be first understood, such as what limits biomass densities as compared to other soluble substrates like sugars. Perhaps media optimization and reactor design could substantial increase these metrics. Mixotrophy may also be an option, though preliminary work indicated that growth on approximately 1 to 3 mM of fructose was diauxic with methanol in *M. thermoacetica*.

5.2.3 The Deep Well reactor

While the proposed deep well reactor was of intellectual interest, substantial work is necessary to develop both catalytic and biologic systems. Currently, the community still does not fully understand all the intricacies of methanotrophy. Moreover, this community, while focused on the interesting biology, has failed to studied methods by which methane conversion rates can be increased.

Once a catalytic or biologic system was successfully developed, a more in depth study of the process must be conducted. One of the key limitations of the model was that reaction rates were averaged throughout the well, despite changes in methane concentration within the water. Even basic kinetic models would be very insigthful for how the reactor would stratify based on mixing patterns and methane concentrations.

If the kinetic models are promising, economic studies must be performed to determine the feasibility of such a distributed system. A key driver of the economics will be how best to service, connect, and harvest from a network of reactors spread across a geologic formation. Another major consideration is the cost of the well and economic productivity, as these wells would produce at relatively slow rates; this is a major reason that complexity of the system must be greatly minimized to decrease costs related to managing and operating the systems.

5.3 Concluding Remarks

The main goal presented within this thesis was improving gas fixation rates, titers, etc. such that industrial gas fixation can in part mitigate the CO_2 and methane released by the power and chemical industries. Over the past 6 years, great strides have been made to address this in a variety of organisms and a variety of pathways. Have we reached a point where industrial waste gas fermentation is economically viable? Yes and no. Lanzatech has been very successful in developing syngas fermentation of CO to ethanol. But this is not as desirable as CO_2 fixation into biofuels. Methanotrophy is also far from implementation, as we still do not fully understand the biology, and only recently has there been a substantial interest by the DOE to fund such research.

A major consideration of any gas fixation process is the product. Specialty chemicals will make money, but will have next to no impact on the (not so special) gigatons of CO_2 released to the atmosphere each year. Moreover, scientists as a community can not assume that tariffs or taxes can pay for that CO_2 fixation. We must instead develop technologies that are economically feasible at those scales.

Regardless, I'm in awe at the strides that the field has taken within these past 6 years; in part due to the influx of funding, and also the intelligent minds that utilized that funding well. I am thankful to consider myself a peer within this community scientists, as they have helped shape how I pursue scientific advances.

Bibliography

[1] Le Quéré C, et al. (2018) Global Carbon Budget 2017. *Earth Syst. Sci. Data* 10(1):405–448.

[2] Saunois M, et al. (2016) The global methane budget 2000-2012. *Earth Syst. Sci. Data* 8(2):697–751.

[3] Godoy MS, Mongili B, Fino D, Prieto MA (2017) About how to capture and exploit the CO2 surplus that nature, per se, is not capable of fixing. *Microb. Biotechnol.* 10(5):1216–1225.

[4] Boot-Handford ME, et al. (2014) Carbon capture and storage update. *Energy Environ. Sci.* 7(1):130–189.

[5] Mikkelsen M, Jørgensen M, Krebs FC (2010) The teraton challenge. A review of fixation and transformation of carbon dioxide. *Energy Environ. Sci.* 3(1):43–81.

[6] Tao Z, Clarens AF (2013) Estimating the carbon sequestration capacity of shale formations using methane production rates. *Environ. Sci. Technol.*

[7] Dai Z, et al. (2016) CO ₂ Accounting and Risk Analysis for CO ₂ Sequestration at Enhanced Oil Recovery Sites. *Environ. Sci. Technol.* 50(14):7546–7554.

[8] Rockström J, et al. (2017) A Roadmap for Rapid Decarbonization. *Science (80-.).* 355(6331):1269–1271.

[9] Lashof Da, Ahuja DR (1990) Relative Contributions of Greenhouse Gas Emissions to Global Warming.

[10] Rodhe H (1990) A comparison of the contributions of various gases to the greenhouse effect. *Science (80-.).* 248(1):1217–1219.

[11] Saunois M, Jackson R, Bousquet P, Poulter B, Canadell J (2016) The growing role of methane in anthropogenic climate change. *Environ. Res. Lett.* 11(12):120207.

[12] Howarth RW, Santoro R, Ingraffea A (2011) Methane and the greenhouse-gas footprint of natural gas from shale formations. *Clim. Change* 106(4):679–690.

[13] Phillips NG, et al. (2013) Mapping urban pipeline leaks: Methane leaks across Boston. *Environ. Pollut.* 173:1–4.

[14] Gvakharia A, et al. (2017) Methane, Black Carbon, and Ethane Emissions from Natural Gas Flares in the Bakken Shale, North Dakota. *Environ. Sci. Technol.* 51(9):5317–5325.

[15] Tollefson J (2013) Oil boom raises burning issues. *Nature* 495(7441):290–1.

[16] Fleisch T (2014) Associated Gas Monetization via miniGTL; Conversion of flared gas into liquid fuels and chemicals, Technical Report January.

[17] Haynes Ca, Gonzalez R (2014) Rethinking biological activation of methane and conversion to liquid fuels. *Nat. Chem. Biol.* 10(5):331–9.

[18] Erb TJ, Zarzycki J (2016) Biochemical and synthetic biology approaches to improve photosynthetic CO2-fixation. *Curr. Opin. Chem. Biol.* 34:72–79.

[19] Hernández-Calderón OM, et al. (2016) Optimal Design of Distributed Algae-Based Biorefineries Using CO2 Emissions from Multiple Industrial Plants. *Ind. Eng. Chem. Res.* 55(8):2345–2358.

[20] Schulz H (1999) Short history and present trends of FischerTropsch synthesis. *Appl. Catal. A Gen.* 186:3–12.

[21] Heng HC, Idrus S (2004) The Future of Gas to Liquids as a Gas Monetisation Option. *J. Nat. Gas Chem.* 13:63–70.

[22] Kirkels AF, Verbong GP (2011) Biomass gasification: Still promising? A 30-year global overview. *Renew. Sustain. Energy Rev.* 15(1):471–481.

[23] (2011) The world's largest gas-to-liquids plant is now fully online.

[24] Tracy BP, Jones SW, Fast AG, Indurthi DC, Papoutsakis ET (2012) Clostridia: the importance of their exceptional substrate and metabolite diversity for biofuel and biorefinery applications. *Curr. Opin. Biotechnol.* 23(3):364–81.

[25] Savage MD, Drake HL (1986) Adaptation Of The Acetogen Clostridium-Thermoautotrophicum To Minimal Medium. *J. Bacteriol.* 165(1):315–318.

[26] Daniel SL, Hsu T, Dean SI, Drake HL (1990) Characterization of the H2- and CO-dependent chemolithotrophic potentials of the acetogens Clostridium thermoaceticum and Acetogenium kivui. *J. Bacteriol.* 172(8):4464–71.

[27] Meulepas RJW, et al. (2009) Enrichment of anaerobic methanotrophs in sulfate-reducing membrane bioreactors. *Biotechnol. Bioeng.* 104(3):458–470.

[28] Hu P, et al. (2016) Integrated Bioprocess for Conversion of Gaseous Substrates to Liquids. *Proc. Natl. Acad. Sci.* 113(14).

[29] Bertsch J, Müller V (2015) Bioenergetic constraints for conversion of syngas to biofuels in acetogenic bacteria. *Biotechnol. Biofuels* 8(1):210.

[30] Boysen L, et al. (2016) Earth ' s Future The limits to global-warming mitigation by terrestrial carbon removal Earth ' s Future. *Earth's Futur.* 5(5):1–12.

[31] Long SP, Marshall-Colon A, Zhu XG (2015) Meeting the global food demand of the future by engineering crop photosynthesis and yield potential. *Cell* 161(1):56–66.

[32] Zhu XG, Long SP, Ort DR (2008) What is the maximum efficiency with which photosynthesis can convert solar energy into biomass? *Curr. Opin. Biotechnol.* 19(2):153–159.

[33] Ort DR, Zhu X, Melis A (2011) Optimizing Antenna Size to Maximize Photosynthetic Efficiency. *Plant Physiol.* 155(1):79–85.

[34] Ghosh A, Kiran B (2017) Carbon Concentration in Algae: Reducing CO2 From Exhaust Gas. *Trends Biotechnol.* 35(9):806–808.

[35] Tredici MR, et al. (2015) Energy balance of algal biomass production in a 1-ha "Green Wall Panel" plant: How to produce algal biomass in a closed reactor achieving a high Net Energy Ratio. *Appl. Energy* 154:1103–1111.

[36] Razzak SA, Ali SAM, Hossain MM, DeLasa H (2017) Biological CO2 fixation with production of microalgae in wastewater A review. *Renew. Sustain. Energy Rev.* 76(September 2015):379–390.

[37] Simionato D, Basso S, Giacometti GM, Morosinotto T (2013) Optimization of light use efficiency for biofuel production in algae. *Biophys. Chem.* 182:71–78.

[38] Gates DM, Keegan HJ, Schleter JC, Weidner VR (1965) Spectral Properties of Plants. *Appl. Opt.* 4(1):11.

[39] Blankenship RE, et al. (2011) Comparing Photosynthetic and Photovoltaic Efficiencies and Recognizing the Potential for Improvement. *Science (80-.).* 332(6031).

[40] Lumb MP, et al. (2017) GaSb-Based Solar Cells for Full Solar Spectrum Energy Harvesting. *Adv. Energy Mater.* 7(20):1–9.

[41] Gordon JM, Polle JEW (2007) Ultrahigh bioproductivity from algae. *Appl. Microbiol. Biotechnol.* 76(5):969–975.

[42] Wolf BM, et al. (2018) Characterization of a newly isolated freshwater Eustigmatophyte alga capable of utilizing far-red light as its sole light source. *Photosynth. Res.* 135(1-3):177–189.

[43] Liu C, Colón BC, Ziesack M, Silver PA, Nocera DG (2016) Water splitting-biosynthetic system with CO2 reduction efficiencies exceeding photosynthesis. *Science (80-.).* 352(6290).

[44] Tanaka K, Ishizaki A, Kanamaru T, Kawano T (1995) Production of poly (D-3-hydroxybutyrate) from CO2, H2, and O2 by high cell density autotrophic cultivation of Alcaligenes eutrophus. *Biotechnol. Bioeng.* 45(3):268–275.

[45] Pohlmann A, et al. (2006) Genome sequence of the bioplastic-producing "Knallgas" bacterium Ralstonia eutropha H16. *Nat. Biotechnol.* 24(10):1257–1262.

[46] Fast AG, Papoutsakis ET (2012) Stoichiometric and energetic analyses of non-photosynthetic CO2-fixation pathways to support synthetic biology strategies for production of fuels and chemicals. *Curr. Opin. Chem. Eng.* pp. 1–16.

[47] Xu J, Liu N, Qiao K, Vogg S, Stephanopoulos G (2017) Application of metabolic controls for the maximization of lipid production in semicontinuous fermentation. *Proc. Natl. Acad. Sci.* 114(27):E5308–E5316.

[48] Rodriguez Ca, Modestino Ma, Psaltis D, Moser C (2014) Design and cost considerations for practical solar-hydrogen generators. *Energy Environ. Sci.* 7:3828–3835.

[49] Nybo SE, Khan NE, Woolston BM, Curtis WR (2015) Metabolic engineering in chemolithoautotrophic hosts for the production of fuels and chemicals. *Metab. Eng.* 30:105–120.

[50] Choi S, Song CW, Shin JH, Lee SY (2015) Biorefineries for the production of top building block chemicals and their derivatives. *Metab. Eng.* 28:223–239.

[51] Vennestrøm PNR, Osmundsen CM, Christensen CH, Taarning E (2011) Beyond petrochemicals: The renewable chemicals industry. *Angew. Chemie - Int. Ed.* 50(45):10502–10509.

[52] Hügler M, Sievert SM (2011) Beyond the Calvin Cycle: Autotrophic Carbon Fixation in the Ocean. *Ann. Rev. Mar. Sci.* 3(1):261–289.

[53] Schuchmann K, Müller V (2014) Autotrophy at the thermodynamic limit of life: A model for energy conservation in acetogenic bacteria. *Nat. Rev. Microbiol.* 12(12):809–821.

[54] Bar-Even A, Noor E, Lewis NE, Milo R (2010) Design and analysis of synthetic carbon fixation pathways. *Proc. Natl. Acad. Sci.* 107(19):8889–8894.

[55] Bogorad IW, Lin TS, Liao JC (2013) Synthetic non-oxidative glycolysis enables complete carbon conservation. *Nature* 502(7473):693–7.

[56] Eia (2013) Technically Recoverable Shale Oil and Shale Gas Resources : An Assessment of 137 Shale Formations in 41 Countries Outside the United States, (U.S. Energy Information Administration), Technical Report June.

[57] Berman A, Pittinger L (2011) US Shale Gas: Less Abundance, Higher Cost.

[58] US Department of Energy (2013) Funding Opportunity Announcement - Advanced Research Projects Agency Energy (ARPA-E) - Reducing Emissions Using Methanotrophic Organisms For Transportation Energy (REMOTE).

[59] Tan SH, Barton PI (2015) Optimal dynamic allocation of mobile plants to monetize associated or stranded natural gas, part I: Bakken shale play case study. *Energy* 93:1581–1594.

[60] Tan SH, Barton PI (2016) Optimal dynamic allocation of mobile plants to monetize associated or stranded natural gas, part II: Dealing with uncertainty. *Energy* 96:461–467.

[61] Crumbley AM, Gonzalez R (2018) *Cracking "Economies of Scale": Biomanufacturing on Methane-Rich Feedstock*, eds. Kalyuzhnaya MG, Xing XH. (Springer International Publishing, Cham), pp. 271–292.

[62] Woolston BM (2017) Ph.D. thesis (MIT).

[63] Kalyuzhnaya MG, Puri AW, Lidstrom ME (2015) Metabolic engineering in methanotrophic bacteria. *Metab. Eng.* 29:142–152.

[64] Henard CA, Guarnieri MT (2018) *Metabolic Engineering of Methanotrophic Bacteria for Industrial Biomanufacturing*, eds. Kalyuzhnaya MG, Xing XH. (Springer International Publishing, Cham), pp. 117–132.

[65] Cantera S, et al. (2018) Technologies for the bioconversion of methane into more valuable products. *Curr. Opin. Biotechnol.* 50:128–135.

[66] Thauer RK (2011) Anaerobic oxidation of methane with sulfate: on the reversibility of the reactions that are catalyzed by enzymes also involved in methanogenesis from CO2. *Curr. Opin. Microbiol.* 14(3):292–9.

[67] Nazem-Bokaee H, Yan Z, Maranas CD, Ferry JG (2018) *The Biochemistry and Physiology of Respiratory-Driven Reversed Methanogenesis*, eds. Kalyuzhnaya MG, Xing XH. (Springer International Publishing, Cham), pp. 183–197.

[68] Haroon MF, et al. (2013) Anaerobic oxidation of methane coupled to nitrate reduction in a novel archaeal lineage. *Nature* 500(7464):567–70.

[69] Ettwig KF, et al. (2010) Nitrite-driven anaerobic methane oxidation by oxygenic bacteria. *Nature* 464(7288):543–8.

[70] Beal EJ, House CH, Orphan VJ (2009) Manganese- and iron-dependent marine methane oxidation. *Science* 325(5937):184–7.

[71] Zheng K, Ngo PD, Owens VL, Yang Xp, Mansoorabadi SO (2016) The biosynthetic pathway of coenzyme F430 in methanogenic and methanotrophic archaea. *Science (80-.).* 354(6310).

[72] Prakash D, Wu Y, Suh SJ, Duin EC (2014) Elucidating the process of activation of methyl-coenzyme M reductase. *J. Bacteriol.* 196(13):2491–2498.

[73] Wongnate T, et al. (2016) The radical mechanism of biological methane synthesis by methyl- coenzyme M reductase. *Science (80-.).* 352(6288).

[74] Laso-Pérez R, et al. (2016) Thermophilic archaea activate butane via alkyl-coenzyme M formation. *Nature* 539:396.

[75] Singh R, Guzman MS, Bose A (2017) Anaerobic Oxidation of Ethane, Propane, and Butane by Marine Microbes: A Mini Review .

[76] Nayak DD, Mahanta N, Mitchell DA, Metcalf WW (2017) Post-translational thioamidation of methyl-coenzyme M reductase, a key enzyme in methanogenic and methanotrophic archaea. *Elife* 6(I):1–18.

[77] Deobald D, Adrian L, Schöne C, Rother M, Layer G (2018) Identification of a unique Radical SAM methyltransferase required for the sp3-C-methylation of an arginine residue of methyl-coenzyme M reductase. *Sci. Rep.* 8(1):1–12.

[78] Girguis PR, Cozen A, DeLong EE (2005) Growth and population dynamics of anaerobic methanotrophic archaea in a continuous flow bioreactor. *Appl. Env. Microbiol.* 71(7):3725–3733.

[79] Deusner C, Meyer V, Ferdelman TG (2010) High-pressure systems for gas-phase free continuous incubation of enriched marine microbial communities performing anaerobic oxidation of methane. *Biotechnol. Bioeng.* 105(3):524–533.

[80] Aoki M, et al. (2014) A long-term cultivation of an anaerobic methane-oxidizing microbial community from deep-sea methane-seep sediment using a continuous-flow bioreactor. *PLoS One* 9(8).

[81] Marlow JJ, et al. (2018) Harnessing a methane-fueled, sediment-free mixed microbial community for utilization of distributed sources of natural gas. *Biotechnol. Bioeng.* 115(6):1450–1464.

[82] Vaksmaa A, et al. (2017) Enrichment of anaerobic nitrate-dependent methanotrophic Candidatus Methanoperedens nitroreducens' archaea from an Italian paddy field soil. *Appl. Microbiol. Biotechnol.* 101(18):7075–7084.

[83] Goncearenco A, Berezovsky IN (2012) Exploring the evolution of protein function in Archaea. *BMC Evol. Biol.* 12(1):1.

[84] Soo VWC, et al. (2016) Reversing methanogenesis to capture methane for liquid biofuel precursors. *Microb. Cell Fact.* 15(1):11.

[85] Lyu Z, et al. (2018) *Assembly of methyl coenzyme M reductase in the methanogenic archaeon Methanococcus maripaludis.* Vol. 200.

[86] McAnulty MJ, et al. (2017) Metabolic engineering of Methanosarcina acetivorans for lactate production from methane. *Biotechnol. Bioeng.* 114(4):852–861.

[87] McAnulty MJ, et al. (2017) Electricity from methane by reversing methanogenesis. *Nat. Commun.* 8(May).

[88] Fontaine F, Peterson W, McCoy E, Johnson M, Ritter G (1942) A New Type of Glucose Fermentation by Clostridium thermoaceticum. *J. Bacteriol.* pp. 701–715.

[89] Ragsdale SW, Pierce E (2008) Acetogenesis and the Wood-Ljungdahl pathway of CO(2) fixation. *Biochim. Biophys. Acta* 1784(12):1873–98.

[90] Drake HL, Gössner AS, Daniel SL (2008) Old acetogens, new light. *Ann. N. Y. Acad. Sci.* 1125:100–28.

[91] Kita A, et al. (2012) Development of genetic transformation and heterologous expression system in carboxydotrophic thermophilic acetogen Moorella thermoacetica. *J. Biosci. Bioeng.*

[92] Iwasaki Y, et al. (2013) Engineering of a functional thermostable kanamycin resistance marker for use in Moorella thermoacetica ATCC39073. *FEMS Microbiol. Lett.* 39073:1–5.

[93] Iwasaki Y, et al. (2017) Homolactic Acid Fermentation by the Genetically Engineered Thermophilic Homoacetogen Moorella thermoacetica ATCC 39073. *Appl. Environ. Microbiol.* 83(8):1–13.

[94] Köpke M, et al. (2010) Clostridium ljungdahlii represents a microbial production platform based on syngas. *Proc. Natl. Acad. Sci.* 107(34):15305–15305.

[95] Liew F, et al. (2016) Insights into CO ₂ Fixation Pathway of Clostridium autoethanogenum by Targeted Mutagenesis. *MBio* 7(3):e00427–16.

[96] Hoffmeister S, et al. (2016) Acetone production with metabolically engineered strains of Acetobacterium woodii. *Metab. Eng.* 36:37–47.

[97] Phillips JR, Klasson KT, Clausen EC, Gaddy JL (1993) Biological production of ethanol from coal synthesis gas. *Appl. Biochem. Biotechnol.* 39-40(1):559–571.

[98] Lundie LL, Drake HL (1984) Development of a minimally defined medium for the acetogen Clostridium thermoaceticum. *J. Bacteriol.* 159(2):700–3.

[99] Mock J, et al. (2015) Energy conservation associated with ethanol formation from H2 and CO2 in Clostridium autoethanogenum involving electron bifurcation. *J. Bacteriol.* 197(18):2965–2980.

[100] Ishizaki A, Tanaka K (1990) Batch culture of Alcaligenes eutrophus ATCC 17697T using recycled gas closed circuit culture system. *J. Ferment. Bioeng.* 69(3):170–174.

[101] Valgepea K, et al. (2017) Maintenance of ATP Homeostasis Triggers Metabolic Shifts in Gas-Fermenting Acetogens. *Cell Syst.* pp. 505–515.

[102] Thauer RK, Jungermann K, Decker K (1977) Energy conservation in chemotrophic anaerobic bacteria. *Bacteriol. Rev.* 41(1):100–180.

[103] Fröstl J, Seifritz C, Drake HL (1996) Effect of nitrate on the autotrophic metabolism of the acetogens Clostridium thermoautotrophicum and Clostridium thermoaceticum. *J. Bacteriol.* 178(15):4597–4603.

[104] Arendsen AF, Soliman MQ, Ragsdale SW (1999) Nitrate-dependent regulation of acetate biosynthesis and nitrate respiration by Clostridium thermoaceticum. *J. Bacteriol.* 181(5):1489–1495.

[105] Drake HL, Daniel SL (2004) Physiology of the thermophilic acetogen Moorella thermoacetica. *Res. Microbiol.* 155(10):869–83.

[106] Valgepea K, et al. (2017) Arginine deiminase pathway provides ATP and boosts growth of the gas-fermenting acetogen Clostridium autoethanogenum. *Metab. Eng.* 41(March):202–211.

[107] Fast AG, Schmidt ED, Jones SW, Tracy BP (2015) Acetogenic mixotrophy: novel options for yield improvement in biofuels and biochemicals production. *Curr. Opin. Biotechnol.* 33:60–72.

[108] Jones SW, et al. (2016) CO2 fixation by anaerobic non-photosynthetic mixotrophy for improved carbon conversion. *Nat. Commun.* 7:12800.

[109] Maru BT, Munasinghe PC, Gilary H, Jones SW, Tracy BP (2018) Fixation of CO2 and CO on a diverse range of carbohydrates using anaerobic, non-photosynthetic mixotrophy. *FEMS Microbiol. Lett.* (February):1–8.

[110] Park JO, et al. (2018) Synergistic substrate cofeeding stimulates reductive metabolism. *Nat. Metab.*

[111] Naidu D, Ragsdale S (2001) Characterization of a three-component vanillate O-demethylase from Moorella thermoacetica. *J. Bacteriol.* 183(11):1–7.

[112] Wang S, et al. (2013) NADP-Specific electron-bifurcating [FeFe]-hydrogenase in a functional complex with formate dehydrogenase in clostridium autoethanogenum grown on CO. *J. Bacteriol.* 195(19):4373–4386.

[113] Nevin KP, et al. (2011) Electrosynthesis of organic compounds from carbon dioxide is catalyzed by a diversity of acetogenic microorganisms. *Appl. Environ. Microbiol.* 77(9):2882–2886.

[114] Bajracharya S, et al. (2015) Carbon dioxide reduction by mixed and pure cultures in microbial electrosynthesis using an assembly of graphite felt and stainless steel as a cathode. *Bioresour. Technol.* 195:14–24.

[115] Chen S, et al. (2018) Enhanced electrosynthesis performance of Moorella thermoautotrophica by improving cell permeability. *Bioelectrochemistry* 121(February):151–159.

[116] Choi O, Sang BI (2016) Extracellular electron transfer from cathode to microbes: Application for biofuel production. *Biotechnol. Biofuels* 9(1):1–14.

[117] Kracke F, Vassilev I, Krömer JO (2015) Microbial electron transport and energy conservation - The foundation for optimizing bioelectrochemical systems. *Front. Microbiol.* 6(JUN):1–18.

[118] Ou X, Zhang X, Zhang Q, Zhang X (2013) Life-cycle analysis of energy use and greenhouse gas emissions of gas-to-liquid fuel pathway from steel mill off-gas in China by the LanzaTech process. *Front. Energy* 7(3):263–270.

[119] Ueki T, Nevin KP, Woodard TL, Lovley DR (2014) Converting carbon dioxide to butyrate with an engineered strain of Clostridium ljungdahlii. *MBio* 5(5):19–23.

[120] Nagarajan H, et al. (2013) Characterizing acetogenic metabolism using a genome-scale metabolic reconstruction of Clostridium ljungdahlii. *Microb. Cell Fact.* 12:118.

[121] Seifritz C, Daniel S, Gossner A, Drake H (1993) Nitrate as a preferred electron sink for the acetogen Clostridium thermoaceticum. *J. Bacteriol.* 175(24).

[122] Seifritz C, Fröstl JM, Drake HL, Daniel SL (2002) Influence of nitrate on oxalate- and glyoxylate-dependent growth and acetogenesis by Moorella thermoacetica. *Arch. Microbiol.* 178(6):457–64.

[123] Lorenzen JP, Kroger A, Unden G (1993) Regulation of Anaerobic Respiratory Pathways in Wolinella- Succinogenes by the Presence of Electron-Acceptors. *Arch. Microbiol.* 159:477–483.

[124] Gunsalus RP (1992) Control of electron flow in Escherichia coli: coordinated transcription of respiratory pathway genes. *J. Bacteriol.* 174(22):7069–74.

[125] Klüber H, Conrad R (1998) Effects of nitrate, nitrite, NO and N₂O on methanogenesis and other redox processes in anoxic rice field soil. *FEMS Microbiol. Ecol.* 25(3):301–318.

[126] Bollag JM, Henninger NM (1978) Effects of nitrite toxicity on soil bacteria under aerobic and anaerobic conditions. *Soil Biol. Biochem.* 10(5):377–381.

[127] Weon SY, Lee CW, Lee SI, Koopman B (2002) Nitrite inhibition of aerobic growth of Acinetobacter sp. *Water Res.* 36(18):4471–4476.

[128] Reddy, D., Lancaster, J., and Cornforth D (1983) Nitrite Inhibition of Clostridium botulinum : Electron Spin Resonance Detection of. *Science (80-.).* 221:769–770.

[129] Ragsdale SW, Wood HG (2008) Enzymology of the Acetyl-CoA Pathway of CO2 Fixation. *Crit. Rev. Biochem. Mol. Biol.* 26:261–300.

[130] Lu WP, Schiau I, Cunningham JR, Ragsdale SW (1993) Sequence and expression of the gene encoding the corrinoid/iron-sulfur protein from Clostridium thermoaceticum and reconstitution of the recombinant protein to full activity. *J. Biol. Chem.* 268(8):5605–14.

[131] Seifritz C, Drake HL, Daniel SL (2003) Nitrite as an energy-conserving electron sink for the acetogenic bacterium Moorella thermoacetica. *Curr. Microbiol.* 46(5):329–33.

[132] Pierce E, Becker DF, Ragsdale SW (2010) Identification and Characterization of Oxalate Oxidoreductase, a Novel Thiamine Pyrophosphate-dependent 2-Oxoacid Oxidoreductase That Enables Anaerobic Growth on Oxalate. *J. Biol. Chem.* 285(52):40515–40524.

[133] Tremblay PL, Zhang T, Dar SA, Leang C, Lovley DR (2013) The Rnf Complex of Clostridium ljungdahlii Is a Proton-Translocating Ferredoxin:NAD+ Oxidoreductase Essential for Autotrophic Growth. *MBio* 4(1).

[134] Spinelli JB, Kelley LP, Haigis MC (2017) An LC-MS Approach to Quantitative Measurement of Ammonia Isotopologues. *Sci. Rep.* 7(1):10304.

[135] Reidlinger J, Muller V (1994) Purification of ATP synthase from Acetobacterium woodii and identification as a Na+-translocating F1F0-type enzyme. *Eur. J. Biochem* 223:275–283.

[136] Kita A, Iwasaki Y, Yano S (2012) Isolation of thermophilic acetogens and transformation of them with the pyrF and kan (r) genes. *Biosci. Biotechnol. Biochem.* 77(2):301–306.

[137] Jang YS, Malaviya A, Lee SY (2013) Acetone-butanol-ethanol production with high productivity using Clostridium acetobutylicum BKM19. *Biotechnol. Bioeng.* 110(6):1646–1653.

[138] Bache R, Pfennig N (1981) Selective isolation of Acetobacterium woodii on methoxylated aromatic acids and determination of growth yields. *Arch. Microbiol.* 130(3):255–261.

[139] Mosser M, et al. (2015) Fractionation of yeast extract by nanofiltration process to assess key compounds involved in CHO cell culture improvement. *Biotechnol. Prog.* 31(4):875–82.

[140] Watson TG (1976) Amino-acid pool composition of Saccharomyces cerevisiae as a function of growth rate and amino-acid nitrogen source. *J. Gen. Microbiol.* 96(2):263–268.

[141] Moreno-Vivián C (1999) Prokaryotic nitrate reduction: molecular properties and functional distinction among bacterial nitrate reductases. *J. Bacteriol.* 181(21).

[142] Hasan SM, Hall JB (1975) The physiological function of nitrate reduction in Clostridium perfringens. *J Gen Microbiol* 87(1975):120–128.

[143] Jormakka M, Byrne B, Iwata S (2003) Protonmotive force generation by a redox loop mechanism. *FEBS Lett.* 545(1):25–30.

[144] Pierce E, et al. (2008) The complete genome sequence of Moorella thermoacetica (f. Clostridium thermoaceticum). *Environ. Microbiol.* 10(10):2550–73.

[145] Tschech A, Pfennig N (1984) Growth yield increase linked to caffeate reduction in Acetobacterium woodii. *Arch. Microbiol.* 137(2):163–167.

[146] Imkamp F, Biegel E, Jayamani E, Buckel W, Müller V (2007) Dissection of the caffeate respiratory chain in the acetogen Acetobacterium woodii: Identification of an Rnf-type NADH dehydrogenase as a potential coupling site. *J. Bacteriol.* 189(22):8145–8153.

[147] Biegel E, Muller V (2010) Bacterial Na+-translocating ferredoxin:NAD+ oxidoreductase. *Proc. Natl. Acad. Sci.* 107(42):18138–18142.

[148] Dugar D, Stephanopoulos G (2011) Relative potential of biosynthetic pathways for biofuels and bio-based products. *Nat. Biotechnol.* 29(12):1074–8.

[149] Huang H, Wang S, Moll J, Thauer RK (2012) Electron bifurcation involved in the energy metabolism of the acetogenic bacterium Moorella thermoacetica growing on glucose or H2 plus CO2. *J. Bacteriol.* 194(14):3689–99.

[150] Fujinaga K, et al. (1999) Analysis of genes involved in nitrate reduction in Clostridium perfringens. *Microbiology* 145 (Pt 1(May):3377–3387.

[151] Campbell BJ, et al. (2009) Adaptations to submarine hydrothermal environments exemplified by the genome of Nautilia profundicola. *PLoS Genet.* 5(2):22–25.

[152] Brandt K, et al. (2013) Functional production of the Na+ F1F(O) ATP synthase from Acetobacterum woodii in Escherichia cioli requires the native AtpI. *J. Bioenerg. Biomembr.* 45(1-2):15–23.

[153] Müller V, Bowien S (1995) Differential effects of sodium ions on motility in the homoacetogenic bacteria Acetobacterium woodii and Sporomusa sphaeroides. *Arch. Microbiol.* 164(5):363–369.

[154] Schneider CA, Rasband WS, Eliceiri KW (2012) NIH Image to ImageJ: 25 years of image analysis. *Nat. Methods* 9(7):671–675.

[155] Woolston BM, Emerson DF, Currie DH, Stephanopoulos G (2018) Rediverting carbon flux in Clostridium ljungdahlii using CRISPR Interference (CRISPRi). *Metab. Eng.* 48(September 2017):243–253.

[156] Leang C, Ueki T, Nevin KP, Lovley DR (2013) A genetic system for Clostridium ljungdahlii: a chassis for autotrophic production of biocommodities and a model homoacetogen. *Appl. Environ. Microbiol.* 79(4):1102–9.

[157] Tan Y, Liu J, Chen X, Zheng H, Li F (2013) RNA-seq-based comparative transcriptome analysis of the syngas-utilizing bacterium Clostridium ljungdahlii DSM 13528 grown autotrophically and heterotrophically. *Mol. Biosyst.* 9(11):2775–84.

[158] Stewart V (1993) Nitrate regulation of anaerobic respiratory gene expression in Escherichia coli. *Mol. Microbiol.* 9:425–434.

[159] Zhang JH, Xiao G, Gunsalus RP, Hubbell WL (2003) Phosphorylation triggers domain separation in the DNA binding response regulator NarL. *Biochemistry* 42(9):2552–9.

[160] Maris AE, et al. (2002) Dimerization allows DNA target site recognition by the NarL response regulator. *Nat. Struct. Biol.* 9(10):771–8.

[161] Liu J, Tan Y, Yang X, Chen X, Li F (2013) Evaluation of Clostridium ljungdahlii DSM 13528 reference genes in gene expression studies by qRT-PCR. *J. Biosci. Bioeng.* 116(4):460–464.

[162] VanBogelen RA, Kelley PM, Neidhardt FC (1987) Differential induction of heat shock, SOS, and oxidation stress regulons and accumulation of nucleotides in Escherichia coli. *J. Bacteriol.* 169(1):26–32.

[163] Galhardo RS, Hastings PJ, Rosenberg SM (2007) *Mutation as a stress response and the regulation of evolvability.* Vol. 42, pp. 399–435.

[164] Grabherr MG, et al. (2011) Full-length transcriptome assembly from RNA-Seq data without a reference genome. *Nat. Biotechnol.* 29(7):644–52.

[165] Pedersen S, Reeh S, Friesen JD (1978) Functional mRNA half lives in E. coli. *MGG Mol. Gen. Genet.* 166(3):329–336.

[166] Esquerré T, et al. (2015) Genome-wide investigation of mRNA lifetime determinants in Escherichia coli cells cultured at different growth rates. *BMC Genomics* 16(1):275.

[167] Allais JJ, Louktibi a, Baratti J (1983) Oxidation of methanol by the yeast Pichia pastoris. Purification and properties of the formate dehydrogenase. *Agric. Biol. Chem.* 47(February 2015):2547–2554.

[168] Schüte H, Flossdorf J, Sahm H, Kula MR (1976) Purification and properties of formaldehyde dehydrogenase and formate dehydrogenase from Candida boidinii. *Eur. J. Biochem.* 62:151–160.

[169] Schauer NL, Ferry JG (1982) Properties of formate dehydrogenase in Methanobacterium formicicum. *J. Bacteriol.* 150(1):1–7.

[170] Blanchard JS, Cleland WW (1980) Kinetic and chemical mechanisms of yeast formate dehydrogenase. *Biochemistry* 19(15):3543–3550.

[171] Moran MA, et al. (2013) Sizing up metatranscriptomics. *ISME J.* 7(2):237–243.

[172] Maier T, et al. (2011) Quantification of mRNA and protein and integration with protein turnover in a bacterium. *Mol. Syst. Biol.* 7(511):1–12.

[173] Kracke F, Virdis B, Bernhardt PV, Rabaey K, Krömer JO (2016) Redox dependent metabolic shift in Clostridium autoethanogenum by extracellular electron supply. *Biotechnol. Biofuels* 9(1):249.

[174] Subramanian A, et al. (2005) Gene set enrichment analysis: A knowledge-based approach for interpreting genome-wide expression profiles. *Proc. Natl. Acad. Sci.* 102(43):15545–15550.

[175] Nishino K, Honda T, Yamaguchi A (2005) Genome-Wide Analyses of Escherichia coli Gene Expression Responsive to the BaeSR Two-Component Regulatory System Genome-Wide Analyses of Escherichia coli Gene Expression Responsive to the BaeSR Two-Component Regulatory System. *J. Bacteriol.* 187(5):1763–1772.

[176] Jens M, Rajewsky N (2015) Competition between target sites of regulators shapes post-transcriptional gene regulation. *Nat. Rev. Genet.* 16(2):113–126.

[177] Huang H, et al. (2016) CRISPR/Cas9-based efficient genome editing in Clostridium ljungdahlii, an autotrophic gas-fermenting bacterium. *ACS Synth. Biol.* p. acssynbio.6b00044.

[178] Straub M, Demler M, Weuster-Botz D, Durre P (2014) Selective enhancement of autotrophic acetate production with genetically modified Acetobacterium woodii. *J. Biotechnol.* 178(1):67–72.

[179] Cataldo D, Maroon M, Schrader L, Youngs V (1975) Rapid colorimetric determination of nitrate in plant tissue by nitration of salicylic acid. *Commun. Soil Sci. Plant Anal.* 6(1):71–80.

[180] Strickland J, T.R. Parsons (1972) *A Practical Handbook of Seawater Analysis* ed. Stevenson J. (Fisheries Research Board of Canada, Ottawa) Vol. 167, Second edi edition, pp. 1–310.

[181] Afgan E, et al. (2016) The Galaxy platform for accessible, reproducible and collaborative biomedical analyses: 2016 update. *Nucleic Acids Res.* 44(May):gkw343.

[182] Langmead B, Salzberg SL (2012) Fast gapped-read alignment with Bowtie 2. *Nat. Methods* 9:357.

[183] Kersey PJ, et al. (2016) Ensembl Genomes 2016: More genomes, more complexity. *Nucleic Acids Res.* 44(D1):D574–D580.

[184] Love MI, Huber W, Anders S (2014) Moderated estimation of fold change and dispersion for RNA-seq data with DESeq2. *Genome Biol.* 15(12):550.

[185] Dillies MA, et al. (2013) A comprehensive evaluation of normalization methods for Illumina high-throughput RNA sequencing data analysis. *Brief. Bioinform.* 14(6):671–683.

[186] Clasquin MF, Melamud E, Rabinowitz JD (2012) LC-MS data processing with MAVEN: A metabolomic analysis and visualization engine. *Curr. Protoc. Bioinforma.* (37):14.11.1–14.11.23.

[187] Millard P, Letisse F, Sokol S, Portais JC (2012) IsoCor: Correcting MS data in isotope labeling experiments. *Bioinformatics* 28(9):1294–1296.

[188] Calvio C, et al. (2005) Swarming differentiation and swimming motility in Bacillus subtilis are controlled by swrA, a newly identified dicistronic operon. *J. Bacteriol.* 187(15):5356–5366.

[189] Ha Dg, Kuchma SL, Toole GAO (2014) Plate-Based Assay for Swimming Motility in Pseudomonas aeruginosa. *Methods Mol. Biol.* 1149:59–65.

[190] Morales-Soto N, et al. (2015) Preparation, Imaging, and Quantification of Bacterial Surface Motility Assays. *J. Vis. Exp.* (98):1–10.

[191] Bainotti AE, Yamaguchi K, Nakashimada Y, Nishio N (1998) Kinetics and energetics of Acetobacterium sp. in chemostat culture on methanol-CO2. *J. Ferment. Bioeng.* 85(2):223–229.

[192] Cereghino JL, Cregg JM (2000) Heterologous protein expression in the methylotrophic yeast Pichia pastoris. *FEMS Microbiol Rev* 24(1):45–66.

[193] Anupama, Ravindra P (2000) Value-added food: Single cell protein. *Biotechnol. Adv.* 18(6):459–479.

[194] Olah Ga (2005) Beyond oil and gas: the methanol economy. *Angew. Chem. Int. Ed. Engl.* 44(18):2636–9.

[195] Orr J, et al. (2012) Methanol.

[196] Olah GA, et al. (2015) Single Step Bi-reforming and Oxidative Bi-reforming of Methane (Natural Gas) with Steam and Carbon Dioxide to Metgas (CO-2H ₂) for Methanol Synthesis: Self-Sufficient Effective and Exclusive Oxygenation of Methane to Methanol with Oxygen. *J. Am. Chem. Soc.* 137(27):8720–8729.

[197] Goeppert A, Czaun M, Jones JP, Surya Prakash GK, Olah Ga (2014) Recycling of carbon dioxide to methanol and derived products - closing the loop. *Chem. Soc. Rev.*

[198] Studt F, et al. (2014) Discovery of a Ni-Ga catalyst for carbon dioxide reduction to methanol. *Nat. Chem.* 6(4):320–4.

[199] Anthony C (1982) *The Biochemistry of Methylotrophs.* (Academic Press) Vol. 75, p. 497.

[200] Sahm H (1977) Metabolism of methanol by yeasts. *Adv. Biochem. Eng. Vol. 6* 6:77–103.

[201] Schrader J, et al. (2009) Methanol-based industrial biotechnology: current status and future perspectives of methylotrophic bacteria. *Trends Biotechnol.* 27(2):107–115.

[202] Ochsner AM, Sonntag F, Buchhaupt M, Schrader J, Vorholt JA (2015) Methylobacterium extorquens: methylotrophy and biotechnological applications. *Appl. Microbiol. Biotechnol.* 99(2):517–534.

[203] Woolston BM, King JR, Reiter M, Van Hove B, Stephanopoulos G (2018) Improving formaldehyde consumption drives methanol assimilation in engineered E. coli. *Nat. Commun.* 9(1):2387.

[204] Gottschalk G, Thauer RK (2001) The Na(+)-translocating methyltransferase complex from methanogenic archaea. *Biochim. Biophys. Acta* 1505(1):28–36.

[205] Sauer K, Thauer RK (1997) Methanol: coenzyme M methyltransferase from Methanosarcina barkeri. Zinc dependence and thermodynamics of the methanol: cob (I) alamin methyltransferase. *Eur. J. Biochem.* 249:280–285.

[206] Sauer K, Thauer RK (1998) Methanol:coenzyme M methyltransferase from Methanosarcina barkeri–identification of the active-site histidine in the corrinoid-harboring subunit MtaC by site-directed mutagenesis. *Eur. J. Biochem.* 253(3):698–705.

[207] Sauer K, Thauer RK (1999) Methanol:coenzyme M methyltransferase from Methanosarcina barkeri - substitution of the corrinoid harbouring subunit MtaC by free cob(I)alamin. *Eur. J. Biochem.* 261(3):674–81.

[208] Blaut M, Gottschalk G (1984) Coupling of ATP synthesis and methane formation from methanol and molecular hydrogen in Methanosarcina Ibarkeri. *Eur. J. Biochem.* 141:217–222.

[209] Matthews RG (2001) Cobalamin-dependent methyltransferases. *Acc. Chem. Res.* 34(8):681–9.

[210] Ferry JG (1993) Methanogenesis. p. 536.

[211] Bernacchi S, Rittmann S, H. Seifert A, Krajete A, Herwig C (2014) Experimental methods for screening parameters influencing the growth to product yield (Y_(x/CH4)) of a biological methane production (BMP) process performed with Methanothermobacter marburgensis. *AIMS Bioeng.* 1(2):72–87.

[212] Ivey DKW (1987) Metabolism of Methanol in Acetogenic Bacteria. *Dr. Thesis Univ. Georg.*

[213] Debra K, Ljungdahl LG (1989) PQQ-Dependent Methanol Dehydrogenase from Clostridium thermoautotrophicum. *PQQ Quinoproteins* pp. 35–39.

[214] Tremblay PL, Höglund D, Koza A, Bonde I, Zhang T (2015) Adaptation of the autotrophic acetogen Sporomusa ovata to methanol accelerates the conversion of CO2 to organic products. *Sci. Rep.* 5(May):1–11.

[215] Genthner BRS, Bryant MP (1987) Additional characteristics of one-carbon-compound utilization by Eubacterium limosum and Acetobacterium woodii. *Appl. Environ. Microbiol.* 53(3):471–476.

[216] Kallen RG, Jencks WP (1966) The with Mechanism of the Condensation of Formaldehyde Tetrahydrofolic Acid. *J. Biol. Chem.* 241(24):5851–5863.

[217] Gelwicks JT, Risatti JB, Hayes JM (1989) Carbon isotope effects associated with autotrophic acetogenesis. *Org. Geochem.* 14(4):441–6.

[218] Hu P, Rismani-Yazdi H, Stephanopoulos G (2013) Anaerobic CO2 fixation by the acetogenic bacterium Moorella thermoacetica. *AIChE J.* 00(00):1–8.

[219] Matthews CB, Kuo A, Love KR, Love JC (2018) Development of a general defined medium for Pichia pastoris. *Biotechnol. Bioeng.* 115(1):103–113.

[220] Ghatta AA (2015) Ph.D. thesis (KTH).

[221] Emerson DF, et al. (2017) Theoretical Analysis of Natural Gas Recovery from Marginal Wells with a Deep Well Reactor. *Aiche J.* pp. 1–9.

[222] Wood Da, Nwaoha C, Towler BF (2012) Gas-to-liquids (GTL): A review of an industry offering several routes for monetizing natural gas. *J. Nat. Gas Sci. Eng.* 9:196–208.

[223] Rahmim II (2003) Gas-to-Liquid Technologies: Recent Advances, Economics, Prospects in *26th IAEE Annu. Int. Conf.* (Prague), No. June, pp. 1–36.

[224] Ilk D, Rushing J (2008) Exponential vs. Hyperbolic Decline in Tight Gas Sands: Understanding the Origin and Implications for Reserve Estimates Using Arps' Decline Curves (SPE 116731). *SPE Annu. Tech. Conf.*

[225] Anderson DM, Nobakht M, Moghadam S, Mattar L (2010) Analysis of Production Data from Fractured Shale Gas Wells (SPE 131787). *SPE Annu. Tech. Conf.*

[226] Moskowitz P (2014) The hidden leaks of Pennsylvania's abandoned oil and gas wells.

[227] Townsend-Small A, Ferrara TW, Lyon DR, Fries AE, Lamb BK (2016) Emissions of coalbed and natural gas methane from abandoned oil and gas wells in the United States. *Geophys. Res. Lett.* 43:2283–2290.

[228] Thomas S, Dawe RA (2003) Review of ways to transport natural gas energy from countries which do not need the gas for domestic use. *Energy* 28(14):1461–1477.

[229] Webb S, Pachymuthu L (2010) Shell becomes biggest investor in Qatar - executive.

[230] Royal Dutch Shell plc (2013) Shell will not pursue US Gulf Coast GTL project.

[231] McGroarty P, Sider A (2015) Scrapped: Oil Prices Shelve an $11 Billion Gulf Coast Project.

[232] Mueller TJ, et al. (2014) Methane oxidation by anaerobic archaea for conversion to liquid fuels. *J. Ind. Microbiol. Biotechnol.* 42(3):391–401.

[233] Nazem-Bokaee H, Gopalakrishnan S, Ferry JG, Wood TK, Maranas CD (2016) Assessing methanotrophy and carbon fixation for biofuel production by Methanosarcina acetivorans. *Microb. Cell Fact.* 15(1):10.

[234] Kraakman NJR, Rocha-Rios J, Van Loosdrecht MCM (2011) Review of mass transfer aspects for biological gas treatment. *Appl. Microbiol. Biotechnol.* 91(4):873–886.

[235] Bredwell MD, Srivastava P, Worden RM (1999) Reactor design issues for synthesis-gas fermentations. *Biotechnol. Prog.* 15(5):834–844.

[236] Jacobs T (2013) Gas-to-Liquids Comes of Age in a World Full of Gas (SPE-0813-0068). *J. Pet. Technol.* (August):68–73.

[237] Montgomery SL, Jarvie DM, Bowker Ka, Pollastro RM (2005) Mississippian Barnett Shale, Fort Worth basin, north-central Texas: Gas-shale play with multi-trillion cubic foot potential. *Am. Assoc. Pet. Geol. Bull.* 89(2):155–175.

[238] Baihly J, Altman R, Malpani R, Luo F (2010) Shale gas production decline trend comparison over time and basins (SPE 135555). *SPE Annu. Tech. Conf.*

[239] Hikita H, Asai S, Tanigawa K, Segawa K, Kitao M (1981) The volumetric liquid-phase mass transfer coefficient in bubble columns. *Chem. Eng. J.* 22(1):61–69.

[240] Deckwer W, Schumpe A (1993) Improved tools for bubble column reactor design and scale-up. *Chem. Eng. Sci.* 48(5):889–911.

[241] Krishna R, Van Baten JM (2003) Mass transfer in bubble columns. *Catal. Today* 79-80:67–75.

[242] Akita K, Yoshida F (1973) Gas Holdup and Volumetric Mass Transfer Coefficient in Bubble Columns. *Ind. Eng. Chem. Process Des. Dev.* 12(1):76–80.

[243] Han L, Al-Dahhan MH (2007) Gas-liquid mass transfer in a high pressure bubble column reactor with different sparger designs. *Chem. Eng. Sci.* 62(1-2):131–139.

[244] Krishna R, Wilkinson P, Van Dierendonck L (1991) A model for gas holdup in bubble columns incorporating the influence of gas density on flow regime transitions. *Chem. Eng. Sci.* 46(10):2491–2496.

[245] Kantarci N, Borak F, Ulgen KO (2005) Bubble column reactors. *Process Biochem.* 40(7):2263–2283.

[246] Lide DR, Haynes W, eds. (2010) *CRC Handbook of Chemistry and Physics.* (CRC Press), 90th edition, pp. 8–82.

[247] Vargaftik N, Volkov B, Voljak L (1983) International Tables of the Surface Tension of Water. *J. Phys. Chem. Ref. Data* 12(3):817–820.

[248] Poling BE, Prausnitz JM, O'Connell JP (2001) *The Properties of Gases and Liquids (5th edition).* 5th edition, pp. 11.21 – 11.23.

[249] Burruss RC, Ryder RT (2003) Composition of crude oil and natural gas produced from 14 wells in the Lower Silurian Clinton sandstone and Medina Group, northeastern Ohio and northwestern Pennsylvania. *USGS Open File Rep.* (03-409):1–70.

[250] Cady HP, McFarland DF (1907) The Occurrence Of Helium In Natural Gas And The Composition Of Natural Gas. *J. Am. Chem. Soc.* 29(11):1523–1536.

[251] Jähne B, Heinz G, Dietrich W (1987) Measurement of the diffusion coefficients of sparingly soluble gases in water. *J. Geophys. Res.* 92(C10):10767–10776.

[252] Witherspoon P, Bonoli L (1969) Correlation of Diffusion Coefficients for Paraffin, Aromatic, and Cycloparaffin Hydrocarbons in Water. *Ind. Eng. Chem. Fundam.* 8(3):589–591.

[253] Ukai T, Kodama D, Miyazaki J, Kato M (2002) Solubility of methane in alcohols and saturated density at 280.15 K. *J. Chem. Eng. Data* 47(5):1320–1323.

[254] Monod J (1949) The Growth of Bacterial Cultures. *Annu. Rev. Microbiol.* 3:371–394.

[255] Gandhi AB, Gupta PP, Joshi JB, Jayaraman VK, Kulkarni BD (2009) Development of unified correlations for volumetric mass-transfer coefficient and effective interfacial area in bubble column reactors for various gas-liquid systems using support vector regression. *Ind. Eng. Chem. Res.* 48(9):4216–4236.

[256] Evans PN, et al. (2015) Methane metabolism in the archaeal phylum Bathyarchaeota revealed by genome-centric metagenomics. *Science* 350(6259):434–8.

[257] Wegener G, Krukenberg V, Riedel D, Tegetmeyer HE, Boetius A (2015) Intercellular wiring enables electron transfer between methanotrophic archaea and bacteria. *Nature* 526:587–590.

[258] Scheller S, Yu H, Chadwick GL, Mcglynn SE, Orphan VJ (2016) Artificial electron acceptors decouple archael methane oxidation from sulfate reduction. *Science (80-.).* 351(6274):703–707.

[259] Bedard C, Knowles R (1989) Physiology, Biochemistry, and Specific Inhibitors of CH4, NH4+, and CO Oxidation by Methanotrophs and Nitrifiers. *Microbiol. Rev.* 53(1):68–84.

[260] Hammond C, et al. (2012) Direct catalytic conversion of methane to methanol in an aqueous medium by using copper-promoted Fe-ZSM-5. *Angew. Chemie* 51(21):5129–33.

[261] Puri AW, et al. (2015) Genetic Tools for the Industrially Promising Methanotroph Methylomicrobium buryatense. *Appl. Environ. Microbiol.* 81(5):1775–1781.

[262] Chen C, Ren N, Wang A, Yu Z, Lee DJ (2008) Simultaneous biological removal of sulfur, nitrogen and carbon using EGSB reactor. *Appl. Microbiol. Biotechnol.* 78(6):1057–1063.

[263] Nielsen PH (1985) Oxidation of sulfide and thiosulfide and storage of sulfur granules in Thiorthirx from activated sludge. *Water Sci. Technol.* 17:167–181.

[264] Harwood JH, Pirt SJ (1972) Quantitative aspects of growth of the methane oxidizing bacterium Methylococcus capsulatus on methane in shake flask and continuous chemostat culture. *J. Appl. Bacteriol.* 35(4):597–607.

[265] Maloney JO (2008) *Perry's Chemical Engineers' Handbook 8th Edition (Section 4).*

[266] (2015) PA Abandoned & Orphaned Well Program, (Department of Environmental Protection), Technical report.

Appendix A

Supporting Information - Enhancing autotrophic growth of *Clostridium ljungdahlii* through nitrate supplementation

A.1 Elemental Composition of *C. ljungdahlii* Biomass and Yeast Extract

The elemental composition of *C. ljungdahlii* and the yeast extract (YE) supplement were measured. The main purpose was for the closure of the carbon and nitrogen balance with the composition of *C. ljungdahlii*, for which biomass was approximately 10% of the total (**Table** 2.1). Measurements were taken from cultures grown on H_2+CO_2 and H_2+CO_2+NO_3^- to ensure there were no large deviations under the two conditions. Such a situation was unlikely, however the reducing agent, cysteine, could have acted as a source of reducing equivalents (similar to H_2). This is not without precedent as seen in S metabolism of certain bacteria with nitrate [262, 263].

The composition of YE also was used to close the mass balance, as it would indicate an upper threshold of C and N that YE could contribute to observed metabolite

products.

Under the two growth conditions, the elemental composition of *C. ljungdahlii* remained largely unchanged. The only notable exception was an increase in the S percentage, increasing from 1.03 ± 0.06 to 2.20 ± 0.27 %. While doubling the sulfur composition was a substantial relative change, the absolute change is small in comparison to the H_2 or nitrate consumed, and acetate produced.

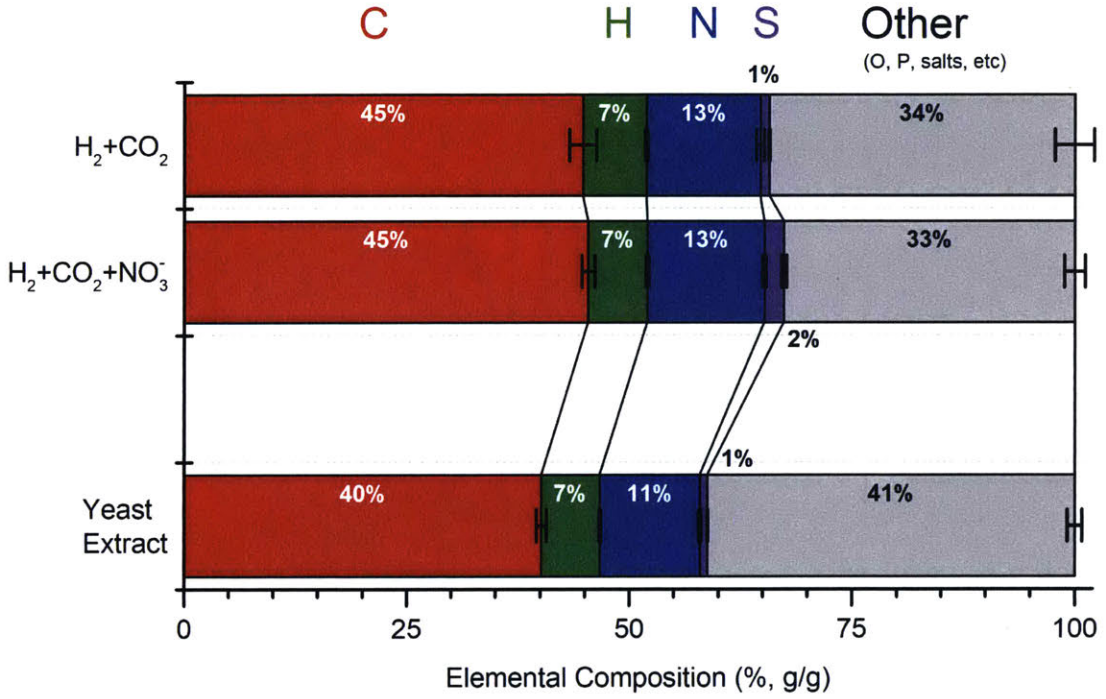

Figure A-1: The elemental composition of *C. ljungdahlii* grown on H_2+CO_2 or H_2+CO_2+NO_3^-, and the elemental composition of yeast extract used as a growth supplement in the PETC media. The composition of C, H, N, and S are given, and the remaining other elements were grouped and were likely composed of O, P, and various salts. Measurements were preformed at the end of growth phase (**Figure** 2-14) and standard deviation was provide for biological triplicates. Red, Carbon; Green, Hydrogen; Blue, Nitrogen; Purple, Sulfur; Gray, Other.

Assuming that the majority of elements in the 'other' category was oxygen, the molecular formula and weight were determined for *C. ljungdahlii* and YE. For *C. ljungdahlii*, the molecular formula was $C_1H_{1.76}N_{0.25}S_{0.018}O_{0.54}$. For YE, the molecular formula was $C_1H_{1.95}N_{0.24}S_{0.008}O_{0.77}$, and the molecular weight was 29.90 g/mol. The molecular formula and weight were used to approximate the H_2-equivalents present 0.1 g/L YE using the degree of reduction [148]. Within 0.1 g/L YE, there were

approximately 6.15 mM H_2-equivalents (2 e^- per H_2).

$$DegRed = 4C + 1H - 3N - 2S - 2O \tag{A.1}$$

$$DegRed = 4(1) + 1(1.95) - 3(0.24) - 2(0.008 + 0.77) = 3.67\frac{e^-}{mol} \tag{A.2}$$

A.2 Correcting H_2 Balance by Accounting for Loss to Pressure Gauge

To ensure the accurate measurement of moles of H_2 consumed when preparing the H_2 balance (**Table** 2.6), the volume of gas lost during the measurement, within the gauge, was determined with **Equations** A.3 - A.5.

$$P_1V_1 = nRT \tag{A.3}$$

$$P_2(V_1 + V_2) = nRT \tag{A.4}$$

$$V_2 = (P_1 - P_2)V_1/P_2 \tag{A.5}$$

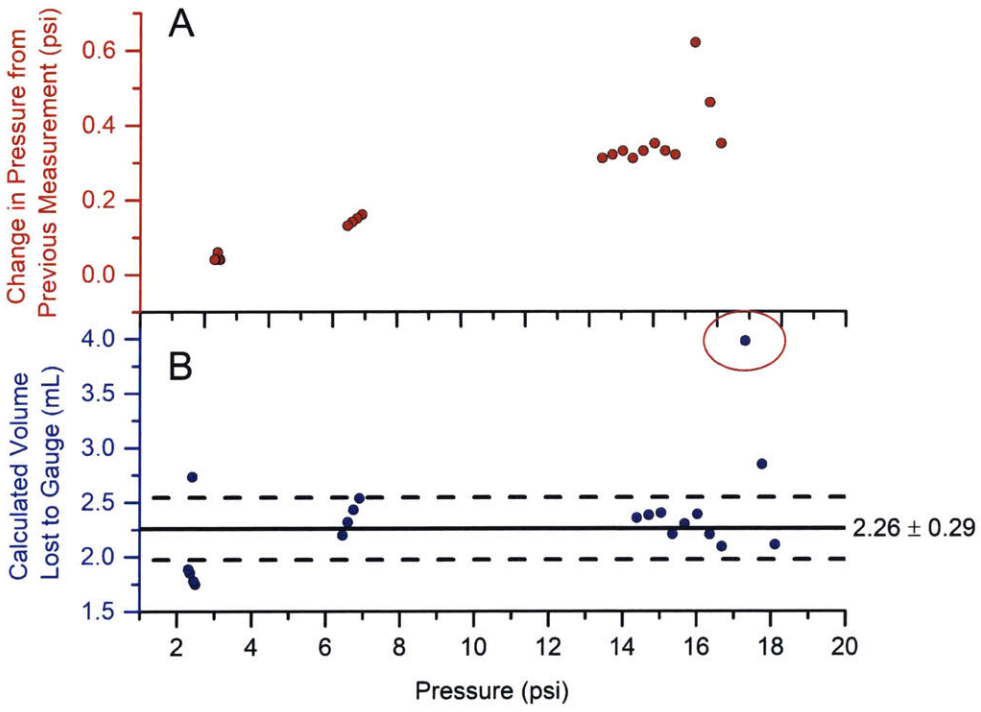

Figure A-2: The deadspace volume of the pressure gauge used to determine headspace pressure was measured to ensure accurate calculation of H_2 consumption (Chapter 2). A serum bottle was prepared with 50 mL of media, and pressurized to approximately 20 psig. The pressure was measure repeatedly, resulting in loss of pressure (A). From this change in pressure (ΔP), the volume in the pressure gauge was calculated with the ideal gas law. The data point circled in red was an outlier and was excluded when calculating the average volume in the pressure gauge.

A.3 qPCR Primers

Table A.1: qRT-PCR primers for standard curve and for qPCR.

Gene	Primer	Sequence	Function
RecA	RecA-std-f	GAATGGTAATAGCTGCAAGTCCT	Standard curve
	RecA-std-r	TCACATGAACACCTCCTTTGCT	
	RecA-q-f	ATGTGGATGCCATTTCAACA	qPCR
	RecA-q-r	TGCCACCGTAGTCTTACCTG	
16s RNA	16sRNA-std-f	CACATGGAGACTGATTTAAAGG	Standard curve
	16sRNA-std-r	AGTTAGACTACGGACTTCGG	
	16sRNA-q-f	GCGAAGAACCTTACCTGGAC	qPCR
	16sRNA-q-r	GGACTTAACCTAACATCTCACGA	
Fhs	Fhs-std-f	CTTAGACACTGAACTCCTACAC	Standard curve
	Fhs-std-r	TCTCCTTACGATTCCAATGAG	
	Fhs-q-f	TACTACTTGAGCATATCCACCT	qPCR
	Fhs-std-r	ACAGCTATAAACCCAACACCT	
RnfC	RnfC-std-f	CTTGTCCTGGTGATAATGCT	Standard curve
	RnfC-std-r	TCTTTATCTGTGCTTCCGCC	
	RnfC-q-f	GTTTATTCCCGTTAGACAGCA	qPCR
	RnfC-std-r	CTCCTATATCTACAACCTTTCCAG	
Putative Nitrate Catalytic Subunit	NitCat-std-f	CCTCCTCTAAAGTAATAGCGTG	Standard curve
	NitCat-std-r	TTTAGCTGTAGGAATGGGTG	
	NitCat-q-f	ATTCCTCGTTATTTGCCCAG	qPCR
	NitCat-q-r	GATGTTCCTTGTGAGATGATACC	
Putative Nitrate Permease	NitPerm-std-f	AAGTTTCAAAGGCATCCTCCCA	Standard curve
	NitPerm-std-r	TTATAGGAATGACAGAACCGCAG	
	NitPerm-q-f	CTTCCAAATGTAGCACTGCCA	qPCR
	NitPerm-q-r	CTTGTTCTCTTCCCACTCCTG	

A.4 DESeq2 Statistical Analysis of Nitrate RNAseq Data and Galaxy Workflow

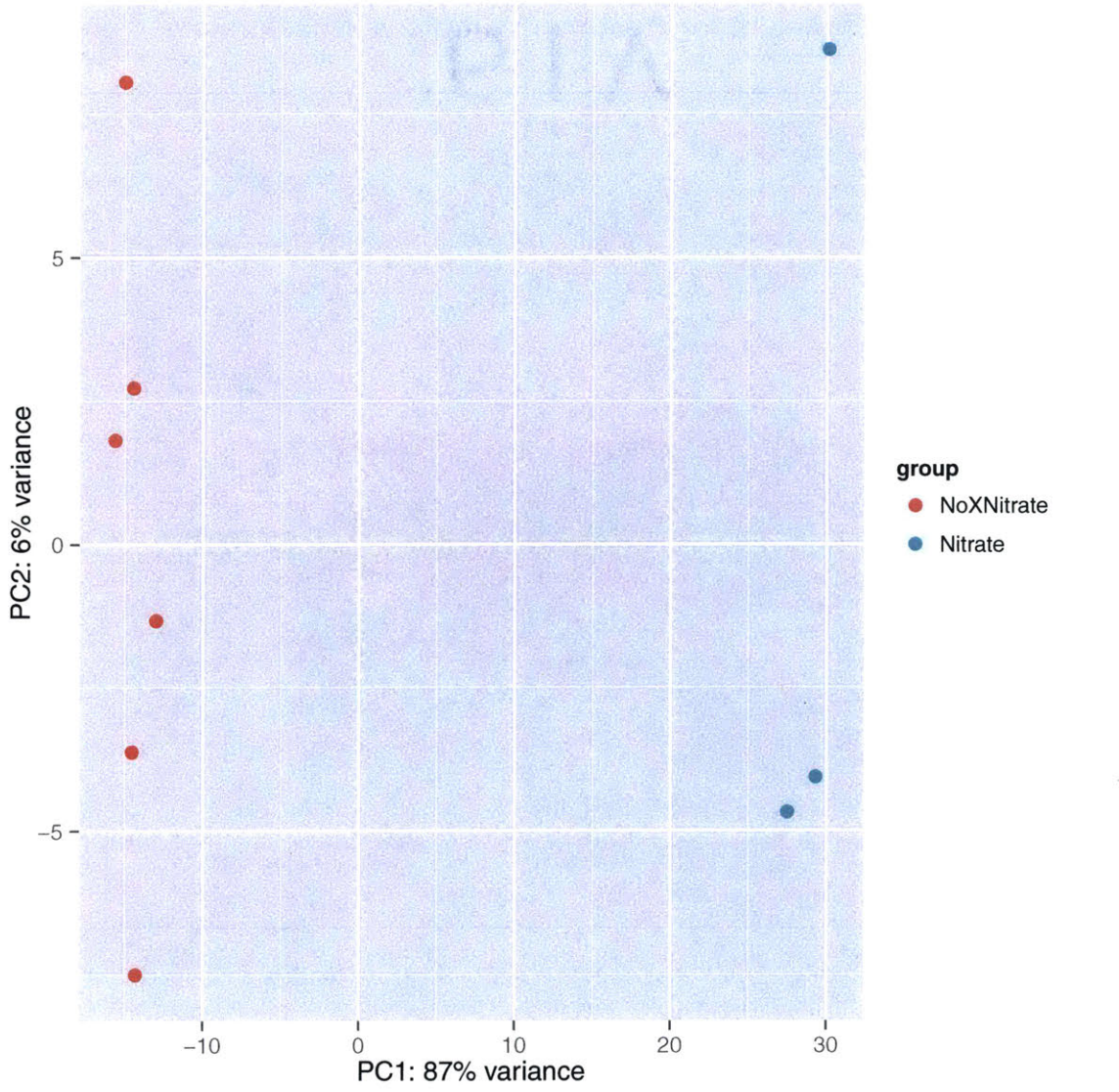

Figure A-3: Principal Component Analysis (PCA) scatter plot of RNAseq data when grown on H_2+CO_2+NO_3^- vs. H_2+CO_2.

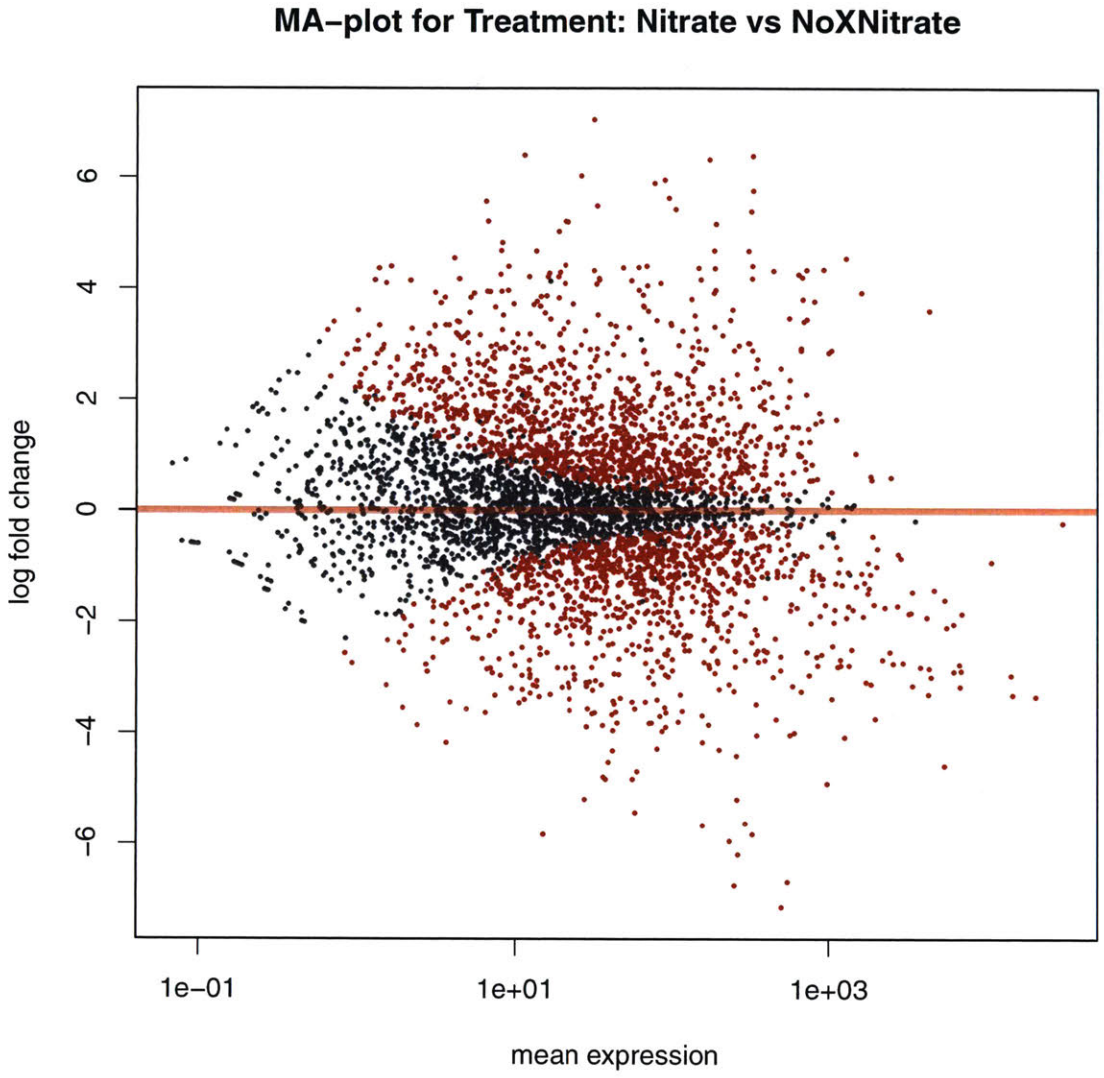

Figure A-4: MA plot (log ratio and mean average scales) scatter plot of RNAseq data when grown on H_2+CO_2+NO_3^- vs. H_2+CO_2. Points were colored red when the adjust p value was less than 0.1.

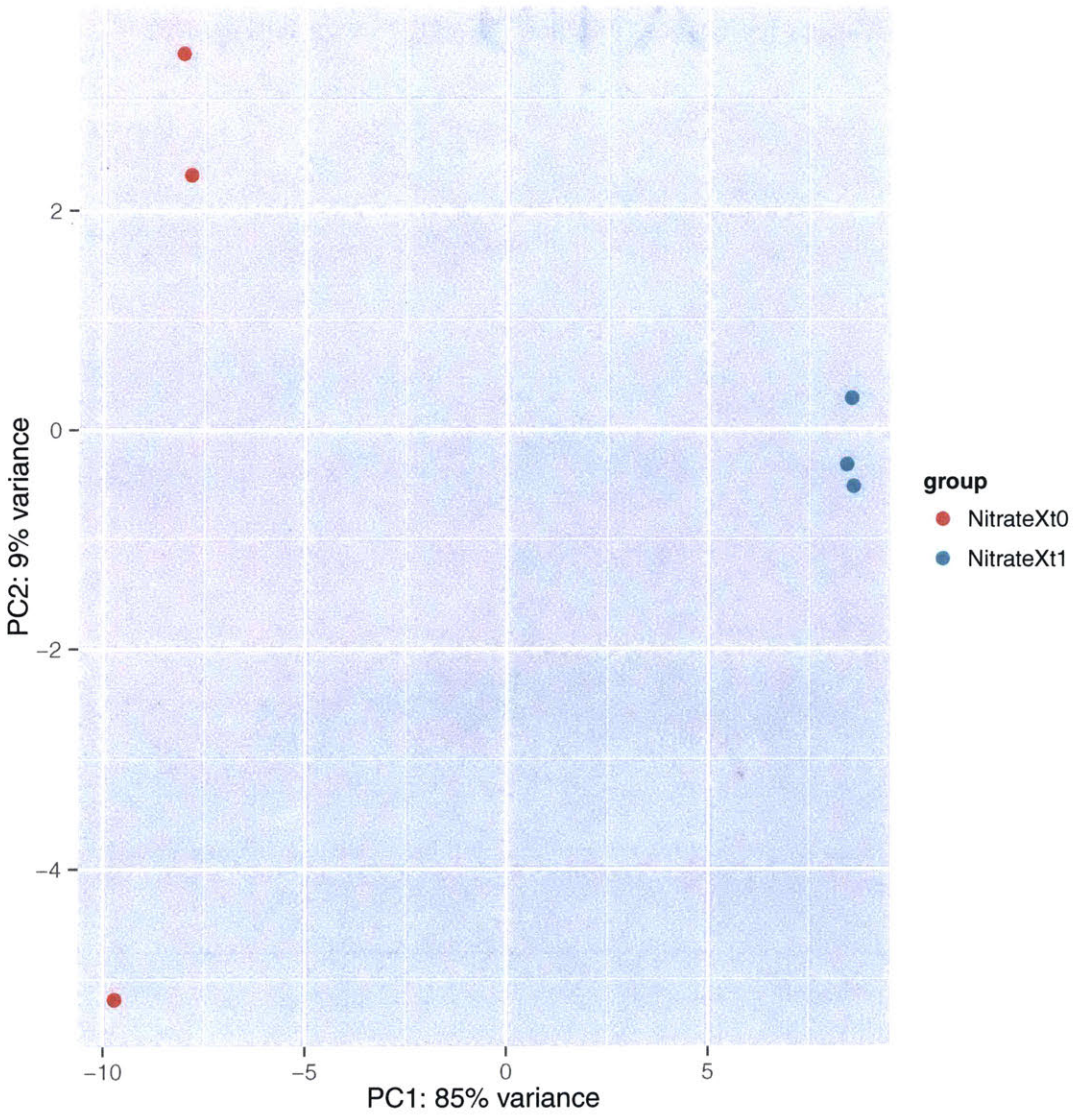

Figure A-5: Principal Component Analysis (PCA) scatter plot of RNAseq data when grown on H_2+CO_2, before and after receiving a spike of nitrate

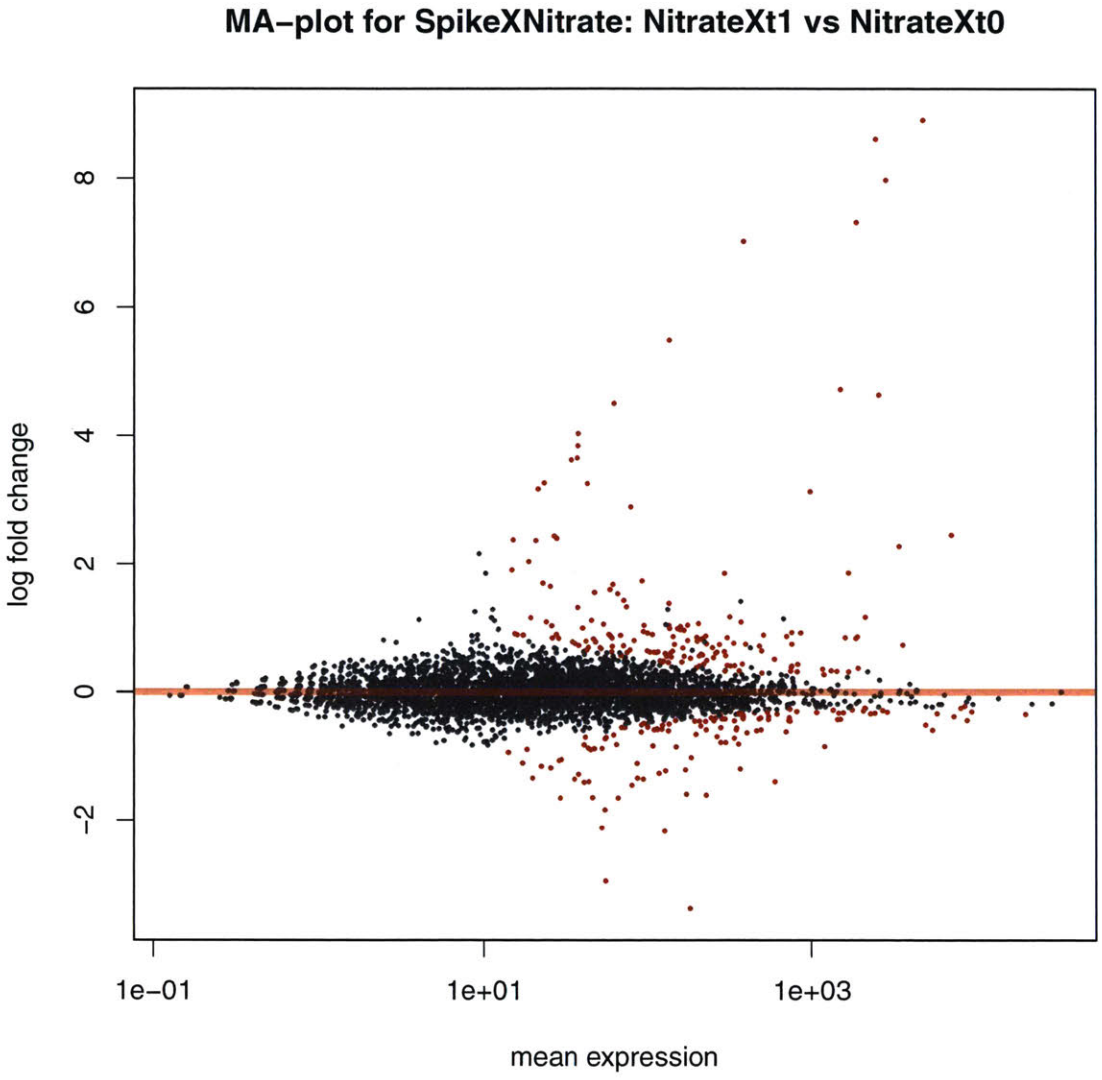

Figure A-6: MA plot (log ratio and mean average scales) scatter plot of RNAseq data when grown on H_2+CO_2, before and after receiving a spike of nitrate. Points were colored red when the adjust p value was less than 0.1.

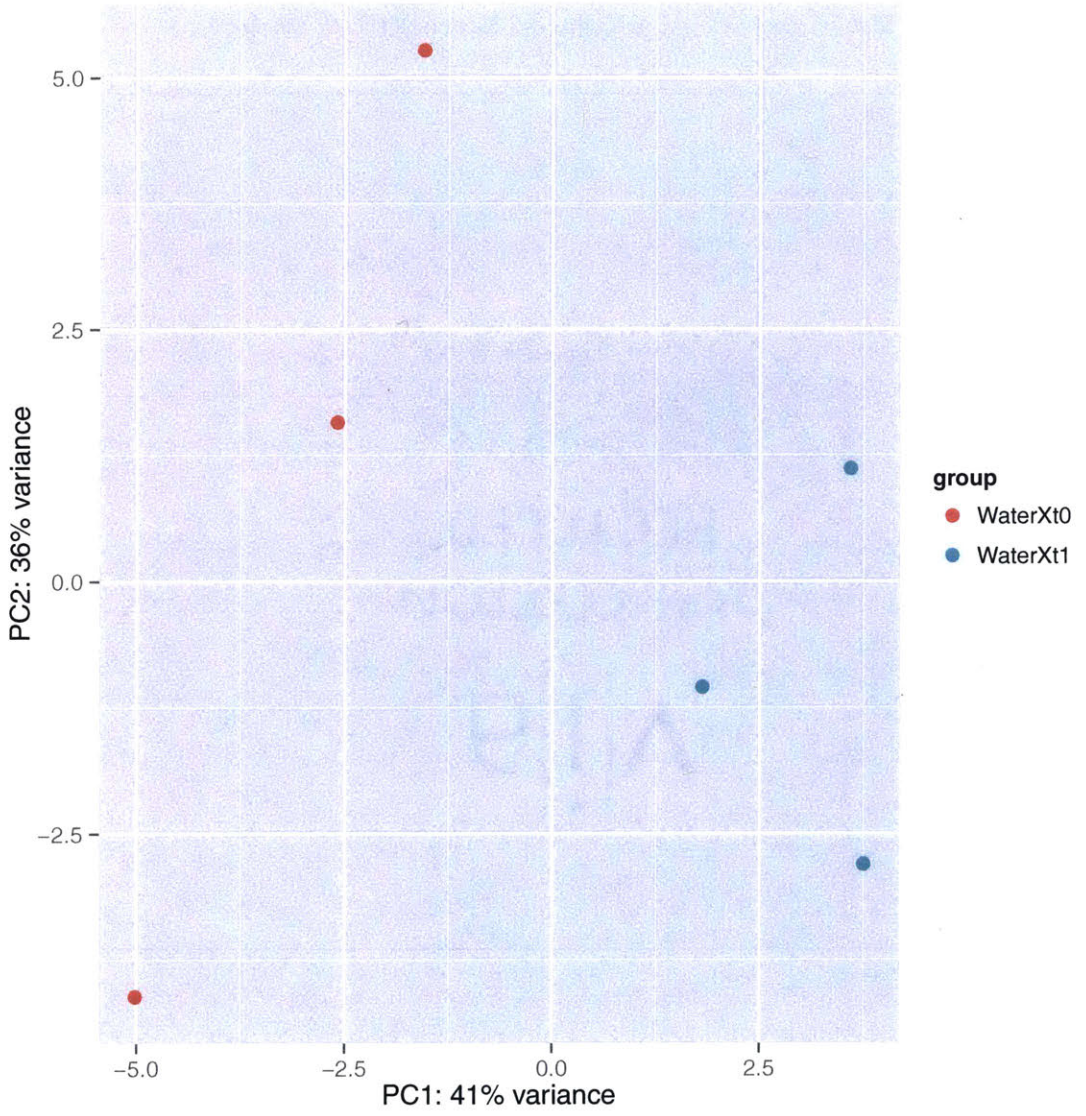

Figure A-7: Principal Component Analysis (PCA) scatter plot of RNAseq data when grown on H_2+CO_2, before and after receiving a spike of water

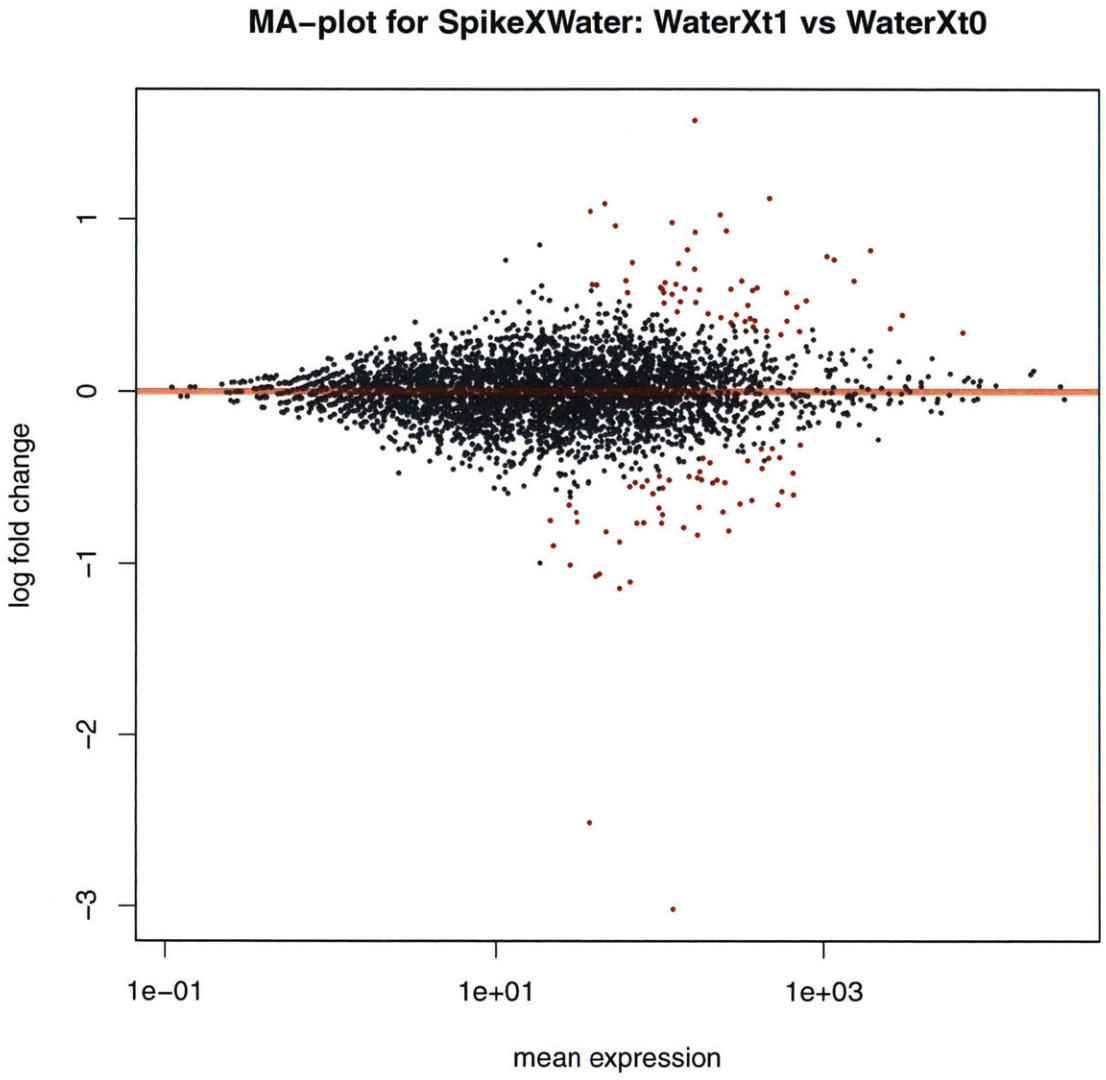

Figure A-8: MA plot (log ratio and mean average scales) scatter plot of RNAseq data when grown on H_2+CO_2, before and after receiving a spike of water. Points were colored red when the adjust p value was less than 0.1.

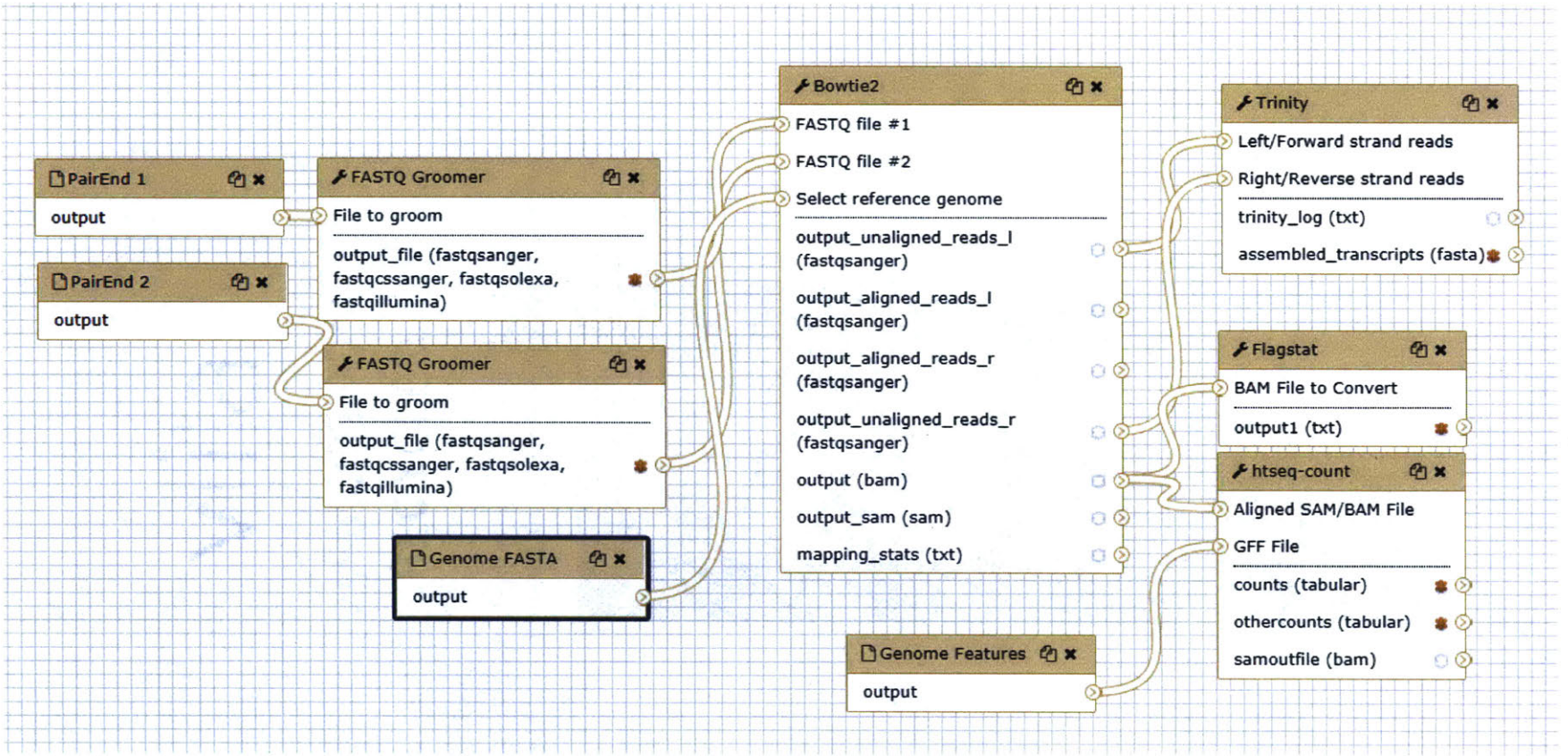

Figure A-9: Galaxy workflow for RNAseq data analysis.

A.5 GSEA Analysis of RNAseq Data

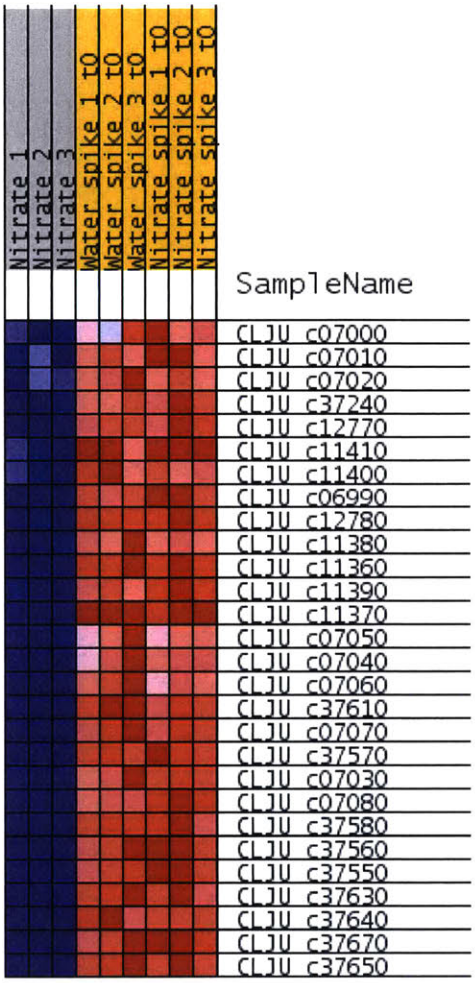

Figure A-10: GSEA gene abundance of the WLP; red represents up-regulation under those conditions and blue represents down-regulation.

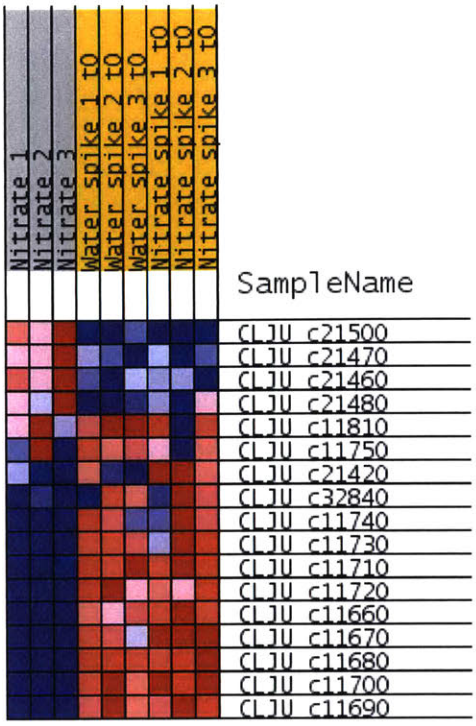

Figure A-11: GSEA gene abundance of histidine metabolism; red represents up-regulation under those conditions and blue represents down-regulation.

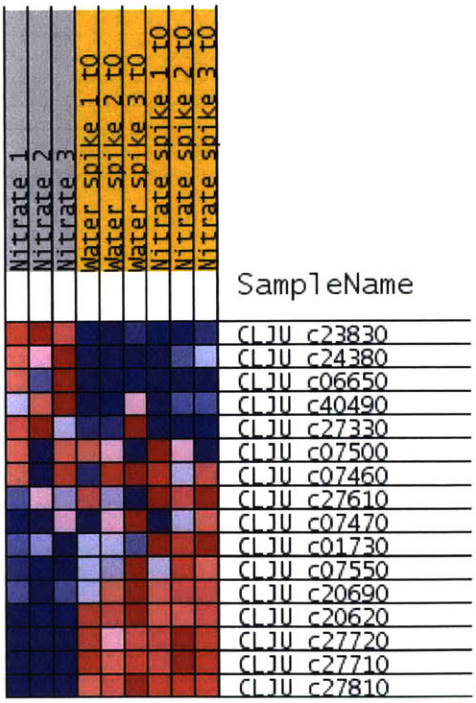

Figure A-12: GSEA gene abundance of selenocompound metabolism; red represents up-regulation under those conditions and blue represents down-regulation.

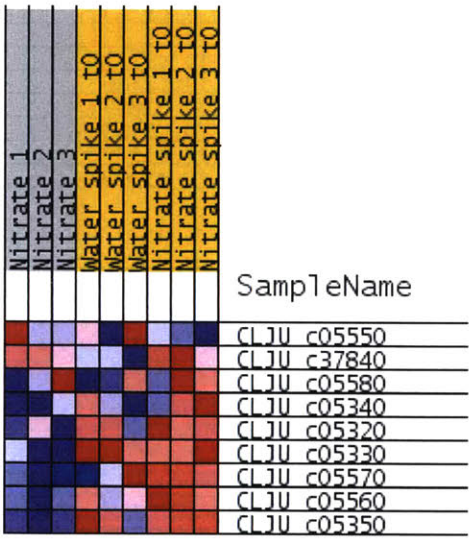

Figure A-13: GSEA gene abundance of polyketide biosynthesis; red represents up-regulation under those conditions and blue represents down-regulation.

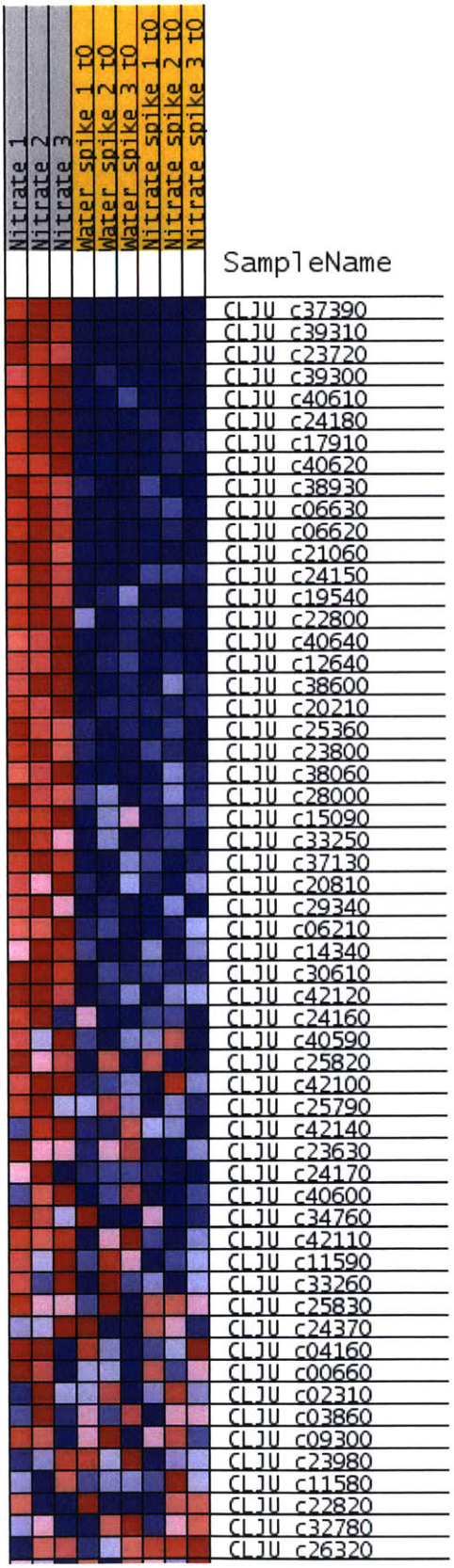

Figure A-14: GSEA gene abundance of carbon metabolism; red represents up-regulation under those conditions and blue represents down-regulation.

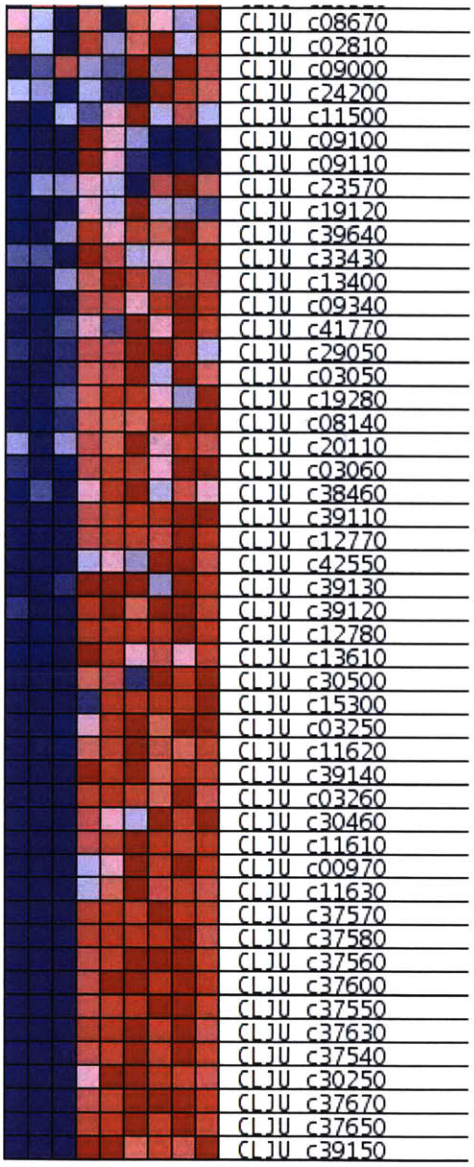

Figure A-15: (Continued) GSEA gene abundance of carbon metabolism; red represents up-regulation under those conditions and blue represents down-regulation.

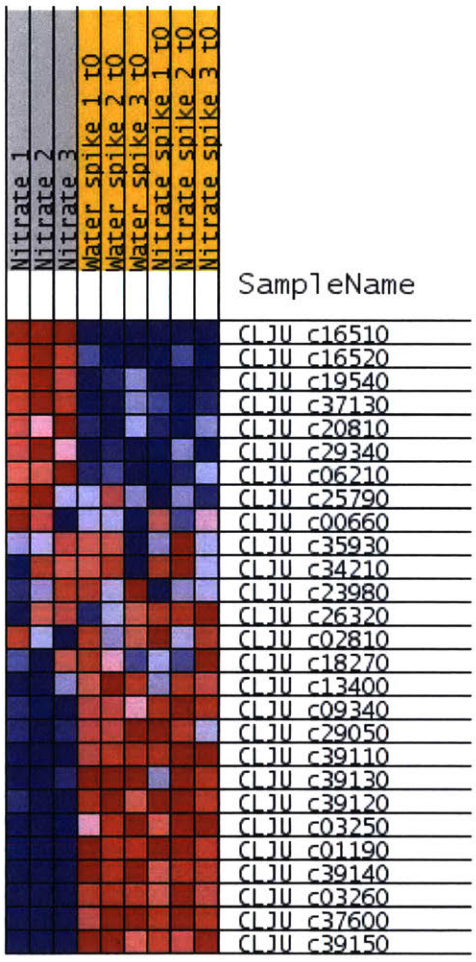

Figure A-16: GSEA gene abundance of gluconeogenesis; red represents up-regulation under those conditions and blue represents down-regulation.

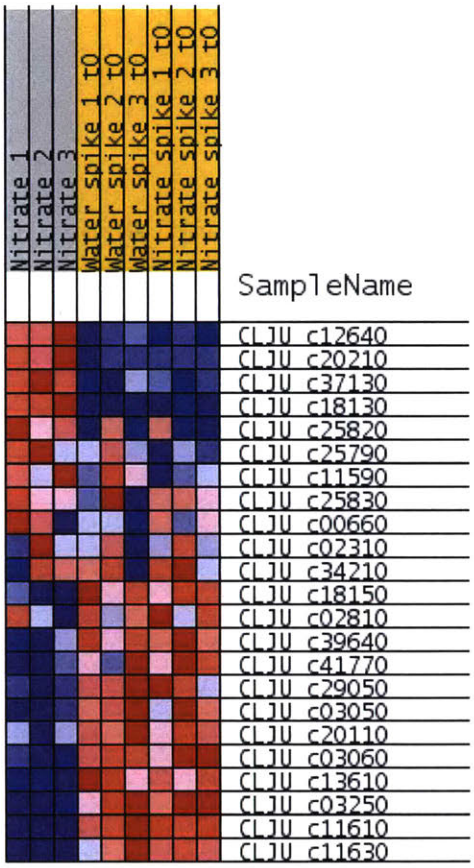

Figure A-17: GSEA gene abundance of the pentose phosphate pathway; red represents up-regulation under those conditions and blue represents down-regulation.

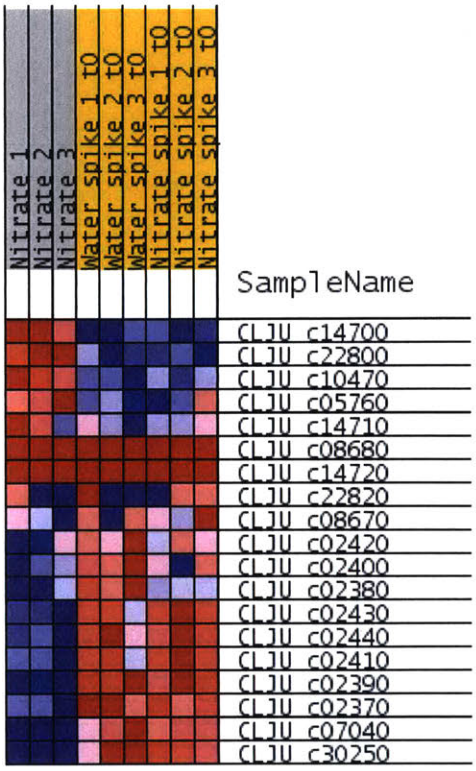

Figure A-18: GSEA gene abundance of oxidative phosphorylation; red represents up-regulation under those conditions and blue represents down-regulation.

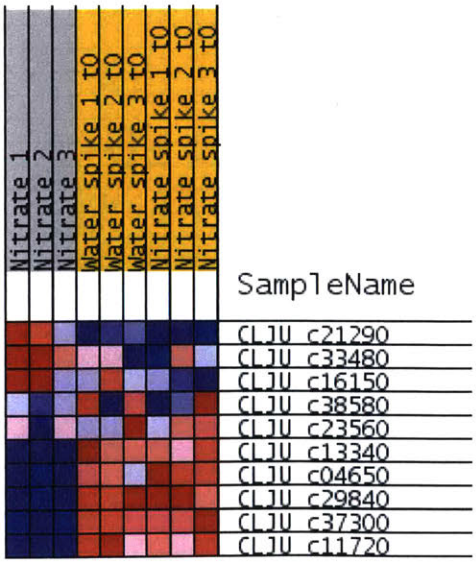

Figure A-19: GSEA gene abundance of phenylalanine metabolism; red represents up-regulation under those conditions and blue represents down-regulation.

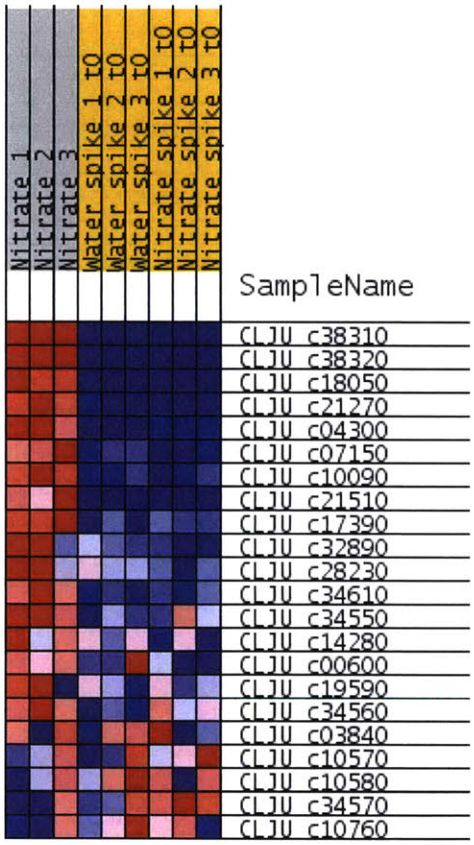

Figure A-20: GSEA gene abundance of lysine metabolism; red represents up-regulation under those conditions and blue represents down-regulation.

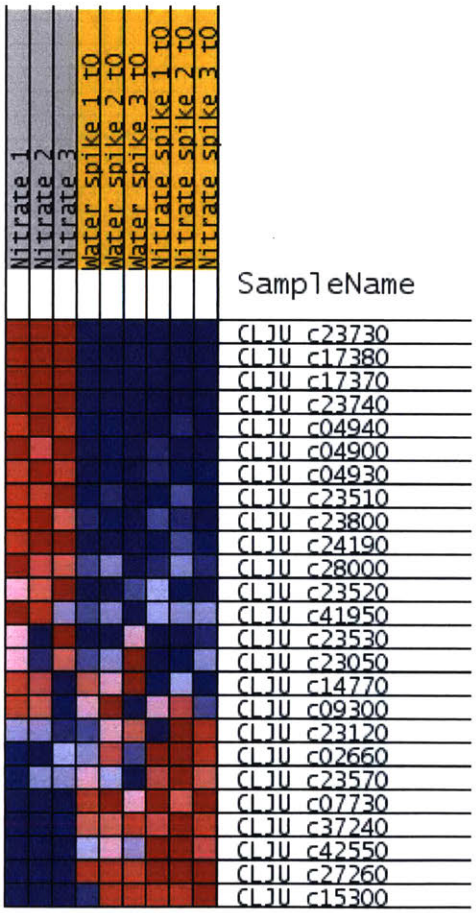

Figure A-21: GSEA gene abundance of nitrogen metabolism; red represents up-regulation under those conditions and blue represents down-regulation.

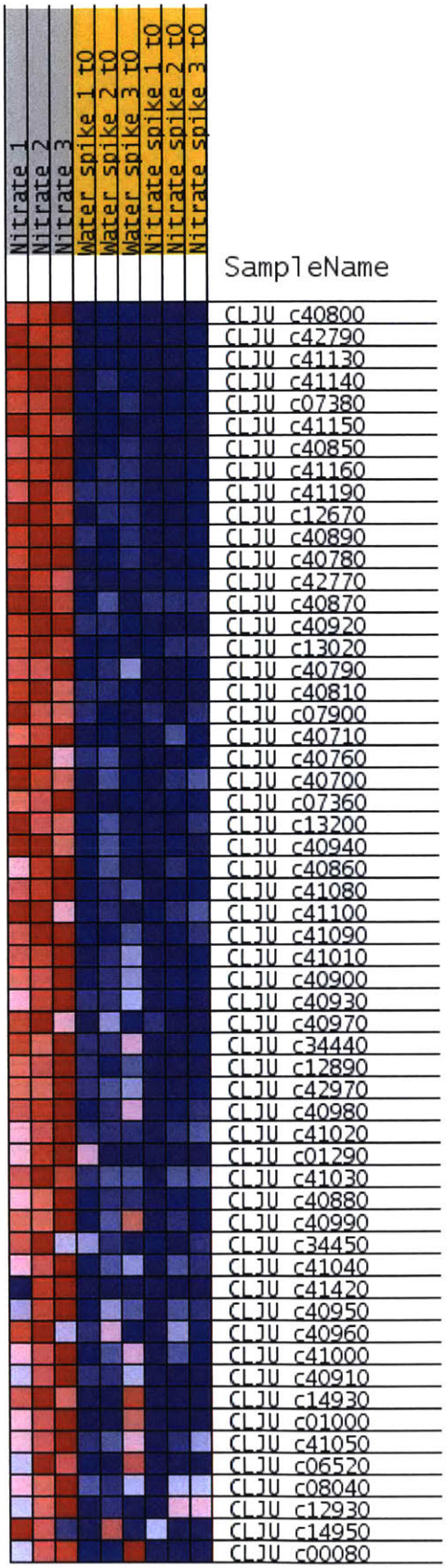

Figure A-22: GSEA gene abundance of ribosome production; red represents up-regulation under those conditions and blue represents down-regulation.

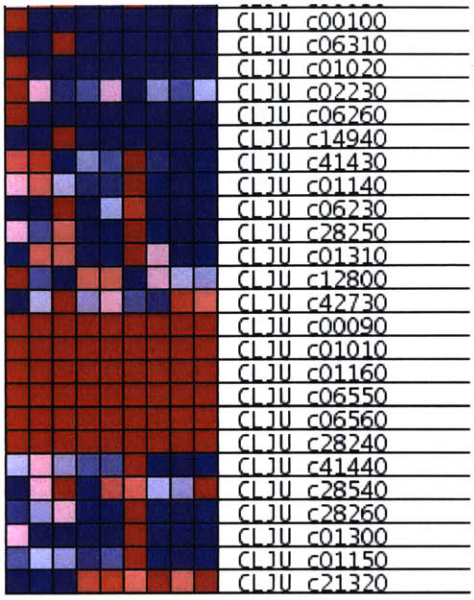

Figure A-23: (Continued) GSEA gene abundance of ribosome production; red represents up-regulation under those conditions and blue represents down-regulation.

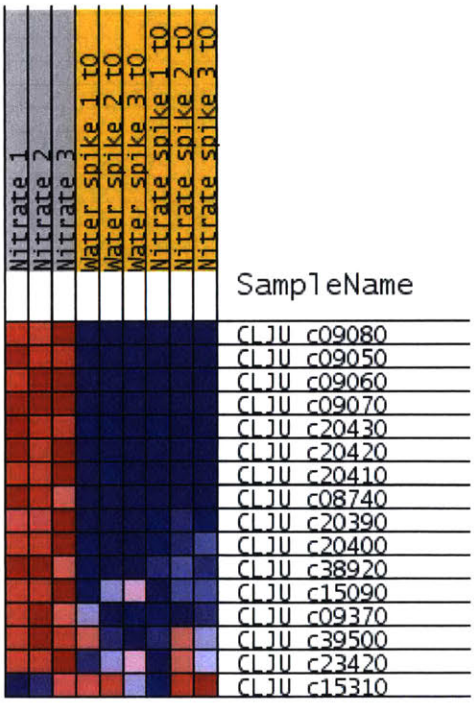

Figure A-24: GSEA gene abundance of valine, leucine, and isoleucine biosynthesis; red represents up-regulation under those conditions and blue represents down-regulation.

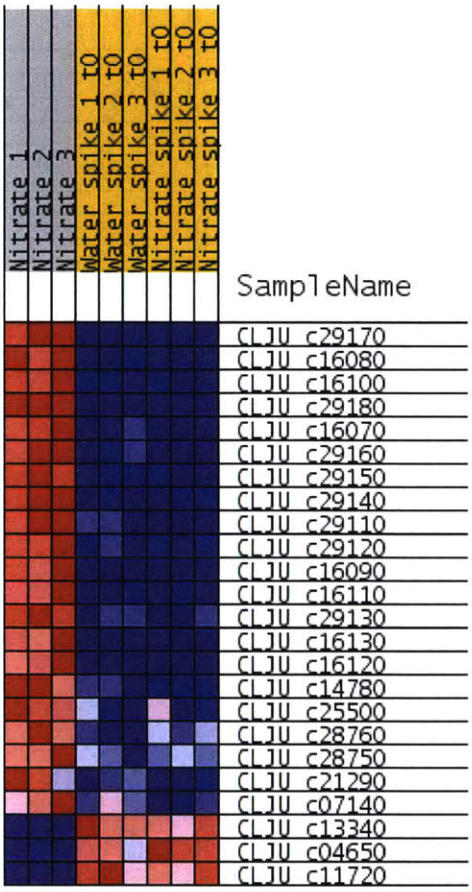

Figure A-25: GSEA gene abundance of phenylalanine, tyrosine, and tryptophan biosynthesis; red represents up-regulation under those conditions and blue represents down-regulation.

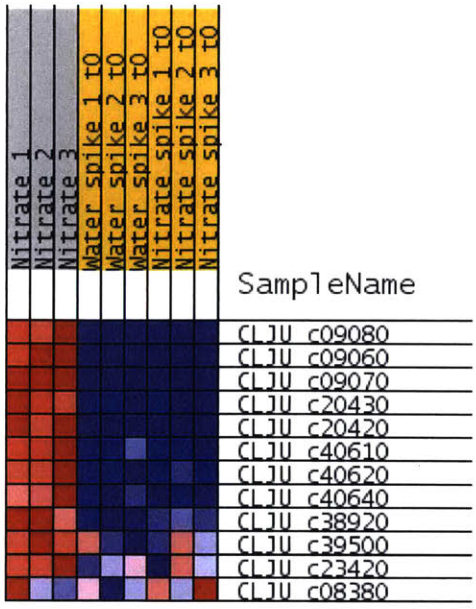

Figure A-26: GSEA gene abundance of C5-branched acid metabolism; red represents up-regulation under those conditions and blue represents down-regulation.

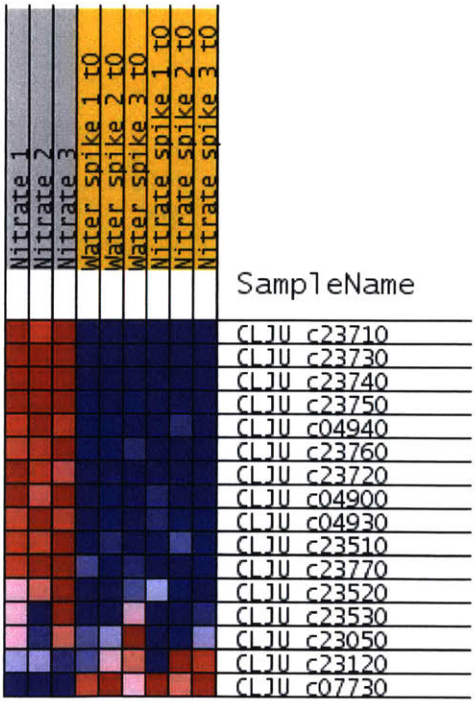

Figure A-27: GSEA gene abundance of nitrate metabolism; red represents up-regulation under those conditions and blue represents down-regulation.

Appendix B

Supporting Information - Theoretical Analysis of Natural Gas Recovery from Marginal Wells with a Deep Well Reactor

B.1 Model Supplemental Information

B.1.1 Transition between gas flow regimes

Correlations for these flow regime transitions have been experimentally verified by other researchers to have an average error of 10% for the liquid and gas properties of the case study [240]. Here u_{trans} is the transition superficial velocity, and u_{sb} and u_{lb} is the superficial rise velocity of small and large bubbles, respectively. From these, the gas holdup for different regimes can be determined (**Equations** B.4 and B.5) [240].

$$\frac{u_{trans}}{u_{sb}} = 0.5 \exp\left(-193\rho_G^{-0.61}\mu_L^{0.5}\sigma_L^{0.11}\right) \tag{B.1}$$

$$\frac{u_{sb}\mu_L}{\sigma_L} = 2.25\left(\frac{\sigma_L^3\rho_L}{g\mu_L^4}\right)^{-0.273}\left(\frac{\rho_L}{\rho_G}\right)^{0.03} \tag{B.2}$$

$$\frac{u_{lb}}{\sigma_L} = \frac{u_{sb}\mu_L}{\sigma_L} + \left[\frac{\mu_L\left(u_G - u_{trans}\right)}{\sigma_L}\right]^{0.757} \left(\frac{\sigma_L^3 \rho_L}{g\mu_L^4}\right)^{-0.077} \left(\frac{\rho_L}{\rho_G}\right)^{0.077} \tag{B.3}$$

$$\epsilon_G = \frac{u_G}{u_{sb}} \qquad \text{when} \qquad u_G \leq u_{trans} \tag{B.4}$$

$$\epsilon_G = \frac{u_G}{u_{sb}} + \frac{u_G - u_{trans}}{u_{lb}} \qquad \text{when} \qquad u_G > u_{trans} \tag{B.5}$$

B.1.2 Physical properties of water

The physical parameters of the system were calculated at the temperature (K) indicated, by curve fitting the data from CRC Handbook of Chemistry and Physics 90th Edition [246] or with published interpolations [247]. Density ($kg\ m^{-3}$) was fit using a second order polynomial with Temperature (**Equation** B.6), viscosity ($Pa\ s$) was fit with the Andrade equation (**Equation** B.7) [248], and surface tension ($N\ m^{-1}$) found by a published correlation (**Equation** B.8) [247]. The unit for 'T' in all equations is Kelvin.

Density of water

$$\rho_L \left(\frac{kg}{m^3}\right) = (-3.033x10^{-3})T^2 + (1.515)T + 815 \tag{B.6}$$

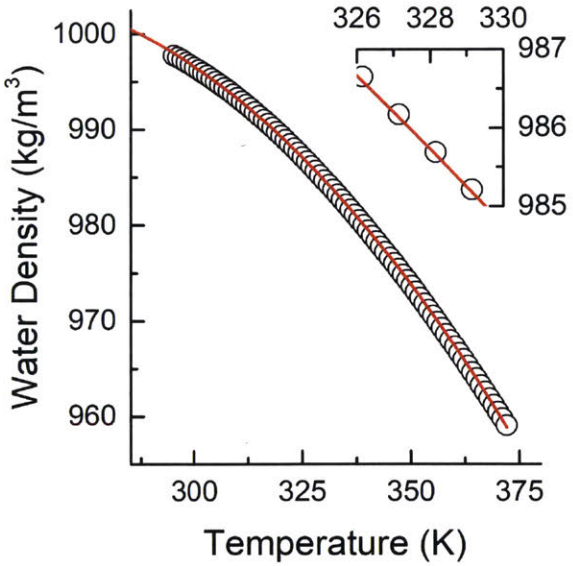

Figure B-1: The density of liquid water, as plotted from the CRC Handbook of Chemistry and Physics 90th Edition [246]. Open circle, data; red line, model correlation. Inset shows data near 55^{o}C.

Viscosity of water

$$\mu_L\ (Pa * s) = (1.066x10^{-3})\ \exp\left[\frac{2.020x10^3}{T}\right] \tag{B.7}$$

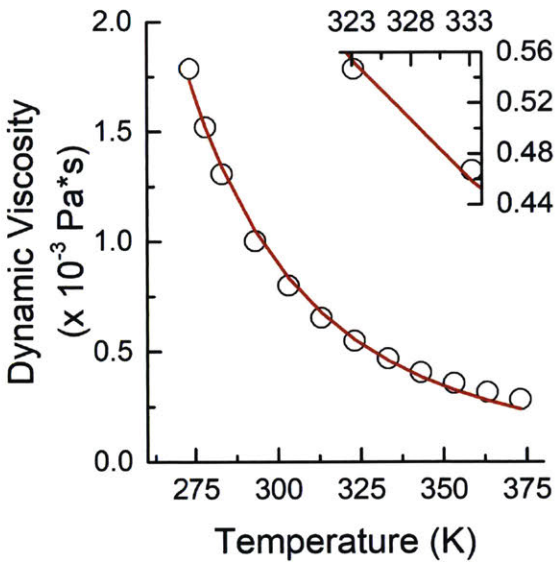

Figure B-2: The dynamic viscosity of liquid water, as plotted from the CRC Handbook of Chemistry and Physics 90th Edition [246] and fit with the Andrade equation [248]. Open circle, data; red line, model correlation. Inset shows data near 55^{o}C.

Surface tension of water

$$\sigma_L\left(\frac{N}{m}\right) = 235.8x10^{-3}\left[\frac{647.15-T}{647.15}\right]^{1.256}\left[1-0.625\left(\frac{647.15-T}{647.15}\right)\right] \qquad \text{(B.8)}$$

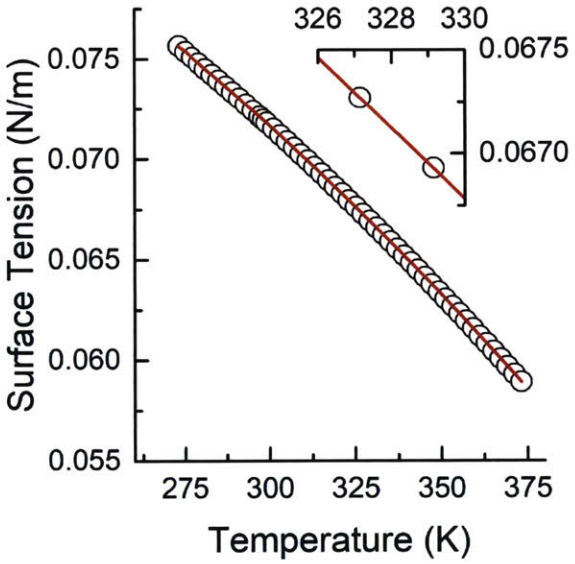

Figure B-3: The surface tension of liquid water, as plotted from the CRC Handbook of Chemistry and Physics 90th Edition [246]. Equation presented from literature [247]. Open circle, data; red line, model correlation. Inset shows data near 55°C.

B.1.3 Diffusion coefficient of methane in water

Diffusivity of a dilute gas in water can be calculated a number of ways; for infinite dilution, the Wilke-Chang correlation is generally used for its simplicity and low error (¡10%) in various solute-solvent systems [248]. However, the error of this approach for methane-water is relatively large at higher temperatures [248]. For this reason, experimental data in literature from Jahne et. al. (10 to 35°C) [251] and Witherspoon et. al. (4 to 60°C) [252] has been used to calculate a consensus activation energy (16.78 $kJ\ mol^{-1}$) and pre-exponential factor ($1543x10^{-9}\ m^2\ s^{-1}$) for the Arrhenius equation [251].

$$D_{CH_4:H_2O}\left(\frac{m^2}{s}\right) = (1542x10^{-9})\exp\left(\frac{-16781}{8.314\ T}\right) \tag{B.9}$$

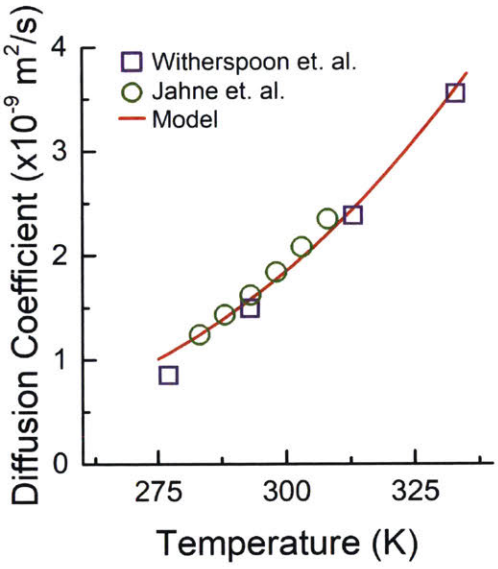

Figure B-4: The diffusion coefficient of methane in liquid water [252, 251].

The Wilke-Chang model equation is another method to estimate diffusion coefficient if experimental data is not present (**Equation** B.10). Here $D_{CH_4:H_2O}$ is the diffusion coefficient of methane at low concentrations in water, ϕ is the association factor of solvent (2.6 is suggested for water), V_{CH_4} is the molar volume of the solute methane at its normal boiling temperature (99.2 $cm^2\ mol^{-1}$), and MW_{H_2O} is the molecular weight of the solvent water (18 $g\ mol^{-1}$). This model generally under pre-

dicts the diffusion coefficient when compared to the experimental data for methane. For this reason, the experimental data will be used.

$$D_{CH_4:H_2O}\left(\frac{m^2}{s}\right) = \frac{7.4x10^{-1}\left(\phi \mathrm{MW}_{H_2O}\right)^{0}.5T}{\mu_L V^0_{CH_4}.6} \tag{B.10}$$

B.1.4 Henry's Law

Due to the low solubility of methane, the interfacial concentration in the liquid phase was modeled with Henrys law (**Equation** B.11) and an empirical correlation from literature (**Equation** B.12) [246]. Here, X_l (**Equation** B.13) is the mole fraction dissolved at 1 atm and $T^* = T/100K$. For methane, A = -115.6477, B = 155.5756, C = 65.2553, and D = -6.1698. The mass transfer limitations in the gas phase are assumed to be negligible, so the bulk and interface concentration in the gas phase are approximately the same (**Equation** B.14).

$$C^*_{Gi} = HC^*_{Li} \tag{B.11}$$

$$\ln(X_l) = A + \frac{B}{T^*} + C\ln(T^*) + DT^* \tag{B.12}$$

$$X_l = \frac{n_i}{n_w + n_i} = \frac{C^*_{Li}}{C_w + C^*_{Li}} \rightarrow C^*_{Li} = \frac{X_l C_w}{1 - X_l} = \frac{X_l \rho_L}{(1 - X_l)\,\mathrm{MW}_{H_2O}} \tag{B.13}$$

$$C^*_{Gi} \cong C_{Gi} = \frac{P_i}{RT} \tag{B.14}$$

The dimensionless Henrys coefficient is found by combining **Equation** B.11, B.12, and B.13, and multiplying the density of water by the molecular weight of the dissolved species (**Equation** B.15). Here P_i is 1 atm as stipulated by the empirical correlation. At 55°C, $X_l = 1.8x10^{-5}$, corresponding to a Henrys coefficient of 38.3.

$$H_i = \left(\frac{1\ atm}{RT}\right)\left(\frac{1 - X_l}{X_l \rho_l}\right)\mathrm{MW}_{H_2O} \tag{B.15}$$

B.2 Compressor Power Requirement

If aerobic methanotrophs are to be used in the system, oxygen (or air) must be supplied. One option is compressing air on site to the necessary pressure and co-feeding with methane. The amount of oxygen to be supplied is set to be stoichiometric with experimental results from aerobic methanotrophs, such as Methylococcus capsulatus [264]:

$$CH_4 + 1.8\ O_2 \rightarrow Bacteria + 0.34\ CO_2 \tag{B.16}$$

Under the base case conditions, the methane flow rate and pressure are $F_{G,mol} = 0.0746\ mole\ CH_4\ s^{-1}$ and $P = 11.21\ atm$. Hence the required oxygen would be 1.8 times the moles of methane. Accounting for the composition of air as 21% O_2, the required flow rate of air would be $F_{G,mol} = 0.639\ mole$ air s^{-1}. This corresponds to $33.1 cfm$.

The power input to adiabatically compress air to the given pressure of 11.21 atm, with inter-stage cooling, is found with the following equation [265], which accounts for an 80% efficiency due to losses from friction:

$$W = \frac{n\gamma F R T_1}{0.8\,(\gamma - 1)} \left[\left(\frac{P_2}{P_1}^{\frac{\gamma-1}{n\gamma}} \right) - 1 \right] = 5.73\ kW \tag{B.17}$$

Where:

$$n = \text{number of stages, here taken as 2} \tag{B.18}$$

$$\gamma = \text{ratio of heat capacities, here taken as 1.41 for air} \tag{B.19}$$

$$T_1 = \text{initial absolute temperature, 298 K} \tag{B.20}$$

$$\frac{P_2}{P_1} = \text{absolute pressure ratio, 11.21 atm / 1 atm} \tag{B.21}$$

$$R = \text{gas constant, 8.314 J/K/mol} \tag{B.22}$$

$$F = \text{molar flow rate of gas, 0.639 mol/s} \tag{B.23}$$

Based on the lower heating value of methane, 802.3 $MJ\ kmol^{-1}$, and the flow rate

of methane into the well, 0.0746 $mol\ s^{-1}$, the energy input into the well is 59.8 kW. Hence, powering the compression of air would result in a 10% decrease in efficiency.

Another option is to supply pure oxygen, as it will reduce the dilution effect of the nitrogen in the gas phase. However this will greatly increase costs so as to separate the two gases.

B.3 Distance between Abandoned Wells in Pennsylvania

Latitude and longitude data for abandoned wells in Pennsylvania can be found online from the Pennsylvania state government (link provided below) [266]. When plotted, there is significant clustering of wells within the geological formation (**Figure** B-5). The distance between each well was computed while accounting for the curvature of Earth, assumed to be a perfect sphere of 6371 km in diameter.

For each well, the nearest 15 neighbors were found and the average distance between the nearest neighbors was calculated (resulting in a group of 16). The average distance between the 16 nearest neighbors was 1100 m, with 69% of these groupings having an average distance of less than 1000 m. Furthermore, 22% of wells have 16 nearest neighbors within an area of 10 hectares (2537 out of 11346; area measured by taking the maximum distance between wells in the group and calculating the circular area).

The grouping was decreased from 16 wells, to 10, 5, and 2, resulting in the following distributions (**Figure** B-6). For groupings of 10 wells, the likelihood of having the 10 nearest neighbors within 10 hectares greatly increases to from 22 to 43% (as compared to 16 wells in 10 hectares). The implication is that these wells can potentially be connected in novel configurations to improve flow rate, productivity, etc.

Abandoned Oil and gas wells in Pennsylvania: http://www.portal.state.pa.us/portal/server.pt/community/abandoned___orphan_well_program/20292

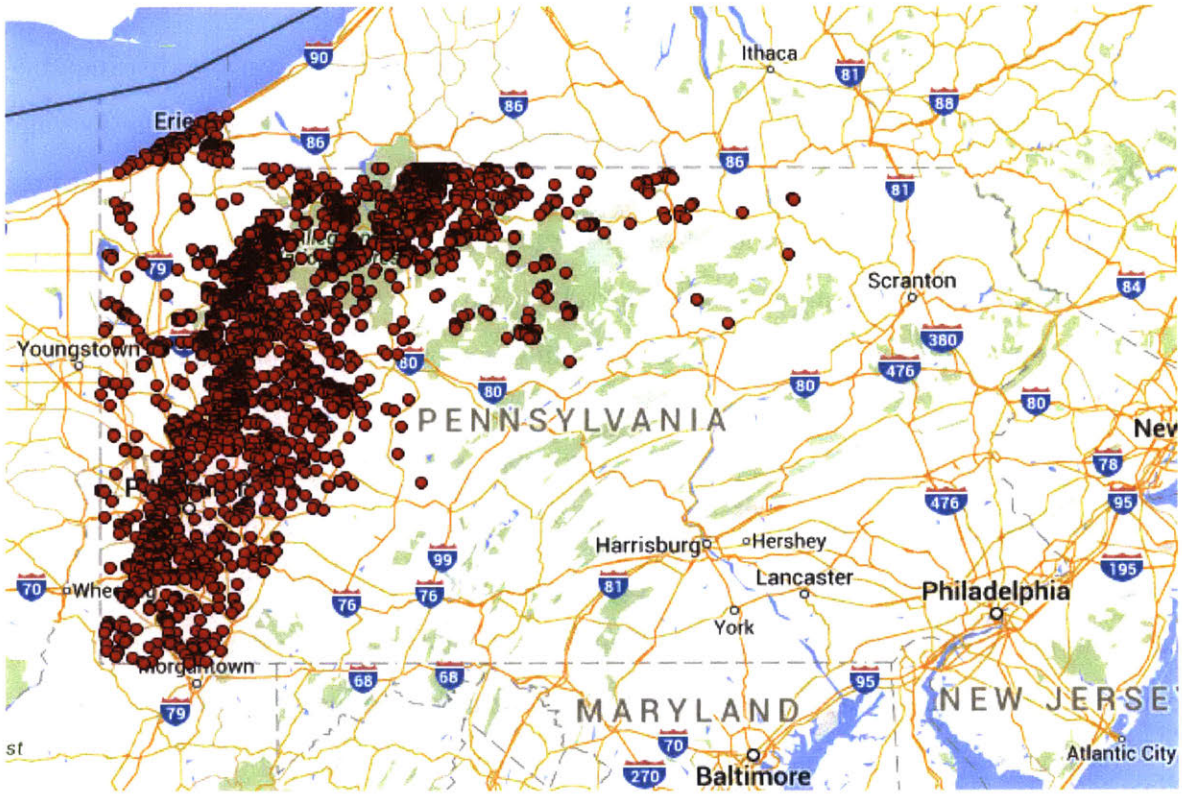

Figure B-5: Map of abandoned oil and gas wells in Pennsylvania, visualized with GPS Visualizer.

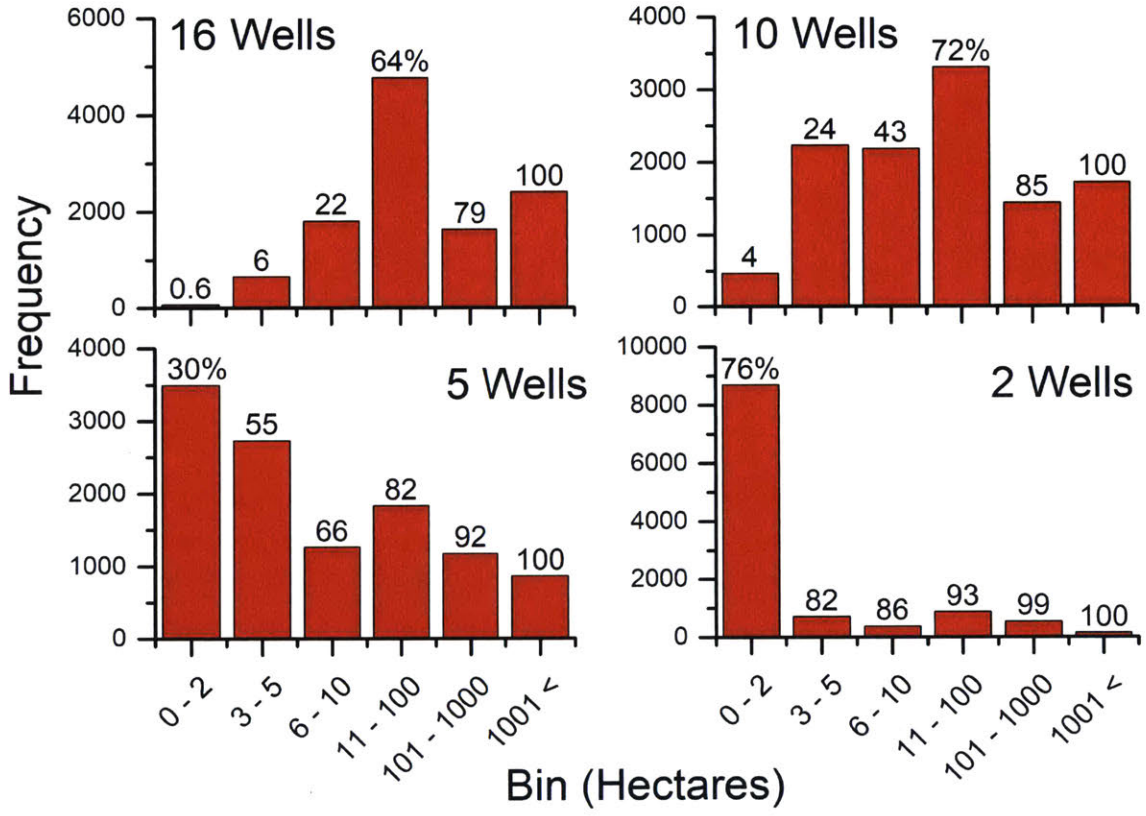

Figure B-6: Frequency of a specified number of abandoned wells appearing within a certain circular area. The distance between all abandoned wells in PA were computed, and the nearest neighbors to each well were determined. For each grouping size of wells (2, 5, 10, and 16), the maximum area occupied by that group was calculated and then plotted as a histogram. The histogram provides a probability of finding a set number of wells within a certain surface area of hectares.

Appendix C

Calculating yields from stoichiometric pathways

The models used in this work were built from lists of the individual pathways in the network [148]. Constraints on the net generation of certain of the species involved in these reactions were then used to determine the linear combination of pathways that stoichiometrically linked substrate use to product synthesis while accounting for generation and consumption of co-factors. This combination was essentially the overall stoichiometry of the process, from which the yield can be easily calculated. Simple pathway networks can be solved by hand, but more complex systems benefit from a linear algebra approach, as will be shown in the example below. The general procedure was as follows: First, all relevant reactions were listed, along with their co-factors (NADH and ATP). Second, this information was converted into a matrix A with each species involved forming a row, and the stoichiometry of each reaction forming a column. The number of degrees of freedom was noted. The equation to be solved was of the form

$$Ax = b \tag{C.1}$$

where x was a vector containing the relative stoichiometry of each pathway, and b was a vector containing the stoichiometric coefficient of each species in the final

equation. Third, a basis was chosen (usually 1 mol of product), and the constraints of no ATP, NADH or intermediate accumulation were applied by setting the relevant values in b to 0. Fourth, as not all coefficients in b were known a priori (i.e. CO_2 and H_2 consumption), these terms were redefined as variables and algebraically relegated to the x vector. Finally, in the case of remaining degree of freedom, this was satisfied by adding reactions corresponding to biomass generation. The result was a well-defined system of equations that can be solved for the relative stoichiometries of the pathways and final overall stoichiometry. It was important to note that such a model contains no kinetic information, merely the relative rates of each pathway.